

DISSERTATION

**Seismicity and structure of a magmatic accretionary centre at
an ultraslow spreading ridge:**

The volcanic centre at 85°E/85°N, Gakkel Ridge

zur Erlangung des Grades Dr. rer. nat.,
vorgelegt dem Fachbereich Geowissenschaften
der UNIVERSITÄT BREMEN
von

Edith I.M. KORGER

Alfred-Wegener-Institut
Helmholtz-Zentrum für Polar- und Meeresforschung
Bremerhaven

Bremerhaven, July 29, 2013

Name: Edith Ingrid Maria Korger

Datum: July 29, 2013

Anschrift: Georg-Seebeck-Str. 60, 27570 Bremerhaven

ERKLÄRUNG

Hiermit versichere ich, dass ich

1. die Arbeit ohne unerlaubte fremde Hilfe angefertigt habe,
2. keine anderen als die von mir angegebenen Quellen und Hilfsmittel benutzt habe
3. die den benutzten Werken wörtlich oder inhaltlich entnommenen Stellen als solche kenntlich gemacht habe.

Bremerhaven, den

Edith I.M. Korger

FAR BETTER AN APPROXIMATE ANSWER TO THE RIGHT QUESTION,
WHICH IS OFTEN VAGUE,
THAN AN EXACT ANSWER TO THE WRONG QUESTION,
WHICH CAN ALWAYS BE MADE PRECISE.

John Tukey (1915-2000)

For my father.

Contents

Erklärung	i
Summary	ix
Zusammenfassungxiii
1 Introduction and Motivation	1
1.1 The spreading of ultraslow mid-ocean ridges	3
1.2 Explorations at the ultraslow spreading Gakkel Ridge	9
1.3 Motivation and scope	12
1.3.1 Framework	12
1.3.2 Outline	12
2 Datasets	15
2.1 Clusters of seismicity	15
2.1.1 1999 teleseismic earthquake sequence, Gakkel Ridge	15
2.1.2 Other seismicity sequences, ARS and SWIR	15
2.2 Local Seismicity - 85°E/85°N	16
3 Methods	19
3.1 Evaluation of the performance of different localization algorithms	19
3.1.1 Quantification of localization errors	20
3.1.2 NonLinLoc localization of teleseismic earthquakes at Lena Trough	23
3.2 Seismicity sequence analysis	26
3.2.1 Types of earthquake clusters	26
3.2.2 Background statistical information	27
3.2.3 Modified Omori-Law	28
3.2.4 Datasets and method	30
3.2.5 Results and interpretation of specific seismicity clusters	35
3.3 Local seismicity at 85°E/85°N	40
3.3.1 Preparation of local dataset and localization with Hyposat	40
3.3.2 Local earthquake tomography	43
4 Contributions to scientific publications	47
4.1 Performance of localization algorithms for teleseismic mid-ocean ridge earthquakes: The 1999 Gakkel Ridge earthquake swarm and its geological interpretation	47

4.2	Characteristics of tectonomagmatic earthquake swarms at the Southwest Indian Ridge between 16°E and 25°E	48
4.3	Seismicity and structure of the 85°E volcanic complex at the ultraslow spreading Gakkel ridge from local earthquake tomography	48
5	First paper: The 1999 earthquake swarm at 85°E/85°N.	51
5.1	Summary	51
5.2	Introduction	52
5.3	Dataset and Methods	54
5.3.1	Teleseismic dataset	54
5.3.2	Methods	55
5.3.2.1	Absolute linearized, iterative localisation routine HYPOSAT	56
5.3.2.2	Absolute probabilistic routine NonLinLoc	57
5.3.2.3	Relative linearized localisation routine Mlocate	59
5.4	Results and interpretation of location algorithm performance	59
5.4.1	Comparison of relocation results by the three routines	60
5.4.2	Performance of location algorithms	63
5.5	Geologic interpretation of the 1999 earthquake swarm	64
5.5.1	Temporal evolution of the swarm	64
5.5.2	Spatial development	65
5.6	Conclusion	71
5.7	Acknowledgments	72
5.8	Literature	72
6	Second paper: Earthquake clusters at the Southwest Indian Ridge . . .	77
6.1	Summary	77
6.2	Introduction	78
6.3	Geological Setting	80
6.4	Methods	81
6.4.1	Extraction of events from the VNA2 data set	81
6.4.2	Relocalization of teleseismic earthquakes	82
6.4.3	Magnitude determination of the regional data set	84
6.4.4	Swarm analysis	85
6.5	Results	86
6.5.1	Relocalization of teleseismic earthquakes	86
6.5.2	Regional earthquakes	87
6.5.2.1	Magnitudes	87
6.5.2.2	Identification of swarms	90
6.5.2.3	Swarm characteristics	90
6.6	Interpretation	93
6.6.1	Regional data set of SWIR seismicity	93
6.6.2	Teleseismic evidence of SWIR swarms	94
6.6.3	Evidence for magmatic accretion episodes witnessed by the VNA2 array	96
6.6.3.1	Swarm origin	96

6.6.3.2	Swarm site - source site of active magmatism?	97
6.7	Conclusion	99
6.8	Acknowledgements	99
6.9	Literature	100
7	Third paper: Seismicity and structure of the 85°E volcanic complex . .	105
7.1	Summary	105
7.2	Introduction	105
7.3	Dataset and methods	108
7.3.1	Local earthquake dataset	108
7.3.2	Reference velocity model and starting hypocentres for tomographic inversion	109
7.3.3	3D Seismic travelttime tomography	111
7.3.3.1	3D Reference model	112
7.3.3.2	Source relocation and grid parametrization	112
7.3.3.3	Model regularization	114
7.4	Results	115
7.4.1	Checkerboard test	118
7.4.2	Restoration test	119
7.5	Interpretation and discussion	122
7.5.1	Distribution of seismicity	122
7.5.1.1	Seismicity rate	122
7.5.1.2	Moho depth	122
7.5.1.3	Hypocentre depths	123
7.5.2	Seismic velocities and structure	124
7.6	Conclusion	126
7.7	Acknowledgments	126
7.8	Supplementary Material	128
7.9	Literature	132
8	Conclusion and Outlook	137
9	Acknowledgements	141
10	Complete Bibliography	143
11	List of Figures	157
12	List of Tables	159
	Curriculum Vitae	161

Summary

Mid-ocean ridges are divergent plate boundaries, where the seafloor spreads apart and new oceanic crust is formed. Yet, there are important differences between these individual ridges, which seem to be linked to the rate with which they spread apart. At full spreading rates of < 20 mm/yr, these ridges are called 'ultraslow' spreading, and their appearance is drastically different from ridges which spread faster.

Generally, ultraslow spreading ridges have a very rugged appearance, with steep rift flanks which contain numerous normal faults, and discontinuous volcanic activity in space and time at discrete volcanic centres. Magma supply is thought to be extremely limited, as mantle flow models infer a reduced melt production owing to the greater conductive cooling compared to faster spreading ridges. Crustal thickness as well is thought to be affected by the greater conductive heat loss of the ascending mantle, resulting in thick crust at volcanic centres, and only thin or absent crust in between. However, the processes which cause this are still only poorly understood. Ultraslow spreading ridges consist of alternating magmatic and amagmatic segments, each emphasizing a primary accretionary mode. Magmatic segments are robustly magmatic, with basalts exposed on the seafloor and axial volcanic ridges. In contrast, at amagmatic segments volcanic activity seems to be almost absent, and plate divergence is accommodated by the uplift of mantle horst blocks. Predominantly peridotites are dredged from the seafloor, interrupted by isolated centres of volcanic activity.

Due to the remote locations of the two main representatives of this spreading class (Arctic Ridge System, Southwest Indian Ridge), only few surveys have so far been conducted. Gakkel Ridge, as part of the Arctic Ridge System, lies in the perennial ice covered Arctic Ocean far from any land, and the Southwest Indian Ridge is located between South Africa and Antarctica in latitudes with frequent storms. Both environmental conditions inhibit seismic surveys by making the loss of instruments likely, therefore so far seismicity studies of local earthquakes in particular are sorely missing. Yet, these kind of surveys are necessary to constrain information about the mechanical and thermal state of the lithosphere.

In 1999, an exceptional earthquake sequence was teleseismically registered. This clustered seismicity was unusual in several aspects: The magnitudes involved (up to $m_b = 5.2$), the number of events registered (252 earthquakes) and the duration of activity (9 months). It originated at $85^\circ\text{E}/85^\circ\text{N}$ at a volcanic centre in the eastern part of Gakkel Ridge where the spreading rate is about 10.2 mm/yr. The major part of this PhD-thesis deals with the investigation of this volcanic centre, first through the teleseismic sequence

dataset and second through analysis of a local dataset gathered in 2007. This was published in two scientific publications. For any kind of analysis of the earthquake sequence of 1999 at 85°E/85°N, reliable earthquake locations were needed. In the first part of my PhD-thesis, I analyzed this entire teleseismic earthquake sequence, first relocating the sequence, and second placing the obtained earthquake locations in a geological context. I relocated the entire teleseismic earthquake sequence with three different localization algorithms (NonLinLoc, Hyposat and Mlocate). While studying parameters which may influence the resulting locations systematically, I compiled a sub-dataset of reliably located events. Yet, locations from the different algorithms sometimes do not even match within their error ellipses. Thus, the choice of location algorithm has a critical influence on the use of a dataset which lacks nearby recording stations, and has to be made carefully. For absolute single-event localization, I preferred earthquake locations calculated by the algorithm NonLinLoc, which were placed closest to the epicentres calculated by the relative algorithm Mlocate. Both programs placed their epicentres farthest from locations calculated by the algorithm Hyposat. A temporal analysis of the earthquake sequence inferred three phases of activity, each with its own distinct character of seismicity. I visualized the most probable centre of earthquake activity in each phase and interpreted a complex interplay of tectonic and magmatic processes. In the first phase of seismicity the crust breaks either accompanying or enabling magmatic intrusion, followed by the second phase of seismicity during which the area producing seismicity got larger. The third phase of seismicity probably resulted from a post-intrusion adjustment of the stress field, or a transition to an effusive stage of volcanism.

The modified Omori-Law describes the declining aftershock rate of tectonic mainshock-aftershock sequences with succeeding time. It can thus be used to determine, if an observed seismicity sequence is tectonic in origin. I extensively researched this relationship for the second part of my PhD-thesis, and tried to match the modified Omori-Law to all suitable seismicity clusters at ultraslow spreading ridges. Yet, an exclusively tectonic origin could not be proved and therefore, the origin of these earthquake clusters most likely was influenced by magmatic interaction.

Figuratively returning to the 85°E/85°N volcanic centre at Gakkel Ridge, I extensively analyzed a 16-day local dataset which had been collected in 2007, using seismometer arrays installed on ice floes which drifted over the survey area. This dataset shows the seismological aftermath of the spreading episode of 1999 at Gakkel Ridge, seven years after the major seismic activity. Due to the drift of the ice-floes, each earthquake was recorded at different station locations. This resulted in a sufficient ray coverage, suitable for the first local earthquake tomography ever done at an ultraslow spreading centre and this analysis formed a major third part of my PhD-thesis.

I picked over 300 seismic events by hand, compiled a local velocity model from confidently-located hypocentres, located 248 hypocentres with this local velocity model, and generated a local earthquake tomographic model. The results infer a Moho at 7 km below seafloor, which implies an exceptionally thick crust. Deep hypocentres point to a cold lithosphere,

in contrast to existing thermal models. An area of slower seismic velocities crosses the rift valley at the supposed site of volcanic activity in 1999. I interpreted the observed velocity anomalies to predominantly stem from the relaxation of thermal stresses following a recent intrusion.

This PhD project gives several important insights into the seismological processes that accompany tectono-magmatic interactions at ultraslow spreading mid-ocean ridges. It culminated in the first local earthquake tomography ever done at a volcanic spreading centre of a magmatic segment at such a ridge. The unique results show that theoretical thermal models may have to be further refined, to accurately reflect spreading processes at ultraslow spreading ridges.

Zusammenfassung

Mittelozeanische Rücken sind divergente Plattengrenzen, an denen sich zwei Platten voneinander wegbewegen und neue ozeanische Kruste gebildet wird. Individuelle mittelozeanische Rücken unterscheiden sich jedoch wesentlich voneinander, diese Unterschiede haben augenscheinlich mit der Spreizungsgeschwindigkeit zu tun. Ab einer Spreizungsrate von weniger als 20 mm pro Jahr ändert sich die Rückenmorphologie drastisch im Vergleich zu schneller spreizenden Rücken. Diese speziellen, extrem langsam spreizenden Rücken werden 'ultralangsam' spreizend genannt.

Generell haben ultralangsam spreizende Rücken ein sehr schroffes Aussehen, das durch steile Riftflanken, die von vielen Abschiebungsbrüchen durchfurcht sind, verursacht wird. An vulkanischen Zentren wird diskontinuierliche vulkanische Aktivität in Raum und Zeit beobachtet. Es wird vermutet, dass der Nachschub an Magma äußerst begrenzt ist, da theoretische Modelle eine Abnahme der Magmenproduktion voraussagen. Man nimmt an, dass diese Abnahme durch einen größeren Wärmeverlust im Vergleich zu schneller spreizenden Rücken verursacht wird. Es wird ebenfalls vermutet, dass auch die Krustendicken dadurch beeinträchtigt werden. Jedoch sind die Prozesse, die zu diesem begrenzten Magmennachschub führen, noch nicht genau verstanden.

Ultralangsam spreizende Rücken bestehen aus abwechselnd magmatischen und amagmatischen Segmenten, die jeweils auf den Hauptprozess krustaler Akkretion hinweisen. Magmatische Segmente sind stabil magmatisch mit bedeutenden vulkanischen Zentren und Basalte liegen frei am Meeresboden. Im Gegensatz dazu fehlt vulkanische Aktivität in amagmatischen Segmenten fast überall. Spreizung an solchen Segmenten geht hauptsächlich durch Dehnung und Ausdünnung der Kruste entlang von Abschiebungsbrüchen die bis in den Mantel reichen, oder basalen Abschiebungen vorstatten, Peridotit ist am Meeresboden aufgeschlossen.

Durch die schwer zugängliche Lage der zwei Hauptvertreter dieser Spreizungsklasse (Arktisches Rückensystem, Südwest-Indischer Rücken) wurden allerdings bis jetzt nur wenig wissenschaftliche Studien durchgeführt. Der Gakkel Rücken, als Teil des Arktischen Rückensystem, liegt weit von den nächsten seismologischen Landstationen entfernt im dauerhaften Eis des Arktischen Ozeans. Der Südwest-Indische Rücken seinerseits erstreckt sich zwischen Südafrika und der Antarktis, in einem Gebiet in dem häufige Stürme wissenschaftliche Studien erschweren. Speziell mikroseismologische Studien fehlen bis dato aufgrund der schwierigen Bedingungen, obwohl diese Informationen zum Verständnis des mechanischen und thermalen Status der Lithosphäre wesentlich beitragen könnten.

1999 wurde außergewöhnliche Erdbebenaktivität an teleseismischen Stationen registriert, ungewöhnlich in Bezug auf die Magnituden der Erdbeben (bis zu $m_b = 5.2$), die Anzahl der Beben (252) und die Dauer der Erdbebenaktivität (9 Monate). Die Beben entstanden an einem vulkanischen Zentrum am Gakkel Rücken bei $85^\circ\text{E}/85^\circ\text{N}$, der an dieser Stelle mit etwa 10.2 mm pro Jahr spreizt. Der Hauptteil meiner Dissertationsschrift besteht aus der Untersuchung dieses vulkanischen Zentrums, zuerst durch Analyse der teleseismischen Erdbebenaktivität, und danach durch Untersuchung von Mikroseismizität, die 2007 von lokalen seismischen Stationen aufgenommen wurde. Diese Analysen wurden in zwei umfassenden wissenschaftlichen Veröffentlichungen dargestellt.

Für die Untersuchung der Erdbebenaktivität von 1999 an $85^\circ\text{E}/85^\circ\text{N}$ war eine verlässliche Bebenlokalisierung unerlässlich. Ich berechnete daher die Bebenherde mit drei sehr unterschiedlichen Lokalisierungsalgorithmen (NonLinLoc, Hyposat und Mlocate). Durch Untersuchung verschiedener Parameter, die das Lokalisierungsergebnis systematisch beeinflussen können, stellte ich ein Datenset aus zuverlässig lokalisierten Herdorten zusammen. Ein Hauptergebnis der Lokalisierung mit diesen unterschiedlichen Algorithmen war, dass die berechneten Bebenherde der drei Lokalisierungsalgorithmen öfter nicht einmal innerhalb der Fehlerellipsen übereinstimmten. Die Wahl des Lokalisierungsalgorithmus hat offensichtlich einen kritischen Einfluß auf die berechneten Herdorte von Erdbeben an mittelozeanischen Rücken, die nicht von nähergelegenen Landstationen aufgezeichnet werden können. Der Algorithmus muß daher sorgfältig gewählt werden. Für Absolutlokalisierung zog ich durch NonLinLoc berechnete Bebenherdorte vor, da sie nahe an den berechneten Bebenorten von Mlocate lagen. Die Bebenorte beider Programme lagen am weitesten von den durch Hyposat berechneten Bebenorten entfernt. Eine zeitliche Analyse der Erdbebenaktivität brachte drei, durch einen jeweils ausgeprägten Seismizitätscharakter definierte Phasen zum Vorschein. Ich stellte das wahrscheinlichste Zentrum der Erdbebenaktivität jeder der drei Phasen bildlich dar und interpretierte, dass ein komplexes Zusammenspiel von tektonischen und magmatischen Prozessen zum Gesamtbild der registrierten Seismizität geführt hat. In der ersten Phase brach die ozeanische Kruste. Dies wurde entweder durch eine magmatische Intrusion verursacht, oder es ermöglichte erst eine magmatische Intrusion. In der zweiten Phase vergrößerte sich das seismisch aktive Gebiet, und die dritte Phase spiegelt vermutlich entweder eine Anpassung des Stressfeldes an die neuen Gegebenheiten, oder zeigt einen Übergang zu effusivem Vulkanismus.

Das modifizierte Omori-Gesetz ('Modified Omori-Law') beschreibt eine abnehmende Nachbebenrate mit fortsetzender Zeit nach dem Mainshock einer tektonischen Bebensequenz. Dadurch kann man es benutzen um festzustellen, ob eine registrierte Erdbebensequenz ausschließlich tektonischen Ursprungs ist. Für den zweiten Teil meiner Dissertationsschrift recherchierte ich genauestens die Hintergründe dieses theoretischen Zusammenhangs und versuchte eine Anpassung an vier Erdbebensequenzen am Südwest Indischen Rücken. Eine Anpassung war jedoch nicht möglich, was den Schluss zulässt, dass diese Erdbebensequenzen sehr wahrscheinlich durch magmatischen Einfluß ausgelöst wurden. Die Ergebnisse meiner Analyse trugen wesentlich zu einer wissenschaftlichen Veröffentlichung bei.

Den dritten großen Beitrag zu meiner Dissertationsschrift lieferte die Analyse eines lokalen mikroseismischen Datensatzes, der am Gakkel Rücken im Gebiet des vulkanischen Zentrums ($85^{\circ}\text{E}/85^{\circ}\text{N}$) mit einer ungewöhnlichen Messmethode registriert wurde. Es wurden in Arrays arrangierte Seismometer eingesetzt, die auf Eisflößen über das Untersuchungsgebiet drifteten. Dieser 2007 aufgenommene Datensatz spiegelt das seismologische Nachspiel der teleseismisch registrierten Spreizungsepisode von 1999 an diesem ultralangsamem Rücken. Durch die Drift der Eisflöße wurde jedes lokale Beben an unterschiedlichen Stationskoordinaten registriert. Dies resultierte in einer ausreichenden Strahlüberdeckung für die erste, jemals durchgeführte Lokaltomographie an einem ultralangsam spreizenden Rückenzentrum.

Ich identifizierte händisch über 300 Erdbeben, erstellte ein lokales Geschwindigkeitsmodell durch Analyse von zuverlässig lokalisierten Bebenherden, und führte eine lokale Erdbeben-tomographie durch. Die Resultate zeigen eine tiefe Moho 7 km unter dem Meeresboden, was auf eine dicke, basaltische Kruste rückschließen läßt. Ungewöhnlich tiefen Bebenherde weisen auf eine kalte und dicke Lithosphäre hin. Dies steht im Widerspruch zu Vorhersagen existierender thermischer Modelle. Eine Zone mit herabgesetzten seismischen Geschwindigkeiten quert das Rifttal an der wahrscheinlichen Stelle vulkanischer Aktivität von 1999. Ich interpretierte, dass die aufgetretenen Geschwindigkeitsanomalien auf thermische Entspannungsprozesse nach magmatischer Aktivität zurückzuführen sind.

Diese Disseration erlaubt wichtige Einblicke in seismologische Prozesse, die tektonisch-magmatische Interaktionen an ultralangsam spreizenden, mittelozeanischen Rücken begleiten und präsentiert die weltweit erste lokalen Erdbebentomographie, an solch einem Rücken. Die einzigartigen Ergebnisse zeigen, dass theoretische thermische Modelle verbessert werden müssen, um Spreizungsprozesse an ultralangsamem Rücken treffend modellieren zu können.

1 Introduction and Motivation

Beneath the oceans of the world, a system of mountain ridges crosses the globe for more than 50,000 km. It has been known for a long time that these submarine mountain ridges exist, yet it was only after the theory of continental drift was formulated by Alfred Wegener at the beginning of the 20th century, that scientists came to recognize that mid-ocean ridges (MORs) form where the seafloor spreads apart and new oceanic crust is generated. This was put forth in the sea-floor spreading theory (e.g. *Vine and Matthews, 1963; Le Pichon, 1968*). Ever since, MORs all over the world have been under investigation.

Aside from spreading apart with spreading rates ranging from < 10 mm/yr to over 150 mm/yr full spreading rate, MORs differ from one another by having a highly varied appearance, at first glance depending on spreading rate (e.g. *Macdonald, 1982*) (Fig. 1.1). Fast spreading ridges look like a smooth mountain ridge (e.g. Fig. 1.1D), slower spreading ridges generally feature a sunken central valley with steep rift walls rising up parallel to the spreading axis at both sides (e.g. Fig. 1.1A).

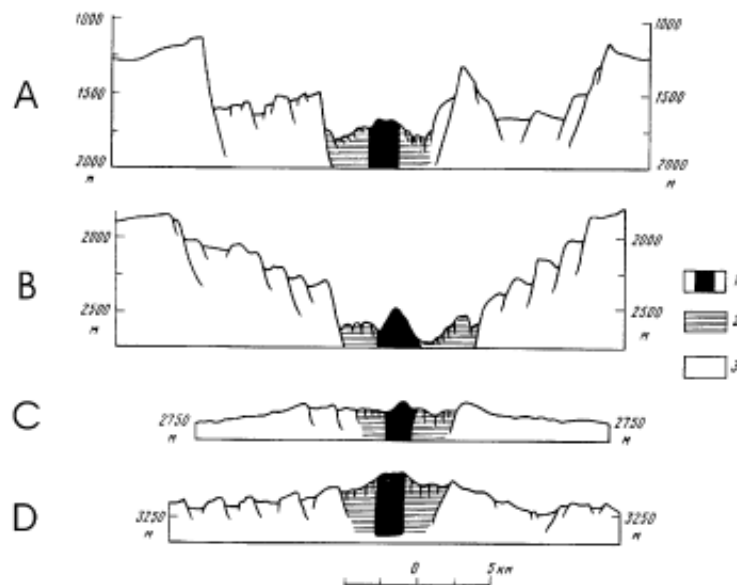


Figure 1.1 – Cross section of MORs with different spreading rates. (A) Red Sea Ridge, 18°N ($v= 1.5$ cm/yr); (B) Mid-Atlantic Ridge, 37°N ($v=2.5$ cm/yr); (C) East Pacific Rise, 21°N ($v= 6$ cm/yr); (D) East Pacific Rise, 3°S ($v=15$ cm/yr). (1) Extrusive zone; (2) axial valley; (3) flanking zone. From *Rundquist and Sobolev (2002)*.

Generally speaking, slow spreading ridges are have a wide axial rift valley with high rising rift flanks at both sides (*Rundquist and Sobolev, 2002*), and the slower the spreading rate, the more rugged the appearance. Transient volcanic activity is found within the rift valley at the segment centres, yet it is discontinuous in space and time (*Solomon, 1992*). *Bown and White* (1994) have shown that MORs at all but the slowest spreading ridges exhibit more or less uniform crustal thicknesses, bulk composition and rare earth element concentration. Yet, as spreading rate drops off below ~ 15 mm/yr, crustal thickness decreases and compositional changes are observed. Mantle flow models infer a decrease in melt production due to the greater conductive cooling (*Reid and Jackson, 1981; Bown and White, 1994*).

'Ultraslow spreading ridges' are fundamentally different from ridges which spread faster. *Dick et al.* (2003) adopted a threshold value of 12 mm/yr for this kind of ridges, below which changes in thermal structure and mantle composition critically affect crustal structure. Between 12 mm/yr and 20 mm/yr, characteristics of these MORs seem to vary between the slow and the ultraslow class. Due to the different values used by varying authors in scientific publications in recent years (e.g. *Bown and White, 1994; Dick et al., 2003; Standish et al., 2008; Sauter and Cannat, 2010*), I use in the following a threshold value of < 20 mm/yr below which I refer to ridges as 'ultraslow spreading ridges' (*Standish and Sims, 2010*).

1.1 The spreading of ultraslow mid-ocean ridges

The two main representatives of this class are the Southwest Indian Ridge (SWIR) (Fig. 1.2a), and the Arctic Ridge System (ARS) (Fig. 1.2b). Due to the inhospitable regions in which the SWIR and the ARS are found, much less is known about them than about faster spreading ridges.

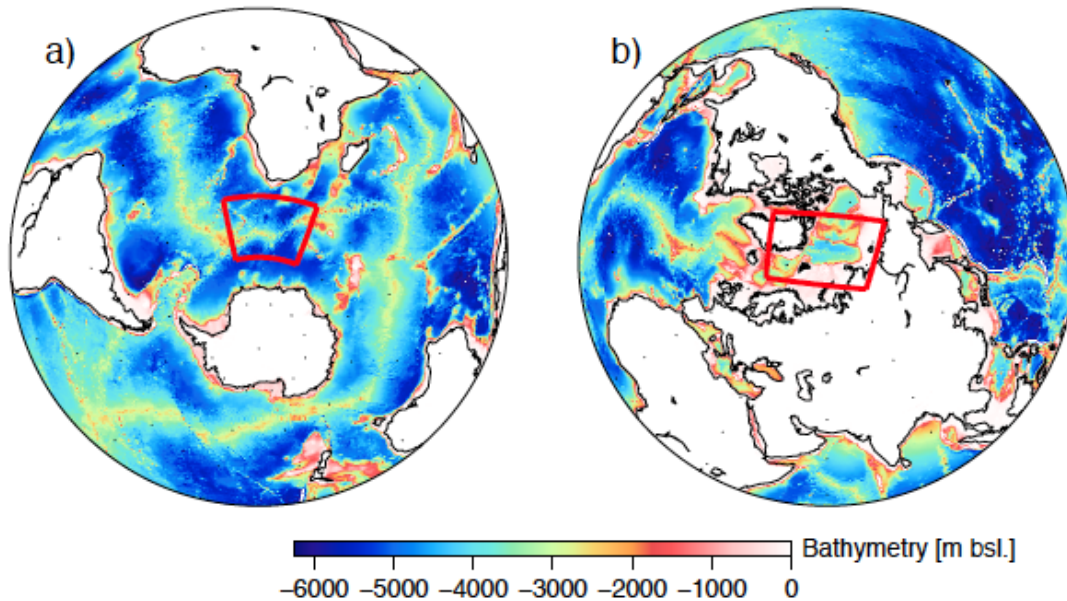


Figure 1.2 – Hemispheric overview of southern hemisphere (a) and northern hemisphere (b). Red boxes denote area of the Southwest Indian Ridge (a) and the Arctic Ridge System (b).

The SWIR is the major plate boundary separating Africa and Antarctica, crossing the 'furious fifties' which are known for their wave heights and frequent storms. It extends between two Triple Junctions, one in the southern Atlantic Ocean (Bouvet Triple Junction) and the other in the Indian Ocean (Rodrigues Triple Junction) (Fig. 1.3). In between, several segments are offset by extended transform faults. The segment extending from 16°E to 25°E is called the magmatic spreading Orthogonal Supersegment, and its seismicity is being analyzed in a part of this PhD thesis.

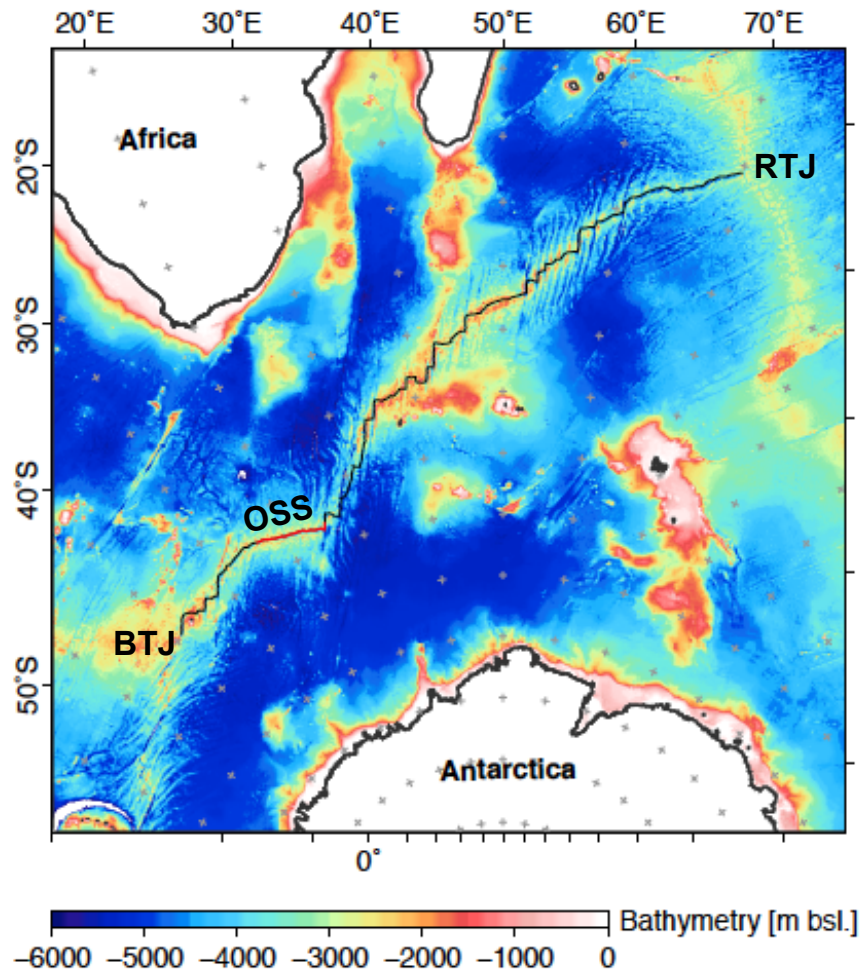


Figure 1.3 – Overview of the Southwest Indian Ridge which is denoted by a thin black line. ETOPO2 bathymetry after (*Smith and Sandwell, 1997*). Marked are the Rodriguez Triple Junction (RTJ), the Bouvet Triple Junction (BTJ), and the Orthogonal Supersegment (OSS), which is also marked by a red line from 16°E to 25°E.

The ARS forms the North America-Eurasia plate boundary with a full spreading rate at its southwestern end of 17.2 mm/yr, and 6.3 mm/yr at its eastern termination (*DeMets et al., 1994*). The most prominent part of the ARS is Gakkel Ridge (GR) as its spreading rate end-member, which spans ~ 1800 km across the Eurasian basin of the perennially ice covered Arctic Ocean, from northeastern Greenland (14.6 mm/yr) to the Siberian shelf (6.3 mm/yr) (*DeMets et al., 1994*) (Fig. 1.4). At the western end of Gakkel Ridge, the ARS bends southwards, continuing with Lena Trough, Molloy Ridge and Knipovich Ridge. In the following I will give more detailed information about Gakkel Ridge as an example of an ultraslow spreading ridge.

Gakkel Ridge has an extremely varied appearance, beginning at its western end with the magmatically robust Western Volcanic Zone (WVZ), continuing with the amagmatic Sparsely Magmatic Zone (SMZ) and ending again with a magmatic segment, the Eastern Volcanic Zone (EVZ) (Fig. 1.4). Such alternating magmatic and amagmatic segments are typical for ultraslow spreading ridges. Transform faults are absent.

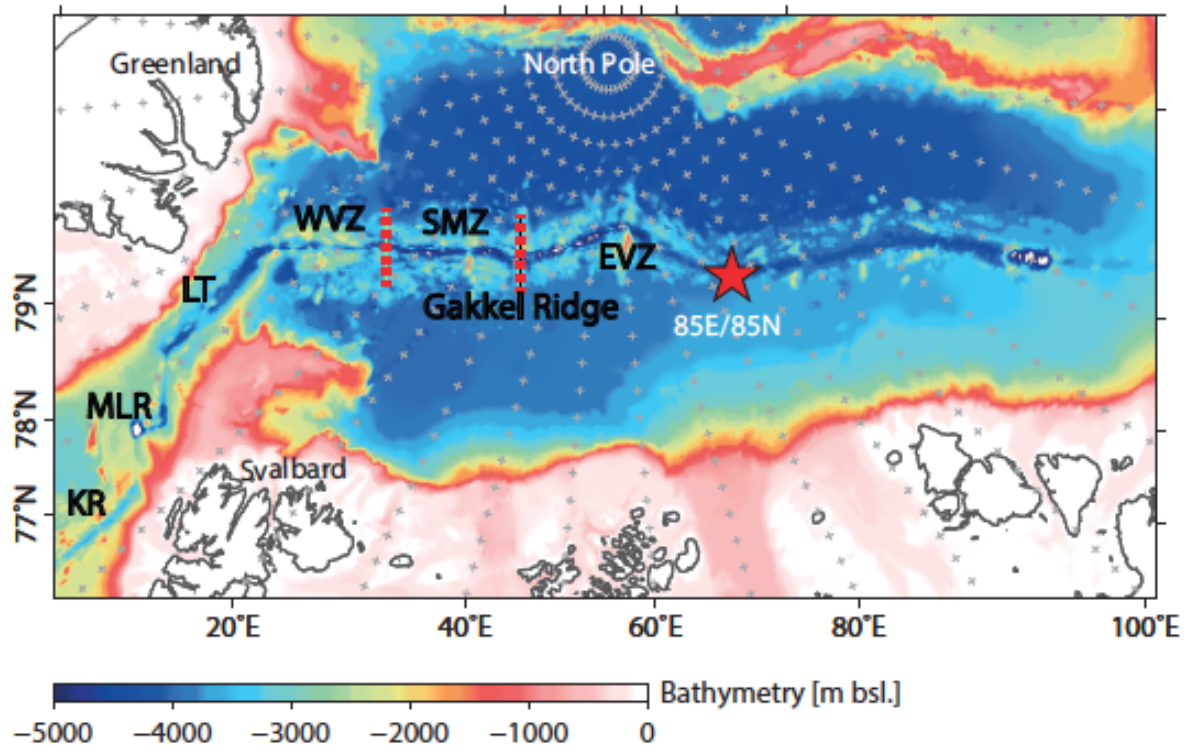


Figure 1.4 – Overview of Gakkel Ridge with Western Volcanic Zone (WVZ), Sparsely Magmatic Zone (SMZ) and Eastern Volcanic Zone (EVZ). The red star denotes the 85°E/85° volcanic complex. Other abbreviations are: Lena Trough (LT), Knipovich Ridge (KR) and Molloy Ridge (MLR). IBCAO2 bathymetry from (*Jakobsson et al., 2008*).

Close to northeastern Greenland, the Western Volcanic Zone (WVZ) from 7°W - 3°E (spreading rate at 7°W: 14.5 mm/yr) is robustly magmatic and has a bathymetric relief which is comparable to the Mid-Atlantic Ridge (*Michael et al., 2003*). Several prominent volcanic ridges are found along axis and predominantly basalts are dredged from the seafloor (Fig. 1.5).

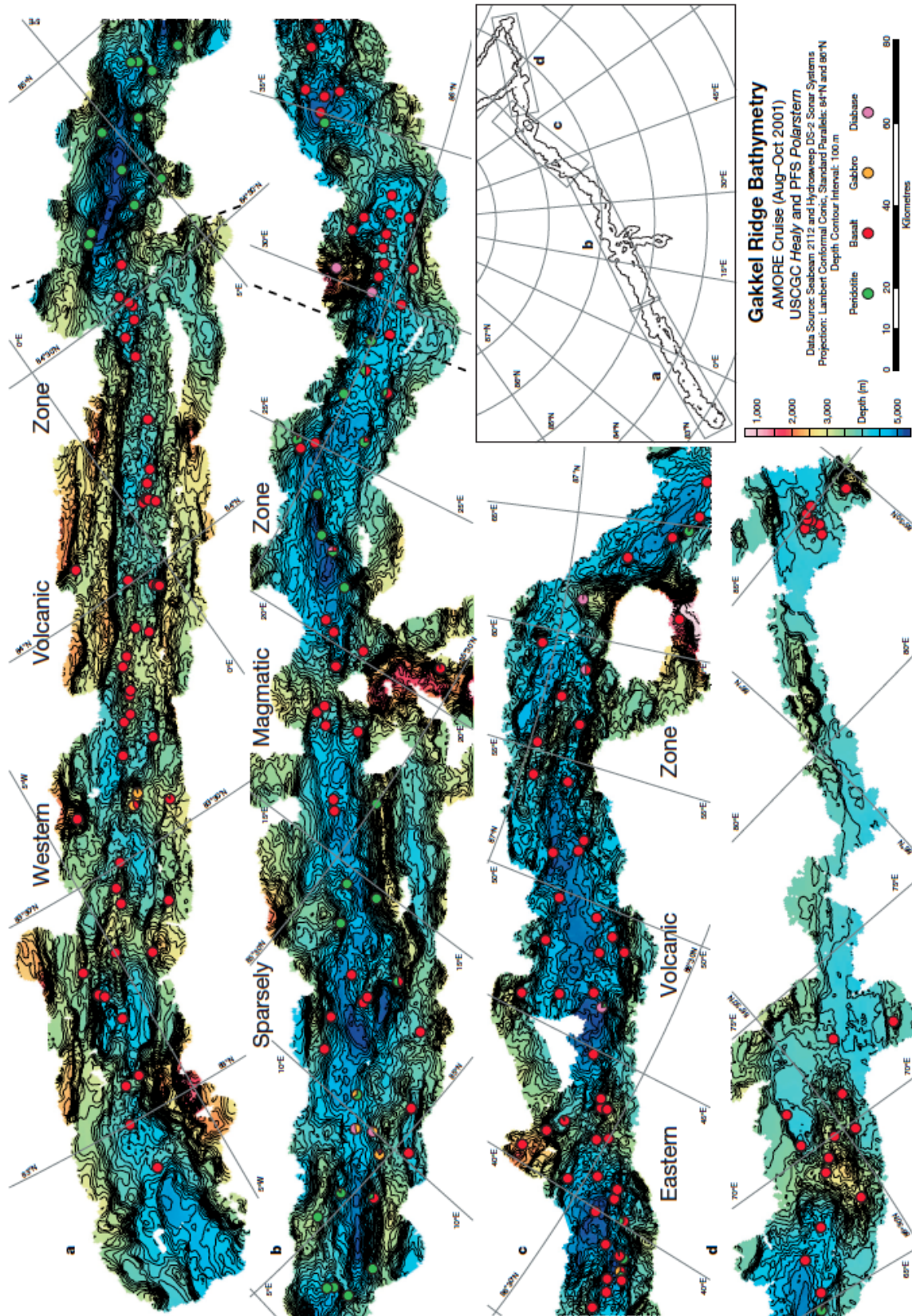


Figure 1.5 – Detailed overview of Gakkel Ridge from *Michael et al.* (2003).

In amagmatic spreading mode, the stresses of plate movement are primarily absorbed by tectonically uplifted mantle horst blocks, which create new seafloor in the process (*Dick et al.*, 2003). The adjoining Sparsely Magmatic Zone (SMZ) from 3°E - 29° (spreading rate at 3°E: 13.5 mm/yr), as Gakkel Ridge's amagmatic segment, shows only small volcanic centres with a deep and narrow rift valley floor (Fig. 1.5). Predominantly peridotites have been dredged (*Michael et al.*, 2003), emphasizing the primary accretion mode. It is followed by the Eastern Magmatic Zone (EVZ) which spans from 29°E eastwards, (spreading rate at 29°E: 12.7 mm/yr), again a robustly magmatic segment. Volcanism is highly focused at prominent volcanic centres, while volcanic rises are absent (*Michael et al.*, 2003). Yet, the processes which cause this focusing of melt are still poorly understood.

As spreading rates at ultraslow spreading MORs get slower, it has been proposed that conductive heat loss should increase (*Bown and White*, 1994; *Reid and Jackson*, 1981) which would inhibit decompression melting. This would in turn produce less melt and consequently lead to a thinner crust. Using a 2D corner flow model, *Montesi and Behn* (2007) modelled the thermal state of the axial lithosphere at ultraslow spreading ridges, yet in this model additional heat loss from e.g. efficient hydrothermal cooling has not been considered. From theoretical modelling, *Standish et al.* (2008) proposed a 3D variation of lithospheric thickness beneath ultraslow spreading ridges (Fig. 1.6). They suggest that the sloping lithosphere-asthenosphere boundary (LAB) serves as a permeability boundary along which melts flow towards volcanic centres, where the LAB is shallowest, resulting in a highly variable melt supply (*Cannat et al.*, 2008) and a thicker crust beneath magmatic centres than at the segments in between.

Schlindwein et al. (2013) found in a short-term observation of local earthquakes at Knipovich ridge a shallowing of hypocentre depths beneath a volcanic centre that may support these 3D-variable models of the thermal state of ultraslow spreading ridges. Yet, because of the inaccessible areas where these ultraslow ridges are found, no geophysical proof has been forthcoming as microseismicity studies are sorely missing. Yet, microseismicity studies have added extensively to the comprehension of processes which are found in a magmatic environment (i.e. Iceland, Afar) (*Tarasewicz et al.*, 2012; *Belachew et al.*, 2011; *Grandin et al.*, 2011; *Einarsson and Brandsdottir*, 1980). At more accessible ridges (i.e. Mid-Atlantic Ridge, Juan de Fuca Ridge), microseismicity studies have been conducted using ocean bottom seismometers (e.g. *Schlindwein et al.*, 2013; *Hoofst et al.*, 2010; *Toomey et al.*, 1985) or hydrophones (e.g. *Dziak and Fox*, 1999; *Dziak et al.*, 2007; *Fox and Dziak*, 1998; *Goslin et al.*, 2012).

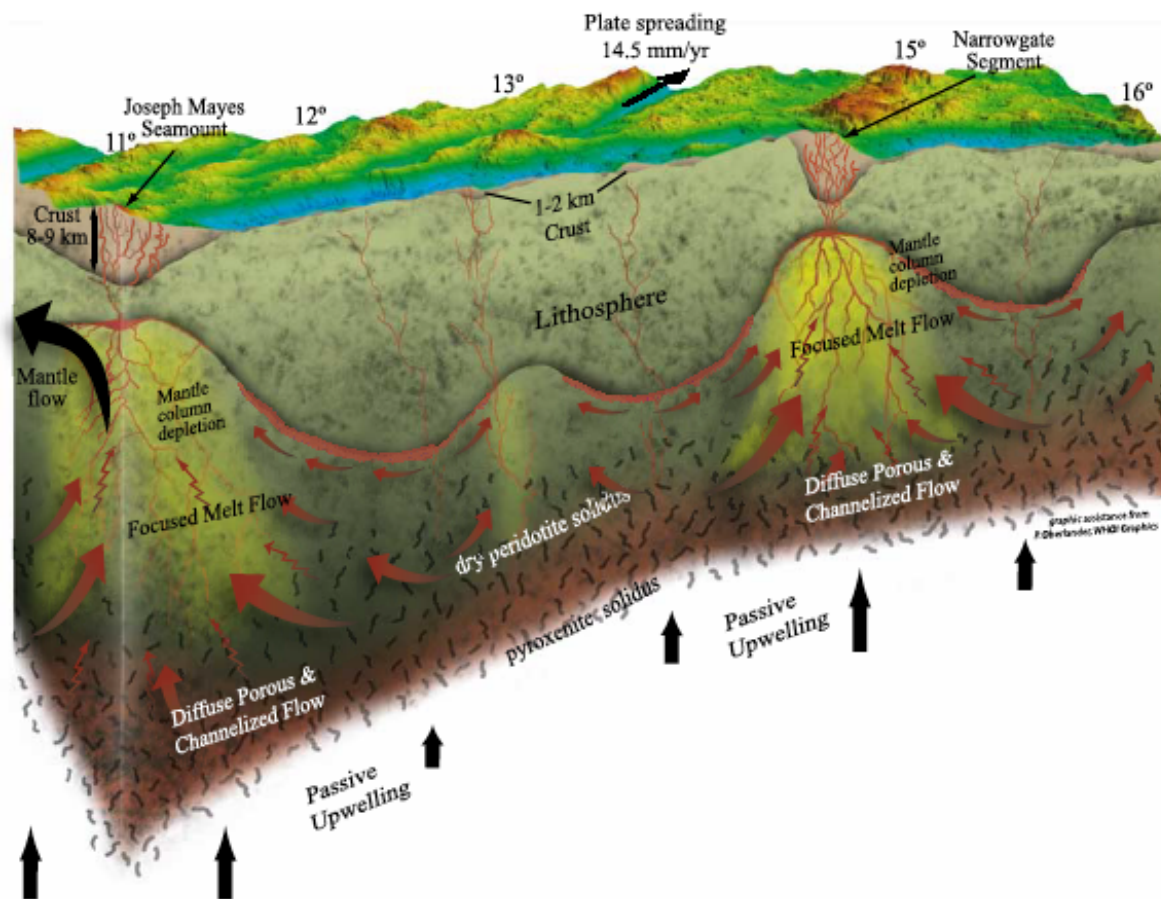


Figure 1.6 – Schematic 3D along-axis cross section illustrating the tectonomagmatic Mid-Ocean Ridge Basalt generation model for the oblique supersegment on the SWIR (9 – 16°E). From *Standish et al.* (2008).

1.2 Explorations at the ultraslow spreading Gakkel Ridge

In 1998 and 1999, the seafloor of the Gakkel Ridge was mapped for the first time by the SCICEX expedition, using submarines and building a detailed bathymetry of Gakkel Ridge (*Edwards et al.*, 2001). During this expedition, a remarkable earthquake sequence was registered on teleseismic recording stations, originating at $\sim 85^\circ\text{E}/85^\circ\text{N}$. The seismicity lasted about 9 months and consisted of over 250 events with body-wave magnitudes of up to 5.2. Some months after, the SCICEX expedition mapped supposedly fresh lava flows in this area (*Edwards et al.*, 2001). First analyses of the teleseismically registered earthquake sequence suggested volcanic origin, owing to a consistently high event rate over an extended period of time, lack of a clear mainshock, no discernible decrease of event magnitudes and an increasing non double-couple part of the earthquake source mechanism with time (*Mueller and Jokat*, 2000; *Tolstoy et al.*, 2001).

The AMORE expedition in 2001 investigated Gakkel Ridge along its length till $\sim 85^\circ\text{E}$, carrying out several experiments: They conducted a bathymetric survey (*Michael et al.*, 2003), dredged rock samples (*Michael et al.*, 2003), collected refraction (*Jokat et al.*, 2003) and seismological data with receivers mounted on ice floes (*Schlindwein et al.*, 2007), investigated hydrothermal signatures (*Edmonds et al.*, 2003; *Baker et al.*, 2004), flew aeromagnetic profiles and measured heat flow (*Jokat et al.*, 2003).

Based on these data, *Michael et al.* (2003) named three magmato-tectonic domains with differing characteristics which have been explained in ch. 1.1 (Fig. 1.5), in the complete absence of transform faults. Close to the northeastern Greenland, the Western Volcanic Zone (WVZ) spans from 7°W - 3°E , the Sparsely Magmatic Zone (SMZ) adjoins from 3°E - 29°E , and the Eastern Magmatic Zone (EVZ) begins at 29°E and while terminating at the Siberian shelf. The EVZ hosts six volcanic centres which are spaced 50 – 160 km apart (31°E , 37°E , 43°E , 55°E , 69°E and 85°E). At each of the volcanic centres along the ridge, signs of hydrothermal activity were found (*Edmonds et al.*, 2003). They detected a massive hydrothermal plume at 85°E , and, among others, a smaller one at 69°E . It was speculated, that this plume at 69°E originated at 85°E which would mean that the plume at 85°E had to have been maintained over more than one year (*Baker et al.*, 2004). Therefore, the hydrothermal event plume would relate to the unusual earthquake activity in 1999 at $85^\circ\text{E}/85^\circ\text{N}$.

The AMORE expedition also conducted seismic experiments at several locations between 0°E and 60°E along Gakkel Ridge, and found evidence for exceptional thin crust at the SMZ and the EVZ. Crustal thickness at the investigated locations comprised 1.2 – 3.3 km, compared to crustal thickness of medium/fast spreading ridges of ~ 7 km (*Jokat et al.*, 2003). In amagmatic segments, they found only thin crust (1.4 – 2.5 km), beneath some of the magmatic centres at the EVZ the crust thickened (up to 3.5 km).

Aeromagnetic measurements imaged the presence of discrete volcanic centres in the SMZ and the EVZ, which was interpreted as the result of strongly focused, three-dimensional magma supply (*Jokat and Schmidt-Aursch, 2007*). They also found indications for crustal thickening beneath these centres of focused magmatism (*Jokat et al., 2003; Jokat and Schmidt-Aursch, 2007*). Along all investigated sections, oceanic layer 3 is either very thin, or completely absent (*Jokat et al., 2003; Jokat and Schmidt-Aursch, 2007*), which is also reflected in a lack of dredged gabbros (*Michael et al., 2003*). *Jokat et al. (2003)* interpreted that crustal thicknesses are not predominantly correlated to the spreading rate, but additionally are controlled by magmatic activity along ridge.

A seismological short-term pilot-experiments with an array of four seismometers mounted on an ice floe at three locations along Gakkel Ridge was conducted, each in one of the three segments (WVZ: 5°W, 4 days; SMZ: 16°E, 4 days; EVZ: 85°E, 11 days), and recorded for the first time local earthquakes at Gakkel Ridge (*Schindwein et al., 2007*). Most of the microseismicity could be attributed to tectonic events, except a swarm-like sequence of earthquakes at the WVZ which is speculated to be of magmatic origin (*Schindwein et al., 2007*), and a swarm of seismoacoustic events at 85°E (*Schindwein et al., 2005*). These seismoacoustic events were interpreted to result from a Strombolian eruption style of bursting gas bubbles in a mild degassing of a magma chamber, rather than a violent volcanic eruption. Finite difference modeling of these signals placed them at the southern rift valley wall (*Schindwein and Riedel, 2010*).

This pilot-experiment with seismometers mounted on ice floes laid the basis for a large portion of my PhD project, as in 2007 the AGAVE expedition returned to the area of 85°E/85°N, and, among others experiments, collected a dataset with this unusual method.

The volcanic complex at 85°E/85°N

The AGAVE expedition (*Sohn et al., 2008*) focused on surveying the 85°E/85°N volcanic complex, conducting several experiments. They collected high resolution bathymetry data, performed extensive hydrothermal measurements, and imaging the seafloor digitally. During these experiments, they also recorded microseismicity.

Sohn et al. (2008) identified two volcanic ridges in the centre of the rift valley, Jessica's Hill and Duque's Hill, and three distinctive volcanic features on a ridge-parallel fissure to the south, which have been named Oden, Thor and Loke volcanoes (Fig. 1.7 a) (*Sohn et al., 2008*). A mixture of lava flows of varying ages have been imaged, with the apparently youngest having been attributed to be sourced from Oden and Loke volcanoes (*Sohn et al., 2008; Pontbriand et al., 2012*). Unconsolidated pyroclastic deposits blanketed the whole axial valley topography, up to 10 cm thick. The varying thickness and age of the deposits is indicative of multiple falls, Oden and Loke volcanoes are only covered by a light dusting. Among the sampled material they found limu o Pele, attesting to explosive volcanism. The high volatile content needed to drive such an eruption at more than 4,000

m water depths points to a deep magma chamber which may build up over long time-intervals within the deep crust, supporting infrequent explosive discharge of volatile-rich magmas (Sohn *et al.*, 2008) with following effusive lava discharge (Pontbriand *et al.*, 2012). Around Oden and Loke volcanoes, signs for widespread diffusive hydrothermal discharge were found (Fig. 1.7b) (Pontbriand *et al.*, 2012).

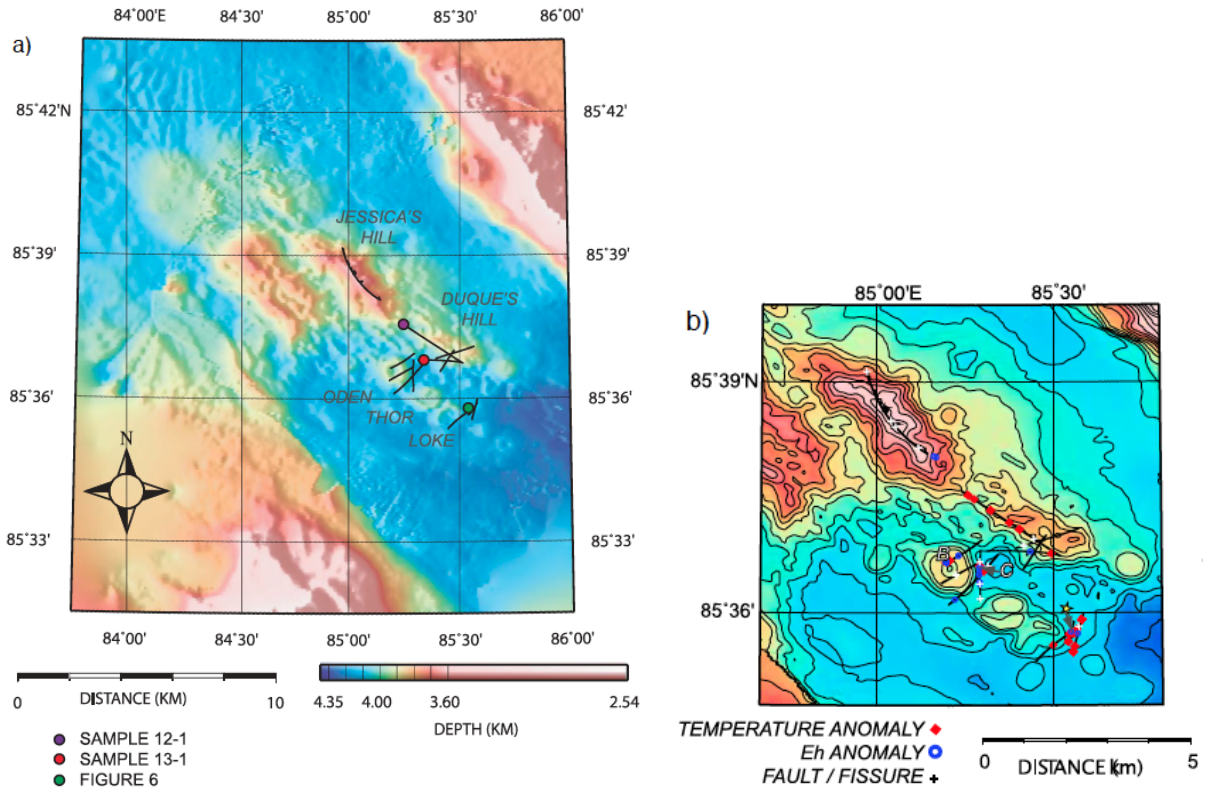


Figure 1.7 – a) Bathymetric chart of the axial valley of the area at 85°E/85°N. Circles denote the locations of samples of volcanoclastic deposits. Black lines denote the paths of near-seafloor CAMPER vehicle deployments. b) Locations of near-seafloor seawater temperature and Eh anomalies and faults and fissures are shown. The yellow star denotes a location of cloudy fluid 90 m above the seafloor of Loke's apron. Both figures are from Pontbriand *et al.* (2012).

During AGAVE 2007, three seismological arrays with four seismometers each drifted over the rift valley at 85°E/85°N. They were installed on three ice floes, being recovered and redeployed when the ice floes drifted too far away from the rift valley. This survey collected 16 days of microseismicity data, which were analyzed and interpreted as major part of my PhD project, for the first time ever imaging the velocity structure of an ultraslow spreading volcanic centre.

1.3 Motivation and scope

1.3.1 Framework

My dissertation was embedded in the research group MOVE (Mid-Ocean Ridge Volcanoes and Earthquakes), which consisted of three scientists during most of the three years of my dissertation, all analyzing seismicity of ultraslow spreading ridges globally, or focusing on specific local or regional datasets. Due to the common goal, overlapping datasets and survey areas, our collaboration was very close. The focus of my PhD thesis and my main contribution to MOVE was the development and improvement of methods for locating earthquakes, analyzing seismicity sequences and inverting a microseismicity dataset at 85°E/85°N for velocity structure. Because of my methodical focus, I naturally contributed to the work of others in my research group. One of these contributions earned a second-authorship in *Läderach et al.* (2012) which is included as the second scientific publication in my dissertation.

1.3.2 Outline

Seismicity at mid-ocean ridges is confined to a narrow region focused along the spreading axis, at first order reflecting the spreading rate (*Bohnenstiehl and Dziak, 2008*). At faster spreading ridges, oceanic spreading largely occurs teleseismically aseismic while at slower spreading ridges an abundance of small- to moderate-magnitude earthquakes is found. Monitoring such small-scale seismicity teleseismically poses a challenge, as the global network of seismometers is land-based and therefore the long distance from seismometer to the individual ridge makes it impossible to completely register earthquakes with smaller magnitudes.

Clustered seismicity at mid-ocean ridges can reflect either extensional tectonics in main-shock-aftershock sequences, or it can accompany the creation of new oceanic crust by intrusion of dykes from a magma chamber. During a seafloor spreading episode, it is also possible that both kinds of earthquake sequences occur sequentially or even overprint each other, reflecting rupture of the crust as a consequence of, or enabling an accompanying dyking event. Spreading episodes are mainly captured by AuH measurements (e.g. *Dziak and Fox, 1999; Dziak et al., 2007*) but for the Arctic and the Southern Ocean such data do not exist. We therefore have to rely on teleseismic data in analyzing the spreading of ultraslow spreading ridges.

Few known subaerial spreading episodes included teleseismic registered events. For example, at the start of the 1975 Krafla rifting episode in Iceland, volcanic activity went along with an intense earthquake swarm, tracking a propagating dyke. During these events, micro- as well as macroearthquakes were registered (*Einarsson and Brandsdóttir, 1980*).

Another example for a volcano-tectonic rifting episode is the 1978 Asal-Ghoubbet rifting episode, in Afar. At the start of this rifting episode, a fissural basaltic eruption was accompanied by up to two dykes, and a seismic swarm that lasted for two months including two major earthquakes with body-wave magnitudes ≥ 5.0 (*Dobre et al.*, 2007a). Yet, seismicity caused by a dyking event itself is largely characterized by very small earthquake magnitudes. Tracking these low magnitudes at mid-ocean ridges is impossible by land-based seismometers, due to the large distances involved.

Spreading episodes at ultraslow spreading ridges are suspected to occur only very rarely, reflecting probably the amount of available mobile magma. The earthquake sequence of 1999 at 85°E/85°N was very unusual in comparison to previously registered sequences, due to its 9 months duration, 252 ISC-registered events and not less than 11 events with a body-wave magnitude of ≥ 5.0 . Additionally, this seismicity sequence originated at a magmatic spreading centre of the ultraslow spreading Gakkel Ridge. The 1999 earthquake sequence therefore posed an unique opportunity to study the development of such a spreading episode, aiming at an interpretation of the spatial and temporal evolution of processes in the ultraslow spreading, magmatic accretionary environment. Earthquake locations as accurate as possible were therefore a major prerequisite.

I localized this earthquake sequence in my diploma thesis with a probabilistic absolute localization algorithm, and also a reliably located sub-dataset with a least-squares localization algorithm. However, the epicentre locations mostly did not match even within their error-ellipses. Teleseismic localization of earthquakes at Gakkel Ridge suffers from less than ideal station distribution and a large magnitude of completeness, resulting in greater error ellipses than with smaller epicentral distances or more equally distributed azimuths. At smaller epicentral distances, localization algorithms seem to perform smoothly (e.g. *Husen et al.*, 2003). The first part of my PhD-thesis therefore focused on analyzing the performance of three different localization algorithms, using the teleseismic dataset from the spreading episode of 1999 at Gakkel Ridge. The results were published as *Korger and Schlindwein* (2012), and answered the following questions:

- Which localization algorithm results in the most reliable hypocentre dataset?
- What do the obtained locations tell us regarding the the physical processes which produced this seismicity?

In a global context, there has been speculation about whether the earthquake sequence of 1999 was related to magmatic activity (e.g. *Mueller and Jokat*, 2000; *Tolstoy et al.*, 2001). *Schlindwein* (2012) examined teleseismically-recorded clustered seismicity at ultraslow spreading ridges around the world, among them the 1999 earthquake sequence, and found that they are almost exclusively located at centres of focussed magmatism. This hints at a probable magmatic origin for these sequences, but does not prove it conclusively. At the same time, *Läderach et al.* (2012) analyzed regionally- and teleseismically-registered earthquakes at the Southwest Indian Ridge, identifying four prominent earthquake sequences at the magmatically spreading Orthogonal Supersegment from regional data.

To rule out an exclusively tectonic origin, the statistical function which is called the modified Omori-Law can be used. The modified Omori-Law is able to fit the parameters of a theoretically-calculated function to the observed aftershock rate of a tectonic mainshock-aftershock earthquake sequence. If this fails, the earthquake sequence in question had not a purely tectonic origin, and would have, at least in part, been driven by magmatism or fluid interaction. The second part of my PhD-thesis as contribution to *Läderach et al.* (2012) consisted of extensively analyzing all suitable earthquake sequences at these ultraslow spreading ridges, and answered the following question:

- Can the analyzed seismicity sequences at the SWIR and the Gakkel Ridge be tied to globally observed magmato-tectonic seismicity?

With the analyses of the earthquake locations and the theoretically calculated aftershock rate of the seismicity in 1999, it was possible to link the spreading episode at 85°E/85°N on Gakkel Ridge to a tectonomagmatic sequence. Yet, further insights into velocity structure and seismicity of this spreading centre can only come from datasets which contain smaller magnitude earthquakes. However, conventional microseismicity surveys with ocean bottom seismometers at Gakkel Ridge are confronted with the threat of instrument loss, due to the perennial ice-cover of the Arctic Ocean. Similarly, at the Southwest Indian Ridge frequent stormy weather also can easily prohibit the recovery of deployed instruments. Therefore, no such surveys have been done before at an ultraslow spreading ridge.

In 2007, the AGAVE expedition had a chance to record microseismicity at the volcanic centre at 85°E/85°N by placing three arrays of four seismometers each on ice floes. With this survey method, the set-up of an ideal, fixed station distribution was not possible due to the wind- and current driven drift of the ice floes. Nevertheless, this unusual survey method resulted in the recording of about 300 microearthquakes. Every single earthquake was constrained by a different set of stations coordinates, which resulted in an abundance of rays crossing the rift valley. Thus, this dataset was used not only for a microseismicity study at 85°E/85°N, but also for the first ever tomographic imaging of a ultraslow spreading volcanic centre. Extensive analysis of this unusual dataset formed a third major part of my PhD-thesis, being submitted to *Korger and Schlindwein* (2013), and answering several important questions, such as:

- Can the seismicity recorded in 2007 still be related to the spreading episode in 1999?
- What is the crustal structure in 1D and 3D of the 85°E/85°N volcanic centre?

2 Datasets

The 85°E/85°N volcanic complex at Gakkel Ridge lies in the Arctic Ocean, far from land. The nearest seismological land-based station lies at Svalbard, nearly 1200 km away. Due to the generally difficult survey conditions on ultraslow spreading ridges (weather, ice cover), seismological studies have been focused at more easily accessible ridges, such as the Mid-Atlantic Ridge or the Juan de Fuca Ridge.

For my PhD project, I used several datasets, teleseismic and local earthquake data from ultraslow spreading ridges. Teleseismic data are available from online seismological databases and are only shortly mentioned here (see ch. 2.1.1). The local dataset I will describe in detail in ch. 2.2.

2.1 Clusters of seismicity

2.1.1 1999 teleseismic earthquake sequence, Gakkel Ridge

To analyze the earthquake sequence of 1999 I extracted data from the reviewed event bulletin of the ISC database (*ISC*, 2008) from January, 17th to September 24th 1999 and between 70° and 90°E, and 80° to 90°N. The reviewed event bulletin became available in 2001 and consists of exclusively reviewed earthquake phase information, which makes using it advantageous in comparison to the dataset used by *Mueller and Jokat* (2000) and *Tolstoy et al.* (2001) who previously investigated this earthquake sequence. I used all phase readings and magnitude information from the reviewed bulletin.

The results of the localization and subsequent analysis were published in *Korger and Schlindwein* (2012) (see ch. 5). For the methodical approach and additional uncertainty information, please refer to ch. 3.1.

2.1.2 Other seismicity sequences, ARS and SWIR

I also used data of clustered seismicity from other ultraslow spreading ridge segments to test statistically whether these earthquake sequences were exclusively tectonic in origin. For details on these analyses, please refer to ch. 3.2.

- **Gakkel Ridge and Southwest Indian Ridge, teleseismic data, 1976 – 2010:** *Schlindwein* (2012) analyzed earthquake clusters at ultraslow spreading ridges, using earthquake location, as well as magnitude data from the ISC database (*ISC*, 2008). I analyzed the largest four seismicity sequences using the modified Omori-Law. Yet, the results were inconclusive and were not included in the publication. I explain the specific analyses and the obtained results in detail in ch. 3.2.
- **Southwest Indian Ridge, regional data, 2001 – 2008:** *Läderach et al.* (2012) extracted array detections of seismicity from the VNA2 seismic array operated by the German Neumayer station in East Antarctica. This array has a high sensitivity for earthquakes in that region. *Läderach et al.* (2012) calculated magnitudes and identified four earthquake sequences with a minimum of 29 events originating at the Orthogonal Supersegment of the Southwest Indian Ridge (16°E to 25°E), between 2001 and 2009. I was involved in testing statistically the relation of these four earthquake clusters to tectonic origins. The analytical approach is detailed in ch. 3.2. This analysis contributed to *Läderach et al.* (2012) (see ch. 6).

2.2 Local Seismicity - 85°E/85°N

In the aftermath of the 1999 spreading episode, the AGAVE expedition collected 16 days of microseismicity data in 2007 from the 85°E/85°N volcanic complex. Three arrays of four seismometers each (Mark L-4C3D, three components, short-period, 100 Hz sample rate) drifted over the survey area, being recovered and redeployed when drifting too far away (Fig. 2.1).

Three seismometer stations were arranged in a triangle (side length ~ 1 km) around a central seismometer station on the same ice floe, each of them equipped with a receiver for the Global Positioning System (GPS) and a data logger. Due to the need to extend battery life, the GPS receiver only searched for its position and logged once per hour, the intervening positions were being extrapolated after recovery of the stations. The central station was also equipped with an Argos sender, who mailed the current position every few hours. When the general drift direction of the ice and the last known position of the Argos sender indicated a drift out of the survey area, helicopters were used to recover, and redeploy the stations on a new ice floe.

The resultant dataset consisted of 303 events, being collected during 15th to 31st of July 2007. Data were available as continuous raw data. Owing to the steep 3D bathymetry at this location and the therefore varying thickness of the water layer underneath the recording stations, this dataset had to be extensively processed. The pertinent techniques which I employed are described in ch. 3.3.1.

Due to favourable drift paths of the ice floes (Fig. 2.2), a multitude of crossing rays ensued, making it possible to analyse this dataset with a local earthquake tomography. The results are presented in *Korger and Schlindwein* (2013) (see ch. 7) and comprise the first ever tomographic insights into an ultraslow spreading volcanic centre.

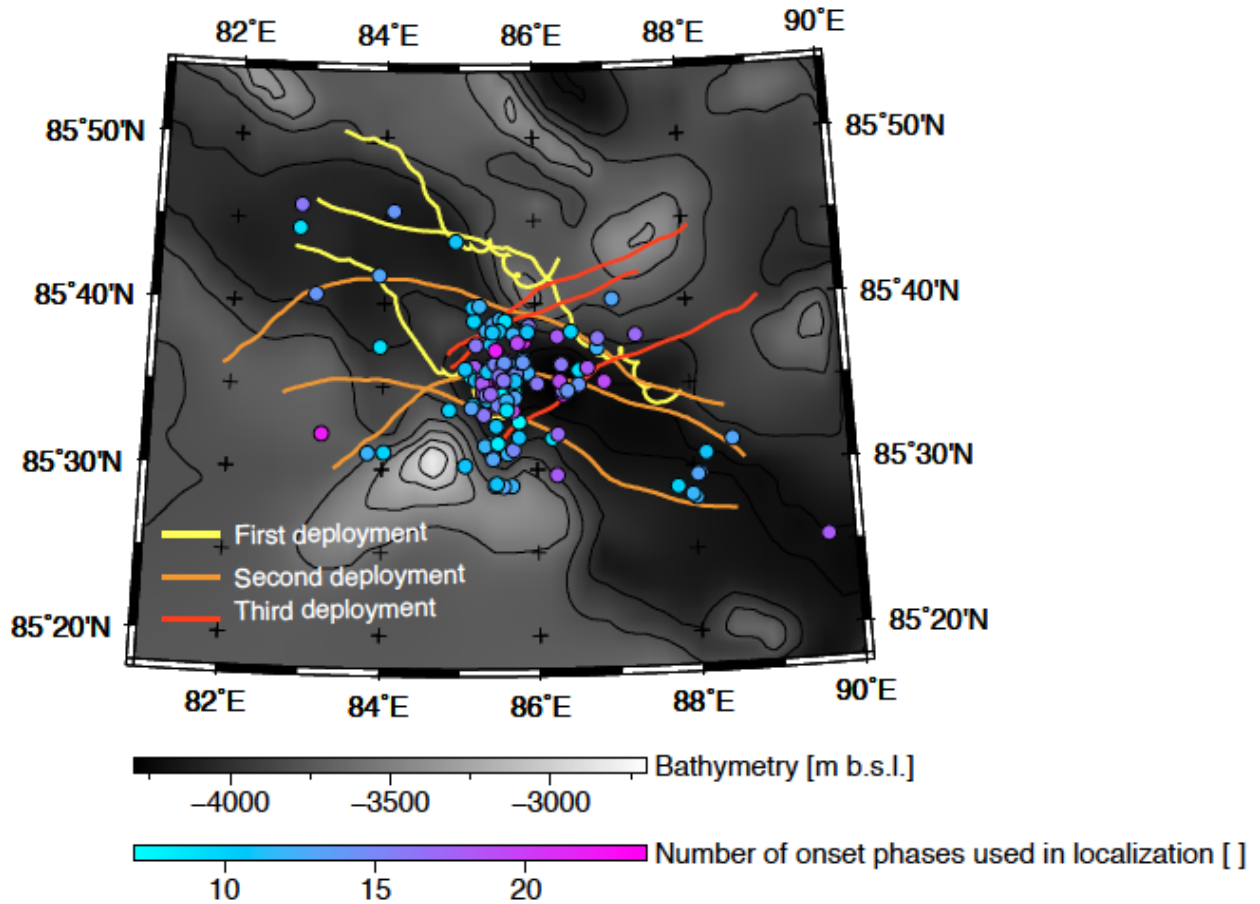


Figure 2.1 – Colored lines denote drift paths of the three ice floes. 128 Epicentres localized by Hyposat (*Schweitzer, 2001*) are plotted with colored circles. IBCAO2 bathymetry from (*Jakobsson et al., 2008*) with 200 m contour lines.

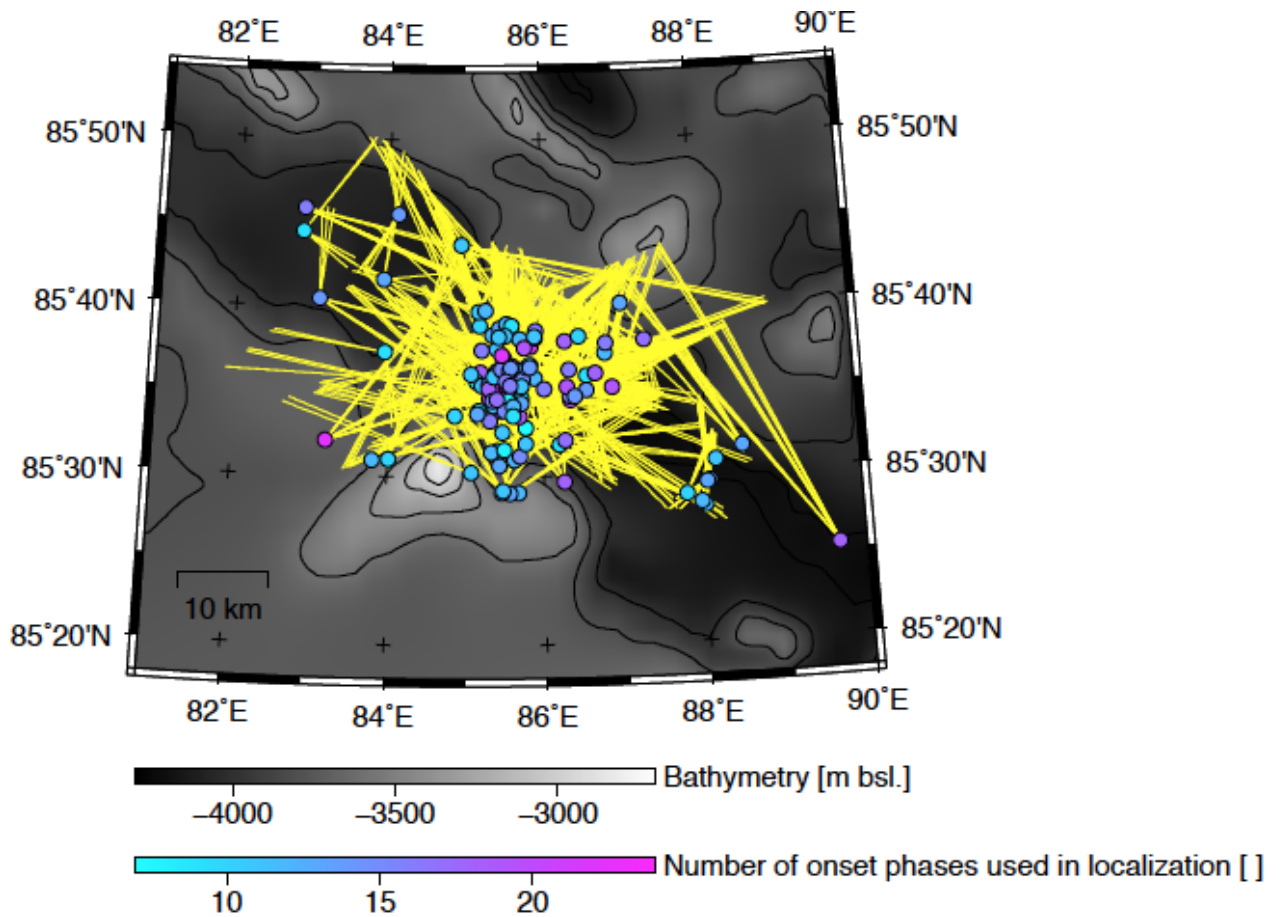


Figure 2.2 – Ray coverage for 128 events which were registered by at least two arrays. Circles denote epicentres, coloured by the number of onset phases used in localization. Yellow lines are ray paths in 2D. IBCAO2 bathymetry from (*Jakobsson et al.*, 2008) with 200 m contour lines.

3 Methods

In this chapter, I explain the specific techniques and software programs I used in research during this methodically focused PhD project. Rather than repeat information I have already published in the individual academic research papers, I aim to discuss more specifically some problems encountered during data analysis, and their solutions. I give background information explaining why I used some specific software programs and not others. I describe not only the specific methods for my own dissertation, especially detailing the methodical work for *Läderach et al. (2012)*, but also present unpublished analyses of clustered seismicity from datasets of *Schlindwein (2012)*.

3.1 Evaluation of the performance of different localization algorithms

The 1999 teleseismic earthquake sequence at $85^{\circ}\text{E}/85^{\circ}\text{N}$ was analyzed by *Mueller and Jokat (2000)* and *Tolstoy et al. (2001)*, using catalogue based earthquake locations. In 2010, *Riedel and Schlindwein (2010)* compiled a local velocity model for this area, based on relocating 237 earthquakes from the International Seismological Centre's (ISC) reviewed database with the linear least-squares algorithm Hyposat (*Schweitzer, 2001*).

Reliable locations of earthquakes are of crucial importance for any kind of detailed analysis of the seismicity sequence of 1999. In my diploma thesis (*Korger, 2010*), I relocated the 1999 earthquake sequence using the probabilistic localization algorithm NonLinLoc (*Lomax et al., 2000*), with the slightly larger ISC dataset of 252 events, and a new local/regional velocity model for the nearest recording stations. The focus of my diploma thesis consisted of testing extensively the influence of the NonLinLoc localization algorithm on earthquake locations. To do this, I used sub-datasets of differing qualities and different global velocity models.

For comparison, I also relocated a reliably located sub-dataset with the least-squares localization algorithm Hyposat (*Schweitzer, 2001*). The most important result of my diploma thesis was, that the epicentre locations as given by the two algorithms mostly did not match within their respective error-ellipses. This demonstrated the important influence of the localization algorithm on the calculated location of earthquakes. Taking this as baseline, I embarked on my PhD project.

The systematic test of the importance of localization algorithms on the dataset of the 1999 earthquake sequence became the content of *Korger and Schlindwein* (2012). We localized the same set of earthquakes (120 events) with three conceptually different earthquake localization algorithms:

1. NonLinLoc; An absolute probabilistic localization algorithm (*Lomax et al.*, 2000)
2. Hyposat; An absolute least-squares localization algorithm (*Schweitzer*, 2001)
3. Mlocate; A relative least-squares localization algorithm (*Jordan and Sverdrup*, 1981)

For details about the localization algorithms, methods and the results, refer to *Korger and Schlindwein* (2012). I wrote shell-scripts producing the input-files for NonLinLoc and Hyposat. For the output-files of NonLinLoc and Hyposat I wrote shell-scripts which presented the location of the hypocentres and the associated uncertainties in a concise form that could easily be compared to the results of the other localization algorithms.

I improved the code of NonLinLoc in two aspects: The first deficiency of NonLinLoc was in dealing with earthquakes that occurred just before midnight on any given day. When phases of such an event were recorded after midnight (i.e. on the next julian day), the resulting location was erroneous. The second problem consisted of erroneously-calculated lengths for error-ellipse axes around high-latitude earthquake locations. Earthquakes at the equator were not affected by this calculation error, yet events at $\sim 85^\circ\text{N}$ most certainly were. NonLinLoc greatly overestimated the lengths of error-ellipse axes of such events. After I brought these subjects to the attention of A. Lomax, the programmer of NonLinLoc, he corrected the source code to exclude these errors in future.

3.1.1 Quantification of localization errors

The biggest issue in dealing with teleseismic earthquake locations was judging location errors due to the usage of a simplified regional 1D velocity model. An equidistant local station network, arranged around an earthquake hypocentre, is able to locate earthquakes with very small errors, but its earthquake locations are sensitive to the local velocity model used in localization. Unfortunately, because of the remote location in the ice-covered Arctic Ocean and the unavoidably large distances to the nearest land-stations, no local or regional network was available to register phases of this earthquake sequence and provide well-constrained locations independent of teleseismic phases for comparison. Additionally, the epicentres lie submerged beneath a $\sim 2500 - 4200$ m thick water layer, therefore ground-truth observations such as fresh faults or fresh lavas were also not available.

In my diploma thesis, I did a sensitivity study to examine the influence of the regional velocity model on the results generated by NonLinLoc (*Korger*, 2010). I found that, for well-constrained events with more than 50 recorded phases, the average difference in epicentre locations calculated with and without the 1D regional velocity model was less than

3 km. This is much less than the mean semi-major error ellipse axis for events in the well-located NonLinLoc dataset of ~ 15 km. It implies that the errors introduced through use of the 1D regional velocity model are less than the errors still inherent in the dataset (i.e. owing to misidentification of phases, and systematic traveltime differences at some recording stations due to 3D geologic structures between station and hypocentre, which differ from the homogeneous 1D velocity model). To test, whether the error introduced through station distribution is also less than the error inherent in the localization algorithm, I used a sub-dataset of the 11 best events ($m_b \geq 5$), which I curtailed in different epicentral distances, reflecting different azimuthal distributions (Korger, 2010). The test showed a mean shift of epicentres in the order of 3 – 4 km, which is again less than the mean of the semi-major error ellipse axis of the well-located dataset of NonLinLoc.

Using Hyposat, Schweitzer and Kennett (2007) relocated an event in the Kara Sea that similarly suffered from a less than ideal station distribution. They noted that the absolute error output by Hyposat may be unrealistically small, due to a limited number of phases used in localization. Korger and Schlindwein (2012) also noted the tendency of Hyposat to calculate very small error axes. We noted, that Hyposat is prone to eliminate phases from usage if they do not fit the preponderance of other phases, and that its calculated error axes for the well-located dataset of the 1999 earthquake sequence are less than half the size of error ellipses calculated by NonLinLoc. Beyond this, it was not possible to judge if the absolute location error output by either NonLinLoc or Hyposat reflected the appropriate uncertainty.

In response to a reviewer’s question, I compared the 57 epicentres in the well-located dataset using three different algorithms to the corresponding epicentres provided by the EHB catalogue. The EHB catalogue is considered as one of the best-located datasets, being compiled by the ISC for events from 1960 to 2008 and includes correction for 3D effects on travel times. While the EHB locations were not analyzed extensively in my publication, the comparison further reinforced the conclusions of my analysis of the performance of the investigated localization algorithms, being closest to the epicentres of NonLinLoc (mean: 3.9 km) and farthest to the epicentres of Hyposat (mean: 7 km) (Fig. 3.1).

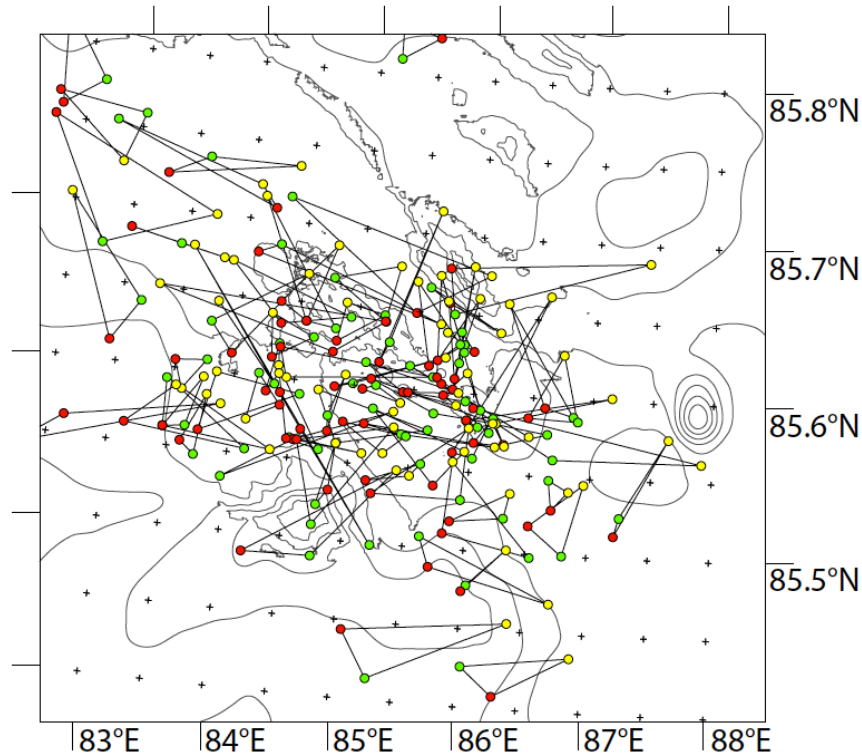


Figure 3.1 – Comparison of epicentres of the well-located dataset by EHB (green circles), NonLinLoc (red circles) and Hyposat (yellow circles).

Visualizing of 'scatter clouds'

During error evaluation, I took note of NonLinLoc's output of 'scatter clouds', which is the region in which the greatest likelihood of the location of the earthquake is found. While not being absolute, such clouds visualize the most probable hypocentre by the highest density of scatter points. Each one describes fully the uncertainty volume, representing the entire posterior probability density function (c.f. Fig. 5.6).

I used the scatter cloud in a completely new approach, writing shell scripts that summed scatter points to investigate the spatiotemporal development of the earthquake sequence. Due to the lack of nearby recorded phases in my dataset, the scatter cloud was almost always elongated vertically, indicating NonLinLoc's relatively poor constraint on hypocentre depth. The spatial coordinates are treated as independent in the calculation of the posterior probability density function. So, even if the hypocentre depth is incorrect, the geographic coordinates are not affected. I therefore restricted my analysis of NonLinLoc locations to epicentres, and the corresponding analysis of scatter clouds to summing in longitude/latitude.

I identified three major temporal phases in the seismicity sequence from the analysis of cumulative seismic moment release M_0 and cumulative number of events (c.f. Fig. 5.4). The phases seem to be related to different processes driving seismicity. I visualized the

normalized sum of scatter points for each of these three phases and found each one to have a characteristic shape (c.f. Fig. 5.7). Rather than interpret individual earthquake locations, I could therefore analyze the most probable centre of earthquake activity in each of the three temporal phases.

3.1.2 NonLinLoc localization of teleseismic earthquakes at Lena Trough

During data analysis in preparation for my first manuscript (*Korger and Schlindwein, 2012*), my colleague C. Läderach relocated teleseismic earthquakes along the Lena Trough and adjacent Molloy Ridge, also including earthquakes at the beginning of the Knipovich Ridge. She used ISC events recorded between 1963 and 2009, in preparation for *Läderach et al. (2011)*. During localization of these earthquakes with Hyposat, she became aware of my preliminary results regarding differences in hypocentres between Hyposat and NonLinLoc. I localized the dataset at Lena Trough with NonLinLoc, differentiating between a presumably well-constrained dataset, consisting of events with ≥ 50 recorded phases (Fig. 3.2), and a less-constrained dataset of events with < 50 recorded phases (Fig. 3.3).

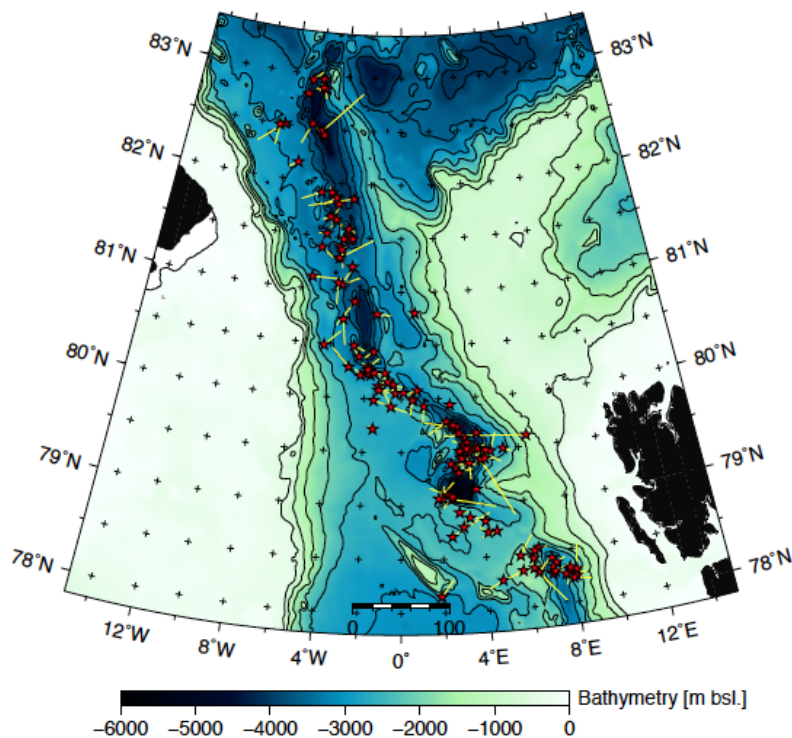


Figure 3.2 – Red stars denote NonLinLoc relocated epicentres of earthquakes with ≥ 50 phases used in localization at Lena Trough between 1963 and 2009. Yellow lines originate at the NonLinLoc epicentres and tip to the corresponding Hyposat epicentres. Bathymetry of IBCAO2 (*Jakobsson et al., 2008*) with 500 m contour lines.

The differences in locations were ~ 13 km for the well-constrained events and ~ 18 km for the less well-constrained ones. C. Läderach preferred the Hyposat locations for her analysis, because locations for its less well-constrained dataset were more often located in the rift valley (Fig. 3.3). Hyposat may better constrain the solution for events with only a small number of recorded phases, because it is able to consider traveltime differences as additional input.

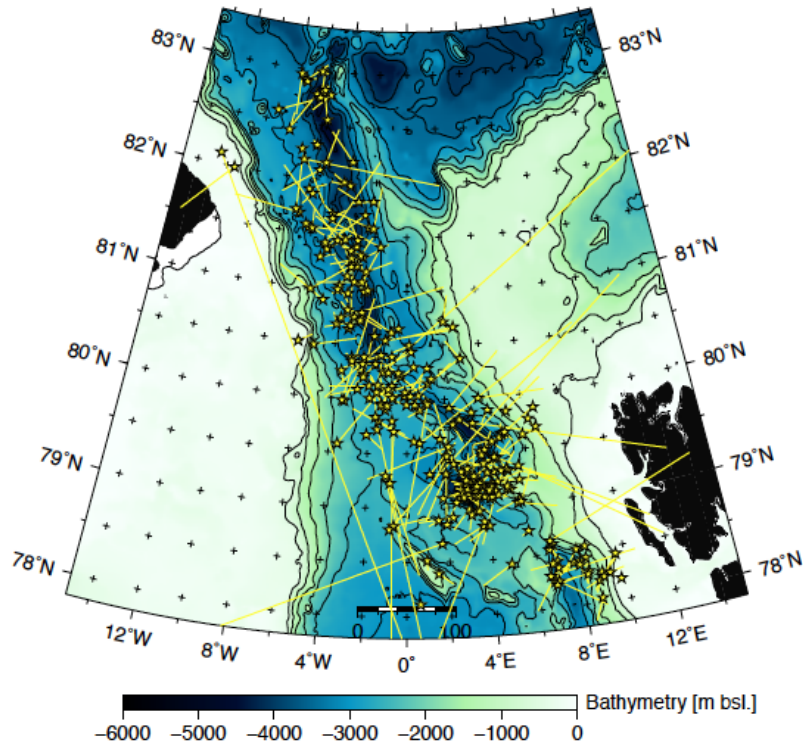


Figure 3.3 – Yellow stars denote Hyposat relocated epicentres of earthquakes with < 50 phases used in localization at Lena Trough between 1963 and 2009. Yellow lines originate at the Hyposat epicentres and tip to the corresponding Non-LinLoc epicentres. Bathymetry of IBCAO2 (Jakobsson *et al.*, 2008) with 500 m contour lines.

At first glance, the choice of Hyposat epicentres by Läderach *et al.* (2011) for the dataset at Lena Trough contradicts my results for the 1999 earthquake sequence regarding NonLinLoc as absolute localization algorithm of choice (Korger and Schlindwein, 2012). However, the datasets are quite different. Läderach *et al.* (2011) examined a set of mostly independent events occurring over 46 years, and over of a whole rift segment. In contrast, the dataset of Korger and Schlindwein (2012) consists of earthquakes which are related to each others, we therefore expected the seismicity to cluster. Läderach *et al.* (2011) did not attempt to analyze individual earthquake sequences with regard to e.g. temporal evolution, but looked at the spatial distribution of well-located individual earthquakes while simply omitting poorly located earthquakes. Thanks to closer land stations at Lena Trough than at $85^{\circ}\text{E}/85^{\circ}\text{N}$ Gakkel Ridge, even earthquakes with few phase observations showed small location errors.

Comparing the results *Korger and Schlindwein (2012)* and *Läderach et al. (2011)*, I conclude that the localization algorithm has to be chosen carefully with regard to the character of the dataset and the aim of the study. For well-constrained seismicity (i.e. ≥ 50 recorded phases), NonLinLoc would be the algorithm of choice, yet, due to the use of traveltimes differences, Hyposat can make the most of less constrained data and also give reasonable hypocentre depths.

3.2 Seismicity sequence analysis

In preparation for the publication of *Läderach et al. (2012)* I undertook extensive research into the statistical background, limitations and interpretation of the modified Omori-Law (MOL) for analysis of clustered seismicity at the Southwest Indian Ridge from regional data. The results of this analysis earned a second authorship in this scientific publication. Also during this time, *Schindwein (2012)* prepared her manuscript and asked me to contribute similar analyses of clustered seismicity of teleseismic data. As these analyses could not contribute substantially to this publication, they were not included in the publication.

In this chapter, I include background information about the modified Omori-Law, specific details about the analyses I did for *Läderach et al. (2012)* and *Schindwein (2012)*, and the resultant conclusions.

3.2.1 Types of earthquake clusters

Earthquakes are caused by brittle failure, yet the observed clustered seismicity pattern varies, according to material heterogeneity, temperature, and source process. *Mogi (1963)* experimentally investigated the effect of the structural state of the material, and the distribution of applied stresses on the frequency of resulting elastic shocks (Fig. 3.4). They observed three patterns, which also occur in nature.

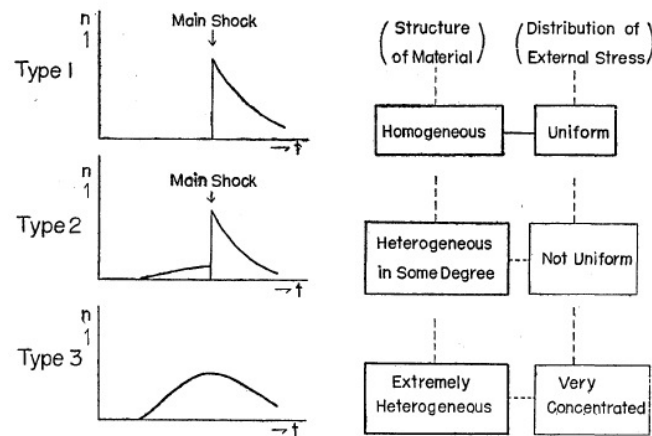


Figure 3.4 – Three types of the successive occurrence of the elastic shocks accompanying fractures and their relations to the structures of materials and the applied stresses, from *Mogi (1963)*.

Type 1 and 2 patterns (mainshock-aftershock sequences, with/without foreshocks) distinguish themselves by a clear mainshock, which is generally at least one magnitude unit above that of the magnitude of the second-largest following aftershock (*McNutt, 1996*), and

rapidly decaying aftershock magnitudes and seismicity rates thereafter. The mainshock releases stress almost instantaneously, the surrounding stress field adjust and releases aftershocks around the main rupture zone, which expands with time. Generally, aftershocks begin immediately after the mainshock.

In contrast to mainshock-aftershock patterns, Type 3 seismicity lacks a dominant mainshock, even though the seismicity stays tightly clustered in time and space. No exact definition can be formulated (*Hainzl, 2002*). *Mogi (1963)* stressed that they result from either a remarkably fractured region, or the application of concentrated stress (e.g. intrusive stress by viscous magma). Mostly these sequences are associated with magmatic activity or fluid migration (*Hainzl, 2002*).

In the following, I will focus on mainshock-aftershock sequences, as they are exclusively tectonic in origin and their time-dependent behaviour can be described by clearly formulated functions (i.e. relation of aftershock frequency to time: Omori-Law).

3.2.2 Background statistical information

Several aspects of statistical analysis of earthquake clusters are made possible by the statistical concept of scale invariance, which is inherent in a power-law distribution.

A power law is a mathematical relationship between two quantities in the form of e.g. $f(x) = ax^k$. If such a process is scaled by a constant, c , $f(cx) = a(cx)^k$. This means, that the original function only gets multiplied by the constant c^k . The log-log plot of such processes show a linear relationship (c.f. Fig. 3.5). Several seismicity distributions can be described by a power-law e.g. aftershock rate (*Omori, 1894*), or earthquake size (*Ishimoto and Iida, 1939; Gutenberg and Richter, 1944*).

A **Poisson process** is a stochastic (i.e. random) process in which events occur continuously and independently of one another (e.g. radioactive decay). The opposite to a stochastic process is called a deterministic process. This means that the outcome is subject to some law, always producing the same output from given starting parameters. A **stationary process** is one whose statistical properties do not change with time. Random processes can be stationary. Global seismicity is assumed to be stationary, but mainshock-aftershock sequences are not because of their relationship to a changing regional stress field. Therefore, individual mainshock-aftershock sequences are assumed to be non-stationary Poisson point processes (*Ogata, 1983*). The mainshock of an earthquake sequence is assumed to be poissonian and stationary, the dependent aftershocks are assumed to show non-poissonian behaviour (*Kagan and Jackson, 1998*).

Aftershock frequency-size statistics can be described by the Gutenberg-Richter Law (*Gutenberg and Richter, 1954*), and the aftershock decay rate by the Omori-Law (*Omori, 1894*) and its modifications (e.g. *Utsu, 1961*).

3.2.3 Modified Omori-Law

During a tectonic sequence, a large magnitude earthquake is typically followed by a sequence of smaller magnitude earthquakes with a time-dependent decaying event rate. The descriptive model of aftershock activity decay is called the Omori-Law (*Omori*, 1894) and simulates a set of aftershocks, succeeding a mainshock. The original Omori-Law

$$\frac{dn(t)}{dt} = K(t + c)^{-1} \quad (3.2.1)$$

utilizes the productivity K , a time offset constant c , and the lapse time t as measured from the time of the mainshock. $\frac{dn(t)}{dt}$ gives the occurrence rate of aftershocks per unit time.

The validity of the Omori-Law and its later modifications is limited to the minimum magnitude of complete observation (i.e. the magnitude of completeness). Often, the Gutenberg-Richter Law is used to estimate this magnitude of completeness (m_c), which is defined as the lowest magnitude at which 100% of the earthquakes in a space-time volume are detected (*Rydelek and Sacks*, 1989). Earthquake catalogues do not contain all actually occurring events, either because events occur that are not recorded by a sufficiently large number of stations, or because they are too small for their signals to be distinguishable from background noise on the seismograph. Also, the complex wavetrain of a large event can overlay an immediately following smaller event of its predecessor, making it impossible to identify the smaller event. Furthermore, the magnitude of completeness can change due to changes in the seismic station network over time (e.g. as stations are added or removed to/from the network).

Following his first Japanese publication in 1957, *Utsu* (1961) published his adaption of the Omori-Law, calling it the modified Omori-Law (MOL). The MOL describes the decay rate of an aftershock sequence $\frac{dn(t)}{dt}$ as

$$\frac{dn(t)}{dt} = K(t + c)^{-p} \quad (3.2.2)$$

including an additional decay exponent, p . For datasets that are overlain by constant background seismicity, a constant which represents background seismicity, can be added. In the following, I will explain the primary parameters of the MOL.

The **decay exponent**, p , varies usually between 0.8 and 1.5, and most frequently between 1.1 and 1.4 (*Utsu*, 1961). *Utsu et al.* (1995) give 0.6 – 2.5 as a worldwide range, with

a median of 1.1. The decay exponent has physical significance. High p -values denote rapid aftershock decay, which can have several causes. Higher p -values may stem from homogeneous distribution of fault strength and/or a more homogeneous distribution of shear strength on the fault (*Mikumo and Miyatake, 1979; Utsu, 1961; Helmstetter and Shaw, 2006*). Greater stress decay can also lead to higher p -values (*Mikumo and Miyatake, 1979, 1983; Dieterich, 1994*). It has been suggested that regions with higher crustal temperatures support a more rapid stress relaxation (e.g. *Kisslinger, 1996; Klein et al., 2006*), thus being reflected in higher p -values. A small p -value in contrast relates to mainshock-aftershock sequences which are found in multifracture areas, and/or areas which are largely heterogeneous. Then, the aftershock rate decays more slowly, which is reflected in a low p -value (*Tsapanos, 1995*). Only events with magnitudes above the magnitude of completeness must be chosen, because only then is the p -value independent of magnitudes. The p -value is also positively correlated to the b -value of the Gutenberg-Richter Law.

The **productivity constant**, K , has not been widely investigated. It is proposed to relate to the stress drop of the main shock that would match the observation, such that productivity is directly related to the magnitude of the mainshock (*Hainzl and Marsan, 2008*).

The **parameter**, c , was included in the formula to explain the apparent saturation of aftershock rate close to the origin time of a mainshock (*Kagan and Houston, 2005*). It typically ranges from 0.5 to 20 hr in empirical studies (e.g. *Utsu, 1961; Utsu et al., 1995*) but is almost always found to be small ($c \leq 0.01$ days) (*Utsu et al., 1995*). The significance of the c -value is still under discussion. *Kagan and Houston (2005)* proposed that the positive value of the c -value could be explained by under-reporting of small aftershocks immediately following the mainshock and hence does not reflect a physical property. Aftershocks usually cannot be registered individually during the mainshock rupture, as they are buried in the complex wavetrain of the mainshock. Other authors have suggested, that the c -value may yet have a physical origin, describing a characteristic time delay after brittle failure, before the onset of a power-law aftershock decay rate (e.g. *Narteau et al., 2002; Shcherbakov et al., 2004; Hainzl and Marsan, 2008*).

Evaluating the parameters of the MOL is most often done with the maximum-likelihood procedure as incorporated, e.g., in the software package SASEIS (*Ogata, 2006*). An initial guess for the parameters must be given as input, in addition to starting time and ending time of the event sequence. The FORTRAN program then computes the maximum likelihood estimates while iteratively minimizing the negative log-likelihood function. It gives standard errors for p , K , c , and the Akaike Information Criterion (AIC). The AIC is a selection criterion for finding the best model fit (*Akaike, 1974*), with the smallest AIC denoting the best fit. It is a relative criterion and therefore only suitable in selecting the best fit among differently defined models of the same dataset.

The task of fitting the MOL is not trivial, and interpretation of its calculated parameters needs to be set in context with supporting information (e.g. composition of material, rheology) due to the great range of possible values of the parameters. In fitting the MOL to a seismicity sequence, its duration, i.e. the starting time t_0 and the ending time t_{end} must be chosen very carefully, as it is critically important to the fit. Also, the parameters p and c are dependent on the length of the unit time interval (*Ogata, 1983*). Additionally, the standard deviation is biased toward higher values by a small number of events (fewer than 10 events) and by short timescales (downwards from 10 days) (*Nyffenegger and Frohlich, 1998*).

An example of a mainshock-aftershock sequence is given in Fig. 3.5. Graphically plotting the cumulative number of aftershocks versus time on a log-log scaled plane shows how the aftershock decay curve approximates a straight line with increasing t . The slope of the straight segment estimates p . This example also illustrates the influence of t_0 on the fit.

Simao et al. (2010) fitted the MOL to several sequences that had been recorded by a hydrophone network at the Mid-Atlantic Ridge. The left panel of Fig. 3.6 shows a purely tectonic sequence at a symmetrical spreading section of the MAR, with a p -value near the global median of 1.1. The middle and the right panel in Fig. 3.6 both show seismicity near detachment faults, where hydrothermal circulation and weak, very altered rocks may promote aseismic transient slip. This is reflected in the fact that more events are expected by the MOL than were actually recorded. The right panel of Fig. 3.6 shows a sequence of events which display migration of epicentres, which is commonly thought to indicate dyke intrusion (*Bergman and Solomon, 1990*). The MOL is fitted well to the tectonic activity in between the dyke intrusions but it cannot fit the seismicity associated with the dyke intrusions.

3.2.4 Datasets and method

The occurrence of earthquakes at mid-ocean ridges generally responds to the mode of spreading and the spreading rate. Earthquakes cluster narrowly along the divergent ridge axis, predominantly being normal faulting events, except at transform faults where strike-slip mechanisms are found. *Solomon et al. (1988)* inferred, from teleseismic records, that earthquakes at faster spreading ridges originate significantly shallower than those at slower spreading ridges, reflecting a systematic relationship of earthquake depth and spreading velocity.

Seismic events cluster in time and space, recording of smaller magnitude events being limited by the distribution and distance of the seismometer network to the earthquake hypocentre. Due to the great distance to land-based recording stations, earthquakes at ultraslow spreading ridges are mainly identified and located solely from teleseismic records in global earthquake catalogues. However, these recordings suffer from the great distances

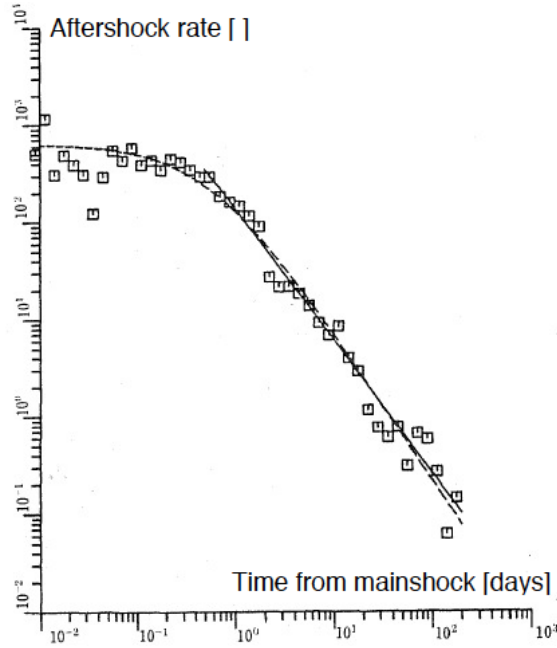


Figure 3.5 – Cumulative number of aftershocks from the Fukui earthquake sequence (1948). Plotted numbers of aftershocks were counted for each time interval of $(10^{i+j/10}, 10^{i+(j+1)/10})$ days with $i = -2, -1, 0, 1, 2$, and $j = 0, 1, \dots, 9$. The solid line gives the fit of the minimum AIC model ($t_0 = \frac{1}{2}$), the dotted line is fitted from $t_0 = 0$. Modified from *Ogata* (1983).

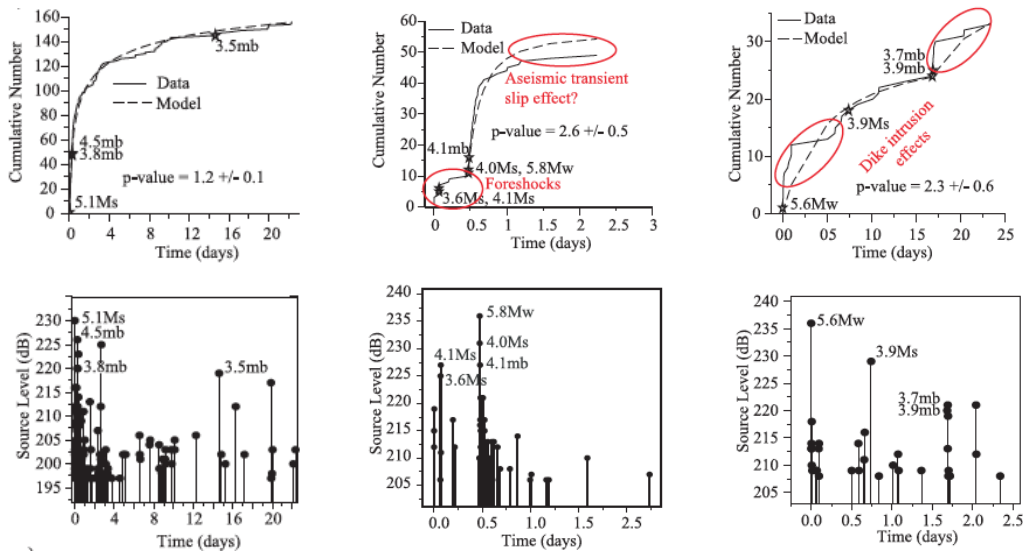


Figure 3.6 – Seismic sequences at the Mid-Atlantic Ridge, the upper panel shows the fit of the modified Omori-Law, the lower panel shows the source level distribution with some teleseismically registered events are marked specially with their magnitude. Left sequence: 2002, March 24. Middle sequence: 2000, Oct 5. Right sequence: 2001, Jul 13. From *Simao et al.* (2010).

between earthquake locations and seismometers. This is reflected in a high magnitude of completeness and only limited location accuracy.

Earthquake clusters that follow high magnitude events can be either isolated aftershock sequences (one mainshock and its aftershocks), or superposed sequences of several isolated aftershock sequences. It is also possible that clustered seismicity features a high magnitude event at its beginning, yet the following magnitude distribution does not follow a power-law (Type 3 seismicity as defined by *Mogi*, 1963).

The modified Omori-Law describes the declining aftershock rate of a single mainshock-aftershock sequence with time as a non-stationary Poisson point process, following a power-law distribution. This scale invariance means that even if recorded at teleseismic distances, a purely tectonic sequence can be fitted by the MOL so long as the aftershock rate decay is clearly defined.

Using the MOL, I analyzed two different datasets of closely spaced earthquake sequences in time and space at the ultraslow spreading ridges at the Southwest Indian Ridge and Gakkel Ridge:

The first dataset was compiled by C. Läderach from recordings of the VNA2 seismic array operated at the German Neumayer station in East Antarctica. *Läderach et al.* (2012) identified and placed four sequences at a magmatic centre on the Orthogonal Supersegment of the Southwest Indian Ridge (Fig. 3.7). Each earthquake cluster's first event was clearly an isolated event with associated events following. The analysis of these four sequences (Tbl. 3.1) with the MOL contributed to *Läderach et al.* (2012).

- 2001: 3rd Dec - 6th Dec
- 2004: 25th May - 27th May
- 2005: 6th Nov - 20th Nov
- 2008: 17th Sept - 22nd Sept

Cluster	Number of events	m_c	Number of events $> m_c$
2001	156	4.5	102
2004	114	4.5	57
2005	147	4.5	69
2008	29	4.5	19

Table 3.1 – Number of events and magnitude of completeness of four seismicity clusters at the SWIR for which a fit with the MOL was attempted.

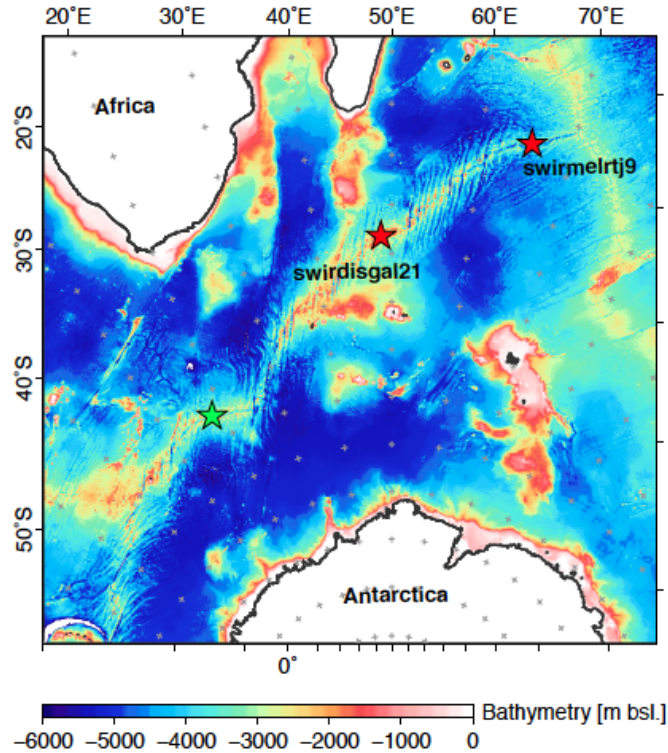


Figure 3.7 – Location of earthquake sequences at the SWIR which were attempted to be fitted with the MOL for *Läderach et al.* (2012) and for *Schlindwein* (2012). Green star denotes location of four earthquake sequences (2001, 2004, 2005, 2008) at the Orthogonal Supersegment of the SWIR (*Läderach et al.*, 2012). Red stars denote locations of two earthquake sequences as analyzed for *Schlindwein* (2012). ETOPO2 bathymetry after (*Smith and Sandwell*, 1997).

The second dataset was compiled from teleseismically registered events of the ISC database (*ISC*, 2008) by *Schlindwein* (2012). She divided the Arctic Ridge System and the Southwest Indian Ridge into 11 geologically distinct sections and used single-link cluster analysis to identify clusters of earthquakes. Four of these had a sufficient number of events to attempt a fit of the MOL (Figs. 3.7, 3.8, and Tbl. 3.2).

- ARS ('arevz37') 1999: 17th Jan - 24th Sept
- ARS ('arevz106') 2008: 5th Aug - 16th Aug
- SWIR ('swirdisgal21') 1997: 13th April - 18th April
- SWIR ('swirmelrtj9') 1996: 31st July - 5th Aug

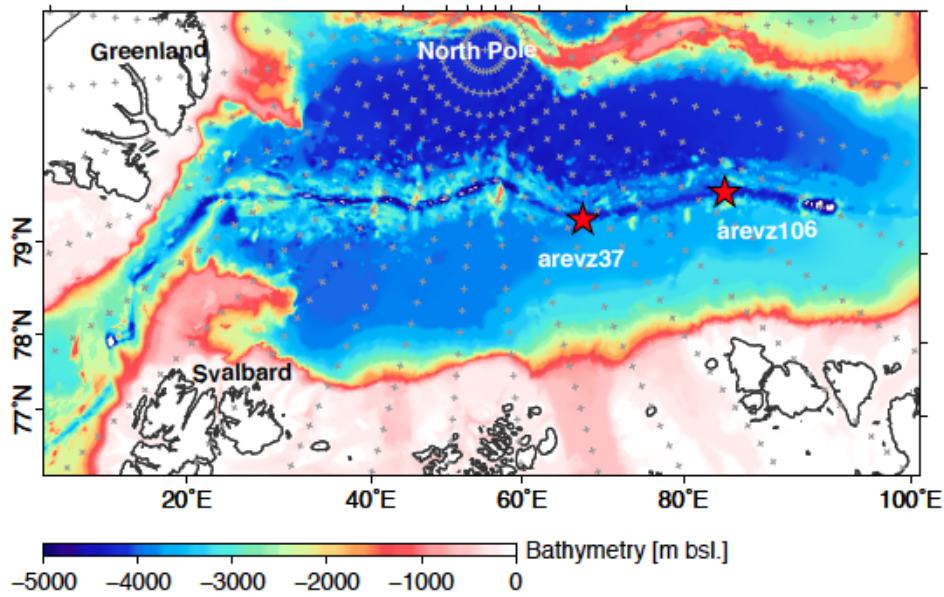


Figure 3.8 – Location of two earthquake sequences at the Gakkel Ridge which were attempted to be fitted with the MOL for *Schlindwein* (2012). Red stars denote locations of two earthquake sequences as analyzed for *Schlindwein* (2012). IBCAO2 bathymetry from (*Jakobsson et al.*, 2008).

Cluster	Number of events	m_c	Number of events $> m_c$
arevz37	220	4.75	71
arevz106	27	4.21	18
swirdisgal21	42	4.5	35
swirmelrtj9	22	4.5	22

Table 3.2 – Number of events and magnitude of completeness of four seismicity clusters at the SWIR and the GR which were attempted to be fitted by the MOL.

In the analysis, I could only use events whose magnitudes were greater than the magnitude of completeness for the corresponding dataset (Tbls. 3.1, 3.2). Unfortunately, due to the great distance between recording stations and hypocentres for all eight sequences, the dataset was complete only for rather high magnitudes and correspondingly, many smaller magnitude events were eliminated. Nonetheless, *Simao et al.* (2010) found a good fit of the MOL to acoustically registered earthquake clusters at the Mid-Atlantic Ridge, with a comparable number of events and timescales to my smallest event clusters. I therefore maintain that the eight earthquake sequences were eligible to be fitted to the theoretical function of the MOL.

I fitted the MOL with the widely used FORTRAN program SASEis2006 (*Ogata*, 2006). It calculates the three parameters K , c , p and the corresponding standard deviations (SD). Originally, I installed the SAPP-package of the R-project software suite for calculation of the MOL, yet this program does not give standard deviations which are sorely needed in

judging if the calculated values can be interpreted.

3.2.5 Results and interpretation of specific seismicity clusters

The four earthquake clusters observed by the Neumayer array at the western SWIR could only be fitted very poorly with the theoretical MOL function (c.f. Fig. 6.9). All earthquake clusters were defined very clearly, seismicity before and after being quiescent. This indicates that the chosen starting and ending times of the clusters are appropriately chosen. The earthquake cluster of 2008 was fitted best, having a well-defined onset and an event rate which is several times higher than the mean event rate in 2008 in this region (5.1 events/yr for the cluster versus 0.2 events/yr during the year 2008), yet also suffered from high standard deviations of all three parameters. For all four sequences, the poor fits and large standard deviations suggest that the analyzed clusters are not purely tectonic mainshock-aftershock sequences (Tbl. 3.3). Interpretation of the individual characteristic values of the MOL (K , c , p) is subsequently not likely to be informative.

Cluster	K -value \pm SD	c -value \pm SD	p -value \pm SD
2001	26830.0 \pm 418.0	5.2 \pm 10.1	3.7 \pm 1.7
2004	113.4 \pm <i>NaN</i>	1473.0 \pm <i>NaN</i>	0.2 \pm <i>NaN</i>
2005	975.6 \pm 148580.0	43.8 \pm 1139.0	1.4 \pm 31.0
2008	24.5 \pm 306.0	2.7 \pm 17.2	1.3 \pm 5.0

Table 3.3 – Calculated MOL parameters for the four earthquake clusters at the SWIR.

The interpretation that these sequences do not show characteristics of tectonic mainshock-aftershock sequences can only be based on the attempt to fit the MOL to the individual datasets, and therefore was integral to the conclusion drawn in *Läderach et al.* (2012). From these same datasets, the b -value of the Gutenberg-Richter Law which is similarly scale-invariant, could be calculated with only small standard errors for all these sequences. I therefore maintain, that the failure to fit the MOL did not result from not enough, or not good enough data, but rather that the MOL simply does not fit.

I also tried to fit the four earthquake clusters from *Schindwein* (2012) with the MOL. Only the cluster 'swirdisgal21' could be fitted using its whole sequence of events (Fig. 3.9), but even then the fit suffers from high uncertainties (Tbl. 3.4). Cluster 'swirmelrtj9' could only be fitted with an adjusted starting time, t_0 , of 0.016 days after the first event, leaving only 18 of 22 events to be fitted, and similarly exhibits high uncertainties (Tbl. 3.4) that may be caused by the small number of events. Cluster 'arevz106' could not be fitted at all, as the program did not converge.

Cluster	K -value \pm SD	c -value \pm SD	p -value \pm SD
swirdisgal21	11.7 ± 14.4	0.4 ± 0.4	2.7 ± 1.3
swirmelrtj9	5.2 ± 4.3	0.2 ± 0.4	1.2 ± 0.7

Table 3.4 – Calculated MOL parameters for two earthquake clusters at the SWIR.

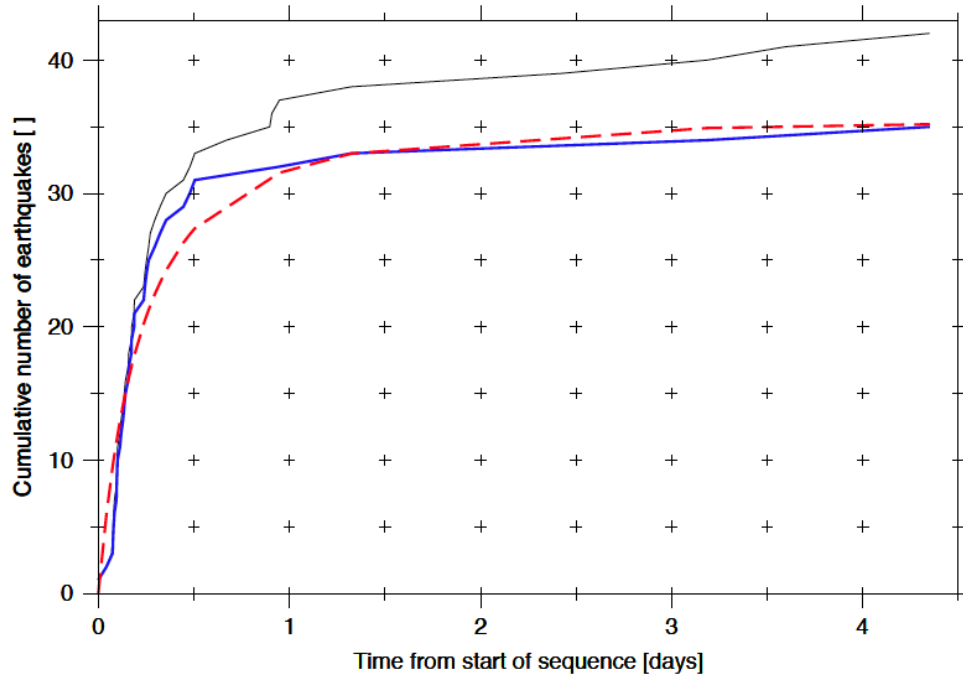


Figure 3.9 – Fit of the modified Omori-Law to the earthquake cluster ‘swirdisgal21’. Black line denotes mainshock-aftershock sequence including all registered events, the blue line denotes sequence of events with $M > m_c$, the red dotted line gives the associated fit of the MOL.

Cluster ‘arevz37’ corresponds to the 1999 teleseismically registered earthquake sequence, which was relocated and analyzed in *Korger and Schlindwein* (2012). This sequence starts with rather low magnitude events, but displays three high magnitude events on the 1st of February, day 16 after the start of the sequence (Fig. 3.10). Additionally, high magnitude events were registered throughout the sequence (c.f. Fig. 5.4). Such behaviour is inconsistent with a single tectonic mainshock-aftershock decay sequence, and suggests either a magmatic influence, or a superposition of tectonic sequences.

Unsurprisingly, the complete earthquake cluster was fitted very poorly by the MOL (dashed black line in Fig. 3.11), which is indicated by the near-zero value of the parameter c (Tbl. 3.5, #1). Due to the scope of *Schlindwein* (2012), a more detailed analysis of the seismicity cluster ‘arevz37’ was not needed and the following detailed analysis was not included as contribution.

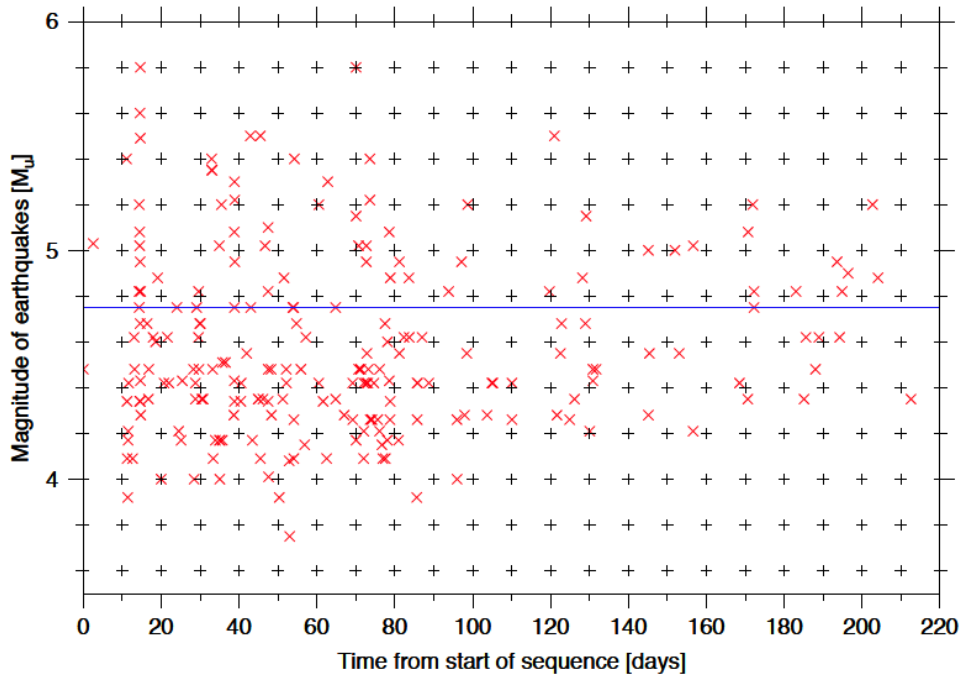


Figure 3.10 – Unified magnitudes (*Scordilis*, 2006) of the earthquake sequence 'arevz37', plotted over time from first event of the sequence. Blue line corresponds to m_c .

In light of the possible geological implications inherent in a eventual fit of the MOL to a sub-dataset of the 1999 earthquake sequence ('arevz37'), I tried accommodating the MOL to a different starting time by visually placing t_0 after the relatively short period of seismic quiescence following the last high magnitude event on February 1st (t_0 on February, 5th) (Tbl. 3.5, #2), and also tried to fit the MOL to a shorted sequence with the same t_0 (Tbl. 3.5, #3). These attempts were not successful, as indicated by their high uncertainties. An attempt to fit the MOL to the sequence starting immediately after the last high magnitude event on February, 1st (Tbl. 3.5, #4) also did not succeed, as the c -value also was calculated near zero.

#	t_0 and t_{end}	Number of events	K -value \pm SD	c -value \pm SD	p -value \pm SD
1	Jan, 17 th - Aug, 9 th	71	1.8 ± 0.5	0.0 ± 0.3	0.4 ± 0.1
2	Feb, 5 th - Aug, 9 th	58	75.3 ± 836.0	63.0 ± 200.0	1.1 ± 1.9
3	Feb, 5 th - Jun, 23 th	48	119.3 ± 5831.0	58.1 ± 221.0	1.3 ± 2.7
4	Feb, 1 st - Aug, 9 th	60	1.0 ± 0.4	0.0 ± 0.2	0.3 ± 0.1
5	March, 28 th - Aug, 9 th	30	0.8 ± 0.7	0.4 ± 2.9	0.4 ± 0.2

Table 3.5 – Calculated MOL parameters for the 1999 earthquake sequence.

The most successful fit was produced by starting the fit after the overall last high magnitude event ($M_u=5.80$) in the later part of the 'arevz37' sequence, placing t_0 on the 28th of March. This fit produced a very low p -value of 0.36, while including only 30 events. De-

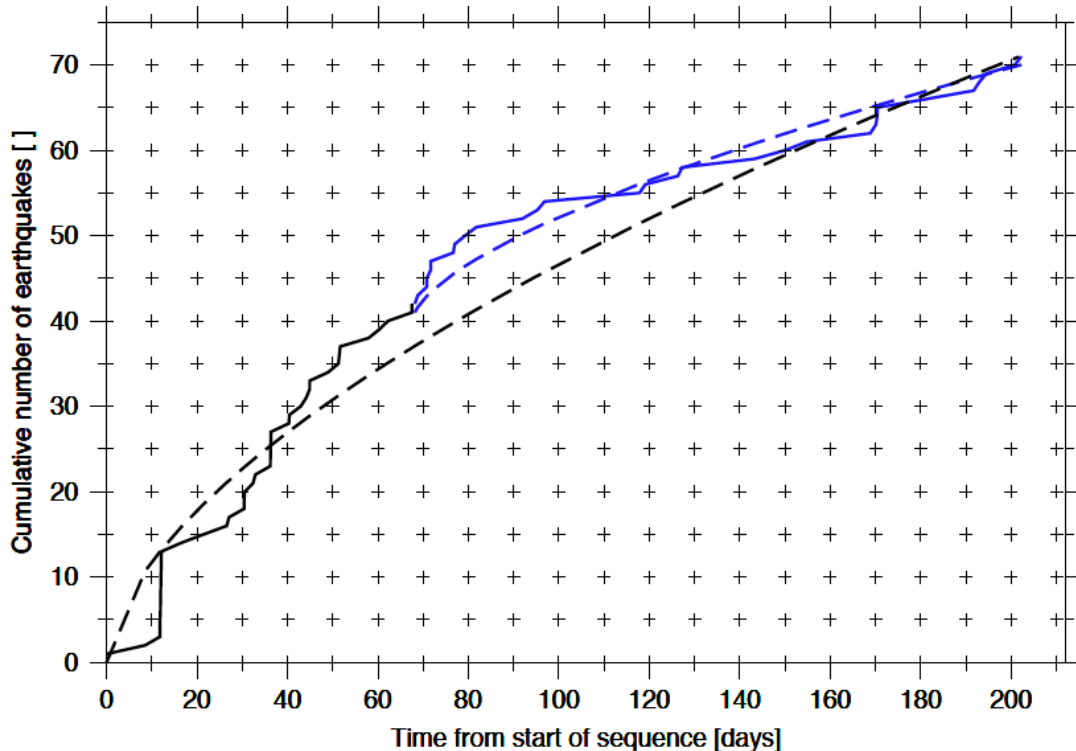


Figure 3.11 – Cumulative number of earthquakes of 71 events ($m > m_c$) of the 1999 earthquake sequence at Gakkel Ridge (black and blue line). Black dashed line indicates fit of the MOL for the whole sequence. Blue dashed line shows the fit of the MOL starting at 28th of March, the corresponding part of the 71 event dataset has been indicated by blue color.

spite the very low p -value in global context (*Utsu et al.*, 1995), this part of the 'arevz37' sequence could in fact be fitted with reasonable uncertainties in contrast to the other trials with varying starting and ending times (Tbl. 3.5, #1-4). This therefore hints at a tectonic release of stress at the very end of the sequence (Fig. 3.11).

The modified Omori-Law describes the aftershock activity decay of a purely tectonic mainshock-aftershock sequence. As such, it can differentiate if a sequence is purely tectonic in origin, or not. The negative result of the attempt to fit these eight sequences to the MOL function indicates a magmatic influence in producing such seismicity, but regrettably, it does not prove it. Due to the remote mid-ocean ridges where these earthquake sequences were registered, it was not possible to collect further supporting evidence (e.g. by placing microseismicity networks and recording smaller magnitude events for a comparable low-magnitude analysis), aside from noting that all these seismicity sequences originated at magmatic segments of ultraslow spreading ridges. These magmatic segments generally display focused magmatism with prominent volcanic centres, consistent with the notion of dyking events at the time of the recorded clustered seismicity.

The attempted fit of the modified Omori-Law to the earthquake sequence of 1999 at 85°E/85°N as presented here, agrees with the results of my spatiotemporal analysis of the same seismicity sequence by *Korger and Schlindwein* (2012). In *Korger and Schlindwein* (2012), I divided the earthquake sequence into three distinct phases of earthquake activity, with the third stage starting on the 7th of April, 1999. *Korger and Schlindwein* (2012) interpreted this third and final stage of seismic activity either an effusive stage of volcanic activity, or a post-intrusive adjustment of the stress field. In the light of this new analysis of the earthquake sequence using the modified Omori-Law, a tectonic component to this later stage of seismicity is evidently involved.

3.3 Local seismicity at 85°E/85°N

3.3.1 Preparation of local dataset and localization with Hyposat

In 2007, the AGAVE expedition returned to 85°E/85°N to conduct extensive research (see ch. 1.2). One of the experiments consisted of collecting microseismicity data, using three ice floes, each with an array of four seismometers. The dataset consisted of a continuous seismic record between 15th and 31st July 2007. Due to the increased noise level while the icebreaker I/B Oden was in motion, events were more clearly seen while the ship was stationary. The dataset included more than 500 events, which showed as a first indicator large amplitudes on the vertical component of the three component seismometers. Comparing stations of arrays among each other and between the arrays, I could identify 303 signals which resulted from local earthquakes. These are clearly distinguishable from icequakes by a clear signal on all three ice floes, in contrast to icequakes which can often only be recorded by seismometers of a single floe. I picked local events per hand on the vertical components. It was not possible to calculate magnitudes, as the efficiency of coupling between the seismometers and the ice floes was not known and no amplitude versus distance function was available for this setting. Also, not one local event which was present in the dataset was also registered by a land station and had a determined magnitude.

About half of the events were characterized by emergent P-phases, the remaining started with impulsive P-phases. The S-wave energy sometimes was buried in a complex wavetrain (two example events are shown in Fig. 3.12). For most of the events, I identified water-multiples due to the water layer of ~ 3900 m, arriving typically ~ 5 s after the first onset.

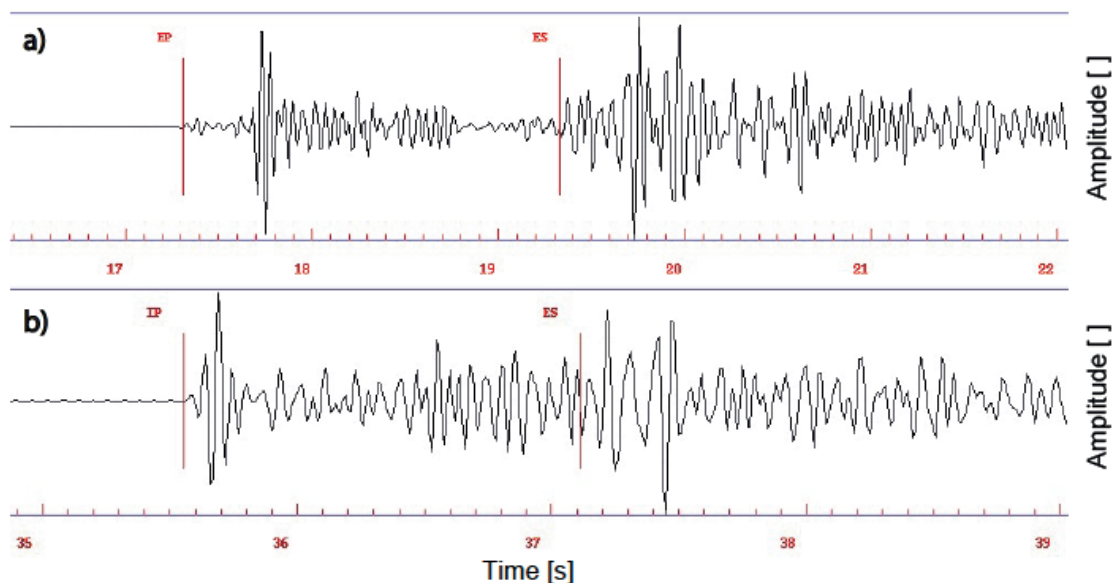


Figure 3.12 – Examples of an emergent P-phase (a) and an impulsive P-phase (b).

In 2010, *Riedel and Schlindwein* (2010) compiled a regional velocity model using teleseismic phases from the 1999 earthquake sequence, which was used in localization of this dataset. Yet, for the local dataset collected by the AGAVE expedition, this regional velocity model had to be optimized. To this end, and in the absence from information about the velocity structure from other sources (i.e. seismic profiles), I had to make use of the the local earthquakes itself.

Ideally, the localization algorithm would take the very rough 3D bathymetry in the survey area into account. NonLinLoc has the ability to include a 3D bathymetry in local mode, so therefore I wrote a FORTRAN77 script to generate the required binary grid bathymetric file. I also programmed shell scripts, which enabled NonLinLoc to localize all events in cycled mode. Yet, the bathymetry could only be included in blocks of 200 m side lengths, which did not approximate the bathymetric variation well. Also, it needed extensive computational time (about 4 days) for locating the dataset once, so I turned to Hyposat even if it can only use a 1D velocity model. Arrival times of all phases were corrected to a compensation depth below which this 1D velocity model applies.

Hyposat locates events first with a fixed starting hypocentre depth, and afterwards, if possible, the hypocentre depth is allowed to vary. It tries to fit not only picked phases, but also traveltimes differences (e.g. S-P, pP-P). The quality of an individual hypocentre is defined by the 2D error ellipse axes, and, when the free depth location succeeded, by the hypocentre depth error. The root mean square of the traveltimes residuals is also given. In this chapter, I refer to this parameter as the 'RMS'.

I generated a suite of 95 velocity models (for details on the velocity models, please refer to ch. 7), and wrote a looped shell script that localized a sub-dataset of 44 well-defined events with each of the velocity models. I first selected either the free or the fixed depth solution for each event, preferring the free depth solution to the fixed depth solution only if the error in hypocentre depth was smaller than 3 km, the RMS got smaller, and the number of phases used in localization got greater compared to the fixed depth solution. Generally, solutions were eliminated when the length of the semi-major error ellipse axis was greater than 10 km, the RMS was greater than 0.2 s, or the error in hypocentre depth exceeded 3 km. Yet, the greater degree of freedom when the hypocentre depth was allowed to vary, caused a systematical, nonlinear change in the value of the error parameters. Free depth solutions were generally defined by a greater number of phases used in localization, a smaller RMS, but a greater length of semi-major error ellipse axis (Fig. 3.13).

As the localized hypocentres of each velocity model included a varying number of free- and fixed depth solutions, and not all velocity models could locate all events of the sub-dataset, it therefore was not possible to select the best velocity model based on a simple comparison of average quality parameters. Thus, I calculated the mean of RMS of traveltime residuals, the mean of the length of semi-major error ellipse axis, and the mean number of phases used in localization for each localized sub-dataset, differentiating between free depth solutions (Fig. 3.13a), fixed depth solutions (Fig. 3.13b), and the entirety of the selected solutions (Fig. 3.14).

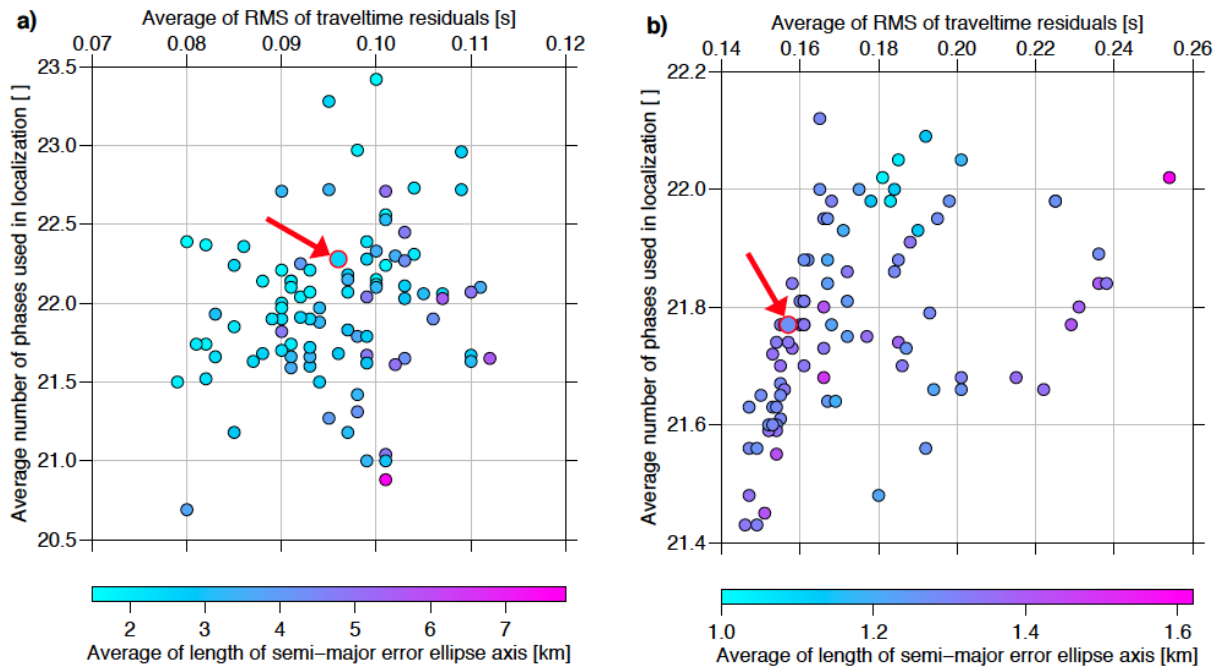


Figure 3.13 – Comparison of the average quality parameters for all tested velocity models with a) only free depth locations and b) only fixed depth locations averaged. The selected velocity model is denoted with a red arrow.

Unfortunately, the velocity models with the smallest RMS, the highest number of phases used in localization, and the smallest length of semi-major error ellipse axis for the free depth solutions were mostly found to be inferior when looking at the plot with the fixed depth solutions, and vice versa. I chose the best possible velocity model (c.f. Fig. 7.4, blue line), taking into account the systematic differences between fixed and free depth locations (Fig. 3.14).

I then located the entire dataset (303 events) with this velocity model (in the following I will refer to this model as '1D model'). Most of the 248 locatable events were localized directly in the rift valley. Due to the drift of the recording stations on their ice floes, the resulting rays of 128 events which were registered by at least two of three seismometer arrays, extensively covered the centre of the rift valley (Fig. 2.2), which enabled me to do a local earthquake tomography (LET).

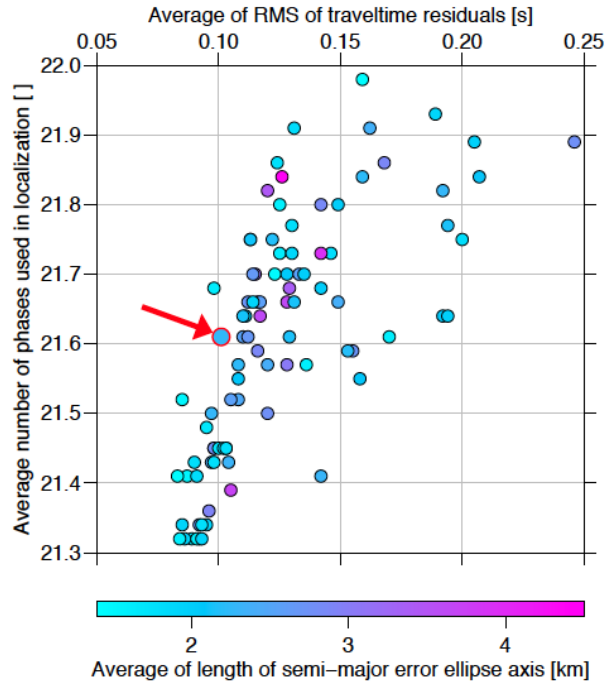


Figure 3.14 – Comparison of the average quality parameters for all velocity models, using the best solution for each earthquake and each velocity model. The chosen velocity model is denoted with a red arrow.

3.3.2 Local earthquake tomography

The survey area and the collected dataset were unusual in several aspects, which limited the selection of possible tomographic algorithms. Also, due to the unusual collection method, highly sophisticated methods (i.e. waveform tomography) could not be used.

The tomography algorithm had to be able to deal with the following:

- Rough 3D bathymetry in survey area → has to be included as fixed 3D interface
- Fixed velocity of water layer → selective inversion for velocity layers must be possible
- Multitude of station coordinates → ability to deal with 1821 receiver coordinates

I evaluated several state-of-the-art traveltim algorithms: SimulPS12 (*Evans et al.*, 1994), FMTOMO (*Rawlinson et al.*, 2006), LOTOS (*Koulakov*, 2009), PSTOMO_eq (*Tryggvason*, 2009). I chose FMTOMO as it could cope with all of above noted requirements without needing to be modified. Also, this algorithm would not require excessive computational time.

I installed and compiled FMTOMO, and generated a flow chart (Fig. 3.15), as this tomography algorithm is a rather complicated package consisting of various programs and subprograms all working together. Grid parametrization is especially complicated:

FMTOMO uses not only a velocity grid which gives velocity information in distinct cell blocks, but also a propagation grid whose cell size is responsible for the appropriateness of ray approximation. Interfaces are also defined in a separate grid file. The 3D reference velocity model is defined by all three of these grids. For details on model structure, calculation and interpolation scheme, please refer to *Korger and Schlindwein (2013)* and citations therein.

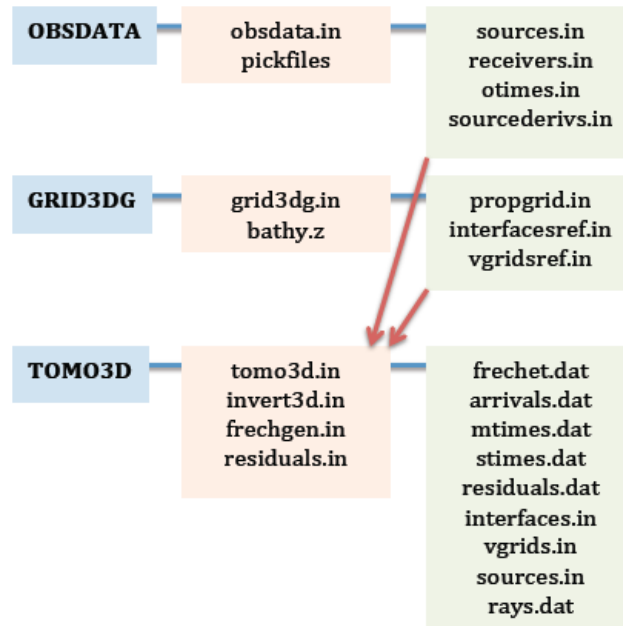


Figure 3.15 – Flow chart for the use of the traveltime algorithm FMTOMO. Main subprograms are highlighted in blue, input files are highlighted in red.

Prior to inversion, specially formatted input files for the main program TOMO3D have to be generated. FMTOMO provides the subprogram OBSDATA to generate hypocentre-related input files (starting hypocentres, station coordinates, traveltimes and associated errors). I chose to use 128 events of the whole dataset, which were registered by seismometers of at least two arrays.

The layered 3D reference velocity model is created by the subprogram GRID3DG. Yet, the vertical block size of the velocity grid would in any case be greater than the thickness of the first layer of the newly compiled 1D model (ch. 3.3.1 and c.f. Fig. 7.4, blue line). I therefore chose to adapt the 1D model, combining layer 1 and 2 into a single layer (c.f. Fig. 7.4, red line). I incorporated the bathymetry of IBCAO2 (*Jakobsson et al., 2008*) with 100 m sample spacing. GRID3DG created the 3D reference velocity model from this 1D reference velocity structure.

Prior to the first inversion, I tested the main program TOMO3D extensively. An adaption of the FORTRAN90 source code became necessary, as the original program was not able to relocate sources during inversion to another layer of the velocity model and aborted

the inversion when encountering such a source. I also fixed a minor shortcoming of the main program, as it only saved the calculated traveltime residuals RMS from the final iteration to a file. With my adaptation, it now was possible to track the improvement of this value through several iterations.

I took care to implement the optimal damping and smoothing values, writing a short FORTRAN90 code which calculated model perturbation and roughness. I then selected the combination of values which produced the model with the lowest possible traveltime residual RMS, in combination with the lowest model perturbation and lowest model roughness (c.f. Fig. 7.6). This indicated the simplest model to fit the data.

Plotting the resultant velocity grid was done using GMTSLICE, another subprogram of FMTOMO. I wrote shell-scripts, running GMTSLICE cycled through several slices in horizontal and vertical directions. In visual inspection, the resultant plots showed a pronounced contrast of increased velocities directly above the Moho (c.f. Fig. 7.7). Based on that, I judged a gradient velocity model to better represent the real velocity structure. I had to edit the velocity grid per hand to create the required gradient model, as GRID3DG is not set up to compile gradient models.

I used this new gradient model as the 3D gradient reference model (c.f. Fig. 7.4, orange line) for a velocity inversion. During elimination of four earthquakes which were suspected of causing unrealistic velocity structures, I fixed an error in the subprogram of FMTOMO which dealt with including only selected sources in the inversion. For judging the region of the final model which is confidently covered by rays (c.f. Fig. 7.8), I wrote a shell-script, summing ray points in longitude, latitude and depth conforming to velocity grid spacing (c.f. Fig. 7.9).

To assess the resolution of the inversion result, I ran a checkerboard test and a restoration test. Synthetic tests such as these can evaluate how well structures are recovered by the inversion. They create a synthetic dataset, generally tracing rays through a synthetic structure while using the same set of receiver and earthquake coordinates as the original dataset. This artificial dataset is then used for an inversion using the original 3D reference velocity model, and then the result is compared to the initial structure. For the checkerboard test I ran GRID3DG again to create a checkerboard pattern and then again adapted the resultant velocity grid file per hand to include it in the 3D gradient reference velocity model (c.f. Fig. 7.10a and c). For the restoration test I adapted the velocity grid file per hand, including a major structure which shows up in the well ray-covered area (c.f. Fig. 7.10e and g).

The results of the LET are limited due to the unusual collection method, whose main drawback is the high noise level of the data. S-waves were especially tricky to identify, sometimes I was completely unable to find them in the wavetrain. Also, the limited survey time resulted in a limited number of registered earthquakes and therefore a limited ray coverage outside of the well-covered region. The final grid parametrization of ~ 2 km in

longitude, latitude and depth therefore cannot resolve smaller structures.

Nevertheless, the seismicity analysis, localization and subsequently performed tomographic traveltimes inversion of the dataset collected by the AGAVE expedition of the 85°E/85°N survey area brought important insights into the seismicity and thermal structure of an ultraslow spreading centre. The survey method of three drifting arrays of seismometers on ice floes made it possible to record and place microseismicity at a location, where a conventional microseismicity survey would be impossible to conduct.

4 Contributions to scientific publications

Here I give a succinct summary of each of the scientific publications which comprise this PhD project, and I detail the individual contributions of each of its authors. The publications are included in full in the following chapters. The pertinent processing and applied methods have been explained in chapter 3.

4.1 Performance of localization algorithms for teleseismic mid-ocean ridge earthquakes: The 1999 Gakkel Ridge earthquake swarm and its geological interpretation

Korger, E. I. M., and V. Schlindwein (2012), Performance of localisation algorithms for teleseismic mid-ocean ridge earthquakes: The 1999 Gakkel ridge earthquake swarm and its geological interpretation, *Geophys. J. Int.*, 188(2), doi: 10.1111/j.1365-246X.2011.05282.x

This publications (see ch. 5) consists of an analysis of teleseismic earthquake sequence data at 85°E/85°N Gakkel Ridge, Arctic Ocean. The unusual number of earthquakes, duration and magnitudes involved pointed to a spreading event at this ultraslow spreading ridge causing this unique seismicity. As a reliable location of teleseismic earthquakes is crucial for geological interpretation, the main body of this article consists of the comparison of earthquake locations as localized by three highly different localization algorithms (Hyposat, NonLinLoc, Mlocate). A spatiotemporal analysis showed three distinct phases of seismicity, the following geological analysis focused on interpreting the most probable centre of earthquake activity in each.

I did the localization of the earthquake sequence with two localization routines, Hyposat and NonLinLoc. Dr. Schlindwein localized the events with Mlocate. I analyzed all locations with regard to quality, did the geologic interpretation and wrote the manuscript. For details on the methodical approach, please refer to chapter 3.1. Dr. Schlindwein supervised the project.

4.2 Characteristics of tectonomagmatic earthquake swarms at the Southwest Indian Ridge between 16°E and 25°E

Läderach, C., E. Korger, V. Schlindwein, C. Müller, and A. Eckstaller (2012), Characteristics of tectonomagmatic earthquake swarms at the Southwest Indian Ridge between 16°E and 25°E, *Geophys. J. Int.*, 190, 429–441, doi: 10.1111/j.1365-246X.2012.05480.x

This publication (see ch. 6) comprises an 8-year-long dataset of the VNA2 seismic array operated by the German Neumayer station in East Antarctica. It includes the analysis of over 700 events and the identification of four clustered earthquake sequences from the Orthogonal Supersegment of the Southwest Indian Ridge. The interpretation focused on relation of these earthquake sequences to tectonic or magmatic processes.

My contribution to this publication consisted of providing statistical analysis of four earthquake sequences at the Orthogonal Supersegment of the Southwest Indian Ridge with the modified Omori-Law, to verify their tectonic or magmatic origin. The data on origin time and magnitude of the events which were registered by the VNA2 seismic array was given to me by C. Läderach. For details on statistical background and analysis, please refer to the methodical chapter 3.2. I also wrote the pertinent section of the manuscript and fielded related questions of the reviewers.

C. Läderach did the event extraction, phase picking and further analysis of the events occurring at the SWIR, and wrote the manuscript. Christian Müller reported on the possibility that clustered seismicity at the SWIR is detected by the VNA2 array. Alfons Eckstaller provided the time-corrected waveform data of the Neumayer observatory and assisted in magnitude calculations. Dr. Schlindwein supervised the project.

4.3 Seismicity and structure of the 85°E volcanic complex at the ultraslow spreading Gakkel ridge from local earthquake tomography

Korger, E. I. M., and V. Schlindwein (2013), Seismicity and structure of the 85°E volcanic complex at the ultraslow spreading Gakkel ridge from local earthquake tomography, Submitted to *Geophys. J. Int.* on June 6th, 2013

This publication (see ch. 7) revolves around detailed analysis of a 16-days-long local seismological dataset collected by the AGAVE expedition in 2007, at 85°E/85°N Gakkel Ridge, Arctic Ocean in the aftermath of its last spreading episode in 1999. It consists of identification of seismic events, compiling a local velocity model from this data, localizing these events, and doing a local earthquake traveltime tomography, the first ever to be done

at an ultraslow spreading ridge. The results were interpreted with regard to earthquake activity, Moho and hypocentre depths, and seismic velocity structure.

The dataset of the AGAVE survey was preliminarily inspected to provide me with data of vertical components of over 500 suspected events. I picked direct phases of seismological events, and did all work regarding localization, velocity model, tomographic analysis and interpretation. The preparation of the dataset is explained in detail in ch. 3.3, for details on the local earthquake tomography, please refer to chapter 3.3.2. I also wrote the manuscript. Dr. Schlindwein supervised the project.

5 First paper: The 1999 earthquake swarm at 85°E/85°N

Korger, E. I. M., and V. Schlindwein (2012), Performance of localisation algorithms for teleseismic mid-ocean ridge earthquakes: The 1999 Gakkel ridge earthquake swarm and its geological interpretation, *Geophys. J. Int.*, 188(2), doi: 10.1111/j.1365-246X.2011.05282.x

5.1 Summary

In 1999, an unusual earthquake swarm at the 85°E/85°N volcanic centre on the Gakkel ridge, Arctic Ocean, was detected teleseismically. The swarm lasted over 9 months and counted 252 events with $m_b \geq 3.1$. The duration, number of events and magnitudes of this swarm were greater than other swarms which were previously recorded at a mid-ocean ridge. This swarm was especially interesting as coming from a ridge with full spreading rate < 20 mm/yr. We relocated the earthquake swarm comparing the performance of three different localization algorithms: (1) the absolute least-squares routine HYPOSAT, (2) the absolute probabilistic routine NonLinLoc and (3) the relative least-squares routine Mlocate. The epicentres as calculated by each algorithm mostly did not agree within their error ellipses. The choice of location algorithm proved more critical than, for example, the choice of a local velocity model. We compiled a set of well-localized events which closely agree in at least two routines, mostly Mlocate and NonLinLoc.

We conclude that the earthquake swarm of 1999 was related to a spreading episode and shows a complex interplay of tectonic and magmatic events. Our geological interpretation revealed three phases in swarm activity: In the first phase from January, 17th up to February 1st fracturing of the crust took place, either as a result of or enabling magmatic intrusion. Seismicity in the second phase from February, 2nd to April, 6th expanded along- and across-axis. It showed signs of magmatic interaction, but a clear dike migration pattern is absent. At the beginning of the third phase, a distinct break in the event rate suggested a change in the physical process, either an adjustment of the stress field to the new regime or a transition to an effusive stage.

5.2 Introduction

Situated in the Arctic Ocean, Gakkel ridge spans from Fram Strait to the continental Siberian shelf (Fig. 5.1a). Due to its very slow spreading between 12 mm/yr full spreading rate at the western and 6 mm/yr at the eastern end (*Sella et al.*, 2002), it was classified as an ultraslow spreading ridge (*Dick et al.*, 2003). Below about 20 mm/y spreading rate, models predict a decreasing production of magmatic melt due to heat loss by conductive cooling (e.g. *Bown and White*, 1994). Magmatic accretion seems to be concentrated in discrete volcanic centres, spaced widely apart with thin oceanic crust (*Cannat*, 1993; *Michael et al.*, 2003). Gakkel ridge and the Southwest Indian Ridge as main representatives of the class of ultraslow spreading ridges are situated in poorly accessible areas with difficult working conditions. Therefore, the mechanisms of crustal accretion and melt distribution at ultraslow spreading ridges are still poorly understood.

In 1999, Gakkel ridge at 85°E/85°N was the site of unusual seismic activity (*Mueller and Jokat*, 2000). During 9 months, a swarm of 252 events was recorded by seismological observatories around the world with magnitudes between m_b 3.1 and 5.2 (Fig. 5.1b). Normally, earthquake swarms at mid-ocean ridges last only a few weeks (e.g. *Dziak et al.*, 1995), consisting of few events large enough to be recorded at seismic stations on land (e.g. *Bergman and Solomon*, 1990).

Preliminarily located, the 1999 earthquake swarm was sited at a volcanic centre where the SCICEX-99 expedition believed to see indications for a recent volcanic eruption (*Edwards et al.*, 2001). Further expeditions to this area observed signs of volcanic activity: A massive hydrothermal plume in 2001 (*Edmonds et al.*, 2003) and explosive seismoacoustic signals originating from the seafloor indicated ongoing volcanic activity (*Schindwein et al.*, 2005; *Schindwein and Riedel*, 2010). Vast amounts of pyroclastic deposits discovered in 2007 pointed to deep submarine explosive volcanism in this area (*Sohn et al.*, 2008). This led to the assumption that the 1999 earthquake swarm marked the onset of a volcanic cycle of at least 2 years duration (*Schindwein and Riedel*, 2010).

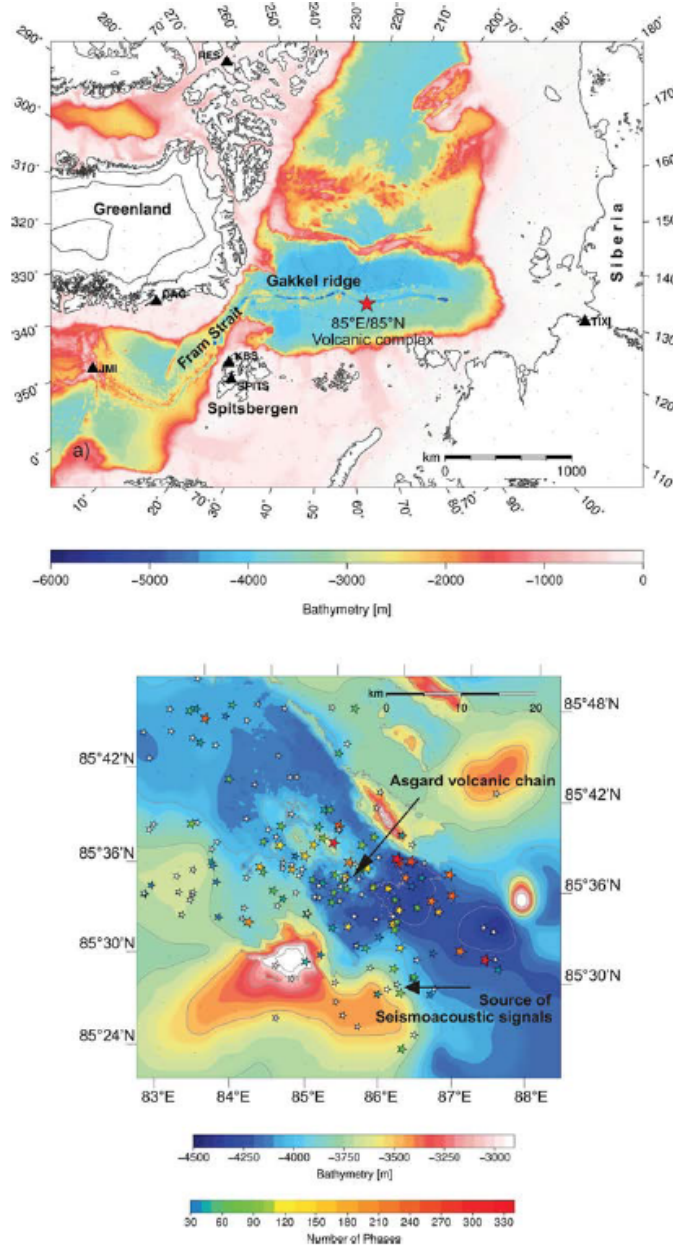


Figure 5.1 – (a) Overview of Gakkel Ridge region with a star designating the source area of the 1999 earthquake swarm. Triangles mark the nearest six seismic stations, IBCAO bathymetry (*Jakobsson et al.*, 2008). (b) Close-up on the 85°E/85°N volcanic complex with ISC-reviewed bulletin epicentres of the 1999 earthquake swarm. Size and colours of stars correspond to the number of recorded phases. Events with less than 30 recorded phases are marked in white. Also indicated are Asgard volcanic chain, which consists of Oden, Thor and Loki volcanoes (*Sohn et al.*, 2008), and the source region for seismoacoustic events (*Schlundwein and Riedel*, 2010). Composite bathymetry grid of *Schlundwein and Riedel* (2010) with contour spacing 250 m.

Migration of earthquake epicentres serves as a key to classify a mid-ocean ridge seismic sequence as a magmatic dyking event (*Bergman and Solomon, 1990; Dziak et al., 1995*). The lack of an elongated shape of teleseismic earthquake swarms at the Mid-Atlantic ridge was interpreted by *Bergman and Solomon (1990)* as a sign for mostly tectonic origin of these swarms. Based on USGS event locations, *Tolstoy et al. (2001)* suggested that the 1999 Gakkel ridge earthquake swarm resulted from magmatic pulses migrating along axis. *Riedel and Schlindwein (2010)* relocated the swarm using published phases by the comprehensive bulletin of the International Seismological Centre (ISC), but could not confirm the proposed migration of epicentres found by *Tolstoy et al. (2001)*.

In order to verify a potential epicentre migration of magmatic spreading events, a reliable earthquake localization is necessary, but difficult to obtain due to a lack of local and regional recording stations. *Pan et al. (2001)* and *Bergman and Solomon (1990)* attempted to improve the earthquake location accuracy at mid-ocean ridges using bathymetry as a constraint and relative relocation methods, respectively. We performed a comprehensive, systematic study to assess the influence of localization parameters, like velocity model and station distribution, on the localization result (*Korger, 2010*).

In this paper, we compare the performance of three localiation algorithms (absolute and relative least-squares method, absolute probabilistic method) for the relocation of the 1999 Gakkel ridge earthquake swarm. We deliberately use three highly different localization algorithms for our study. Based on the relocation, we extract trustworthy information on the earthquake epicentres and assess the results in the light of previous studies.

5.3 Dataset and Methods

5.3.1 Teleseismic dataset

We use phase arrival times of 252 events between 17th January and 24th September 1999 in the vicinity of a volcanic centre of Gakkel ridge at about 85°E/85°N as archived in the reviewed ISC bulletin (International Seismological Centre 2001).

Body-wave magnitudes range between m_b 3.1 and 5.2 with 73 events having $m_b \geq 4.3$. The total number of recorded phases per event for the original dataset ranges between 3 and 339 with a mean of 45 phases. Although the nearest recording stations (Fig. 5.1a) are situated on Spitsbergen (KBS, SPITS), Jan-Mayen-Island (JMI), Greenland (DAG), Canada (RES) and at the northern coast of Siberia (TIXI) with a minimum epicentral distance of 10.75°, Fig. 5.2a) shows that most phases were recorded by stations which are between 30° and 60° away. As a consequence, the localization algorithms tolerate large travel-time residuals at the few near-stations in order to better fit the

abundance of large distance stations (Korger, 2010; Riedel and Schlindwein, 2010). These travel-time residuals probably result from an inadequate representation of heterogeneous upper mantle structure in 1D velocity models. Tests using only a subset of stations with epicentral distances $< 30^\circ$ resulted in significant shifts of the epicentre (about 20 km) with respect to using the full set of recorded phases (Korger, 2010). We therefore limit our comparative study to 120 events with a minimum number of 30 recorded phases (Fig. 5.2a) covering usually from 11° to more than 60° epicentral distance. Compared to the epicentral station distribution, the distribution of the backazimuths (Fig. 5.2b) proved less critical (Korger, 2010). Most events display a minimum gap of 50° in observation distribution with an average gap of 76° of the 120 events studied here.

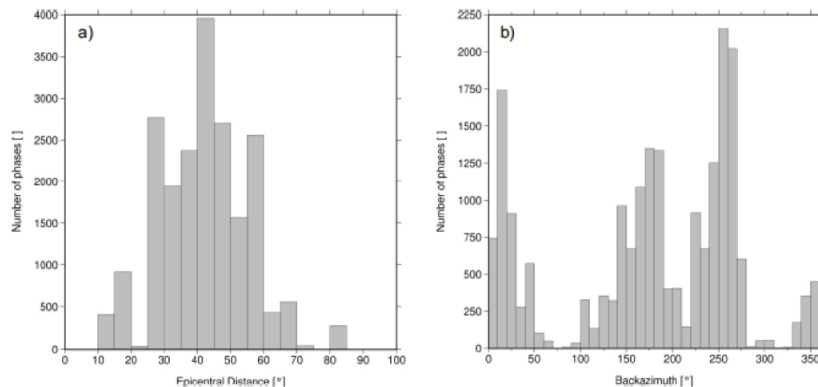


Figure 5.2 – Spatial distribution of recording stations of the 1999 earthquake swarm, expressed as number of ISC recorded phases versus epicentral distance (a) and backazimuth (b).

In the following we analyze the influence of three localization algorithms on the localization results for events with the described problematic station distribution which is typical for mid-ocean ridge earthquakes.

5.3.2 Methods

The earthquake location problem is non-linear which arises from the lack of a simple linear relationship between the observed arrival times and the source coordinates in space and time in the form

$$t_{OBS} = t_0 + \int_{x_{SRC}}^{x_{REC}} u(\vec{x}) ds \quad (5.3.1)$$

This relationship expresses the observed arrival time t_{OBS} for a given model of slowness $u(\vec{x})$, integrated along the seismic ray path ds between source and receiver locations (x_{SRC}, x_{REC}) , with respect to an origin time t_0 .

Linearized methods are based on a Taylor series expansion of eq. 5.3.1 around a prior estimate of source parameters with the linearization obtained by usage of only the first two terms of the expansion (*Husen and Hardebeck, 2010*). Combining all available arrival time observations in a vector-matrix equation gives

$$A_{NxM}x_M = d_N \quad (5.3.2)$$

where the hypocentral parameters (hypocentre coordinates and origin time) in the vector x_M are related to the arrival time misfits in the vector d_N through the hypocentral adjustment matrix A_{NxM} which includes partial derivatives (*Lin and Shearer, 2005*). N is the number of defining phases.

Non-linear methods do not use partial derivatives as included in A_{NxM} , they are based on deterministic or stochastic searches. These searches explore likelihood functions and gather information globally throughout a prior probability density function to produce a complete location probability density function (*Husen and Hardebeck (2010)* and references within) and give information about local or global maxima of the location likelihood and about uncertainty in the location.

Earthquake localization can be done for each event independently of every other event; the method is then called absolute as it uses a fixed geographic system and absolute time. Relative methods localize earthquakes relative to one or more other earthquakes. These methods assume that all earthquakes to be localized are so closely grouped that path anomalies are the same for all events which were recorded at the same station, and therefore the error introduced by incorrect assumptions of the Earth's structure is nearly the same for arrival times measured at the same stations (e.g. *Wolfe, 2002; Lin and Shearer, 2005*).

Errors estimates of all algorithms describe the formal uncertainty of the hypocentre solution, incorporating only the measurement errors of the arrival times. Errors introduced by an incorrect velocity model or phase misidentification result in systematic biases, which limit the hypocentre accuracy (*Husen et al., 2003*). These latter errors cannot easily be quantified.

5.3.2.1 Absolute linearized, iterative localisation routine HYPOSAT

HYPOSAT solves the over-determined problem of hypocentre parameter inversion by a stepwise linearized, iterative algorithm. The system of equations is solved with the Generalized-Matrix-Inversion technique using the Single-Value decomposition theorem (*Schweitzer (2001)* and references within). A starting solution for time is obtained by *Wadati's* approach (*Wadati, 1933*), a starting location has to be manually selected. The

equation system is weighted with the standard deviation of the input parameters. At each iteration step the matrix is recalculated and reweighted by the calculated standard deviation of the modeled parameters by the former iteration until convergence is reached. If a specific travel time residual is unusually high, this phase will not be used as defining in the next iteration.

The main advantage of HYPOSAT for teleseismic localization in remote regions lies in the use of travel-time differences (e.g. S-P; pP-P) as independent observations. This considerably improves hypocentre location, especially for a sparse network of recording stations. It also yields reasonable hypocentre depths (*Riedel and Schlindwein, 2010*). The possibility to incorporate a local velocity model is also important for event localization at mid-ocean ridges like Gakkel Ridge, whose crustal structure differs considerably from theoretical velocity models with 30 km of continental crust (*Jokat and Schmidt-Aursch, 2007*).

The uncertainty of the hypocentre solution is indicated by the 95% confidence ellipse and by the root-mean-square (RMS) of the travel-time residuals. The calculation of the confidence ellipse is based on the assumption of uncorrelated and normally distributed measurement errors of seismic arrival times (*Husen et al., 2003*). This assumption may result in unreasonably small error ellipses (*Schweitzer and Kennett, 2007*).

For localization we used the ak135 travel-time tables (*Kennett et al. 1995*) combined with a regional velocity model for the 85°E/85°N volcanic complex (Tbl. 5.1) which was compiled by *Riedel and Schlindwein (2010)*. We localized firstly with a fixed hypocentre depth of 15 km, followed by an inversion for depth.

In order to prefer the solution with inverted hypocentre depth, the number of defining phases had to be equal or higher, and RMS and the semi-axes of the 95% confidence ellipse had to be smaller than in the hypocentre solution with a fixed depth.

5.3.2.2 Absolute probabilistic routine NonLinLoc

The probabilistic inversion routine NonLinLoc (*Lomax et al., 2000*) uses probability density functions (pdf) for earthquake localization (*Tarantola and Valette, 1982; Moser and Eck, 1992; Wittlinger et al., 1993*). A description of the probabilistic earthquake location problem can be found in *Lomax et al. (2009)*. Basically, a conditional density function relates prior information about hypocentral parameters and observed phase arrival times to the complete probabilistic solution, the posterior pdf. The conditional density function is called a likelihood function and expresses a measure of how good any model explains the observed data, assuming Gaussian uncertainties for the predicted and observed travel-times.

The posterior pdf in NonLinLoc can be evaluated by three different methods which are also

described by *Lomax et al.* (2009). We use the Oct-tree Importance sampling algorithm which recursively subdivides cells in 3-D. It follows the value of the posterior pdf in the centre of each cell and draws samples accordingly, therefore sampling a higher number of cells where the value of the pdf is highest. The number of samples drawn in each cell is proportional to the value of the pdf and the volume of each grid cell. All scatter points together define a relative volume which gives the most likely region for the maximum likelihood hypocentre. A higher density of scatter points indicates where the probability for the maximum likelihood hypocentre is highest.

However, the scatter volume need not be ellipsoidal in shape. Samples drawn from such a volume reflect its irregularity. Confidence ellipsoids based on Gaussian error estimates and calculated from covariance matrices for comparison purposes do not fit well to an irregular scatter cloud. In these cases, the confidence ellipsoid cannot be used and the expectation hypocentre which is calculated from the confidence ellipsoid also does not match the maximum likelihood hypocentre. A small difference between the expectation- and the maximum likelihood hypocentre can be an indication that the scatter cloud is similar to an ellipsoidal shape and the confidence ellipsoid can be interpreted. Examples can be found in e.g. *Husen et al.* (2003) and *Lomax et al.* (2009).

NonLinLoc makes use of observation- and instrument-related errors when given in the phase arrival file and can incorporate a local velocity model for defined receiver stations. Travel-time differences are also used in the calculation of the posterior pdf through the equal-differential-time likelihood function (*Zhou, 1994; Font et al., 2004*).

We used the ak135 travel-time tables as global velocity model, combined with the regional velocity model by *Riedel and Schlindwein* (2010) (Tbl. 5.1). As quality indicators for the maximum-likelihood hypocentre we used the scatter volume, the number of phases, and the difference between the maximum likelihood- and the expectation hypocentre in 2D because, due to a lack of local or regional observed phases, the focal depth is in most cases poorly constrained.

Depth [km]	V_P [ms^{-1}]	V_S [ms^{-1}]
0.0	5.5	3.17
5.0	5.5	3.17
10.0	5.5	3.17
10.0	7.8	4.2
16.0	7.8	4.2
16.0	8.04	4.47
35.0	8.04	4.47

Table 5.1 – Local velocity model for the 85°E/85°N region as compiled by *Riedel and Schlindwein* (2010)

5.3.2.3 Relative linearized localisation routine Mlocate

The relative linearized algorithm Mlocate is based on the hypocentroidal decomposition theorem (*Jordan and Sverdrup, 1981*). It states that the location perturbations of clustered events can be broken up in two vectors, the hypocentroid vector and the cluster vector. The hypocentroid gives the average absolute location of the earthquake cluster and the cluster vectors describe the relative location of events with regard to the hypocentroid. Mlocate as modified by *Wiens et al. (1994)* first locates each event independently from each other to find the location of the hypocentroid. Secondly, the cluster vectors are calculated jointly for all hypocentres. Based on numerical tests, *Wolfe (2002)* found that this method removes a constant path bias. Relative locations improve significantly within the cluster (*Lin and Shearer, 2005*).

The individual hypocentres are constrained by two errors: The absolute location error of the hypocentroid, and the location error of the individual cluster events relative to the hypocentroid.

With Mlocate only the global IASP91 traveltimes-tables (*Kennett and Engdahl, 1991*) could be used for our relocalization. A parameter sensitivity study for NonLinLoc using the Gakkel ridge earthquake swarm (*Korger, 2010*) showed that epicentres of well-constrained events with more than 50 usable phases are stable with respect to the globally applied velocity model (mean difference in epicentres 1.33 km). We did not use a local velocity model as it can only be defined as a flat 1D earth model which is not reasonable for about 1000 km distance to the nearest recording station. In the parameter sensitivity study for NonLinLoc (*Korger, 2010*), a local velocity model produced only a mean difference in epicentres of 2.26 km for well-constrained events. We assumed this stability also for Mlocate. For inversion, a hypocentral depth of 15 km was fixed.

5.4 Results and interpretation of location algorithm performance

We localized the dataset of 120 events with 30 or more phases (Fig. 5.1b) using the three described localization algorithms. Due to the lack of local and regional recorded phases which could constrain depth within reasonable errors for two of the three routines, we compare only the epicentres of events. Ideally, for each event, the location solutions of the individual routines should match within their error ellipsoids. However, it turned out that the three epicentres calculated from the three algorithms for each event differed significantly. For example, the mean difference in epicentres (Tbl. 5.2) between the Mlocate result and the HYPOSAT result is greater than the mean semi-axes of the corresponding 95% epicentre confidence ellipses (Tbl. 5.3). The bigger errors of NonLinLoc are the result of a more comprehensive error estimation including an additional Gaussian matrix for the errors introduced by an incorrect velocity model.

More than half of the original 120 events were localized within a close distance by two or all algorithms. We believe that the epicentre solution of these events is largely insensitive to the localization algorithm and therefore trustworthy. To evaluate localization results and identify interpretable locations, we therefore implemented cut-off criteria for the calculated distance between the epicentre solutions for each individual event.

Algorithms	Mean difference in epicentres [km]
NonLinLoc - mlocate	7.56
mlocate - Hyposat	8.65
Hyposat - NonLinLoc	8.66

Table 5.2 – Mean difference in epicentres as localized by HYPOSAT, NonLinLoc and Mlocate

Algorithms	Mean	
	Semi-minor axis [km]	Semi-major axis [km]
mlocate	4.40	5.63
Hyposat	6.39	7.74
NonLinLoc	16.58	22.54

Table 5.3 – Mean 95% error ellipse semi-axes for the three localization routines

5.4.1 Comparison of relocation results by the three routines

A comparison of the distances between the epicentre solutions for each event yields in effect three categories of location results which we illustrated in Fig.5.3. Good quality events are denoted by closely fitting epicentres in all three routines (Fig. 5.3a). We included only events which are described by less than 5 km distance between two epicentres and less than 10 km distance to the third epicentre. So-called outlier events (Fig. 5.3b) have two epicentres which are less than 5 km away from each other, but the third epicentre is more than 10 km away. This epicentre is named the outlier.

We compiled a dataset for each localization routine which includes the locations of 57 good quality events and 21 outlier events, excluding the respective outlier location. Of the outlier events, the outlying epicentres in 12 out of 21 cases were produced by HYPOSAT. The remaining 9 outliers are divided almost equally between Mlocate and NonLinLoc (5 and 4 respectively). 42 events which do not fall into either the well located or the outlier category are considered poorly located and hence will not be interpreted. Examples of poorly located events which differ by more than 5 km, can be found in Fig. 5.3.

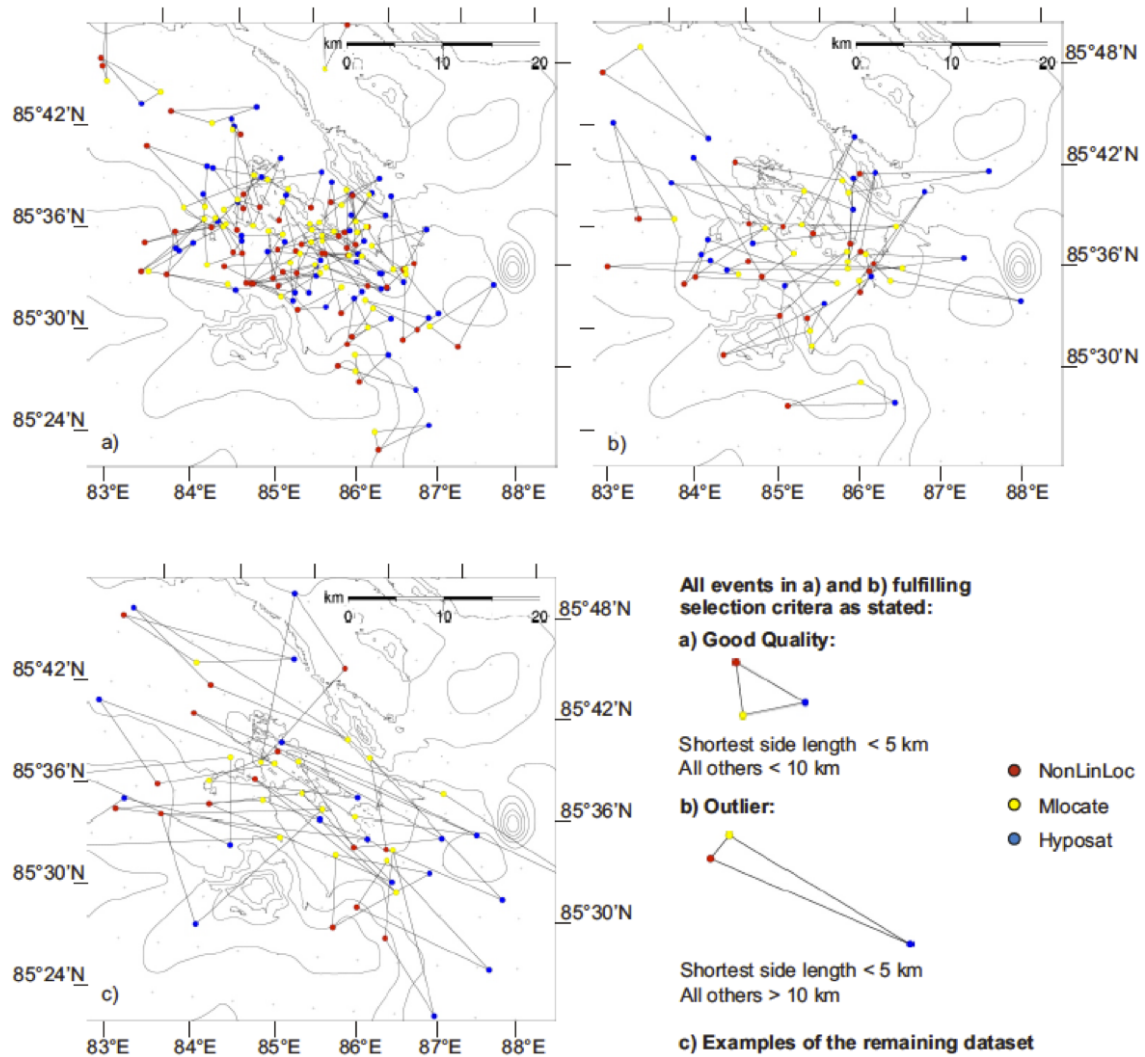


Figure 5.3 – Comparison of epicentres relocated by HYPOSAT, NonLinLoc and Mlocate. Each event is defined by a triangle of three epicentre solutions. Contour lines of bathymetry as in Fig. 5.1b (a) Well-located events, (b) outlier events, (c) badly located events. See figure and text for description of selection criteria.

Tbl. 5.4 summarizes the quality parameters for the well- and badly located epicentres associated with each localization routine. For NonLinLoc, an adjustment for the 3D, 68% error ellipsoid parameters to a comparable 2D, 95% error ellipse has been made following *Ghilani* (2010).

Well-located dataset			Mean			
Algorithms	Number of events	Number of Phases	Semi-minor axis [km]	Semi-major axis [km]	RMS [sec]	Scatter volume [km ³]
mlocate	73	71	3.80	4.84	0.49	—
Hyposat	66	96	5.14	5.96	0.92	—
NonLinLoc	74	79	12.96	15.77	1.24	6.5*10 ³
Badly-located dataset			Mean			
Algorithms	Number of events	Number of Phases	Semi-minor axis [km]	Semi-major axis [km]	RMS [sec]	Scatter volume [km ³]
mlocate	47	34	5.48	6.53	0.50	—
Hyposat	54	50	6.76	8.27	1.05	—
NonLinLoc	46	44	20.07	27.56	1.41	1.97*10 ⁴

Table 5.4 – Mean quality parameters of epicentres for the well-located and the badly-located dataset for the three localization routines. Error ellipse parameters are given for the 95% confidence interval

Due to the remote region, ground-truth observations are not available to quantify the absolute location error, not even from a nearby region. Of the 78 events used in this study, 57 events have more than 50 defining phases. *Korger* (2010) performed an extensive sensitivity study for NonLinLoc locations, testing the effects of different local or global velocity models. The mean difference in epicentre locations when applying the local velocity model is 3.00 km. I also compiled a reduced dataset in different epicentral distances with a homogeneous station distribution for the 11 best events ($m_b \geq 5.0$). A skewing of epicentres to the southwest was revealed, the more pronounced if less phases were used in localization. Good quality events (mean: 48 recorded phases) were just slightly shifted by a mean of 3.3 km which is less than the median of the semi-major error ellipse axis of 12.67 km. We therefore conclude that the influence of the localization algorithm exceeds both the influence of the local velocity model and the influence of a dataset-inherent low quality as represented in a limited number of recorded phases.

5.4.2 Performance of location algorithms

Läderach et al. (2011) found, that for teleseismic events with few phases (less than about 50) located at the Lena Trough, HYPOSAT clustered events in the rift valley better than NonLinLoc due to an intensive use of travel-time differences. But also apparently well-constrained epicentres of events with few phases have to be used with care: *Schweitzer and Kennett* (2007) mentioned for HYPOSAT and a teleseismic dataset with 40 registered phases in the Kara Sea that the location can still be biased and not show the true epicentre, even if the quality parameters RMS and error ellipse indicate a good solution. In our study, HYPOSAT yielded most of the outlier solutions. Yet it was the only routine able to yield reasonable hypocentre depths by using sparse observations of pP-P phase differences (*Riedel and Schlindwein*, 2010). As our further interpretation is based on well located events with 50 or more recorded phases, we prefer to use NonLinLoc epicentres. NonLinLoc also offers the possibility to use the scatter volume in estimation of localization quality. The scatter volume itself is a relative parameter, but a more reliable quality indicator than the RMS (*Korger*, 2010). Additionally, the highest density of scatter points indicates the most probable source sites.

For an earthquake swarm which is supposed to originate in a narrow source region, the length of the cluster vectors further allows to assess the performance of the location algorithms. The individual cluster vectors are calculated as the distance of each epicentre from the hypocentroid of the swarm. For the 120 events used in this study, the mean cluster vector length of HYPOSAT is 13.9 km, NonLinLoc gives 9.7 km and Mlocate 9.5 km. As a relative location routine, Mlocate enhances the relative location accuracy (*Lin and Shearer*, 2005), calculating small error ellipses and a low median RMS for the localized events which is about half of the amount given by HYPOSAT (Tbl. 5.4). However, Mlocate locates events relative to the hypocentroid which itself has an additional error ellipse of a semi-major axis of 2.1 km and a semi-minor axis of 1.9 km. This uncertainty need not be considered if the interpretation of epicentres is limited to relative positions of the events to each other but it needs to be taken into account when comparing epicentre positions to geological structures. Here, we use Mlocate results only for relative positioning of events and rely on NonLinLoc solutions for comparing epicentres and topography.

5.5 Geologic interpretation of the 1999 earthquake swarm

5.5.1 Temporal evolution of the swarm

Fig. 5.4 shows the temporal evolution of the swarm in terms of event rate, cumulative seismic moment release M_0 and all available centroid moment tensor solutions (CMT) from the Harvard catalogue (*Ekström et al.*, 2005). The Harvard catalogue also lists eigenvalues which we use to calculate ϵ -values as a measure of the deviatoric component of the full moment tensor (*Ekström*, 1994). We calculated M_0 from M_S values, using *Bormann* (2002)

$$\log M_0 = M_S + 12.2 \quad (5.5.1)$$

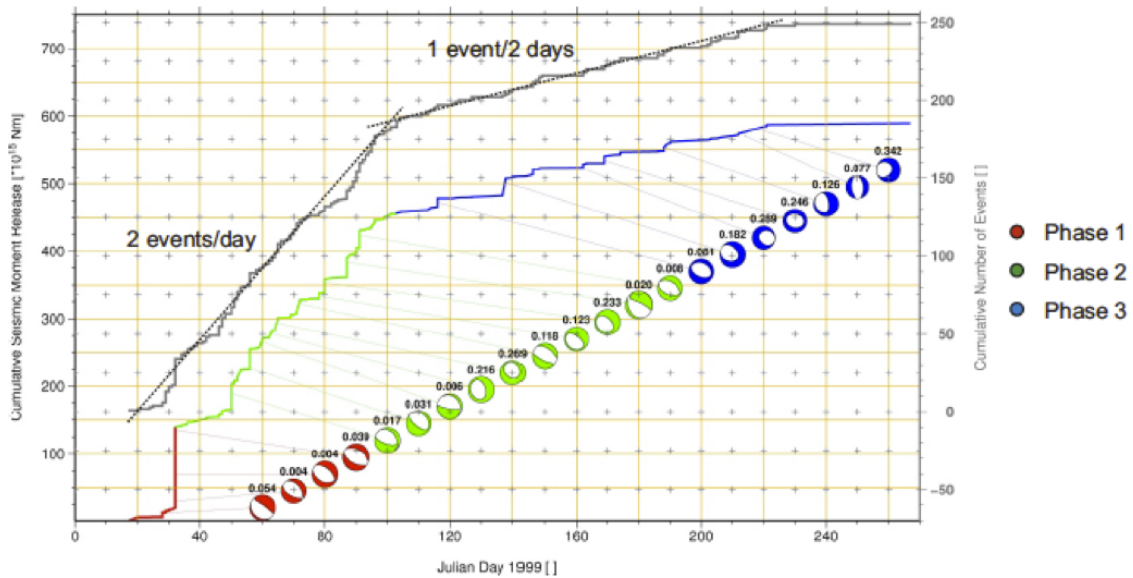


Figure 5.4 – Cumulative number of events (solid grey) with a regression line (dotted grey) and cumulative seismic moment release (coloured to show the three temporal phases). Available CMTs are associated with their origin time on the seismic moment release graph and denoted by their ϵ -values. Note the distinct break in event rate and increase in non-double couple source mechanisms.

We propose that the earthquake swarm can be divided in three distinct phases:

1. The first phase lasted from the beginning of the activity on Julian day 17 (January, 17th) to Julian day 32 (February, 1st). February 1st shows a high seismic moment release rate which is mainly due to three events with $m_b = 5$ on this day. All four reported CMT solutions for this phase of activity show normal faulting mechanisms with a mean ϵ -value of 0.02. We believe that in this phase an initial breaking of crust took place.
2. In phase two from February 2nd up to Julian day 96 (April, 6th), the seismic moment release rate also remains high, but the ten CMTs include more events with non-double-couple components (mean ϵ -value of 0.10, maximum 0.27) which cannot easily be explained by simple shear failure on planar faults. Up to the end of phase two the event rate is high with about 2 events per day.
3. At the beginning of the third phase on April, 7th, the event rate drops suddenly from two events per day to one event per two days. The third phase is characterized by seven CMTs which almost exclusively display a major non-double-couple component (mean ϵ -value of 0.19, maximum 0.34) and by a comparatively low seismic moment release. Yet, high magnitude events still take place in the first two months of phase 3. The swarm ends on September, 24th (Julian day 267) with a single event after more than a month of quiescence. The drop in event rate has also been observed by *Tolstoy et al.* (2001) who used it to distinguish between a former and a later phase in swarm activity.

5.5.2 Spatial development

In Fig. 5.5, we plot NonLinLoc epicentres of the well-located dataset and of the outlier dataset when NonLinLoc was not the offending routine. In total this yielded 74 event locations. The majority of events are located within the central rift valley, in the vicinity of the Asgard volcanic chain (c.f. Fig. 5.1b). The southern rift valley wall also seems to be activated. However, the traditional confidence ellipse uncertainties of the NonLinLoc well-located epicentres remain large (Tbl. 5.4 and Fig. 5.5). We therefore refrain from interpreting individual epicentres geologically, but alternatively visualize the most likely centres of earthquake activity by combining the pdfs of all events (Fig. 5.6). Fig. 5.6b illustrates the pdfs of two well-localized events as scatter clouds. The highest likelihood for the epicentre is represented by the location with the highest density of scatter points. Fig. 5.6a shows the summation of the scatter clouds of all events by counting the number of scatter points in grid cells of 0.125° latitude/ 0.15° longitude. The centre of activity for the whole swarm lies in prolongation of the central volcanic edifice, close to the Asgard volcanic chain. Interestingly, it is not situated at the crest of the volcanic mound but to its southeast at water depths of about 4 km. The small difference in average length of the semi-axes of the error ellipses (Tbl. 5.4; c.f. circular shape of scatter clouds in

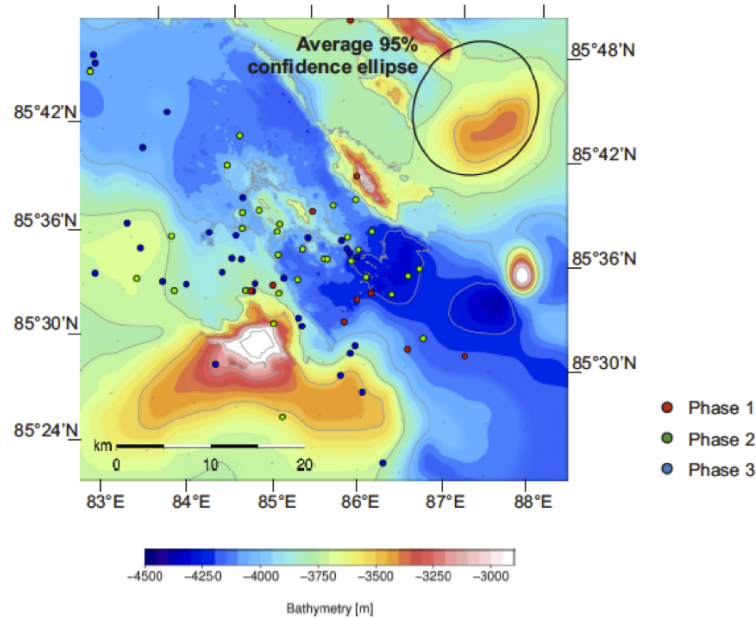


Figure 5.5 – NonLinLoc maximum likelihood epicentres for well located events. Bathymetry and contour lines as in Fig. 5.1b. The average 95% error ellipse is plotted in the upper right corner. See text and Fig. 5.4 for definition of temporal phases.

Fig. 5.6b) indicate that the rift-parallel elongation of the combined likelihood grid in Fig. 5.6a is not a function of a preferential orientation of individual pdfs but rather reflects the distribution of individual epicentres and can therefore be interpreted. The activity is clearly oriented parallel to the rift axis. The likelihood of seismic activity drops sharply at the northern rift valley wall, but it extends well over the southern rift valley wall including the source site of volcanic explosion sounds in 2001; c.f. Fig. 5.1b; *Schindwein and Riedel* (2010).

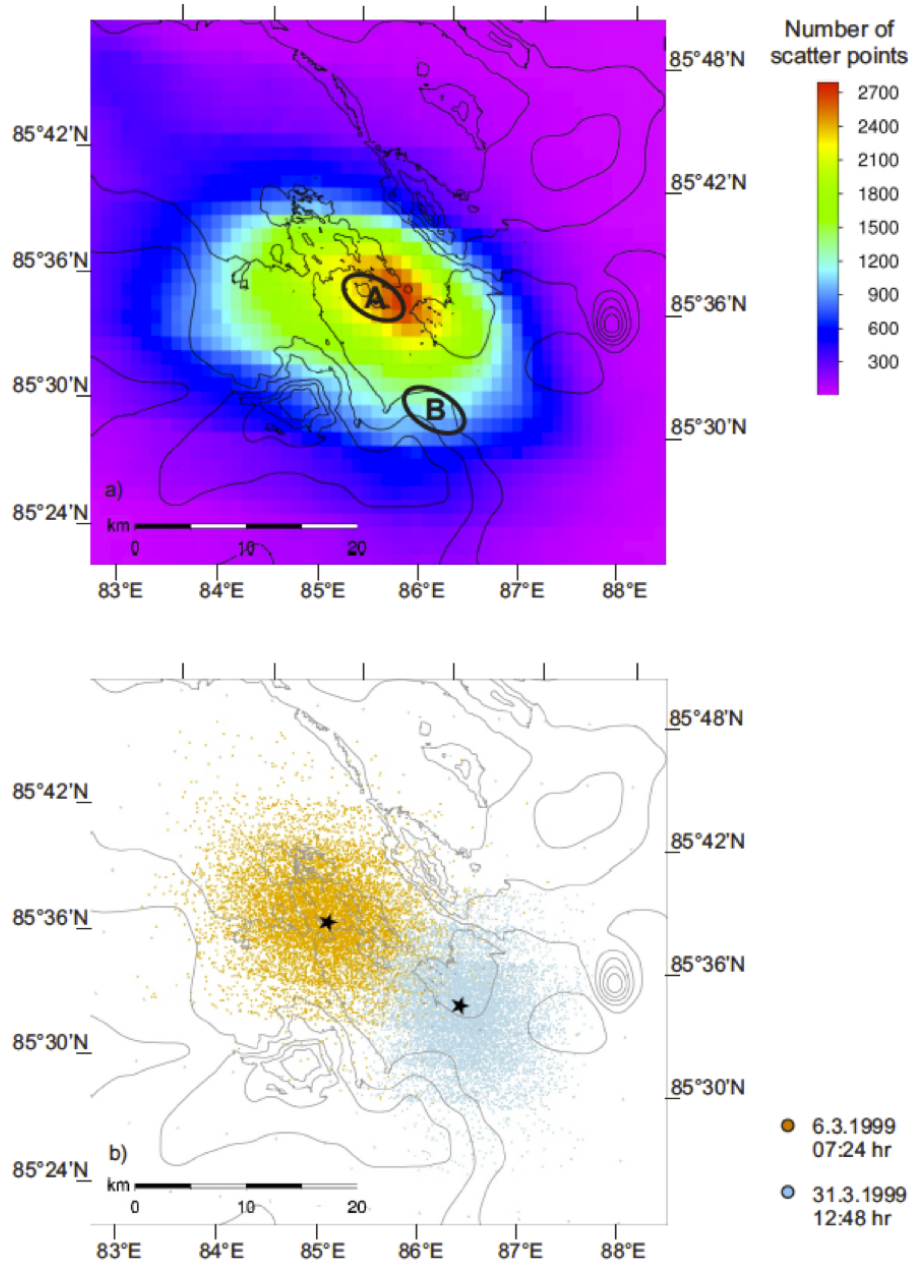


Figure 5.6 – (a) Combined NonLinLoc PDF of all well-located epicentres over 250 days of swarm activity, represented as sum of scatter points in cells of 0.125° latitude/ 0.25° longitude size. A indicates the area of the Asgard volcanic chain, site B is the source site of the seismoacoustic signals (*Schlundwein et al.*, 2005). (b) Scatterclouds of two exemplary events (March 6th and March 31st). Contour lines of bathymetry as in Fig. 5.1b.

For the spatiotemporal development of the swarm activity we then summed up all scatter points pertaining to NonLinLoc well-located epicentres in each temporal phase and normalized by the total number of scatter points in each phase (Fig. 5.7):

In the first phase (Fig. 5.7a) we see a highly localized centre of activity south of the Asgard volcanic chain and near the deepest part of the rift valley, with the higher likelihood region following the elongated form of the rift valley. We believe that in this first phase a breaking of crust along major pre-existing normal faults either enables or responds to a magmatic intrusion.

In phase two (Fig. 5.7b), the highest likelihood region is enlarged and extends to the 86°E deep. The activated region loses its rift parallel shape as it includes a bigger area especially of the southern rift valley walls than in the first phase. Seismicity accompanying dike emplacement has been intensively studied, for example in Iceland (e.g. *Einarsson and Brandsdottir*, 1980) and Afar (e.g. *Keir et al.*, 2009). A dike typically propagates with slow velocities (about 1 km/h) during hours or days, and produces clustered seismicity at the dike tip at magnitudes too small to be detected teleseismically. Our large, teleseismically observed swarm earthquakes are unable to track ascending magma to the surface as seen in microearthquake studies, for example the recent Eyjafjallajökull eruption (*Hjaltadottir et al.*, 2011) and thus cannot mark a potential eruption site. The freshest lava flows were found in 2007 on Oden and Loke volcanoes (*Sohn et al.*, 2008). However, widespread, diffuse venting (*Stranne et al.*, 2010) and a layer of pyroclastics material of variable thickness throughout the whole area suggested multiple sources of volcanic activity (*Sohn et al.*, 2008). The observation of volcanic explosion sounds stemming from the southern rift valley wall in 2001 (*Schlindwein et al.*, 2005; *Schlindwein and Riedel*, 2010) adds further support to the interpretation of widespread volcanic activity.

Seismicity in phase three (Fig. 5.7c) is scattered throughout the rift valley and the valley walls, also including a large area along axis to the north and south. It has a markedly different characteristic than phase one and two, lacking such a clearly defined centre as apparent in the previous phases and including almost exclusively non-double couple CMTs. We interpret that in this phase a distinctly different process is taking over. For example, the clear break in event rate at the transition between phase two and three might indicate a change from an intrusive stage to an effusive stage of magmatism as commonly observed for other volcanoes (e.g. *Dziak et al.*, 1995; *McNutt*, 1996). Alternatively, this phase could represent the adjustment of the stress field to a new regime following dike intrusion as postulated by *Tolstoy et al.* (2001) and *Riedel and Schlindwein* (2010).

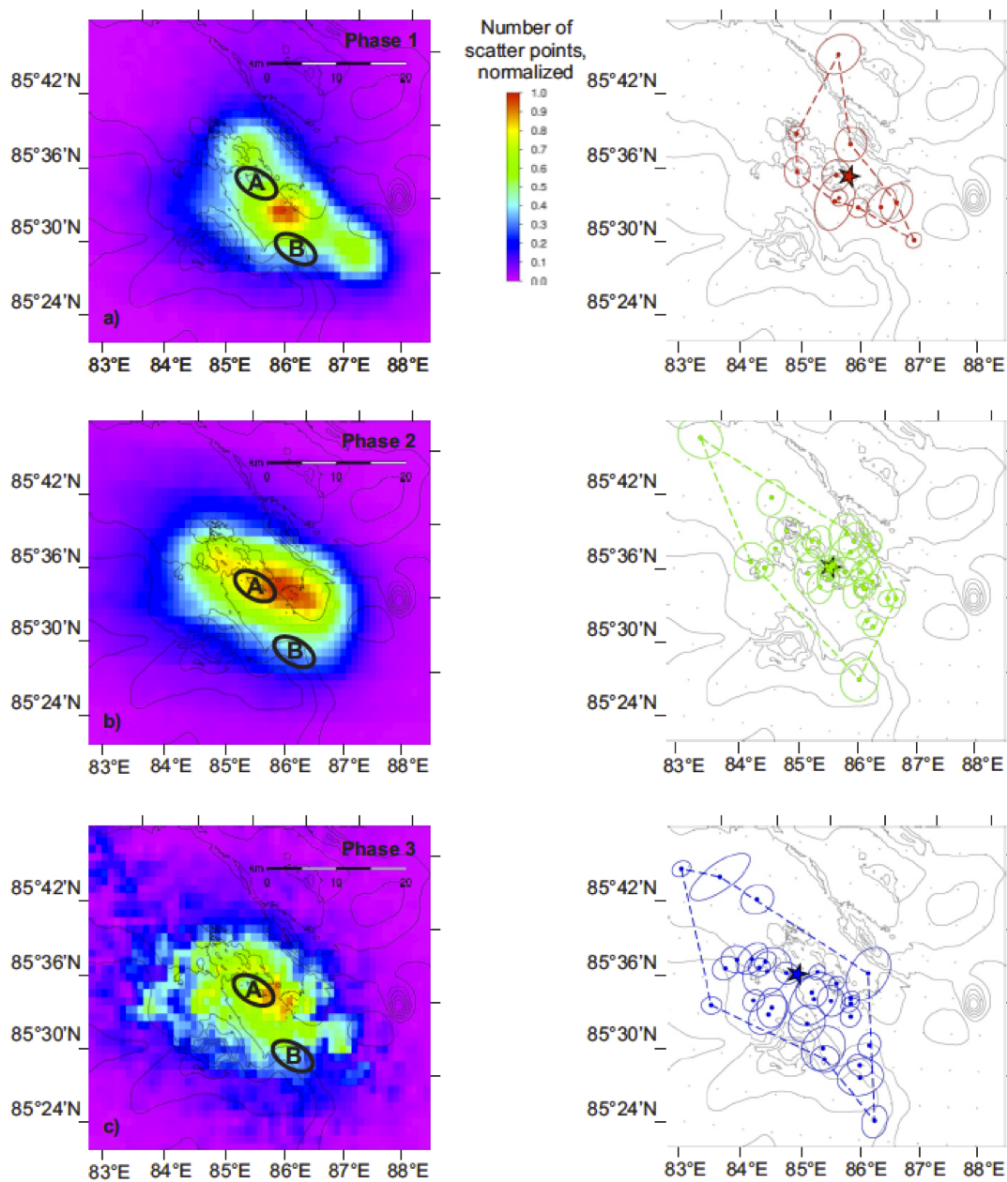


Figure 5.7 – (a - c) Sum of NonLinLoc scatter points (c.f. Fig. 5.6a) for the three temporal phases as described in the text, normalized by the total number of scatter points in each phase. Areas A and B as in Fig. 5.6a. (d - f) Mlocate epicentres for the three temporal phases with their error-ellipses, plotted with a rough regional extension of each phase (dashed line). Star indicates the location of hypocentroid in each phase. Contour lines of bathymetry as in Fig. 5.1b.

In a divergent environment, an uniformly extensional stress-regime develops during long periods of quiescence between spreading episodes (Foulger *et al.*, 1989). During actual seafloor spreading, stress is released through tensile cracking in predominantly normal faulting events, leaving a heterogeneous stress field to evolve again until the next spreading episode. Earthquakes with non-double-couple components are often attributed to

some kind of volumetric change, for example induced by nearly instantaneous migration of material, rapid phase change or cavity collapse. An alternative explanation involves high fluid pressure or thermal contraction, causing tensile fracture (*Foulger and Julian, 1993*). An ϵ -value of > 0.33 defines, somewhat arbitrarily, non-double-couple earthquakes (*Ekström, 1994*). *Tolstoy et al. (2001)* attributed the increasing non-double-couple components of the earthquakes to a distortion of the moment tensor solutions by changes of the elastic moduli due to a nearby magma-body. However, the epicentres associated with the individual events are not systematically located at or around a potential intrusion site (*Korger, 2010*). *Mueller and Jokat (2000)* postulated caldera collapse as cause of the non-double-couple components, as observed for example at Nyiragongo volcano (East African Rift, ?), but the AGAVE expedition did not find the accordant geologic structure. We interpret the higher ϵ -values in phase two and three to result from some form of magmatic event, potentially dike intrusions, causing spatially variable elastic moduli (*Tolstoy et al., 2001*).

To investigate further a possible magmatic influence we tried to fit the modified Omori law (*Utsu, 1961*) to the data. We could make a rough fit when defining the first event on February, 1st as the mainshock but when starting with the observed onset of the swarm on January 17th, the fit was poor. In both cases, high c -values show an abnormally high number of missing events below the completeness magnitude $m_C = 4.3$, immediately following the mainshock. The absence of a clear separation between mainshock and aftershocks suggests high fluid activity and high heat flow which often is the case in magmatic active regions (*Mogi, 1967; Utsu, 2002*). This supports our theory that the swarm of 1999 was not exclusively tectonic in origin.

Bergman and Solomon (1990) proposed that lateral propagation of epicentres within a narrow area in the central rift valley is indicative of a mid-ocean ridge spreading event with dike intrusion. Most of their teleseismically observed swarms along the Mid-Atlantic ridge lacked an along-axis elongation and were therefore interpreted to be of tectonic origin. Based on USGS localizations, *Tolstoy et al. (2001)* interpreted such a lateral propagation for the 1999 earthquake swarm. However, the uncertainty of the original localization for individual events and even after relocation and identification of reliable epicentres is still too high to allow such a conclusion.

To investigate a possible migration of epicentres we plotted Mlocate epicentres in each phase with their error-ellipses (Fig. 5.7d,e,f). The relative relocation technique results in more reliable relative positioning of the events and therefore gives a more accurate picture of spatial evolution of the swarm. The extent of the activated area was marked by connecting the bordering event locations. In the first phase (Fig. 5.7d), the activated area is very localized and lies in the central rift valley, matching the result from the NonLinLoc scatterplot (Fig. 5.7a). In the second phase (Fig. 5.7e) the activated area gets larger, roughly fitting the form observed from the NonLinLoc scatterplot (Fig. 5.7b). Mlocate epicentres of the third phase (Fig. 5.7f) also agree to the NonLinLoc maximum likelihood region (Fig. 5.7c), with a large area of decentralized Mlocate epicentres scattered all over

the central rift valley and the southern rift flanks. Compared to the former two phases of activity, the centre of activity in phase three is shifted distinctly to the south (Fig. 5.7f).

However, a migration of epicentres towards the northwest as a result of propagating magmatic pulses as proposed by *Tolstoy et al.* (2001) cannot be observed. Activity at about 83°E occurs already in phase two and still persists in phase three. Instead of a clear migration, we see an along-axis distribution of epicentres though not in a classical migration pattern. The swarm does not collapse to a narrow area after relocalization with Mlocate, but rather expands throughout time over 50 km in the rift valley, a single event of the well-located dataset even was localized at 73°E. The seismic activation of a broader along-axis region may point to an along-axis melt distribution through rapid lateral diking which has been postulated by *Cannat et al.* (2003) to explain the pronounced along-axis variations in crustal thickness on the Southwest Indian Ridge. Alternatively, the extended seismicity may denote the reaction of a ridge segment with a thick, stiff lithosphere to a magmatic intrusion at its centre. *Dziak et al.* (2004) observed instantaneous segment-scale normal faulting earthquakes, following a dike intrusion at Lucky Strike segment (Mid-Atlantic Ridge).

5.6 Conclusion

1. The choice of location algorithms has a critical influence on the localization results of mid-ocean ridge earthquakes lacking nearby recording stations. We identified reliably located events which produced similar location solutions in three different location methods. For absolute location and datasets with a greater number of recorded phases we prefer NonLinLoc. Its calculated epicentres match within a close distance the epicentres obtained by the relative algorithm Mlocate. Single earthquake locations are difficult to interpret, therefore we interpret only the most likely areas of swarm activity obtained by stacking the scatter points of individual NonLinLoc events. The spatiotemporal evolution of swarms can best be examined for potential migration processes using the relative localization routine Mlocate.
2. We determine that the earthquake swarm of 1999 was related to a spreading episode and shows a complex interplay of tectonic and magmatic events. A purely tectonic origin is unlikely due to multiple indications of volcanic activity in the following years (*Edmonds et al.*, 2003; *Schindwein et al.*, 2005; *Sohn et al.*, 2008). Despite the absence of a clear dike migration pattern we find numerous indications for a magmatic interaction. We propose three phases of activity for this swarm: The first phase we believe to result from a breaking of crust, either as a result or enabling a magmatic intrusion. The seismicity of the second phase shows a spatial expansion of the activity both along-axis and across-axis. In the third phase, a break in the event rate indicates a change in physical process, either a transition to a effusive

stage or a post-intrusion adjustment of the stress field.

This study of the 1999 earthquake swarm with its long duration and large number of strong earthquakes gives an unprecedented view into a magmatic accretion event at an ultraslow spreading ridge. Due to the location uncertainty and the lack of local recording stations, conclusions on melt ascent and distribution and the magmatic plumbing system remain limited. Local seismicity studies are needed to shed further light on the structure of this recently active volcanic complex.

5.7 Acknowledgments

We particularly thank Anthony Lomax and Doug Wiens for their respective localization programs and many helpful discussions. The manuscript was much improved by the helpful comments of I. Grevemeyer, D. Bohnenstiehl and an anonymous reviewer. The facilities of the ISC were used for access to the catalogue data used in this study. This study was funded by the Emmy-Noether Program of the DFG under grant Schl. 853/1-1.

5.8 Literature

- Bergman, E. A., and S. C. Solomon (1990), Earthquake Swarms on the Mid-Atlantic Ridge: Products of Magmatism or Extensional Tectonics?, *J. geophys. Res.*, *95*(B4), 4943–4965.
- Bormann, P. (2002), Seismic Scaling Relations, Sources and Source parameters, in *New manual of seismological observatory practice (NMSOP): Chapter 3 Seismic Sources and Source Parameters*, edited by P. Bormann, pp. 82–93, Deutsches GeoForschungsZentrum GFZ, Potsdam, doi: 10.2312/GFZ.NMSOP_r1_ch3.
- Bown, J. W., and R. S. White (1994), Variations with spreading rate of oceanic crustal thickness and geochemistry, *Earth planet. Sci. Lett.*, *121*, 435–449.
- Cannat, M. (1993), Emplacement of Mantle Rocks in the Seafloor at Mid-Ocean Ridges, *J. geophys. Res.*, *98*(B3), 4163–4172.
- Cannat, M., C. Romevaux-Jestin, and H. Fujimoto (2003), Melt supply variations to a magma-poor ultra-slow spreading ridge (Southwest Indian Ridge 61° to 69°E), *Geochem. Geophys. Geosys.*, *4*(9104), doi: 10.1029/2002GC000480.
- Cannat, M., D. Sauter, A. Bezos, C. Meyzen, E. Humler, and M. L. Rigoleur (2008), Spreading rate, spreading obliquity, and melt supply at the ultraslow spreading Southwest Indian Ridge, *Geochem. Geophys. Geosys.*, *9*(Q04002), doi: 10.1029/2007GC001676.

-
- Dick, H. J., J. Lin, and H. Schouten (2003), An ultraslow-spreading class of ocean ridge, *Nature*, *426*, 405–412, doi: 10.1038/nature02128.
- Dziak, R. P., C. G. Fox, and A. E. Schreiner (1995), The June–July 1993 seismo-acoustic event at CoAxial segment, Juan de Fuca Ridge: Evidence for a lateral dike injection, *Geophys. Res. Lett.*, *22*(2), 135–138, doi: 10.1029/94GL01857.
- Dziak, R. P., D. K. Smith, D. R. Bohnenstiehl, C. G. Fox, D. Desbruyeres, H. Matsumoto, M. Tolstoy, and D. J. Fornari (2004), Evidence of a recent magma dike intrusion at the slow spreading Lucky Strike segment, Mid-Atlantic Ridge, *J. geophys. Res.*, *109*(B12102), doi: 10.1029/2004JB003141.
- Edmonds, H., et al. (2003), Discovery of abundant hydrothermal venting on the ultraslow-spreading Gakkel ridge in the Arctic Ocean, *Nature*, *421*, 252–256, doi: 10.1038/nature01351.
- Edwards, M., G. Kurras, M. Tolstoy, D. Bohnenstiehl, B. Coakley, and J. Cochran (2001), Evidence of recent volcanic activity on the ultraslow-spreading Gakkel Ridge, *Nature*, *409*, 808–812, doi: 10.1038/35057258.
- Einarsson, P., and B. Brandsdottir (1980), Seismological evidence for lateral magma intrusion during the July 1978 deflation of the Krafla volcano in NE-Iceland, *Journal of Geophysics*, *47*, 160–165.
- Ekström, G. (1994), Anomalous earthquakes on volcano ring-fault structures, *Earth planet. Sci. Lett.*, *128*, 707–712, doi: 10.1016/0012-821X(94)90184-B.
- Ekström, G., A. Dziewonski, N. Maternovskaya, and M. Nettles (2005), Global seismicity of 2003: Centroid-moment-tensor solutions for 1087 earthquakes, *Earth and Planetary Inter.*, *148*, 327–351, doi: 10.1016/j.pepi.2004.09.006.
- Font, Y., H. Kao, S. Lallemand, C.-S. Liu, and L.-Y. Cio (2004), Hypocentral determination offshore Eastern Taiwan using the Maximum Intersection method, *Geophys. J. Int.*, *158*(2), 655–675, doi: 10.1111/j.1365-246X.2004.02317.x.
- Foulger, G., R. Long, P. Einarsson, and A. Björnsson (1989), Implosive earthquakes at the active accretionary plate boundary in northern Iceland, *Nature*, *337*, 640–642, doi: 10.1038/337640a0.
- Foulger, G. R., and B. R. Julian (1993), Non-Double-Couple Earthquakes at the Hengill-Grensdalur Volcanic Complex, Iceland: Are they Artifacts of Crustal Heterogeneity?, *Bull. seism. Soc. Am.*, *83*(1), 38–52.
- Ghilani, C. (2010), Error Ellipse, in *Adjustment Computations: Spatial Data Analysis*, edited by C. Ghilani and P. Wolf, Fifth ed., Wiley Online Library, doi: 10.1002/9780470586266.ch19.

- Hjaltadóttir, S., K. Vogfjörð, and R. Slunga (2011), A seismological image of the Eyjafjallajökull Plumbing System during 2009-2010, *Geophys. Res. Abstr.*, *13*, EGU2011–12,221.
- Husen, S., and J. Hardebeck (2010), Earthquake location accuracy, *Community Online Resource for Statistical Seismicity Analysis*, doi: 10.5078/corssa-55815573.
- Husen, S., E. Kissling, N. Deichmann, S. Wiemer, D. Giardini, and M. Baer (2003), Probabilistic earthquake location in complex three-dimensional velocity models: Application to Switzerland, *J. geophys. Res.*, doi: 10.1029/2002JB001778.
- Jakobsson, M., R. Macnab, L. Mayer, R. Anderson, M. Edwards, J. Hatzky, H. Schenke, and P. Johnsson (2008), An improved bathymetric portrayal of the Arctic Ocean: Implications for ocean modeling and geological, geophysical and oceanographic analyses, *Geophys. Res. Lett.*, *35*(L07602), doi: 10.1029/2008GL033520.
- Jokat, W., and M. Schmidt-Aursch (2007), Geophysical characteristics of the ultraslow spreading Gakkel Ridge, Arctic Ocean, *Geophys. J. Int.*, *168*, doi: 10.1111/j.1365-246X.2006.03278.x.
- Jordan, T., and K. Sverdrup (1981), Teleseismic location techniques and their application to earthquake clusters in the south-central Pacific, *Bull. seism. Soc. Am.*, *71*(4), 1105–1130.
- Keir, D., et al. (2009), Evidence for focused magmatic accretion at segment centers from lateral dike injections captured beneath the Red Sea rift in Afar, *Geology*, *37*, 59–62, doi: 10.1130/G25147A.1.
- Kennett, B., and E. Engdahl (1991), Traveltimes for global earthquake location and phase identification - IASP91 model, *Geophys. J. Int.*, *105*, 429–465.
- Korger, E. (2010), The Volcanic Earthquake Swarm of 1999 at the Eastern Gakkel Ridge, Arctic Ocean: A Case Study for a Comparison between a Probabilistic- and a Conventional Teleseismic Algorithm, Master's thesis, University of Vienna.
- Läderach, C., V. Schlindwein, H.-W. Schenke, and W. Jokat (2011), Seismicity and active tectonic processes in the ultra-slow spreading Lena Trough, Arctic Ocean, *Geophys. J. Int.*, *184*(3), doi: 10.1111/j.1365-246X.2010.04926.x.
- Lin, G., and P. Shearer (2005), Tests of relative earthquake location techniques using synthetic data, *J. geophys. Res.*, *110*(B04304), doi: 10.1029/2004JB003380.
- Lomax, A., J. Virieux, P. Volant, and C. Berge (2000), Probabilistic earthquake location in 3D and layered models: Introduction of a Metropolis-Gibbs method and comparison with linear locations, *Advance in Seismic Event Location*, *452*, 101–134.
- Lomax, A., A. Michelini, and A. Curtis (2009), Earthquake Location, Direct, Global-Search Methods, *Encyclopedia of Complexity and System Science*, *5*.

- McNutt, S. (1996), Seismic Monitoring and Eruption Forecasting of Volcanoes: A Review of the State of the Art and Case Histories, in *Monitoring and Mitigation of Volcano Hazards*, edited by R. Scarpa and R. Tilling, pp. 99–146, Springer-Verlag, Berlin.
- Michael, P., et al. (2003), Magmatic and amagmatic seafloor generation at the ultraslow-spreading Gakkel ridge, Arctic Ocean, *Nature*, *423*, 956–961, doi: 10.1038/nature01704.
- Mogi, K. (1967), Earthquakes and fractures, *Tectonophysics*, *5*, 35–55.
- Moser, T., and T. V. Eck (1992), Hypocenter Determination in Strongly Heterogeneous Earth Models Using the Shortest Path Method, *J. geophys. Res.*, *97*(B5), 6563–6572.
- Mueller, C., and W. Jokat (2000), Seismic Evidence for Volcanic Activity Discovered in Central Arctic, *Eos, Trans. Am. geophys. Un.*, *81*(24), 265–269, doi: 10.1029/00EO00186.
- Pan, J., M. Antolik, and A. Dziewonski (2001), Locations of mid-oceanic earthquakes constrained by seafloor bathymetry, *J. geophys. Res.*, *107*(B11), doi: 10.1029/2001JB001588.
- Riedel, C., and V. Schlindwein (2010), Did the 1999 earthquake swarm on Gakkel Ridge open a volcanic conduit? A detailed teleseismic data analysis, *Journal of Seismology*, *14*(3), 505–522, doi: 10.1007/s10950-009-9179-6.
- Schlindwein, V., and C. Riedel (2010), Location and source mechanism of sound signals at Gakkel ridge, Arctic Ocean: Submarine Strombolian activity in the 1999-2001 volcanic episode, *Geochem. Geophys. Geosys.*, *11*(Q01002), doi: 10.1029/2009GC002706.
- Schlindwein, V., C. Müller, and W. Jokat (2005), Seismoacoustic evidence for volcanic activity on the ultraslow-spreading Gakkel Ridge, Arctic Ocean, *Geophys. Res. Lett.*, *32*(L18306), doi: 10.1029/2005GL023767.
- Schweitzer, J. (2001), HYPOSAT - an enhanced routine to locate seismic events, *Pure applied Geophysics*, *158*, 277–289.
- Schweitzer, J., and B. Kennett (2007), Comparison of Location Procedures: The Kara Sea Event of 16 August 1997, *Bull. seism. Soc. Am.*, *97*, doi: 10.1785/0120040017.
- Sella, G., T. Dixon, and A. Mao (2002), REVEL: A model for recent plate velocities from space geodesy, *J. Geophys. Res.*, *107*(B4), ETG 11–1 – ETG 11–30, doi: 10.1029/2000JB000033.
- Sohn, R. A., et al. (2008), Explosive volcanism on the ultraslow-spreading Gakkel ridge, Arctic Ocean, *Nature*, *453*, 1236–1238, doi: 10.1038/nature07075.
- Stranne, C., R. A. Sohn, B. Liljebladh, and K. ichi Nakamura (2010), Analysis and modeling of hydrothermal plume data acquired from the 85°E segment of the Gakkel Ridge, *J. geophys. Res.*, *115*(C06028), doi: 10.1029/2009JC005776.

- Tarantola, A., and B. Valette (1982), Inverse problems = quest for information, *J. Geophys.*, *50*, 159–170.
- Tolstoy, M., D. Bohnenstiehl, M. Edwards, and G. Kurras (2001), Seismic character of volcanic activity at the ultraslow-spreading Gakkel Ridge, *Geology*, *29*(12), 1139–1142, doi: 10.1130/0091-7613(2001)029.
- Utsu, T. (1961), A statistical study on the occurrence of aftershocks, *Geophys. Mag.*, *30*, 521–605.
- Utsu, T. (2002), Statistical features of seismicity, in *International Handbook of Earthquake and Engineering Seismology, Part A*, edited by W. Lee, H. Kanamori, P. Jennings, and C. Kisslinger, pp. 719–732, Academic Press, New York, doi: 10.1016/S0074-6142(02)80246-7.
- Wadati, K. (1933), On the travel time of earthquake waves, *Geophys. Mag.*, *7*, 101–111.
- Wiens, D., J. McGuire, P. Shore, and M. Bevis (1994), A deep earthquake aftershock sequence and implications for the rupture mechanism of deep earthquakes, *Nature*, *372*, 540–543.
- Wittlinger, G., G. Herquel, and T. Nakache (1993), Earthquake location in strongly heterogeneous media, *Geophys. J. Int.*, *115*, 759–777.
- Wolfe, C. (2002), On the Mathematics of Using Difference Operators to Relocate Earthquakes, *Bull. seism. Soc. Am.*, *92*(8), 2879–2892.
- Zhou, H. (1994), Rapid 3D hypocentral determination using a master station method, *J. geophys. Res.*, *99*, 15,439–15,455.

6 Second paper: Earthquake clusters at the Southwest Indian Ridge

Läderach, C., E. Korger, V. Schlindwein, C. Müller, and A. Eckstaller (2012), Characteristics of tectonomagmatic earthquake swarms at the Southwest Indian Ridge between 16°E and 25°E, *Geophys. J. Int.*, 190, 429–441, doi: 10.1111/j.1365-246X.2012.05480.x

6.1 Summary

The ultraslow spreading Southwest Indian Ridge (SWIR) is a prominent end-member of the global mid-ocean ridge system. It spreads with a full-rate of 14 – 16 mm y⁻¹ and shows several segments of various obliquities. The western SWIR consists of the Oblique and Orthogonal Supersegments lying at an epicentral distance of $\sim 21^\circ$ to the VNA2 seismic array operated by the German Neumayer station in East Antarctica. The array monitors backazimuth, apparent velocity and signal-to-noise ratio of arriving waves and provides a data set of seismicity from the western SWIR over several years. Compared to the global seismological network, its detection threshold for earthquakes occurring at the western SWIR is more than 0.5 m_b lower enabling a more comprehensive study of mid-ocean ridge processes than the teleseismic earthquake catalogues. We identified a total number of 743 earthquakes occurring at the western part of the SWIR and calculated the body-wave magnitudes (m_b) from P-wave amplitude picks on the VNA2 broad-band sensor obtaining a magnitude range from m_b 3.18 to m_b 5.34. In the years of 2001, 2004, 2005 and 2008, significantly increased event rates indicated four earthquake swarms with up to 164 events lasting for several days. All swarms had strong events registered in the International Seismological Centre catalogue. The relocalization of these events confirmed that all swarms occurred in the same region on the Orthogonal Supersegment. We analyzed event and moment release rate histories, b-values and aftershock decay rates (Modified Omori Law) finding that the swarms of 2001, 2004 and 2005 have similarities in the temporal distribution of seismic moment and event numbers. The swarm of 2008 is smaller with high magnitude events at the swarm's onset which represent shear failure on normal faults. The application of the Modified Omori Law and the b-value show that the earthquakes of the swarms do not follow the classical main shock-aftershock pattern of purely tectonic earthquake sequences. At the Orthogonal Supersegment, a continuous positive magnetic anomaly along the rift axis, a negative mantle Bouguer anomaly, basalts at the seafloor and potentially volcanic edifices indicate robust magmatic crustal accretion. The high-resolution bathymetry shows ubiquitous rift-parallel ridges with steep flanks

towards the rift axis indicating high-angle normal faults. The high-magnitude earthquakes detected teleseismically during the swarms are generated there. We interpret that the swarms are caused by magmatic accretion episodes at a suggested volcanic centre of the Orthogonal Supersegment and that possible magma injection activates the steeply dipping fault planes.

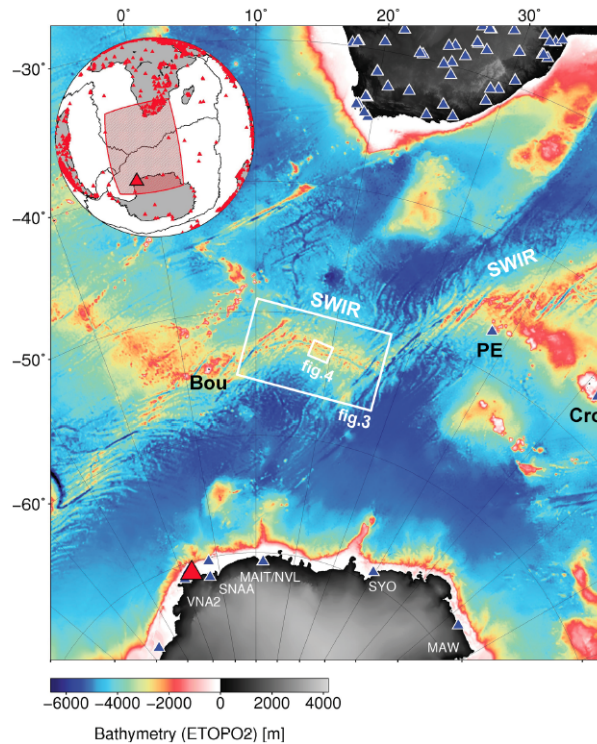


Figure 6.1 – Overview of the SWIR with ETOPO 2 bathymetry (*Smith and Sandwell, 1997*) and global seismological stations (some labelled with ISC station code). Boxes mark the outline of Figs 6.3 and 6.44. Bou, Bouvetoya; Cro, Iles Crozet; PE, Prince Edward Islands; SWIR, Southwest Indian Ridge. Red shaded box on globe shows outline of the figure.

6.2 Introduction

The remote location of mid-ocean ridges makes it a difficult task to monitor their seismicity as a potentially vast amount of small earthquakes is assumed to go undetected. Seismic studies of active mid-ocean ridge processes are usually done using short-term (weeks up to year) local networks of ocean bottom seismometers (OBS). Regional autonomous underwater hydrophone (AUH) arrays can be in operation for several years (e.g. *Smith et al., 2002; Bohnenstiehl and Dziak, 2008; Simao et al., 2010*) providing a comprehensive earthquake data set for events of a magnitude $M \geq \sim 2$ (*Bohnenstiehl and Dziak, 2008*). Teleseismic earthquake catalogues span several decades (International Seismological Centre 2001) with the disadvantage of a great epicentral distance to the study area

lowering the detection capability. The situation is especially bad for ultraslow spreading ridges as they are situated in the ice covered Arctic Ocean or the windy latitudes of the southwest Indian Ocean. These remote regions lack local OBS studies, solely allowing limited studies on ice floes (e.g. *Läderach et al., 2011; Läderach and Schlindwein, 2011*) and limited deployment of AUH arrays (*Sohn and Hildebrand, 2001*). Hence, seismicity studies of ultraslow ridges have to fall back on the data recorded by the global network of land stations archived by the International Seismological Centre (ISC).

In case of the western Southwest Indian Ridge (SWIR; Fig. 6.1), the closest stations are located in Antarctica at a distance of $\sim 21^\circ$. Among them is the VNA2 array on Halvfar Ryggen operated by the German Neumayer station (Fig. 6.1). The array is constantly monitoring backazimuth, apparent velocity and signal-to-noise ratio of arriving waves (Fig. 6.2). Together with the opening of the new Neumayer III station in 2009, the data acquisition system of the array has been replaced and the new system is in operation since 2010. The VNA2 data set from the years 2001 to 2009 contained a conspicuous cluster of events arriving with backazimuth and slowness values which indicate an origin at the western part of the SWIR. The event rates are much higher than teleseismic detections in this area thus providing the unique possibility to study ultraslow mid-ocean ridge processes at a regional distance. Four episodes of intense earthquake activity bear the opportunity to analyze swarms possibly caused by an active accretion episode at the western SWIR.

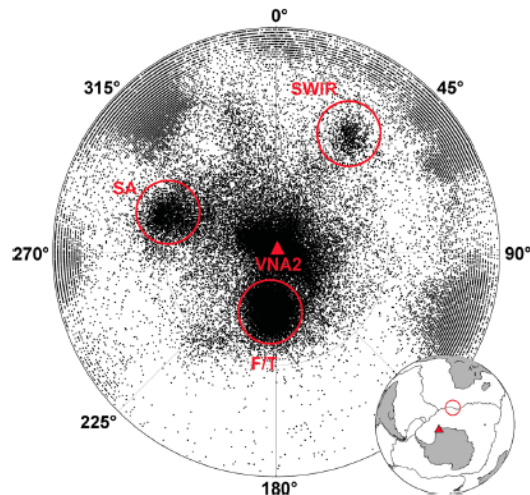


Figure 6.2 – Backazimuth and slowness (in s deg^{-1}) of detections from the VNA2 array (red triangle in the centre). Low slowness values positioned in the centre, slowness values of 16 s deg^{-1} on the outline of the circle. Detections from seismically active regions cluster at specific backazimuth and slowness values. Detections from the western SWIR have a backazimuth of $\sim 35^\circ$ and a slowness of $\sim 10 \text{ s deg}^{-1}$. F/T, Fiji/Tonga islands; SA, South America; SWIR, western Southwest Indian Ridge. Globe with VNA2 (red triangle) in the centre and the Orthogonal Supersegment marked with a red circle.

6.3 Geological Setting

The ultraslow spreading SWIR and Arctic Gakkel Ridge are the end-members of the global mid-ocean ridge system. The SWIR spreads with a velocity of $14 - 16 \text{ mm y}^{-1}$ full-rate and consists of magmatic and amagmatic accretionary ridge segments (*Dick et al.*, 2003). The latter can be established with any orientation to the spreading direction. The rift valley floor is mainly composed of peridotite and shows a weak magnetization. Mantle horst blocks are the main topographic element and detachment faults can expose mantle material to the seafloor (*Dick et al.*, 2003). Magmatism is focused in isolated volcanic centres and along-axis melt flow mechanisms have been proposed (e.g. *Grindlay et al.*, 1998; *Cannat et al.*, 2008).

Magmatic segments are found mostly on orthogonal spreading ridge segments and show elongated rift-parallel ridges in the rift valleys accompanied by normal faults forming the staircase topography of the rift valley walls. At magmatic centres, bull's eye circular patterns of mantle Bouguer anomalies (MBAs) are abundant and suggest focused melt/mantle flow forming a thicker crust (e.g. *Tolstoy et al.*, 1993).

From 10°E to 16°E , the so-called 'Oblique Supersegment' is highly oblique spreading with an effective spreading rate (ESR; half spreading rate in ridge-perpendicular direction) of

merely 3.9 mm y^{-1} (*Dick et al.*, 2003). It consists of extended amagmatic segments and only two volcanic centres (Narrowgate magmatic segment and Joseph Mayes seamount; Fig. 6.3).

From 16°E to 25°E , the SWIR spreads nearly orthogonal with an ESR of 7.2 mm y^{-1} . Mostly basalts were found along this 'Orthogonal Supersegment' (*Dick et al.*, 2003). It is interpreted as a magmatic segment and shows a continuous positive magnetic anomaly at the rift axis. The lithosphere of ultraslow spreading ridges such as the SWIR is expected to be cold and brittle (e.g. *Tolstoy et al.*, 1993). Consequently, tectonic earthquakes with high magnitudes could be generated by shear failure of faults.

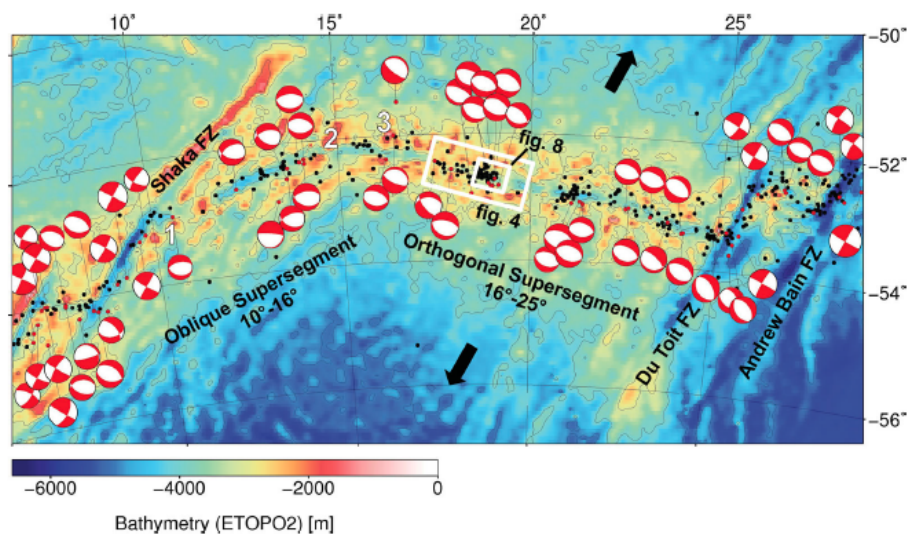


Figure 6.3 – Oblique and Orthogonal Supersegment of the SWIR with spreading direction after *Dick et al.* (2003). Black dots plot teleseismic earthquakes from 2001 to 2009 (ISC 2001) and available focal mechanisms with best fitting double-couple solutions from the Global CMT catalogue (e.g. *Ekström et al.*, 2005). White boxes denote the outline of Figs 6.4 and 6.8. FZ, fracture zone; 1, Joseph Mayes magmatic segment; 2, Narrowgate magmatic segment; 3, 16°E discontinuity (*Dick et al.*, 2003). Bathymetry as in Fig. 6.1.

6.4 Methods

6.4.1 Extraction of events from the VNA2 data set

Operated by the German Neumayer station in eastern Antarctica, the station VNA2 is detecting local, regional and teleseismic earthquakes (Fig. 6.1; Buesselberg et al. 2001). The VNA2 array is located $\sim 50 \text{ km}$ southeast of the Neumayer station on the Halvfar Ryggen. It consists of one central three-component broad-band sensor (LE-3D/20s) and three concentric rings of 15 vertical short-period sensors (MARK L-4/C), each ring with

an odd number of sensors (A-ring, three sensors; B-ring, five sensors; C-ring, seven sensors). The outermost C-ring has a radius of ~ 1 km. The Lennartz PCM-5800 data logger is sampling with a rate of 62.5 Hz and data are sent constantly via radio link to Neumayer station. Due to the polar night with a duration of 8 weeks, the VNA2 array faces energy problems as the solar panels stop producing electricity and charging the batteries. The battery capacity is not sufficient to bridge the dark winter time and thus, the VNA2 array has outages of up to 150 d which cause a seasonal bias on the data. The array is constantly monitoring backazimuth, slowness and signal-to-noise ratio of arriving waves by automatic beamforming and frequency-wavenumber analysis using the NORSAR detection processing/event processing algorithm (*Schweitzer et al., 2009*). The slowness is estimated assuming that the wave front is plane (*Schweitzer et al., 2009*), which is nearly the case for small aperture arrays with diameter of < 5 km. The plot of all triggered detections of the array shows several clusters of detections with different slowness values (Fig. 6.2). Local tectonic and cryogenic seismicity (e.g. crevassing of glaciers, ice bergs colliding with the shelf; *Mueller et al. 2005*) have high slowness values, whereas teleseismic earthquakes have low slowness values as their waves arrive from steep below the array (e.g. *Iyer, 1971*). Subduction zone earthquakes in the Fiji-Tonga region and South America appear as clusters with backazimuths centred at 180° and 290° , respectively (Fig. 6.2). A third prominent cluster of detections originating at closer distances lies at a backazimuth of $\sim 35^\circ$ and a slowness of ~ 10 s deg $^{-1}$. This cluster contains earthquakes from the western SWIR.

We extracted array detections arriving within a slowness range of 4.0 – 12.5 s deg $^{-1}$ and backazimuths ranging from 22° to 45° . These backazimuths encompass the region of the Oblique and the Orthogonal Supersegments (*Dick et al. 2003*; Figs 6.1 and 6.3). By limiting the slowness values, we tried to exclude signals generated by local events and ice signals.

We then extracted the waveforms of ~ 1850 triggered signals by cutting a 120 s window starting 20 s before the triggered wave. These seismograms were bandpass filtered from 0.5 to 5 Hz as recommended by the International Association of Seismology and Physics of the Earth's Interior (IASPEI) for magnitude determination. P-wave onsets were picked on the vertical-component seismogram of the broad-band station VNA2 and on the vertical component of the short-period sensor WA1 located at the innermost A-ring of the array. Amplitudes were picked in the P-wave train of the VNA2 and the WA1 vertical-component seismogram. However, due to insufficient quality of the amplitude picks on the short-period seismogram, it was not used for magnitude determination.

6.4.2 Relocalization of teleseismic earthquakes

With an epicentral distance of $\sim 21^\circ$, it is not possible to localize the hypocentres solely with data from the VNA2 array (Fig. 6.1). Therefore, we collected phases from ISC for the time period from 2001 to 2009 for earthquakes in the study area (ISC 2001) and

relocalized them using HYPOSAT, a least-squares algorithm of *Schweitzer* (2001), and a velocity model of *Kennett* (1992), which is an adapted version of iasp91 for oceanic environment. To improve the quality of the relocalization, we performed a simple master event (ME) localization technique as described by *Fitch* (1975), which we used already for a study in the Arctic Ocean (*Läderach et al.*, 2011). This technique is based on the assumption that the arrival time residuals of a localized earthquake are caused solely by velocity anomalies along the wave path. Furthermore, it is assumed that the wave paths of events occurring in the same region at different times are nearly identical and thus one high magnitude event with reported phases of many stations can be used as an ME to correct the time residuals for weaker events occurring in the same region. We can clearly correlate the relocated teleseismically recorded earthquakes with VNA2 detected earthquakes occurring at the same time and hence identify teleseismically detected events in the VNA2 data set. We tried to correlate the reported backazimuth of the triggered events with the relocalized epicentres to attribute backazimuth ranges to certain earthquake source areas. Unfortunately, this correlation is too inaccurate to make any reliable conclusions. The backazimuth shows great variations depending on where in the wave train it was determined. Hence, the backazimuth is of little value to further constrain the source location.

6.4.3 Magnitude determination of the regional data set

From the peak-to-peak amplitude (A) of the P-wave train and its period (T), we calculated the intermediate-period/broad-band body wave magnitude (m_b) for 743 events using (ISC 2006).

$$m_b = \log_{10}\left(\frac{A}{T}\right)_{max} + Q(\Delta, h) \quad (6.4.1)$$

where

$$\left(\frac{A}{T}\right)_{max} = \frac{V_{max}}{2\pi} \quad (6.4.2)$$

where V_{max} = ground velocity in $\mu\text{m/s}$ associated with the maximum trace-amplitude in the entire P-wave train (ISC 2006). We used a Q-value of 6.1 for the attenuation function for P-waves recorded on the vertical component established by *Gutenberg and Richter* (1956) depending on the focal depth (h) and the epicentral distance in degrees (Δ). To evaluate the calculated magnitudes, we compared them with the magnitudes of 71 earthquakes as reported by ISC.

For further investigation, we calculated the unified magnitude (M) after the following formula (*Scordilis, 2006*):

$$M = 0.85(\pm 0.04)m_{bu} + 1.03(\pm 0.23) \quad (6.4.3)$$

where for local catalogues the unified body-wave magnitude $m_{bu} = m_b$.

We calculated the moment release M_0 for each event after the formula of *Kanamori* (1977):

$$M = \frac{2}{3}(\log M_0 - 9.1) \quad (6.4.4)$$

The magnitude of completeness (M_c) was determined using the maximum-curvature method of *Woessner and Wiemer* (2005) and the b-value after the maximum likelihood estimate of ? from unified magnitudes M. The magnitude of completeness is M 4.50 calculated for all the 743 events and the b-value is 1.28 ± 0.06 for all 743 events. Furthermore, we calculated b-values for each of the four swarm periods.

6.4.4 Swarm analysis

The Modified Omori Law (*Utsu et al.*, 1995) states a causal relationship of earthquakes organized in tectonic sequences. The main shock triggers aftershocks which in turn trigger the next aftershock with the magnitudes decreasing from one event to the next. The aftershock rate follows a power-law decay and is expressed by the following formula:

$$n(t) = \frac{K}{(c + t)^p} \quad (6.4.5)$$

where $n(t)$ is the aftershock frequency at time t after the main shock. The activity parameter K , the time offset parameter c and the decay exponent p are empirical constants. The p -value describes the rate of strain release during the aftershock sequence. Typically, it ranges from 0.8 to 1.2 but values between 0.6 and 2.5 have also been observed (*Utsu et al.*, 1995).

A total of 462 earthquakes were organized in four swarms. We applied the Modified Omori Law to these four swarms using only 247 events above the magnitude of completeness. The calculations were done with the software package of SASEis2006 (Ogata 2006).

6.5 Results

6.5.1 Relocalization of teleseismic earthquakes

We performed an ME relocalization of 82 events reported by ISC. We chose a m_b 5.1 event of 2007 August 2, 07:19:21 UTC, as ME (at $52^{\circ}30\text{S}/17^{\circ}43\text{E}$). Its location at the westernmost end of the study area is not ideal for an ME, but it provided a total of 842 phase readings, whereas all other events have much fewer phases. Therefore, we haven't used other MEs. We commented on the effect of using different MEs in our study of the Arctic Lena Trough, where several MEs were used (*Läderach et al.*, 2011). The relocalization yielded 43 events whose length of the semi-major axis of the 95 per cent error ellipse (S_{maj}) is < 30 km. These event locations have a mean rms error of 0.85 s and a mean S_{maj} of 16.3 km. They are based on an average of 37 phases. Compared to our study in the Arctic Ocean (*Läderach et al.*, 2011), the relocalization of events at the western SWIR has a lower percentage of relocalized events of minor quality and with fewer phases. This is due to the remote location of the SWIR with the closest stations at an epicentral distance of $\sim 21^{\circ}$ (Fig. 5.1). Fig. 6.4 shows the epicentres used for interpretation. The relocation of the ME differs about ~ 10 km from the ISC location, whereas some of the other events are shifted up to 50 km from the initial location. The relocation vectors do not point towards the ME but rather in a northwest-southeast direction. West of $18^{\circ}30\text{E}$, the events cluster along the ridge axis. To the east, most events cluster at the rift valley or south of it. Three events occur on the rift-parallel ridges up to ~ 30 km north of the ridge axis (at $\sim 52^{\circ}31\text{S}/18^{\circ}49\text{E}$ and $52^{\circ}30\text{S}/19^{\circ}02\text{E}$) and two events are located in a similar setting ~ 30 km south of the ridge axis (at $\sim 52^{\circ}58\text{S}/18^{\circ}48\text{E}$). One single event is located further east at the southern flank of a rift-parallel ridge (at $52^{\circ}53\text{S}/19^{\circ}18\text{E}$). The seven available focal mechanisms from the Global CMT catalogue (e.g. *Ekström et al.*, 2005) for the relocated events show normal faulting mechanisms proposing steeply dipping fault planes (Fig. 6.4).

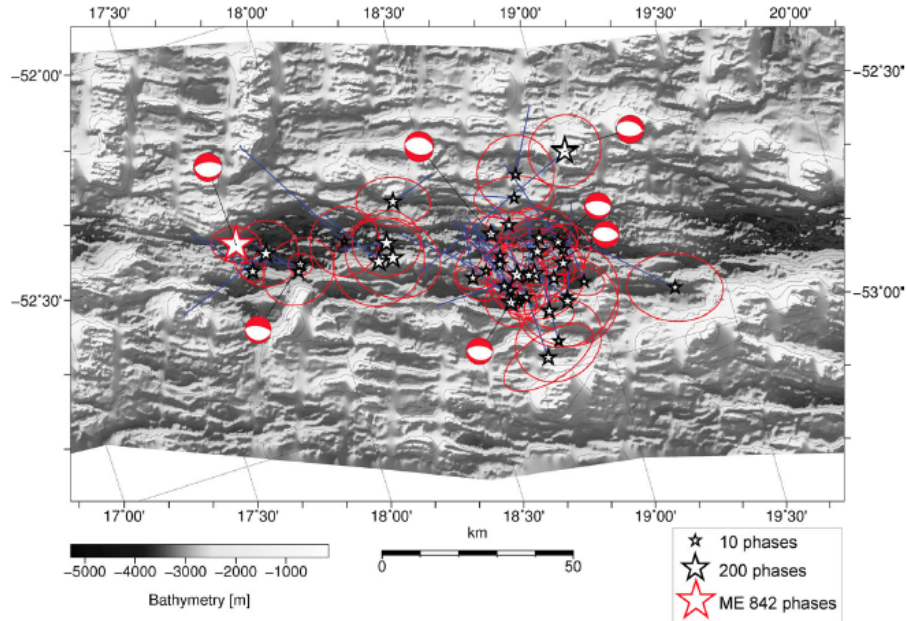


Figure 6.4 – Relocalization of events reported by ISC. Master Event (ME) plotted as white star with red outline, symbol size of events according to number of phases used for relocalization. 95 per cent error ellipse plotted in red. Tip of blue line pointing towards ISC location. Focal mechanisms as in Fig. 6.3. Interpolated high-resolution bathymetry after *Grindlay et al.* (1998).

6.5.2 Regional earthquakes

6.5.2.1 Magnitudes

Of the total amount of ~ 1850 triggered detections at the VNA2 array, we identified 743 earthquakes originating in the study area during a time span of 8 yr (Fig. 6.5). The low percentage of earthquakes compared to the detections is due to the fact that waves within a single wave train are often triggered several times and periods of high noise level tend to generate wrong detections.

We estimated body-wave magnitudes from the amplitude picks on the VNA2 broad-band sensor. The magnitudes range from m_b 3.18 to m_b 5.34. The smallest ISC-detected earthquakes on the Oblique and Orthogonal Supersegment have a magnitude of m_b 3.6. Hence, the detection threshold of the VNA2 array is $\sim 0.4 m_b$ lower than ISC. Comparing the VNA2 magnitudes to those reported by ISC, we observed a systematic shift with VNA2 magnitudes being on average $0.37 m_b$ higher than ISC magnitudes (Fig. 6.6). Taking this discrepancy into account, the detection threshold of VNA2 is probably $\sim 0.8 m_b$ lower than the ISC detection threshold. However, the magnitude difference between VNA2 magnitudes and ISC magnitudes is highly variable, ranging from -0.5 to 1.3 (cf. Fig. 6.6). Differentiating the teleseismic earthquakes according to their location on the western

SWIR (Fig. 6.5c), we note that the events located on the Orthogonal Supersegment Centre, especially the high magnitude events during the four swarms on the Orthogonal Supersegment Centre, show on average $\sim 0.6 m_b$ higher magnitudes at VNA2 relative to the ISC magnitude (cf. box in Fig. 6.6). At the remaining segments of the Oblique and the Orthogonal Supersegments, the magnitudes of VNA2 are on average ~ 0.2 to ~ 0.3 higher than the ISC magnitudes. Interestingly, the VNA2 magnitudes of events occurring at Shaka fracture zone (FZ; FZW in Figs 6.5c and 6.6) and Du Toit/Andrew Bain FZ (FZE in Figs 6.5c and 6.6) have lower magnitudes than the ISC magnitudes. These events predominantly show strike-slip focal mechanisms (Fig. 6.3).

Hence, we conclude that: (1) the VNA2 magnitudes are generally higher than the ISC magnitudes; (2) the magnitude difference scatters strongly and (3) the magnitude difference is different for the various SWIR segments with the biggest differences found for the Orthogonal Supersegment.

The magnitude of completeness is M 4.50. Due to the overestimated magnitude values, the magnitude of completeness might correspond to a magnitude of M 4.2 in ISC values.

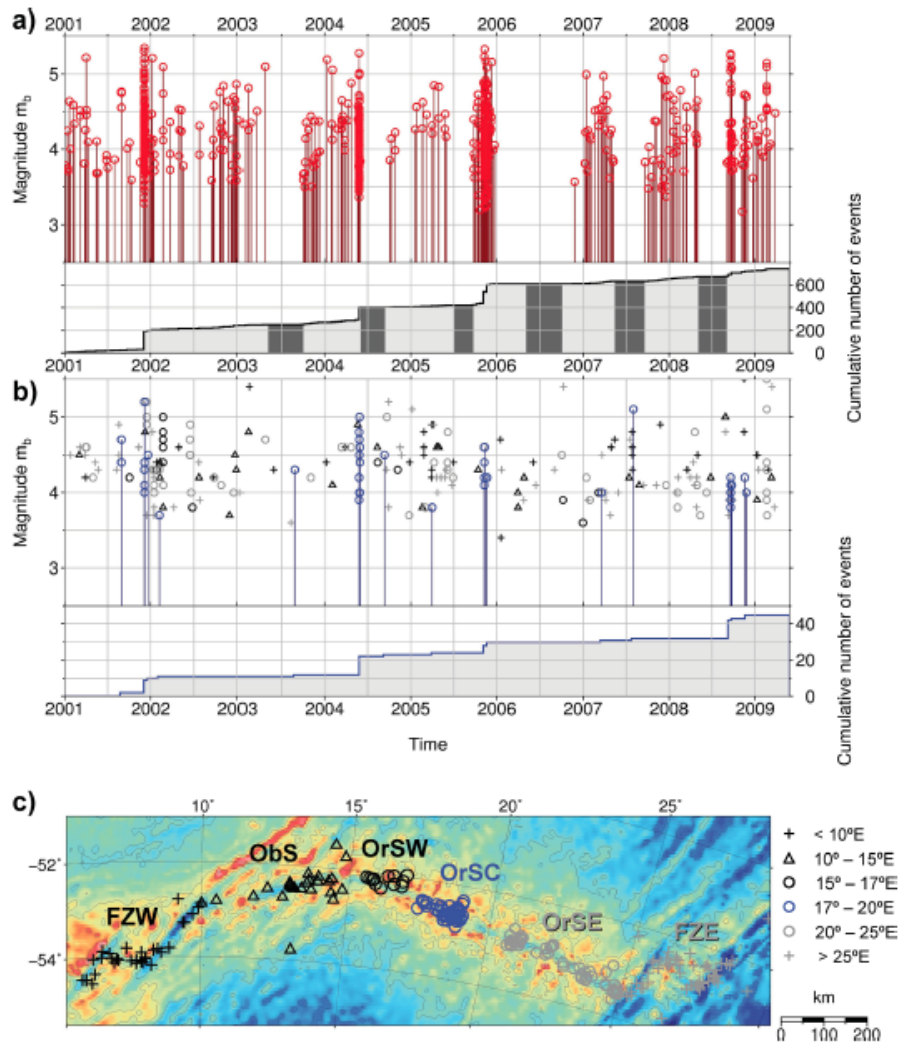


Figure 6.5 – (a) Magnitudes and cumulative seismicity of events at the Oblique and Orthogonal Supersegment of the SWIR detected from the VNA2 array. Events plotted as red circles with calculated body-wave magnitude (m_b , upper panel), cumulative seismicity plotted as thick black line (lower panel) with station outages during Antarctic winter in dark grey. (b) Magnitudes and cumulative seismicity of events at the western SWIR detected with the global ISC stations. Events plotted as different symbols according to legend in (c) with reported body-wave magnitude (m_b , upper panel), cumulative seismicity plotted for events occurring at the central Orthogonal Supersegment (blue circles in upper panel) as thick blue line (lower panel). (c) Oblique and Orthogonal Supersegment with epicentres of the teleseismic events plotted with different symbols according to their location. FZE, Fracture Zone East; FZW, Fracture Zone West; ObS, Oblique Supersegment; OrSC, Orthogonal Supersegment Centre; OrSE, Orthogonal Supersegment East; OrSW, Orthogonal Supersegment West. Bathymetry as in Fig.6.1.

6.5.2.2 Identification of swarms

Earthquake sequences are classified in different types depending on the distribution of magnitudes within the sequence. If an event of high magnitude followed by events of decreasing magnitudes is present at the beginning of the sequence, it is classified as a main shock aftershock sequence (with or without preceding foreshocks; Mogi 1963). Main shock aftershock sequences are commonly observed in tectonic settings and can be fitted to an aftershock decay rate law such as the Modified Omori Law (*Utsu et al.*, 1995). Sequences lacking a main shock and a decreasing trend of magnitudes are classified as swarms (*Mogi*, 1963) and cannot be fitted by the Modified Omori Law. As one criterion to identify a swarm, the event rate has to exceed 10 per cent of the variance of the long-term background seismicity (*Bohnenstiehl and Dziak*, 2008).

At the Neumayer station, the event rate recorded was 0.34 events per day (event rates are calculated disregarding the outage periods) over the 8-yr period. We identified four swarm sequences showing manifold increased event rates ranging from 5.2 events per day to 38.3 events per day in 2001, 2004, 2005 and 2008 (Figs 6.5a and 6.7; Table 1). Excluding the swarm periods from the calculation, the background seismicity in years without swarms was 0.10 – 0.13 events per day. During the four swarm periods, the ISC-based teleseismic event rate was also increased to 0.46 – 2.79 events per day from background rate of 0.05 – 0.08 events per day. Hence, the regionally detected swarms can also be identified in teleseismic data, even if event rates are an order of magnitude lower (cf. Schlindwein 2012).

The duration, event rate and other specifications of the four swarms are listed in Tbl. 6.1. During the four swarm periods, ISC reports 32 teleseismic events of which 30 events occurred at the ridge segment we refer to as Orthogonal Supersegment Centre (Fig. 6.5c). None of the other rift segments displayed swarm-like behaviour during the period of our study. Of these 30 events occurring at the Orthogonal Supersegment Centre, we could relocalize 17 events with an adequate quality (Fig. 6.8). Interestingly, all the relocations plot in the same region of about 80×40 km (with the long side across the rift valley; Fig. 6.8).

6.5.2.3 Swarm characteristics

To get a first impression if a sequence of earthquakes shows a main shock-aftershock pattern or a swarm pattern, *McNutt* (1996) provides a useful rule of thumb. Tectonic main shock-aftershock sequences show differences of >1 in the magnitude of the main shock and the second largest aftershock, whereas swarms show differences of < 0.5 . For the four identified swarms of 2001, 2004, 2005 and 2008, the magnitude differences were 0.04, 0.23, 0.09 and 0.01, respectively, clearly indicating the lack of a prominent main shock.

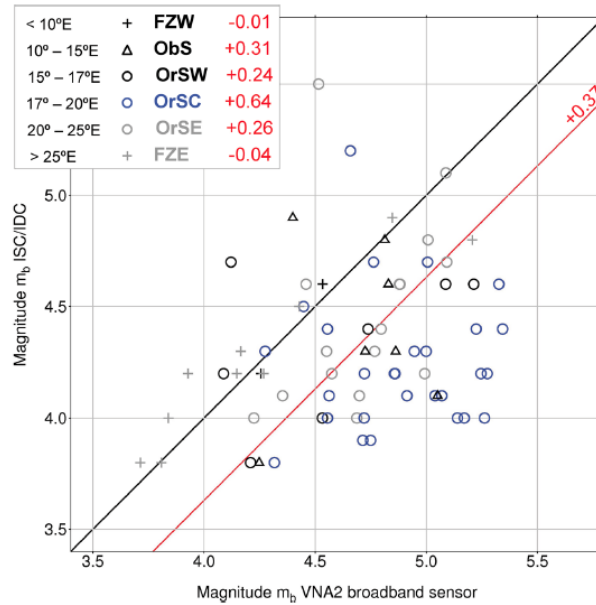


Figure 6.6 – Comparison of magnitudes computed by ISC and magnitudes calculated from amplitude picks on VNA2. Black line denotes correlation of magnitudes, red line shows average misfit of magnitudes of 0.37. Symbol legend in upper left corner with abbreviation of subsegments (cf. Fig. 6.5c) and average misfit of magnitudes per subsegment in red.

Normalizing the cumulative moment release, event rate and swarm duration allows the comparison of the four swarms' temporal development with each other (Fig. 6.9). The swarms of 2001, 2004 and 2005 display a similar evolution with low moment release at the swarm initiation followed by a 'staircase' pattern with a relatively constant gradient (moment release rate) of ~ 1 (Fig. 6.9, red curve). The swarm of 2008 shows a steeper gradient as the first seven events of the swarm release >70 per cent of the seismic moment. At half time of the swarm duration, the activity comes to a complete stop and only after 90 per cent of the swarm duration some additional events occur.

Comparing the normalized cumulative event rate with the normalized cumulative moment release, the swarm of 2008 differs considerably from the others (Fig. 6.9). The swarms of 2001, 2004 and 2005 show a balance between event rate (Fig. 6.9, grey and black) and moment release (Fig. 6.9, red) which means that events of moderate magnitudes are dominating the swarms. During short phases, the swarms of 2001 and 2005 show a strong moment release which raises the moment release curve above the event rate curve. The swarm of 2008 is dominated by high magnitude events which is responsible for the separation of the two curves (Fig. 6.9).

The calculated b-values for each swarm (with events numbers noted in Table 1) are listed in black at the top of each panel in Fig. 6.9. They range from 1.03 ± 0.24 to 1.78 ± 0.22 with the lowest value for the swarm of 2008. The swarms of 2001, 2004 and 2005 show b-values ≥ 1.25 which is considerably higher than the value for the 2008 swarm.

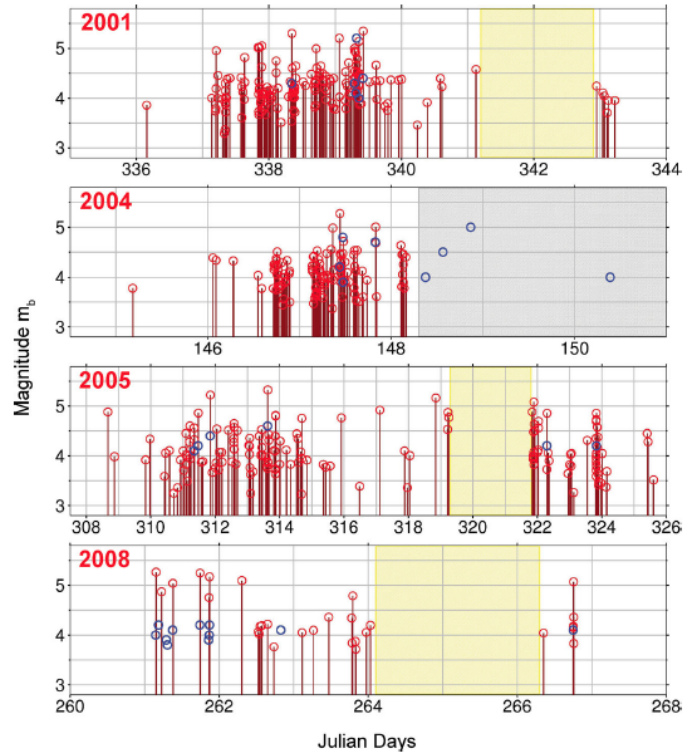


Figure 6.7 – Body-wave magnitudes (m_b) of four swarms at the Orthogonal Supersegment with year in the upper left corner of each panel. Note the different spacing of the time axis for all swarms. Red circles denote events detected by the VNA2 array, blue circles globally detected ISC events. Gaps in swarm activity are yellow shaded, whereas data outage for the VNA2 array is grey shaded (cf. Tbl. 6.1).

The Modified Omori Law could not be fitted well to any of the four swarms (Fig. 6.9). All of them have very high uncertainties for the p-value, which is possibly a consequence of the short duration of the individual swarms in combination with the small numbers of events above the magnitude of completeness. However, *Simao et al.* (2010) fitted the Modified Omori Law to AUH detected swarms at the Mid-Atlantic Ridge consisting of a comparably low number of events and showing similarly short swarm durations. Hence, we conclude that the Modified Omori Law can be used for such swarms and the fact that it does not fit our four swarms shows that their event rate does not follow a power-law decay typical for tectonic earthquake sequences.

	Swarm 2001	Swarm 2004	Swarm 2005	Swarm 2008
Start	2001 Dec 3 (336)	2004 May 24 (145)	2005 Nov 4 (308)	2008 Sept 17 (261)
End	2001 Dec 9 (343)	2004 May 27 (148)	2005 Nov 21 (325)	2008 Sept 22 (266)
Duration [<i>d</i>]	7.1	3.0	16.9	5.6
No. of events	164	115	154	29
Event rate [<i>per d</i>]	23.1	38.3	9.1	5.2
mb range	3.29-5.34	3.37-5.27	3.23-5.33	3.71-5.26
Moment release [<i>Nm</i>]	3.62E+18	1.51E+18	2.89E+18	1.34E+18
No. of ISC events	7	8	6	11
Relocalized ISC events	7	2	2	6
Remarks	Activity gap of 1.7 d (341.2-342.9)	Data gap of 3.3 d (148.3-151.6)	Activity gap of 2.5 d (319.3-321.8)	Activity gap of 2.2 d (264.1-266.3)

Table 6.1 – Summary of the four swarms with start and end date, duration, number of events, event rate, magnitude range, total moment release, number of teleseismically detected events during the swarm, number of these which could be relocalized and remarks such as gap in data or activity. Julian Days in brackets.

6.6 Interpretation

6.6.1 Regional data set of SWIR seismicity

With an orientation almost perpendicular to the rift axis of the Orthogonal Supersegment (Fig. 6.1), the VNA2 array seems to be in a favourable location to detect normal faulting earthquakes occurring there. The magnitude determinations based on the P-wave amplitudes picked on the VNA2 broad-band sensor are shifted towards higher magnitudes relative to the ISC magnitudes. The average magnitude difference of m_b 0.37 is not consistent for all events but shows a dependence on the event location (Fig. 6.6). The majority of the western SWIR seismicity displays normal faulting extensional focal mechanism with the direction of the least compressive stress (σ_3) parallel to the spreading direction and the maximal compressive stress (σ_1) pointing steeply down (Fig. 6.3). Hence, the maximal P-wave radiation is perpendicular to the ridge axis and favourable to be detected at the VNA2 array for extensional events. In contrast to this, many stations reporting magnitudes for the magnitude calculation of ISC are found in prolongation of the rift axis

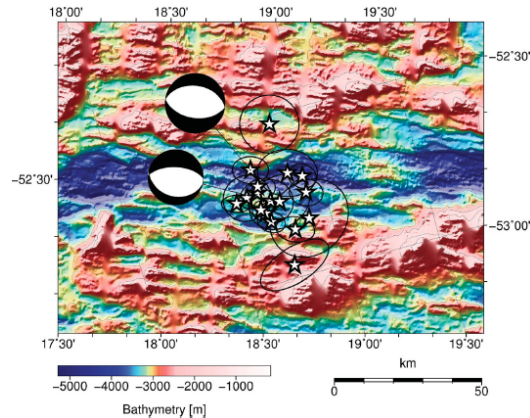


Figure 6.8 – Map of the central Orthogonal Supersegment with the relocated ISC events occurring during the four swarm periods. Focal mechanisms as in Fig. 6.3, bathymetry as in Fig. 6.4.

(e.g. South America and Southeast Asia; cf. Fig. 6.1 globe inset). In this direction, the theoretical P-wave radiation of normal faulting events at the western SWIR is low resulting in lower magnitudes which have an impact on the final magnitude reported by ISC.

With a different focal mechanism and fault orientation, the P-wave radiation pattern changes and the Neumayer array no longer lies in a direction of maximum P-wave radiation. Events with strike-slip focal mechanisms occur at Shaka FZ (FZW in Fig. 6.5c) and at Du Toit/Andrew Bain FZs (FZE in Fig. 6.5c). The magnitudes of these events display the best agreement between the ISC and VNA2 determinations and the smallest average discrepancy (black and grey crosses in Fig. 6.6 and red numbers in box).

Another possibility for the discrepancy of VNA2 and ISC magnitudes is a systematic error of the magnitude values of VNA2 as the array is located on an ice sheet of several hundred metres thickness covering the bedrock beneath. Such or other receiver site effects like underlying structural anomalies would enhance waves arriving from a narrow backazimuth and slowness band in the same way. However, the observed magnitude differences vary greatly for events with nearly the same propagation path, depending on which segment of the western SWIR the events occurred. Therefore, we conclude that the difference of VNA2 magnitudes for events with extensional focal mechanism is probably caused by the directional characteristics of extensional earthquakes emitting energy preferentially in the direction of the VNA2 array.

6.6.2 Teleseismic evidence of SWIR swarms

Due to the remoteness of mid-ocean ridges, studies of mid-ocean ridge seismicity often have to fall back on stations on-shore (cf. Schlindwein 2012). This lowers the detection

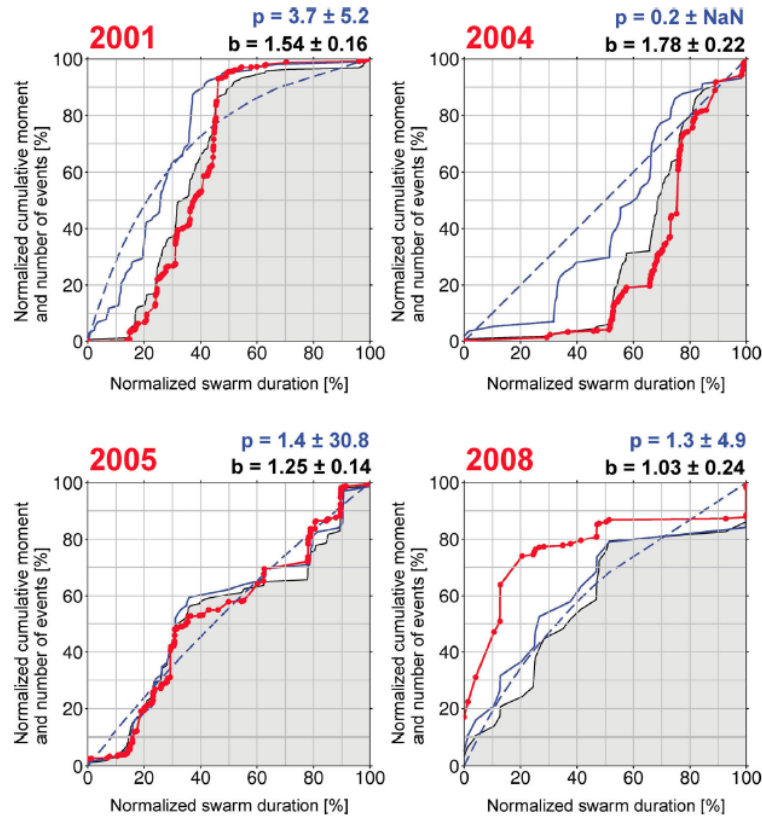


Figure 6.9 – Normalized cumulative moment release (red line with events marked by dots) and normalized cumulative number of events (black line with grey background) versus normalized swarm duration. Events above the magnitude of completeness of M 4.50 (blue solid line) and model (blue dashed line) show results of the Modified Omori Law. The p-value of the calculated model (blue) and the b-value (black) for each swarm is listed with its standard deviations.

capability and the amount of undetected events increases.

Local studies on mid-ocean ridges of intermediate- and fast spreading velocities (e.g. Juan de Fuca Ridge and East Pacific Rise) showed that accretion episodes coincide with swarms of low magnitudes (*Fox and Dziak, 1998*) but these swarms lack teleseismic events as the lithosphere at such ridges is thin and ductile. Hence, only local studies and AUH studies detect swarms and accretion events at these ridges (e.g. *Fox and Dziak, 1998; Dziak and Fox, 1999*). Another example is the dyking episode at Krafla volcano 1975-1984 in Iceland. It culminated in few single earthquakes with magnitudes of $m_b > 4$ (e.g. *Einarsson, 1991; Buck et al., 2006*). These earthquakes would not have been identified as a swarm at teleseismic distances. However, the swarm contained numerous earthquakes of m_b 3 – 3.5. A detection threshold of m_b 3.2 would have allowed to identify the swarm. Hence, we expected that the lowered detection threshold of the Neumayer array compared to the global station network would allow the identification of additional swarms at the Orthogonal Supersegment. Surprisingly, the regional data set of the VNA2 array does not

show any additional swarms which are teleseismically undetected (cf. Schlindwein 2012). Both the regional and the teleseismic data set show four swarms in the 8-yr survey period as high magnitude events occur during each swarm (Figs 6.5a and b).

The fact that swarms routinely generate high magnitude events of tectonic origin is probably due to the ultraslow spreading regime with a cold and brittle lithosphere. As a consequence, the teleseismic record is a useful tool to potentially detect earthquake swarms at ultraslow spreading ridges, whereas this is not possible at fast spreading ridges.

6.6.3 Evidence for magmatic accretion episodes witnessed by the VNA2 array

6.6.3.1 Swarm origin

Earthquake swarms are often generated during dyke intrusions in volcanic settings and consist of magmatically triggered events caused by cracking in the vicinity of the dyke tip (Bohnenstiehl and Dziak 2008). These are of magnitudes m_b 1 – 2 (Rubin and Gillard, 1998) and undetected over teleseismic distances. Their hypocentres/epicentres track the ascending magma and the propagating dyke tip (e.g. Bohnenstiehl and Dziak, 2008; Tarasewicz *et al.*, 2012). Rubin and Gillard (1998) estimate that during the 1983 Kilauea intrusion 85 per cent of all detected events have magnitudes m_b 1 – 2, whereas only 5 per cent have magnitudes m_b 2 – 3.

In contrast to these events, most earthquakes with a sufficiently high magnitude to be recorded teleseismically occur on pre-existing fault surfaces and are shear failures representing the tectonic reaction to the dyke emplacement (e.g. Dziak *et al.*, 2004; Bohnenstiehl and Dziak, 2008; Tarasewicz *et al.*, 2012). Hence, they are often labelled as tectonic events even though they are not part of a tectonic earthquake sequence.

In 2001, a major earthquake swarm was detected at the Lucky Strike segment of the Mid-Atlantic Ridge by teleseismic stations and a regional AUH array (Dziak *et al.*, 2004). An observed broad-band (>3 Hz) intrusion tremor suggested volcanic origin. Additionally, an unusually high number of teleseismic events for a dyking episode was also present and led to the suggestion that dyke emplacements at slow and ultraslow spreading ridges activate tectonic faults in the vicinity (Dziak *et al.*, 2004). Such swarms are commonly called tectonomagmatic swarms.

With a detection threshold of magnitude $m_b \sim 3.2$, the regional VNA2 data set records more earthquakes than the global station network with a detection threshold of $m_b \sim 3.6$. These events with magnitudes of $\sim m_b < 4$ represent most probably shear failures on top and ahead of the dyke (e.g. Rubin and Gillard, 1998). Events generated in other magmatic processes, such as fluid circulation processes detected on other mid-ocean ridges (Tolstoy *et al.*, 2008) and cracking at the dyke tip (Bohnenstiehl and Dziak, 2008) hav-

ing magnitudes of m_b 1 – 2 (*Rubin and Gillard, 1998*) may be present but below the detection threshold of the VNA2 array. The high magnitude events of magnitudes $\sim m_b > 4$ recorded over teleseismic distances are most probably tectonic earthquakes at pre-existing normal faults responding to the new stress regime caused by magma injection. A clear differentiation between events of shear failures at the dyke tip and high magnitude events occurring on normal faults is difficult and not possible, especially without the focal mechanisms of the events.

The moment release history shows the temporal distribution of low and high magnitude events during a swarm and allows an initial interpretation of the swarm origin. For our swarms, it is changing from the swarm of 2001 to 2008 (Fig. 6.9). Studies performed on swarms caused by dyke intrusions at an incipient seafloor-spreading segment at the Afar Rift found similar forms of moment release versus time plots (*Belachew et al., 2011*). The authors suggest that the different forms are influenced by the amount of tectonic or magmatic processes generating the swarms. Apparently, swarms with a staircase pattern similar to those of the swarms of 2001, 2004 and 2005 reflect a tectonomagmatic swarm origin. Swarms generated in a single process of purely magmatic or purely tectonic origin show strong moment releases at the beginning of the swarm with a strong decrease in the event rate (*Belachew et al., 2011*). We expect tectonic earthquakes to release large amounts of seismic moment as they are generated on normal fault planes in the brittle crust of the SWIR. Apart from short episodes of strong moment release, the swarms of 2001, 2004 and 2005 are dominated by events of moderate moment releases (Fig. 6.9). The swarm of 2008 differs markedly as it shows a predominance of events with large seismic moments of tectonic origin.

Apart from the swarm of 2008, all swarms showed high b-values of > 1.25 (Fig. 6.9) and clearly did not fit a Modified Omori Law. From these three evaluations, we conclude that the swarms show all the attributes of classical earthquake swarms and, even with tectonic normal faulting events present, they clearly show no main shock-aftershock distribution.

6.6.3.2 Swarm site - source site of active magmatism?

The relocalization of teleseismic earthquakes reported by ISC confirmed that the four swarms occurred in the same region of the Orthogonal Supersegment at $52^{\circ}36'S/18^{\circ}54'E$ (Fig. 6.8). The bathymetric data set shows abundant rift-parallel ridges at the rift valley walls. These ridges have a steeper side looking towards the rift valley and a side with a lower slope gradient oriented away of the rift valley. We assume that they are fault scarps of normal faults which are present all along the entire Orthogonal Supersegment (*Grindlay et al., 1998*). Hence, tectonic earthquakes can be expected to occur at these normal faults along the entire Orthogonal Supersegment. Contrary to this, the swarm activity is restricted to a narrow area at $52^{\circ}36'S/18^{\circ}54'E$ (Fig. 6.8). Thus, we argue that the repeated swarm events are triggered by magmatism focused in that area causing failure on the adjacent normal faults. At ultraslow spreading mid-ocean ridges, magmatic accre-

tion events is thought to be concentrated at discrete volcanic centres where magma pools, ascents and propagates laterally in the crust to the more distal parts of the segment (*Canat et al.*, 2003). At SWIR's Orthogonal Supersegment, individual volcanic centres are less obvious. These are typically characterized by MBA lows, topographic highs, off-axis elevated ridges perpendicular to spreading directions and locally high positive magnetic anomalies. At the Orthogonal Supersegment, magmatic anomalies are continuous with amplitudes of ~ 450 nT (*Maus*, 2009) and some elongated rift-parallel ridges on the rift valley floor are present. At Gakkel Ridge, the western volcanic zone (WVZ; 7°W - 3°E) has similarities to the Orthogonal Supersegment. There, elongated rift-parallel volcanic ridges with a length from 15 to 50 km indicate magmatic accretion style (*Michael et al.*, 2003). A continuous positive magnetic anomaly is present at the rift axis (*Jokat and Schmidt-Aursch*, 2007) and solely basalts were dredged (*Michael et al.*, 2003). Thus, the Orthogonal Supersegment bears affinities to the WVZ (cf. Schlindwein 2012), even if other features are absent.

However, *Grindlay et al.* (1998) identified a possible source site of magmatism at the Orthogonal Supersegment. Her accretionary segment 5 coincides with the location where the swarms occur. In the same region, an off-axis V-shaped ridge of potential volcanic origin indicates the presence of volcanic edifices. *Grindlay et al.* (1998) calculated the MBA from the observed free air gravity anomaly and negative values at the location of Grindlay's segment 5 indicate active volcanism. Hence, we conclude that a volcanic centre is present in this specific region and that the swarms are generated by magmatic accretion episodes.

The only site at ultraslow spreading ridges, where magmatism could convincingly be related to magmatic accretion episodes is Gakkel Ridge. There, magmatism is focused at axial volcanoes in the eastern volcanic zone (EVZ; 29°E - 85°E) where fresh basalts were dredged (*Michael et al.*, 2003). One of these axial volcanoes is the $85^{\circ}\text{N}/85^{\circ}\text{E}$ volcanic centre where a major teleseismically recorded swarm occurred in 1999 (*Mueller and Jokat*, 2000). This swarm could convincingly be attributed to a magmatic accretion episode by the observation of a hydrothermal event plume, fresh basalts, explosion sounds (*Schlindwein and Riedel* 2010 and references therein). The teleseismic earthquakes of this swarm are divided in three phases with different event rates and focal mechanisms and seem to be of tectonomagmatic origin (*Korger and Schlindwein*, 2012).

The swarms of SWIR's Orthogonal Supersegment are considerably smaller showing individual dyking episodes rather than a volcanic cycle, with durations comparable to other swarm episodes (Afar Rift; *Belachew et al.* 2011). The high magnitude events reflect the tectonic reaction to such accretion episodes, whereas the actual magma injection with a migration of the seismicity is not evident in the data set.

The absence of off-axis volcanic ridges parallel to the spreading direction indicates that the establishment of this potential volcanic centre of the Orthogonal Supersegment is geologically very young and that such centres at this segment of the SWIR are not persistent.

This assumption is supported by the suggestion of a migrating point-source of magmatism (*Grindlay et al.*, 1998) and the idea that mantle heterogeneities potentially influence where and how long volcanic centres are established (e.g. *Cannat et al.*, 2008).

6.7 Conclusion

In the regional data set of the Neumayer array, we found four swarm periods in 2001, 2004, 2005 and 2008 occurring at the Orthogonal Supersegment of the SWIR. With the relocalization of the teleseismically detected earthquakes, we confirmed that the swarms occurred repeatedly at a position of 52°36S/18°54E. The swarms are of tectonomagmatic origin with high angle normal faults reacting to the perturbed stress regime during/after dyke injection. We suggest a volcanic centre at this location causing the swarms during magmatic accretion episodes. Summing up three main points, we state:

(1) that the Neumayer seismological observatory has a favourable location to detect the seismicity of the western SWIR. It is positioned in the direction of maximal P-wave radiation of normal fault earthquakes in the study area. The regional data set lowers the detection threshold of ISC by $>0.5 m_b$.

(2) that all regionally detected swarms are also identified teleseismically, the swarm periods exceeding in both data sets 10 per cent of the variance of long-term background seismicity. The brittle lithosphere of an ultraslow spreading regime seems to be able to routinely generate high magnitude events uncommon for magmatic swarms at faster spreading ridges. Thus, the teleseismic record can be used as a valuable tool to detect spreading episodes at ultraslow spreading mid-ocean ridges.

(3) that the four swarms witness magmatic accretion episodes of tectonomagmatic origin at the Orthogonal Supersegment of the SWIR. The high magnitude tectonic events of the swarms are stress releases on the normal faults adapting to a new stress regime caused by magma emplacement or dyke injection, restricted to this area. We assume a volcanic centre to exist at this location possibly migrating eastward as indicated by a negative MBA gravity anomaly.

6.8 Acknowledgements

We thank N.R. Grindlay for the high-resolution bathymetry grid. The manuscript greatly benefited from helpful comments of editor I. Grevemeyer and the reviewers R. Sohn and D. Sauter. This study was funded by the Emmy-Noether Program of the DFG under grant Schl. 853/1-1. Figures were created using the public domain GMT software (*Wessel and Smith*, 1998).

6.9 Literature

- Belachew, M., C. Ebinger, D. Coté, D. Keir, J. Rowland, J. Hammond, and A. Ayele (2011), Comparison of dike intrusions in an incipient seafloor-spreading segment in Afar, Ethiopia: Seismicity perspectives, *J. geophys. Res.*, *116*(B06405), 23 PP., doi: 10.1029/2010JB007908.
- Bohnenstiehl, D., and R. Dziak (2008), Mid-ocean ridge seismicity, in *Encyclopedia of Ocean Sciences*, edited by J. Steele, S. Thorpe, and K. Turekian, p. 15, Academic Press, London, First online update.
- Buck, W., P. Einarsson, and B. Brandsdóttir (2006), Tectonic stress and magma chamber size as controls on dike propagation: Constraints from the 1975-1984 krafla rifting episode, *J. geophys. Res.*, *111*(B12404), doi: 10.1029/2005JB003879.
- Cannat, M., C. Romevaux-Jestin, and H. Fujimoto (2003), Melt supply variations to a magma-poor ultra-slow spreading ridge (Southwest Indian Ridge 61° to 69°E), *Geochem. Geophys. Geosys.*, *4*(9104), doi: 10.1029/2002GC000480.
- Cannat, M., D. Sauter, A. Bezos, C. Meyzen, E. Humler, and M. L. Rigoleur (2008), Spreading rate, spreading obliquity, and melt supply at the ultraslow spreading Southwest Indian Ridge, *Geochem. Geophys. Geosys.*, *9*(Q04002), doi: 10.1029/2007GC001676.
- Dick, H. J., J. Lin, and H. Schouten (2003), An ultraslow-spreading class of ocean ridge, *Nature*, *426*, 405–412, doi: 10.1038/nature02128.
- Dziak, R. P., and C. G. Fox (1999), The January 1998 earthquake swarm at Axial Volcano, Juan de Fuca Ridge: hydroacoustic evidence of seafloor volcanic activity, *Geophys. Res. Lett.*, *26*(23), 3429–3432, doi: 10.1029/1999GL002332.
- Dziak, R. P., D. K. Smith, D. R. Bohnenstiehl, C. G. Fox, D. Desbruyeres, H. Matsumoto, M. Tolstoy, and D. J. Fornari (2004), Evidence of a recent magma dike intrusion at the slow spreading Lucky Strike segment, Mid-Atlantic Ridge, *J. geophys. Res.*, *109*(B12102), doi: 10.1029/2004JB003141.
- Einarsson, P. (1991), Earthquakes and present-day tectonism in Iceland, *Tectonophysics*, *189*, 261–279, doi: 10.1016/0040-1951(91)90501-I.
- Ekström, G., A. Dziewonski, N. Maternovskaya, and M. Nettles (2005), Global seismicity of 2003: Centroid-moment-tensor solutions for 1087 earthquakes, *Earth and Planetary Inter.*, *148*, 327–351, doi: 10.1016/j.pepi.2004.09.006.
- Fitch, T. (1975), Compressional velocity in source regions of deep earthquakes: an application of the master event technique, *Earth planet. Sci. Lett.*, *26*(2), 156–166, doi: 10.1016/0012-821X(75)90083-7.

- Fox, C., and R. Dziak (1998), Hydroacoustic detection of volcanic activity on the Gorda Ridge, February-March 1996, *Deep-Sea Res.*, *45*(12), 2513–2530, doi: 10.1016/S0967-0645(98)00081-2.
- Grindlay, N., J. Madsen, C. Rommevaux-Jestin, and J. Sclater (1998), A different pattern of ridge segmentation and mantle Bouguer gravity anomalies along the ultra-slow spreading Southwest Indian Ridge (15°30'E to 25°E), *Earth planet. Sci. Lett.*, *161*, 243–253.
- Gutenberg, B., and C. Richter (1956), Magnitude and energy of earthquakes, *Ann. Geophys.*, *53*, 7–12.
- Humphreys, E., and R. Clayton (1988), Adaption of back projection tomography to seismic travel time problems, *J. geophys. Res.*, pp. 1073–1085.
- Husen, S., E. Kissling, N. Deichmann, S. Wiemer, D. Giardini, and M. Baer (2003), Probabilistic earthquake location in complex three-dimensional velocity models: Application to Switzerland, *J. geophys. Res.*, doi: 10.1029/2002JB001778.
- Iyer, H. (1971), Variation of apparent velocity of teleseismic P Waves across the large-aperture seismic array, Montana, *J. geophys. Res.*, *76*, 8554–8567.
- Jokat, W., and M. Schmidt-Aursch (2007), Geophysical characteristics of the ultraslow spreading Gakkel Ridge, Arctic Ocean, *Geophys. J. Int.*, *168*, doi: 10.1111/j.1365-246X.2006.03278.x.
- Kanamori, H. (1977), The energy release of earthquakes, *J. geophys. Res.*, *82*, 2981–2987.
- Kennett, B. (1992), Locating oceanic earthquakes: the influence of regional models and location criteria, *Geophys. J. Int.*, *188*(2), 848–854.
- Kissling, E., W. Ellsworth, D. Eberhart-Phillips, and U. Kradorfler (1994), Initial reference models in local earthquake tomography, *J. geophys. Res.*, *99*(B10), doi: 10.1029/93JB03138.
- Korger, E. I. M., and V. Schlindwein (2012), Performance of localisation algorithms for teleseismic mid-ocean ridge earthquakes: The 1999 Gakkel ridge earthquake swarm and its geological interpretation, *Geophys. J. Int.*, *188*(2), doi: 10.1111/j.1365-246X.2011.05282.x.
- Läderach, C., and V. Schlindwein (2011), Seismic arrays on drifting ice floes: experiences from four deployments in the Arctic Ocean, *Seismological Research Letters*, *82*(4), 488–497, doi: 10.1785/gssrl.82.4.494.
- Läderach, C., V. Schlindwein, H.-W. Schenke, and W. Jokat (2011), Seismicity and active tectonic processes in the ultra-slow spreading Lena Trough, Arctic Ocean, *Geophys. J. Int.*, *184*(3), doi: 10.1111/j.1365-246X.2010.04926.x.
- Magde, L., A. Barclay, D. Toomey, R. Detrick, and J. Collins (2000), Crustal magma plumb-

- ing within a segment of the Mid-Atlantic Ridge, 35°N, *Earth Planet. Sci. Lett.*, 175, doi: 10.1016/S0012-821X(99)00281-2.
- Maus, S. (2009), EMAG2: A 2-arc min resolution earth magnetic anomaly grid compiled from satellite, airborne, and marine magnetic measurements, *Geochem. Geophys. Geosys.*, 10(8), doi: 10.1029/2009GC002471.
- McNutt, S. (1996), Seismic Monitoring and Eruption Forecasting of Volcanoes: A Review of the State of the Art and Case Histories, in *Monitoring and Mitigation of Volcano Hazards*, edited by R. Scarpa and R. Tilling, pp. 99–146, Springer-Verlag, Berlin.
- Michael, P., et al. (2003), Magmatic and amagmatic seafloor generation at the ultraslow-spreading Gakkel ridge, Arctic Ocean, *Nature*, 423, 956–961, doi: 10.1038/nature01704.
- Mogi, K. (1963), Some Discussion on Aftershocks, Foreshocks and Earthquake Swarms - the Fracture of a Semi-infinite Body Caused by an Inner Stress Origin and Its Relation to the Earthquake Phenomena, *Bulletin of the Earthquake Research Institute*, 41, 615–658.
- Mueller, C., and W. Jokat (2000), Seismic Evidence for Volcanic Activity Discovered in Central Arctic, *Eos, Trans. Am. geophys. Un.*, 81(24), 265–269, doi: 10.1029/00EO00186.
- Rawlinson, N., M. de Kool, and M. Sambridge (2006), Seismic wavefront tracking in 3D heterogeneous media: applications with multiple data classes, *Exploration Geophysics*, 37, doi: 10.1071/EG06322.
- Rubin, A. M., and D. Gillard (1998), Dike-induced earthquakes: theoretical considerations, *J. geophys. Res.*, 103(B5), 10,017–10,030.
- Schweitzer, J. (2001), HYPOSAT - an enhanced routine to locate seismic events, *Pure applied Geophysics*, 158, 277–289.
- Schweitzer, J., J. Fyen, S. Mykkeltveit, and T. Kvaerna (2009), xxx, in *New Manual of Seismological Observatory Practice*, p. 52, GFZ, Potsdam.
- Scordilis, E. (2006), Empirical global relations converting m_s and m_b to moment magnitude, *Journal of Seismology*, 10, 225–236.
- Simao, N., J. Escartin, J. Haxel, M. Cannat, and R. Dziak (2010), Regional seismicity of the Mid-Atlantic Ridge: observations from autonomous hydrophone arrays, *Geophys. J. Int.*, 183, 1559–1578, doi: 10.1111/j.1365-246X.2010.04815.x.
- Smith, D., M. Tolstoy, C. Fox, D. Bohnenstiehl, H. Matsumoto, and M. Fowler (2002), Hydroacoustic monitoring of seismicity at the slow-spreading Mid-Atlantic Ridge, *Geophys. Res. Lett.*, 29, doi: 10.1029/2001GL013912.

- Smith, W., and D. Sandwell (1997), Global seafloor topography from satellite altimetry and ship depth soundings, *Science*, *277*, 1956–1962.
- Sohn, R. A., and J. Hildebrand (2001), Hydroacoustic earthquake detection in the Arctic Basin with the Spinnaker Array, *Bull. seism. Soc. Am.*, *91*(3), 572–579.
- Spakman, W., and G. Nolet (1988), Imaging algorithms, accuracy and resolution in delay time tomography, in *Mathematical Geophysics*, pp. 155–187, Springer Netherlands.
- Tarasewicz, J., B. Brandsdóttir, R. White, M. Hensch, and B. Thorbjarnardóttir (2012), Using microearthquakes to track repeated magma intrusions between the Eyjafjallajökull stratovolcano, Iceland, *J. geophys. Res.*, *117*, doi: 10.1029/2011JB008751.
- Tolstoy, M., A. Harding, and J. Orcutt (1993), Crustal thickness on the Mid-Atlantic Ridge: bull’s-eye gravity anomalies and focused accretion, *Science*, *262*, 726–729.
- Tolstoy, M., F. Waldhauser, D. Bohnenstiehl, R. Weekly, and W.-Y. Kim (2008), Seismic identification of along-axis hydrothermal flow on the East Pacific Rise, *Nature*, *451*, 181–185, doi: 10.1038/nature06424.
- Utsu, T., Y. Ogata, and R. S. Matsu’ura (1995), The Centenary of the Omori Formula for a Decay Law of Aftershock Activity, *J. Phys. Earth*, *43*, 1–33.
- Wessel, P., and W. Smith (1998), New, improved version of generic mapping tools released, *Eos, Trans. Am. geophys. Un.*, *79*, 579.
- Woessner, J., and S. Wiemer (2005), Assessing the quality of earthquake catalogues: estimating the magnitude of completeness and its uncertainty, *Bull. seism. Soc. Am.*, *95*, 684–698.

7 Third paper: Seismicity and structure of the 85°E volcanic complex

7.1 Summary

Accretion mechanisms at ultraslow spreading ridges are still only poorly understood due to difficult survey conditions for seismic experiments at these ridges. Melts gets focused by distinct magmatic centres, with thin crust in between.

At the 85°E/85°N volcanic complex at Gakkel ridge, Arctic Ocean, where a recent spreading episode has been observed, perennial sea ice cover challenges traditional survey investigations of seismic structure and microseismicity. We used an unusual survey set-up to gather seismological data during 16 days in July 2007, using seismometer arrays mounted on ice floes. Despite only 12 stations, the drift of the ice floes over the survey area resulted in a multitude of crossing rays in the rift valley.

The data included 303 microearthquakes of which 248 events could be confidently located. We compiled a 1D velocity model by localizing a subset of these earthquakes with a suite of randomly created velocity models. In this model, the Moho is placed at 7 km depth below seafloor, inferring a thick, basaltic crust. Using 124 events which were recorded by at least two arrays, we inverted for P-wave velocity structure in a local earthquake tomography. Resolution tests indicate reliable results in the central rift valley, illuminating thermal structure underneath Asgard volcanic chain in the aftermath of its most recent spreading episode.

Our results show microearthquake activity down to 16 km beneath seafloor, inferring a cold lithosphere. Most hypocentres cluster at the centre of the rift valley at the site the Asgard volcanic chain. This may mean that existing thermal models for this class of ridges have to be refined. An area of decreased seismic velocities crosses the rift valley at this location, microearthquake activity is located at the eastern fringe where the velocity gradient is highest. We therefore speculate that the reduced velocities may be caused by warm intruded material and that the observed seismicity predominately reflects the relaxation of thermal stresses following recent intrusion.

7.2 Introduction

Among the 80,000 km long global network of mid-ocean ridges, ultraslow spreading ridges are classified as opening with less than 20 mm/yr full spreading rate (*Dick et al.*, 2003).

They are characterized by a unique rift morphology, which sets them apart from faster spreading ridges, featuring magmatic and amagmatic segments with very different morphological and geological characteristics. Yet, far less is known about how these ridges work compared to faster spreading ridges. This is due in no small part to difficult survey conditions, which severely inhibit traditional surveys for seismicity and crustal structure with ocean bottom seismometers and/or ship-towed seismic receivers. In the case of the Southwest Indian ridge which separates Antarctica and Africa, difficult weather conditions and large wave heights challenge such surveys, whereas Gakkel ridge in the Arctic Ocean (Fig. 7.1a) is perennially covered by sea ice. This poorly accessible area calls for unusual seismic survey methods (Jokat *et al.*, 2003; Schlindwein *et al.*, 2007; Läderach and Schlindwein, 2011). In this paper we describe results of a microseismicity survey with seismometers on ice floes drifting over a volcanic centre at eastern Gakkel Ridge.

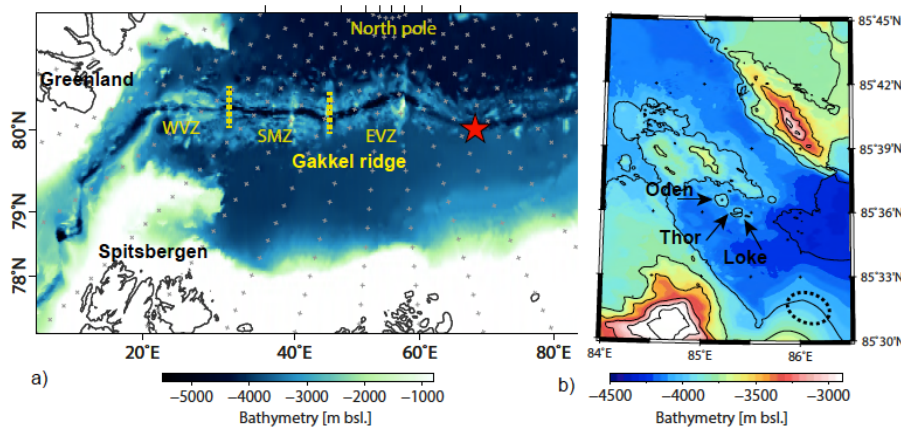


Figure 7.1 – (a) Overview of Gakkel ridge with IBCAO2 bathymetry (Jakobsson *et al.*, 2008). The 85°E/85°N volcanic complex is marked by the red star. Abbreviations are as follows: WVZ: Western Volcanic Zone, SMZ: Sparsely Magmatic Zone, EVZ: Eastern Volcanic Zone. (b) Close-up on the 85°E/85°N volcanic centre. Composite bathymetry of IBCAO2 (Jakobsson *et al.*, 2008), bathymetric grid collected by the AMORE 2001 expedition (Michael *et al.*, 2003) and the high definition bathymetric grid of AGAVE 2007 (Pontbriand *et al.*, 2012). The location of Oden, Thor and Loke volcanoes are marked by arrows. The source region of the seismoacoustic signals (Schlindwein and Riedel, 2010) which were recorded by the pilot experiment of ice floe based seismometers of the AMORE 2001 expedition is encircled by a dotted line.

At the eastern end of Gakkel ridge, the Eastern Volcanic Zone (EVZ) is a magmatically robust segment, with discrete magmatic centres, which are thought to focus melts (Michael *et al.*, 2003). In between these magmatic centres the crust is thought to be unevenly thick, depending on the distance to the magmatic centre (Jokat and Schmidt-Aursch, 2007). The 85°E/85°N volcanic complex (Fig. 7.1b) is a distinguished volcanic centre at a spreading rate of about 10 mm/yr (Sella *et al.*, 2002). It has first come to prominence in 1999, when as a teleseismic earthquake swarm at this location was discovered to be unusually long in duration and magnitude, signing the onset of a spreading episode (Mueller and Jokat, 2000; Tolstoy *et al.*, 2001; Riedel and Schlindwein, 2010; Korger and Schlindwein,

2012) and going along with explosive submarine volcanism of at least two years duration (*Sohn et al.*, 2008; *Schindwein and Riedel*, 2010).

In 2001, the AMORE expedition investigated the area, dredging almost exclusively basalt (*Michael et al.*, 2003) and finding a hydrothermal megaplume within the rift valley (*Edmonds et al.*, 2003; *Baker et al.*, 2004). Making use of the sea ice, a pilot survey was done using seismometers mounted on an ice floe. Even if only one ice floe drifted 11 days about 35 km northwest of the volcanic centre, this array (4 seismometers) recorded 59 shallow local and regional events which were mostly located between rift valley and array (*Schindwein et al.*, 2007). Additionally, a swarm of seismoacoustic signals has been interpreted to stem from an ongoing submarine eruption (*Schindwein et al.*, 2005; *Schindwein and Riedel*, 2010).

The AGAVE expedition returned to the area in 2007. It imaged fresh and weathered lavas on the seafloor and sampled rocks and pyroclastic material, which covered the rift valley (*Sohn et al.*, 2008; *Pontbriand et al.*, 2012). In addition, it investigated hydrothermal activity (*Stranne et al.*, 2010) mainly located at the site of axis-parallel lineaments in the middle of the rift valley, which host a chain of volcanic cones named Oden, Thor and Loke (Fig. 7.1b). The vast occurrence of pyroclastic deposits stemming from deep submarine explosive volcanism raised the question how significant amounts of gas can accumulate to drive explosive eruptions at water depths in excess of 3.6 km depth. Long repose intervals between eruptions, but also a crust and upper mantle structure that allow to retain gas at depth may be pre-requisites more easily met at ultraslow spreading ridges than elsewhere (*Sohn et al.*, 2008). Detailed three dimensional studies of the crustal and upper mantle structure of ultraslow spreading ridges, in particular their volcanic centres are therefore urgently needed but difficult to accomplish in these remote areas.

Building on the success of the first pilot survey with ice floe based seismometers, *Schindwein and Linder* (2007) instrumented three ice floes each with an array of four seismometers, letting them drift over the 85°E volcanic complex. During the 16 days of this survey, the arrays were recovered and redeployed two times, when the ice floes drifted out of the survey area (Fig. 7.2a). Assuming that there was seismicity to be recorded at and around the volcanic centre, this unique method would not only make it possible to locate microearthquakes with good accuracy, it would potentially ensure sufficient ray coverage to do a seismic tomography - the first to be done at an ultraslow spreading ridge. We report here on the results of this microseismicity survey and present P-wave tomographic images of the volcanic centre, interpreting the results in the context of ultraslow-spreading ridges.

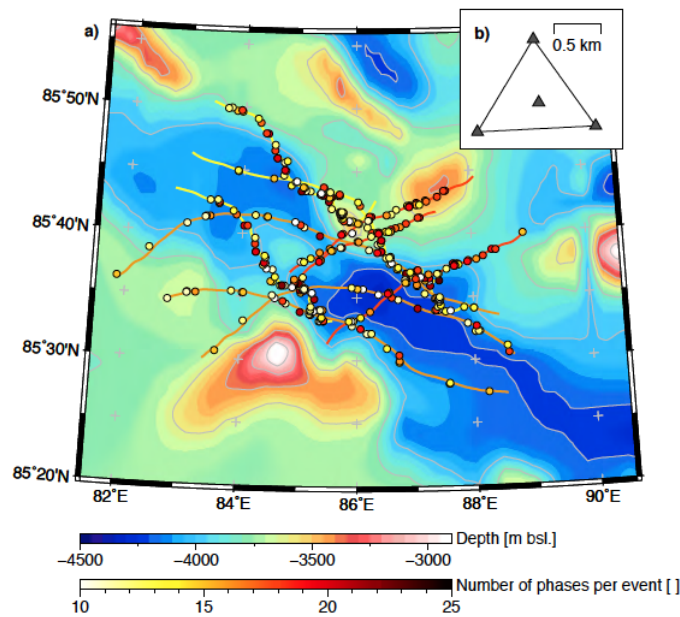


Figure 7.2 – (a) Survey region of the 85°E/85°N volcanic complex with IBCAO2 bathymetry (*Jakobsson et al.*, 2008) and contour spacing of 200 m. Yellow, orange and red lines mark the driftpaths of the ice floes of three consecutive deployments. Coloured circles denote number of picked phases of each earthquake, plotted at the location of each central array station at the corresponding source time. (b) Close-up on an example seismometer array. Triangles show seismometer locations.

7.3 Dataset and methods

7.3.1 Local earthquake dataset

Between 15th and 31st July 2007, the Arctic Gakkel Vents (AGAVE) expedition onboard the icebreaker I/B Oden carried out a microseismicity survey with seismometers installed on ice floes drifting over the rift valley at 85°E/85°N Gakkel ridge. Three small-aperture arrays with four seismometers each (Mark L-4C3D three-component; short-period; 100 Hz sample rate) were deployed on three separate ice floes. Each array consisted of a central seismometer and three seismometers arranged in a rough triangle of about 1 km side length (Fig. 7.2b). Earning to currents, wind and tide, the ice floes drifted over the survey area. When they drifted too far away from the rift valley, they were redeployed on different ice floes (Fig. 7.2a). All stations included a GPS receiver, which logged the position every 60 min. A pilot study for this type of survey (*Schlindwein et al.*, 2007) found that the error in array positioning does not contribute significantly to errors in earthquake epicentre location.

All 12 seismometer yielded continuous seismic records including ice-generated noise and

local earthquakes. Due to an increased noise level when the ship was in motion (*Läderach et al.*, 2011), we used data only from the time when the ship was stationary, unless earthquake signals were very clear (Fig. 7.3). We identified earthquakes by visual inspection selecting events with larger signals on the vertical components of all four seismometers of an array. Icequakes produced larger signals on the horizontal component and were excluded from further study. All earthquakes were picked by hand on the vertical components, bandpass filtered with 8 – 25 Hz. We picked first (P phase) and second arrivals (SP phase) of a total of 303 events.

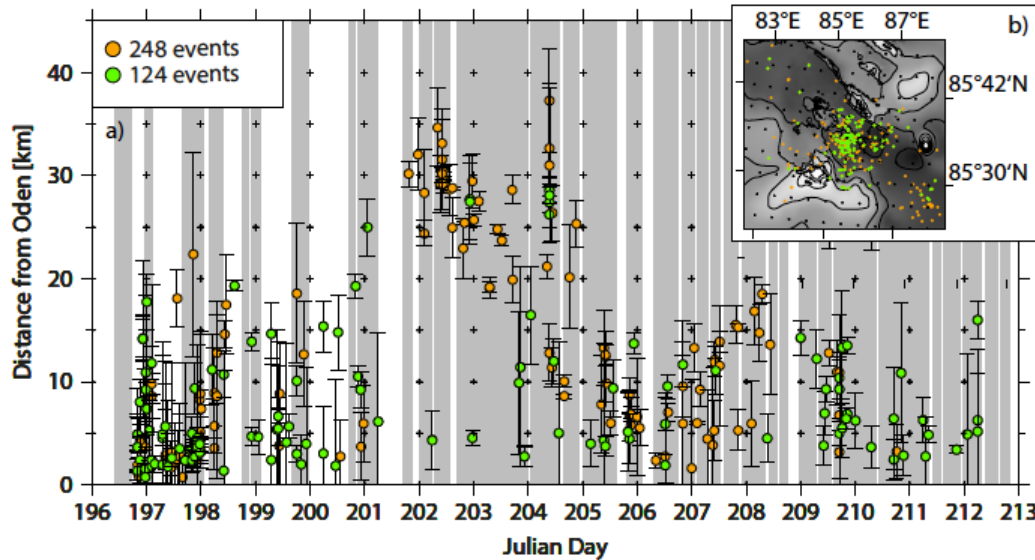


Figure 7.3 – (a) Distance of HYPOSAT located epicentres of the locatable dataset (orange circles, 248 events) and the relocated epicentres of 124 events used in tomographic inversion (green circles) to Oden volcano. Error bars denote HYPOSAT semi-major error ellipse axis length, but the direction of the error bars does not necessarily give the azimuth of the error ellipse. (b) Inset shows epicentres of both datasets, plotted on a composite grid of IBCAO2 (*Jakobsen et al.*, 2008) and the high definition bathymetry collected by the AGAVE 2007 expedition (*Pontbriand et al.*, 2012) with contour spacing of 250 m.

7.3.2 Reference velocity model and starting hypocentres for tomographic inversion

Grid-based seismic tomography involves finding solutions for velocity structure relative to a reference velocity model (e.g. *Kissling et al.*, 1994; *Rawlinson et al.*, 2006).

We started with constructing a 1D velocity model, using a subset of 44 well-defined earthquakes (observations on all arrays, at least 3 stations per array recorded phases), using a suite of 95 randomly created 3-layered velocity models (Fig. 7.4). We included a surface layer of unconsolidated material (thickness: 0.5 – 3.5 km; P-wave velocity range

at top: 2.5 – 4.5 km/s; P-wave velocity range at bottom: 3.5 – 5.0 km/s), a basaltic layer (thickness: 4.0 – 14 km; P-wave velocity range at top: 3.5 – 5.0 km/s; P-wave velocity range above the Moho: 6.2 – 7.2 km/s) and a mantle layer down to 40 km depth (P-wave velocity below the Moho: 7.4 km/s; P-wave velocity at 40 km depth: 8.1 km/s). Corresponding S-wave velocities were calculated using a ratio of P- to S-wave velocity of 1.73. Only models with an increasing velocity gradient were allowed.

Prior to earthquake localization, we had to compensate for the varying thickness of the water layer underneath the individual arrays by correcting the traveltimes under the assumption of vertical ray incidence to a reference horizon below sea level of 3,900 m. As correction velocities we used $v_P = 4.0$ km/s and $v_S = 2.31$ km/s as well as a water velocity of 1.5 km/s, respectively. *Läderach et al.* (2011) showed that the assumption of vertical ray incidence does not result in traveltime errors greater than the error inherent in pick uncertainties and misestimates the water depth by about 230 m which is less than the misestimation of water depth by the 1.85 km grid spacing of the IBCAO2 (*Jakobsson et al.*, 2008) bathymetry. We then localized our subset of 44 earthquakes with each of the 95 velocity models both with a fixed starting depth of 10 km and a free depth using the linear least-squares algorithm HYPOSAT (*Schweitzer*, 2001). Solutions with a root mean square (RMS) of more than 0.2 s and a length of the semi-major axis of the error ellipse (Smaj) greater than 10 km were discarded. Among the remaining solutions, we preferred the free depth solution to the fixed depth solution only if the error in hypocentre depth was smaller than 3 km, the RMS got smaller, and the number of phases used in localization got greater compared to the fixed depth solution.

We then averaged the RMS, number of phases and Smaj of all located events for each individual velocity model, and compared these values among the 95 velocity models. We selected the best velocity model based on the best possible combination of a small Smaj, a large number of phases used in localization, a small RMS, and a high number of locatable events.

Fig. 7.4 (blue line) shows the resulting velocity model among the 95 tested models. It includes a rapid velocity increase down to a Moho depth of 7 km below seafloor. We then located all 303 picked events with this 1D velocity model. 248 events had an Smaj of less than 10 km and a RMS less than 0.2 s (Fig. 7.3b). Of these, 128 events with a total of 1105 P- and 716 S-wave phases were recorded by at least two arrays and were subsequently used as our dataset for tomographic inversion.

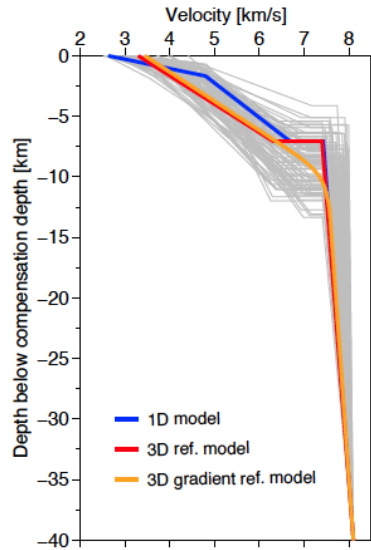


Figure 7.4 – Suite of 95 randomly created velocity models in gray. Specially indicated are the 1D velocity model (blue), the 3D reference velocity model including a Moho discontinuity (red), and the 3D gradient reference velocity model (orange). Depth is specified starting from compensation depth at 3,900 m.

7.3.3 3D Seismic traveltimes tomography

We used the iterative, non-linear 3D traveltimes tomography algorithm FMTOMO (*Rawlinson et al., 2006*). For our special problem with receivers above a water layer with strongly varying thickness, FMTOMO’s ability to incorporate the 3D bathymetry as the first interface is crucial, as well as the possibility to exclude this interface and the velocity of the water layer above from inversion. FMTOMO can simultaneously or individually invert for source location, velocity of individual layers and individual interfaces and it can deal with a multitude of receiver coordinates. However, it can only separately invert for P- and for S-wave velocity.

To describe the model volume in FMTOMO, two distinct grids are used: The propagation grid discretely samples the velocity field and is used for wavefront tracking by a grid-based eikonal solver. The inversion grid represents the velocity continuum and continuous interface surfaces. It is described by cubic B-spline functions, which are in turn defined by the regular grid of velocity and interface control nodes. Each velocity layer spans the entire model volume, but only appropriate nodes are activated. The horizontal spacing of interface grid nodes has to be the same for all interfaces, but velocity layer grid spacing can be defined individually.

For forward traveltimes prediction, FMTOMO uses a grid-based eikonal solver, the fast marching method (FMM) (*Sethian, 1996; Sethian and Popovici, 1999*) in 3D. Inversion is done by a subspace inversion scheme (*Kennett et al., 1988; Rawlinson and Sambridge, 2003*), which minimizes an objective function

$$S(\mathbf{m}) = \frac{1}{2}[(\mathbf{g}(\mathbf{m}) - \mathbf{d}_{obs})^T \mathbf{C}_d^{-1}(\mathbf{g}(\mathbf{m}) - \mathbf{d}_{obs}) + \epsilon\Phi(\mathbf{m}) + \mu\Omega(\mathbf{m})] \quad (7.3.1)$$

where \mathbf{m} is the vector of unknown model parameters which is adjusted during the inversion, $\mathbf{g}(\mathbf{m})$ represents the traveltimes predictions associated with a model, \mathbf{d}_{obs} the observed traveltimes, and \mathbf{C}_d the data covariance matrix (*Rawlinson and Kennett, 2008*). ϵ and μ are the damping and smoothing operators, respectively. $\Phi(\mathbf{m})$ encourages models to stay similar to the reference model and $\Omega(\mathbf{m})$ attempts to satisfy the observational traveltimes with a minimum amount of structural variation. FMTOMO iteratively applies FMM and the subspace inversion (*Rawlinson and Sambridge, 2003*), updating the traveltimes each time FMM is run.

7.3.3.1 3D Reference model

The ice floes drifted over a region of about 76×66 km. We defined the model region from 81.5°E to 90.56°E and 85.33°N to 85.93°N as it had to extend to all possible receiver and source locations (Fig. 7.2a). Due to coarse depth parameterization (see cpt. 7.3.3.2) we simplified the 1D velocity model (Fig. 7.4, blue line) to include a fixed water layer with the velocity of water 1.5 km/s from sea level down to the variable bathymetry. We solved the problem of SP converted phases travelling through the water layer by assigning the S-velocity model a velocity of 1.5 km/s in the water layer (c.f. *Läderach et al., 2011*). Below, a crustal layer extends from the seafloor down to the Moho at 7 km below sea floor ($v_P = 3.3$ km/s to 6.3 km/s) and a mantle layer down to 40 km depth bsl. ($v_P = 7.4$ km/s to 8.1 km/s) in the 3D P- and S-wave reference velocity models. We then incorporated the 3D bathymetry as a fixed interface, resampling the pertaining region of the IBCAO2 bathymetry (Fig. 7.2a) (*Jakobsson et al., 2008*) with a grid-spacing of 100 m, which corresponds to 766×667 horizontal nodes.

7.3.3.2 Source relocation and grid parametrization

We used the original traveltimes because the 3D representation of the water layer no longer requires a correction to a compensation depth. We then relocated all 128 earthquakes in the 3D reference model, using the HYPOSAT-obtained hypocentres as starting locations.

For this relocation we parameterized the propagation grid with a fine grid spacing of 0.27 km in latitude, 0.33 km in longitude and 0.25 km in depth to be sure to approximate the real ray paths as closely as possible. FMTOMO additionally subdivides the propagation grid cells directly around and including the source cell to account for the high curvature

of the wavefront in the vicinity of the source. The velocity grid was parameterized with a node spacing of 0.56 km in latitude, 0.66 km in longitude and 0.51 km in depth. After re-localization we corrected the picked traveltimes with the source origin time perturbations. Subsequently we only inverted for P-wave velocity structure, using these new hypocentres and traveltimes.

Model parametrization in seismic tomography must account for a priori knowledge of the earth's structure and the resolution capability of the available data set (*Kissling et al.*, 2001). To find the optimal parameterization of the propagation and velocity grids, we inverted our dataset for P-wave velocity variation with 10 different combinations of node numbers in the propagation and velocity grids, respectively, and compared the overall RMS traveltime residual after 4 iterations for each combination (Tbl. 7.1). A propagation grid with $81 \times 121 \times 121$ nodes (depth x latitude x longitude) combined with a velocity grid with $20 \times 30 \times 30$ cells yielded the best results. This corresponds to a velocity grid spacing of 2.3 km in latitude, 2.7 km in longitude and 2.1 km in depth (Fig. 5).

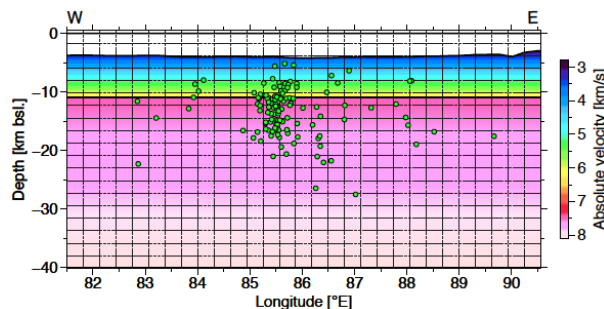


Figure 7.5 – EW slice through the modelled region, showing absolute velocities of 3D reference velocity model (c.f. Fig. 7.4, red line). Green circles show earthquakes after relocation. Dotted grey lines depict cell boundaries for the chosen velocity grid spacing.

Propagation Grid Number of cells in z-lat-lon	Velocity Grid Number of cells in z-lat-lon	RMS [ms]
61-91-91	20-30-30	127.11
81-121-121	20-30-30	125.81
31-46-46	30-45-45	129.96
61-91-91	30-45-45	127.66
91-136-136	30-45-45	126.04
121-181-181	30-45-45	125.91
81-121-121	40-60-60	127.12
121-181-181	40-60-60	126.65
81-121-121	80-120-120	130.19

Table 7.1 – Overall traveltime residual RMS after velocity inversion of each combination of grid cells in depth x latitude x longitude of propagation grid and velocity grid.

7.3.3.3 Model regularization

Model regularization handles the underdetermined parts of the inversion problem and hence is strongly dependent on the number of rays crossing individual inversion cells, and hence on model parameterization and the appropriateness of ray approximation (*Kissling et al.*, 2001). Used correctly, it can reduce model errors and increase solution stability, yet incorrect choice of parameters can result in unrealistic model perturbations as structural artefacts (e.g. *Husen et al.*, 2003)

Our approach in finding optimal damping and smoothing parameters was to test different combinations of parameters, covering a range of values between 0.01 to 10 for damping and 0 to 50 for smoothing, while inverting solely for P-wave velocity. For the resulting velocity models we calculated model roughness and model perturbation and compared with the overall RMS traveltimes residuals (Fig. 7.6). We selected the combination of damping and smoothing values which produced the model with the lowest possible traveltimes residual RMS in combination with the lowest model perturbation and lowest model roughness, indicating the simplest model to fit the data.

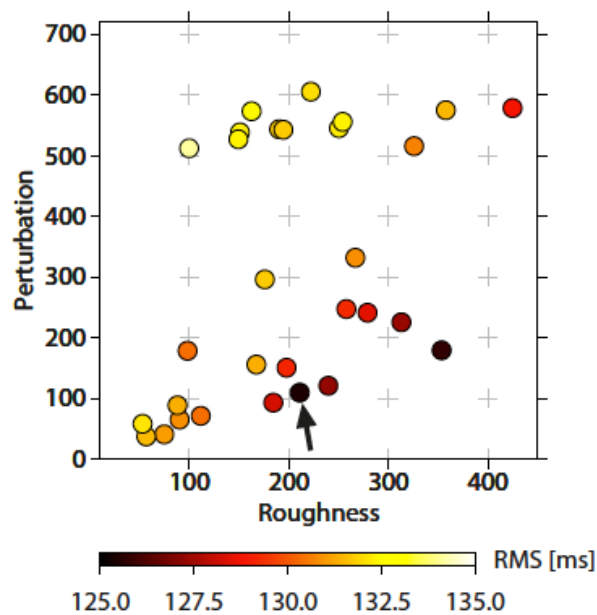


Figure 7.6 – Model perturbation and model roughness for the tested combination of damping and smoothing values. The color gives the corresponding overall traveltimes residual RMS. Best model (arrow) has low RMS while still being smooth.

7.4 Results

The P-wave velocity inversion based on the layered 3D reference velocity model reduces the data misfit variance to $0.016 s^2$, and the RMS of the traveltimes residual from 133.58 ms to 127.28 ms.

To test if the distribution of sources influences the tomography result, we subdivided our 128 events into three sub-datasets while eliminating every third event, effectively using for each sub-dataset only two thirds of the data. After P-wave velocity inversion of all three sub-datasets, we found that the source distribution does not alter the resulting model significantly, mainly influencing the fringe of the model region where only a scattering of rays constrains the result. After visual inspection, we eliminated 4 earthquakes from the full dataset, which we suspected of causing unrealistic velocity structures, retaining 124 events as our new dataset.

The P-wave velocity inversion based on the new dataset (124 events) further reduced the RMS of the traveltimes residual to 117.78 ms and the data misfit variance to $0.014 s^2$. The resultant P-wave velocity model still shows a pronounced contrast of increased velocities directly above the Moho to reduced velocities directly beneath the Moho (Fig. 7a, km 30 – 50). This may indicate that our 3D reference model overestimates the velocity contrast at the Moho. We therefore modified the 3D reference velocity model and included a gradual velocity increase instead of a velocity step at the depth of the Moho (11 km) (Figs. 7.4 and 7.7c). During inversion, this new gradient velocity model has to fit roughness and smoothness constraints throughout the entire model in contrast to the previous layered velocity model, where a velocity discontinuity at the Moho was allowed. The P-wave inversion of 124 sources with the 3D gradient reference velocity model therefore shows both a higher traveltimes residual RMS of 164.39 ms and a higher data misfit variance of $0.027 s^2$. The predominant velocity anomalies above 11 km depth remain essentially unchanged, but the P-wave velocity inversion based on the 3D gradient reference velocity model produces a smoother result (Fig. 7.7a and b) showing structures more realistically than based on the 3D layered reference velocity model. We therefore choose the 3D gradient reference model despite the higher values of traveltimes residual RMS and data variance as our preferred reference model. Fig. 7.8 shows the results of the P-wave velocity inversion relative to this reference model. A full sequence of slices and depth sections of the inversion result are shown in the supplement, Fig. S1.

Most prominently, the inversion result shows a 0.3 km/s negative, right next to a 0.3 km/s positive P-wave velocity perturbation in the central part of the model near 85°E and $85^\circ35'\text{N}$ as shown in Fig. 7.8(a), going down to more than 10 km depth (Figs. 7.8b and c) and extending from the southern to the northern rift valley wall across the rift valley (km 10 to 30 in Fig. 7.8d). Most earthquakes form a dense cluster in the central part of the model, at the intersection of slices C-C' and H-H' (Fig. 8b), from near bathymetry down to about 20 km depth (Fig. 7.8c). They mostly are located below 10 km, at the

changeover from decreased to increased seismic velocities. This can be seen most clearly in the depth slice Fig. 7.8(b) as well as in the section along the rift valley C-C' in Fig. 7.8(c). In the region with decreased velocities, only a scattering of earthquakes lies at a shallower depth (Figs. 7.8a and d).

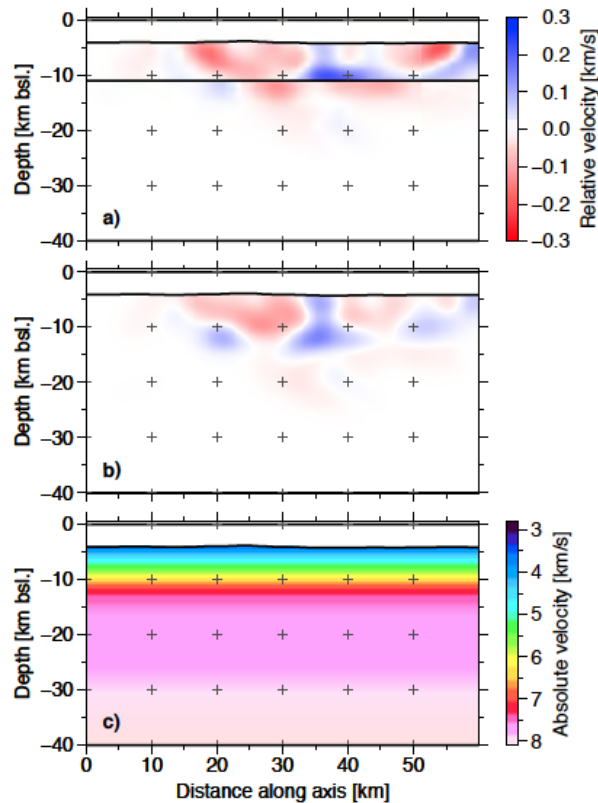


Figure 7.7 – Comparison of the P-wave velocity inversion based on the 3D layered reference velocity model (a) and based on the 3D gradient reference velocity model (b) as along-axis slice (Fig. 7.2a). Also shown is the absolute velocity of the 3D gradient reference velocity model along the same slice (c). The pair of velocity anomalies at km 40 requires a less prominent velocity contrast at the Moho, realized in b) and c). The major features in a) remain unchanged.

The region which is extensively covered by rays extends about 10 km along axis from the intersection of slices C-C' and H-H' to the northwest and the southeast (Fig. 7.9c, from km 20 to 45) and laterally from km 10 to 30 in Fig. 7.9(d). Horizontally, the high ray density in a depth of 5 km (Fig. 7.9a) and 9 km (Fig. 7.9b) in the described region confirms the generally good ray coverage in the central part of the model. The full sequence of sections showing the ray cover is included in the supplement, Fig. S2.

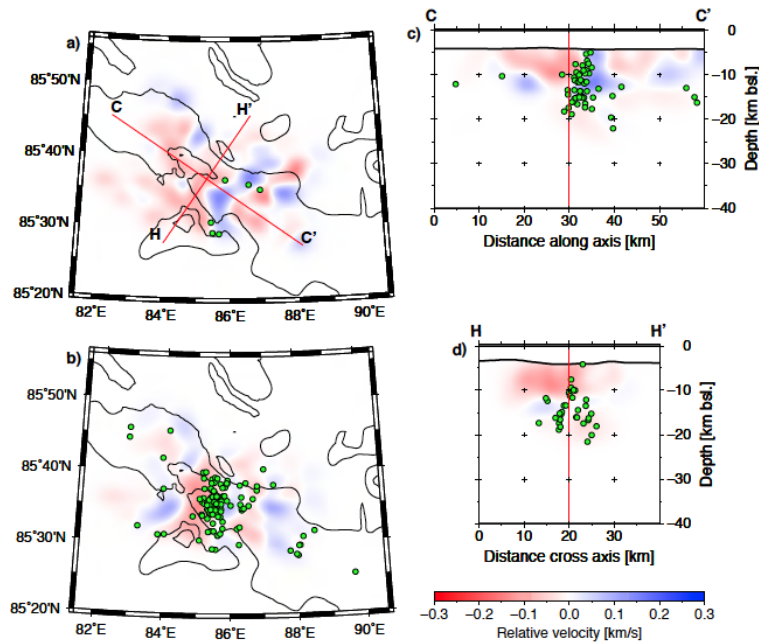


Figure 7.8 – P-wave velocity inversion result in two depth slices (a) at 6 km, and (b) at 9 km depth, with bathymetry of IBCAO2 (*Jakobsson et al.*, 2008) with 500 m contour spacing. (c) shows the inversion result along axis and (d) cross axis. The red line in (c) and (d) depicts the intersection between both profiles for clarification purposes. Hypocentres in the vertical slices (c, d) are shown as green circles, within 2.5 horizontal km of the respective slice. In the horizontal slice at 6 km depth (a), green circles denote relocated earthquakes with hypocentres less than 7.5 km bsl., in the horizontal slice at 9 km (b) depth we plotted all deeper hypocentres.

7.4.1 Checkerboard test

We extensively assessed the resolution of the inversion result to evaluate how well structures are recovered by the inversion and to identify possible artefacts. To this end, synthetic tests have been devised which, generally, trace rays through a synthetic structure using the same set of receiver and earthquake coordinates as the original dataset to generate an artificial dataset. The synthetic traveltimes are then used as input to the tomographic inversion using the 3D reference velocity model as starting model and the result is compared with the initial structure.

The most common resolution test is the checkerboard test (e.g. *Humphreys and Clayton*, 1988; *Spakman and Nolet*, 1988), which assigns three-dimensional blocks of positive and negative velocity perturbations to the velocity grid. The recovered pattern can give important information about well-recoverable regions and image blurring. We assigned a velocity perturbation of ± 0.5 km/s for every three blocks laterally and vertically, alternating between positive and negative anomalies, and added a data covariance of 0.1 to each traveltimes pick (Figs. 10a and c). The resulting P-wave velocity model recovers the

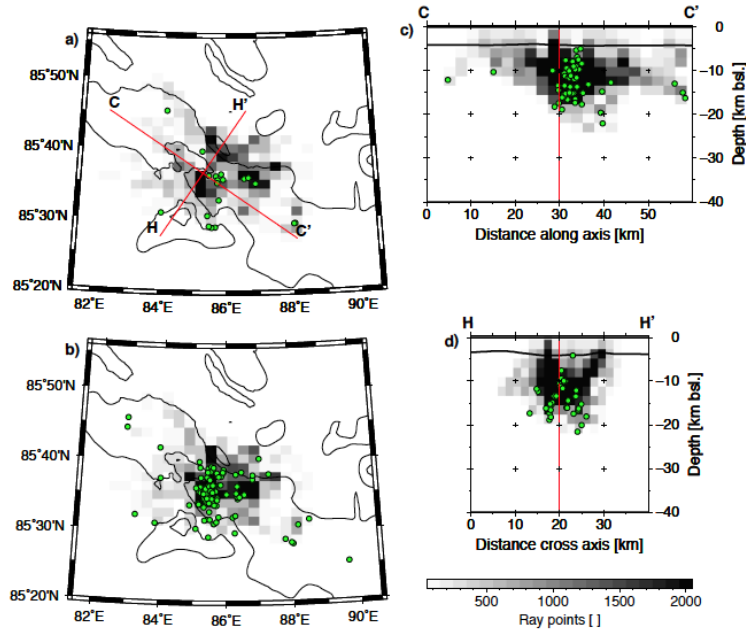


Figure 7.9 – Sum of ray points from FMTOMO in two depth slices (a) at 6 km, and (b) at 9 km depth and along axis (c), and (d) cross axis. We summed ray points according to velocity grid node spacing and showed in each slice the respective sum of ray points in each velocity grid cell. Red line and green circles as in Fig. 7.8. The sum of ray points serves as a measure of ray coverage. See text for discussion.

anomaly in the central part of the model well, down to about 11 km depth. Laterally, the anomalies are recovered between 84.5°E to 87.5°E , and between $85^{\circ}30'\text{N}$ and $85^{\circ}40'\text{N}$ (Figs. 7.10b and d). The negative anomaly beyond 88°E gets pulled by smearing to about 87.5°E at the depth slice 6 km, therefore we interpret only the recovered area.

7.4.2 Restoration test

A restoration test is useful to test if and how realistic structures, which show up in the inversion result, are constrained by the data. We followed the approach of *Zhao* (1992) and built a synthetic velocity model, which contains simplified velocity structures of the final velocity model. Then, the same basic approach is followed as in the checkerboard test, comparing the result of the inversion with the initial synthetic structure.

We built two synthetic models, including the same main lateral structure in the well-covered area (c.f. Figs. 7.8a and 7.9a) with ± 0.3 km/s velocity perturbation in each, only placing the structure at different depths in both models: A negative anomaly extending between km 10 and 30 (Fig. 7.8d) and a positive anomaly adjacent to the southeast between km 35 and 45 of Fig. 7.8(d), which is bracketed by the tail of a second negative anomaly. Owing to velocity grid cell size, one model includes the structure between 4 and

6 km depth and the second model places it at 8 – 10 km depth (Figs. 7.10e and g). We performed the restoration test for both models and found that the structure is laterally well reconstructed at both depths (Figs. 7.10f and h), affirming the good ray coverage in the central part of the model region. However, the recovered amplitudes of the velocity perturbations are diminished by about two thirds.

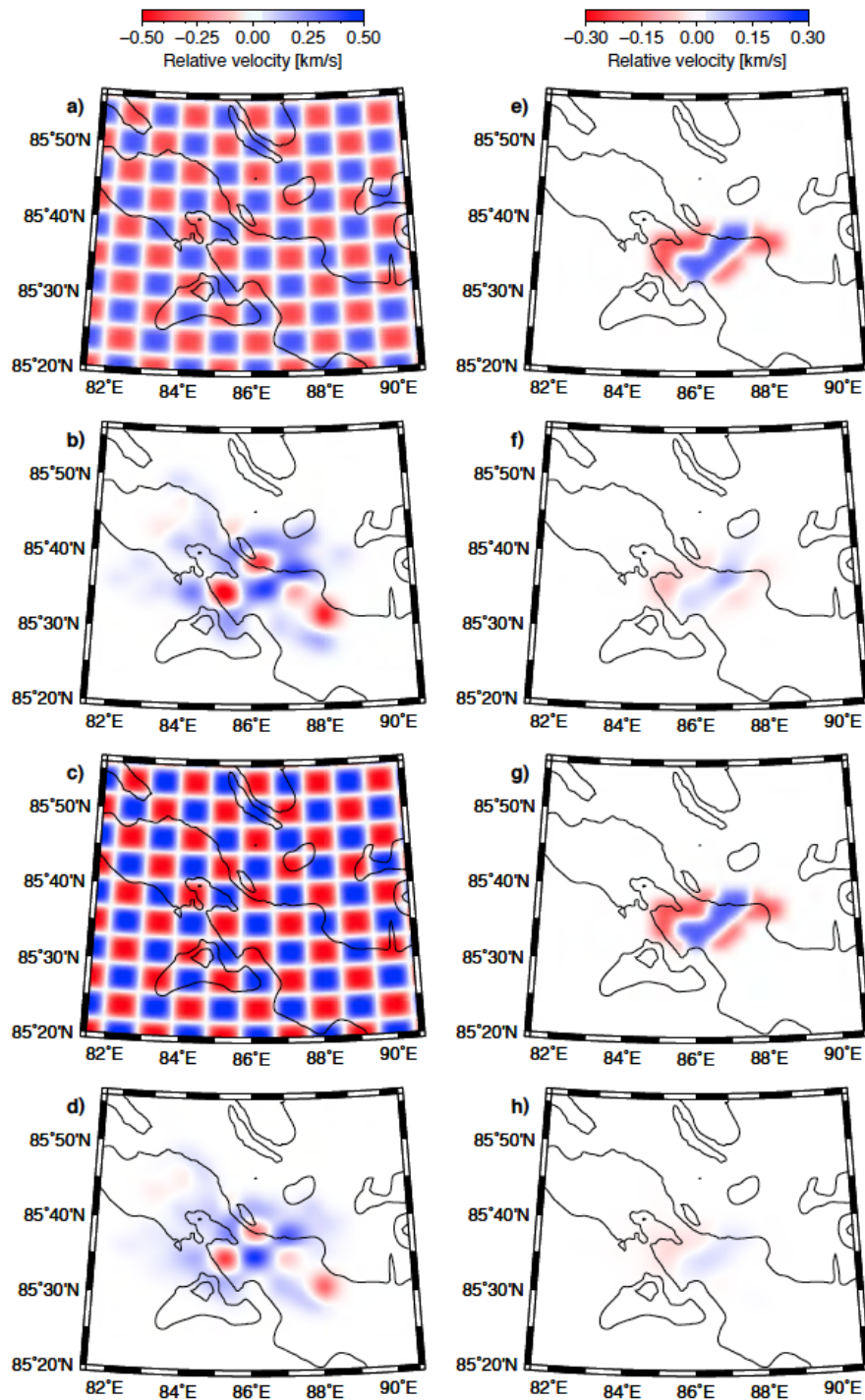


Figure 7.10 – Checkerboard reference model and recovered model, respectively at 6 km depth (a) and (b), and 9 km depth (c) and (d). (e-h) show restoration reference model and recovered model respectively at 6 km (e and f), and at 10 km (g and h). Bathymetry (a-h) as in Fig. 7.8.

7.5 Interpretation and discussion

7.5.1 Distribution of seismicity

7.5.1.1 Seismicity rate

During 16 days, our instruments recorded 248 locatable earthquakes, mostly within the median valley. The seismicity rates have been calculated excluding times of ice breaking by I/B Oden, which increases the noise level and detection threshold considerably. During the first 28 hours, alone 52 of these events originated within 5 km of Oden volcano (Fig. 7.3a), which corresponds to a peak in seismicity with an event rate of 1.3 events per hour, compared to the overall seismicity rate of 0.93 events per hour. A second small cluster of earthquakes on Julian day 204 was located at about 88°E which is clearly visible in the full dataset of 248 Hyposat located events (Fig. 7.3b). We do not further interpret this cluster due to sparse ray coverage in this area.

The overall seismicity rate of 22.4 locatable events per day exceeds the seismicity as recorded by AMORE 2001 (5.3 events per day) in the same area by far (*Schlindwein et al.*, 2007). However, it is comparable to the seismicity recorded at a volcanic edifice at 4.5°W/83°35'N in the median valley of the Western Volcanic Zone (18.2 events per day) (*Schlindwein et al.*, 2007). There, a swarm of microearthquakes directly at an elongated ridge has been interpreted to be related to magmatism.

In 2001, most of the seismicity has been located north of the rift valley (*Schlindwein et al.*, 2007), with the centre of the rift valley being seismically quiescent. We did not record further seismoacoustic signals as found in the recordings of AMORE 2001, which had been interpreted as a sign of an on-going submarine eruption originating at the southern rift valley flank (*Schlindwein and Riedel*, 2010). This points to a ceasing of this specific eruption process during the elapsed years.

7.5.1.2 Moho depth

From our best fitting 1D velocity model we infer a depth of the Moho of about 7 km below seafloor, pointing to a thick, predominantly basaltic layer at our survey area. As gabbro is hardly been exposed on the seafloor (*Michael et al.*, 2003), the crust is considered to mainly of basalt (*Jokat and Schmidt-Aursch*, 2007). This Moho depth is greater than what up till now has been observed at an ultraslow spreading ridge. At amagmatic segments of Knipovich ridge, the crust is on average about 4.5 km thick, underneath Logachev seamount the crust measures 5.7 km (*Jokat et al.*, 2012). Moho depths of 1.4 to 4.9 km are found at more westerly profiles at Gakkel ridge (*Jokat and Schmidt-Aursch*, 2007), the varying depths having been interpreted to denote magmatic activity. Yet, our larger

Moho depth of 7 km agrees with theoretical considerations of *Standish et al.* (2008) who inferred that a significantly thicker crust would exist at magmatic centres than at the segments in between.

7.5.1.3 Hypocentre depths

At the time of our survey, the deepest earthquakes at the 85°E/85°N region of Gakkel ridge originated 20 km below sea surface (16 km beneath seafloor). This is well below what *Solomon et al.* (1988) interpreted from the correlation of centroid depths to spreading rate. At a full spreading rate of 10 mm/yr, they extrapolated a maximum hypocentre depth of about 12 km below seafloor, interpreting this depth as the extent of the brittle lithosphere. *Montesi and Behn* (2007) modelled the thermal state of the axial lithosphere at ultraslow spreading ridges using a 2D corner flow model. Following their approach, we calculated the depth of the 600°C isotherm which we take as the boundary of brittle faulting (*McKenzie et al.*, 2005). We obtained a maximum depth of 12.6 km below seafloor, yet we observe earthquakes at significantly greater depths in our survey area, pointing to an unusually cold lithosphere. Processes like efficient hydrothermal cooling have not been considered in the theoretical models, but may lead to a colder lithosphere than expected. Our hypocentre depths agree with those of local earthquakes at the ultraslow spreading Lena Trough and Knipovich ridge (*Läderach et al.*, 2011; *Schlindwein et al.*, 2013), which also extend well into the lithospheric mantle, beyond a theoretically predicted brittle-ductile boundary.

Beneath Logachev Seamount, an axial volcanic edifice at Knipovich ridge, local earthquakes have only been found down to 8 km below seafloor, but deepening considerably away from Logachev Seamount (*Schlindwein et al.*, 2013). This has been interpreted to delineate a shallowing of the 600°C isotherm at the location of Logachev Seamount. Yet surprisingly, our deep earthquakes are located below a recently active volcanic centre. Oden and Loke volcanoes are considered to be the sites of most recent volcanic activity (*Sohn et al.*, 2008; *Pontbriand et al.*, 2012), probably starting during the 1999 earthquake swarm (*Korger and Schlindwein*, 2012) with eruptive activity lasting at least until 2001 (*Schlindwein et al.*, 2005; *Schlindwein and Riedel*, 2010). While immediately underneath Oden volcano there is no seismicity and earthquakes underneath Loke volcano are relatively shallow, the immediate vicinity shows earthquakes down to 20 km depth (Fig. 7.11). A clear seismic gap as on Logachev Seamount cannot be identified with any confidence.

The dense cluster of deep earthquakes is not aligned along the axis of the rift valley or at an obvious major fault plane. At the extension-dominated environment of a mid-ocean ridge, earthquakes often originate at deep reaching rift-parallel faults, accommodating a tensile stressfield, yet, *Pontbriand et al.* (2012) report a lack of recent faulting. We also observe only scant seismicity elsewhere in the survey area. Therefore, we speculate that seismicity at this recently active volcanic centre is probably not the result of rift parallel extensional faulting but might be the reaction to a recent intrusion.

7.5.2 Seismic velocities and structure

This is the first time a local earthquake tomography was done using data collected by seismometers mounted on ice floes. It also constitutes the first 3D passive seismic experiment at an ultraslow spreading ridge whereas many such studies have been done at faster spreading ridges using ocean bottom seismometers (e.g. *Toomey et al.*, 1985; *Barclay and Wilcock*, 2004; *Tolstoy et al.*, 2006). Due to the drift of the stations, a multitude of crossing ray paths is produced. Therefore the P-wave velocity inversion of this unusual local dataset gives interpretable results in the centre of the survey area, extending at least from 84.5°E to 87.5°E, and between 85°30'N and 85°40'N (Figs. 7.9b and d). Yet, synthetic tests showed that velocity contrasts were not recovered with the full amplitude and it is therefore likely, that the real velocity anomalies are greater than reproduced.

At faster spreading ridges, a symmetric pattern of velocity anomalies with respect to the rift axis is commonly observed (e.g. *Toomey et al.*, 1990). Here we do not see such a pattern shaped parallel to the rift axis, rather a prominent 'bridge' of reduced velocities crosses the rift valley, perpendicular to the rift axis and passing the site of Asgard volcanic chain (Fig. 7.11). The amplitude of the anomaly is about -0.3 km/s, which is smaller than what is usually found in similar volcano-tectonic environments (e.g. *Magde et al.*, 2000) but can probably be explained by possible underestimation of velocity anomalies. During AGAVE 2007, several low-temperature hydrothermal discharge sites were discovered on the volcanic lineaments, which point to the presence of a heat source underneath (*Pontbriand et al.*, 2012). Conspicuously, most of the clustered events are located right between the negative and a positive velocity perturbation (Figs. 7.11 and 7.8c), clustering in the area with the highest velocity gradient. Intruded magmas would cool at the scale of months for a 2-m-wide dyke (*Sohn et al.*, 2004), generating tensile stresses from thermal contraction. We find it likely that the observed reduced P-wave velocities at depth stem from warm, intruded material from recent volcanic activity and that the observed microseismicity reflects relaxation of thermal stresses.

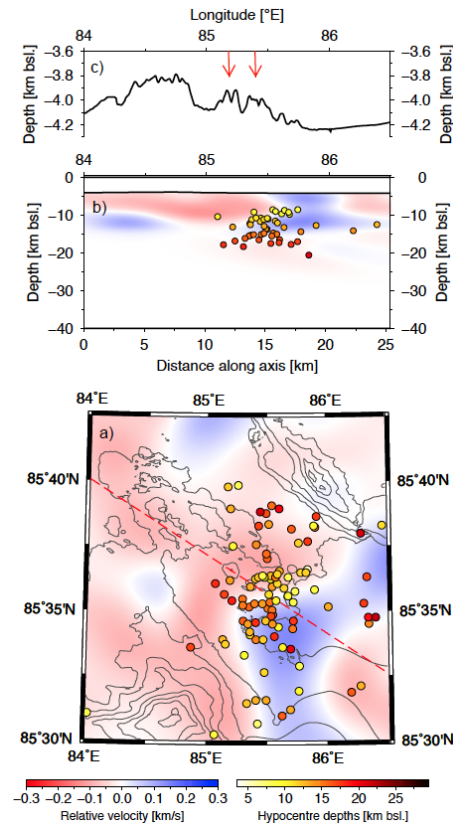


Figure 7.11 – (a) P-wave velocity inversion result plotted in a close-up of the volcanic centre. Circles denote relocated epicentres with color coding of hypocentre depth. Bathymetry as in Fig. 7.10 with contour spacing of 200 m. Dashed line shows location of axial bathymetric profile which is plotted in (c) with a vertical exaggeration of 10. Arrows in (c) give location of Oden (85°) and Loke volcanoes (85°). (b) shows the P-wave velocity inversion result along the axial profile and relocated hypocentres within 2.5 horizontal km from the profile. Note that hypocentres cluster underneath Loke volcano, while Oden volcano seemed to be seismically quiescent (b and c).

7.6 Conclusion

This was the first time a local earthquake tomography at an ultraslow spreading ridge was done. Gakkel ridge lies in the perennially ice-covered Arctic Ocean, which makes for difficult survey conditions. We therefore used an unusual method of seismometers mounted on ice floes to collect this unique dataset. The ensuing ray coverage was suitable for a local earthquake tomography, due to the recovery and redeployment of the seismometers when the ice floes drifted too far away from the survey area.

Our so collected dataset gives important insights into the thermal structure of an ultraslow spreading volcanic centre at 85°E/85°N, where a recent spreading episode was observed:

(1) We recorded over 300 microearthquakes, confidently locating 124 hypocentres up to a depth of 16 km beneath seafloor, inferring a thick, basaltic crust with a deep Moho at about 7 km beneath seafloor. This implies an exceptionally thick crust and cold lithosphere in spite of recent activity at this volcanic centre.

(2) The seismic tomography revealed an area of decreased seismic velocities crossing the rift valley at the location of the Asgard volcanic chain, which is believed to be the site of recent volcanic activity. We speculate that the reduced velocities may be caused by warm intruded material.

A prominent cluster of earthquakes is located in a region east of Loke volcano with a high velocity gradient and probably, thermal gradient. We suggest that the observed seismicity predominantly reflects the relaxation of thermal stresses following recent intrusion.

Our study yielded the first structural image of a volcanic centre at an ultraslow spreading ridge. It gives insights into the aftermath of its most recent spreading episode, which started in 1999 with the largest teleseismic earthquake swarm observed globally on a mid-ocean ridge. It adds to a growing body of evidence that melts at the volcanic centres of ultraslow spreading ridges have to penetrate an unusually thick and cold lithosphere, challenging existing thermal models for these ridges.

7.7 Acknowledgments

We particularly thank Nicholas Rawlinson for his tomography algorithm and subsequent help. Also we would like to express our gratitude to the officers and crew of the I/B Oden for their support during AGAVE 2007. Instruments were provided by IRIS PASSCAL and the GIPP at Potsdam, Germany. This study was funded by the Emmy-Noether Program of the DFG under grant Schl. 853/1-1.

7.8 Supplementary Material

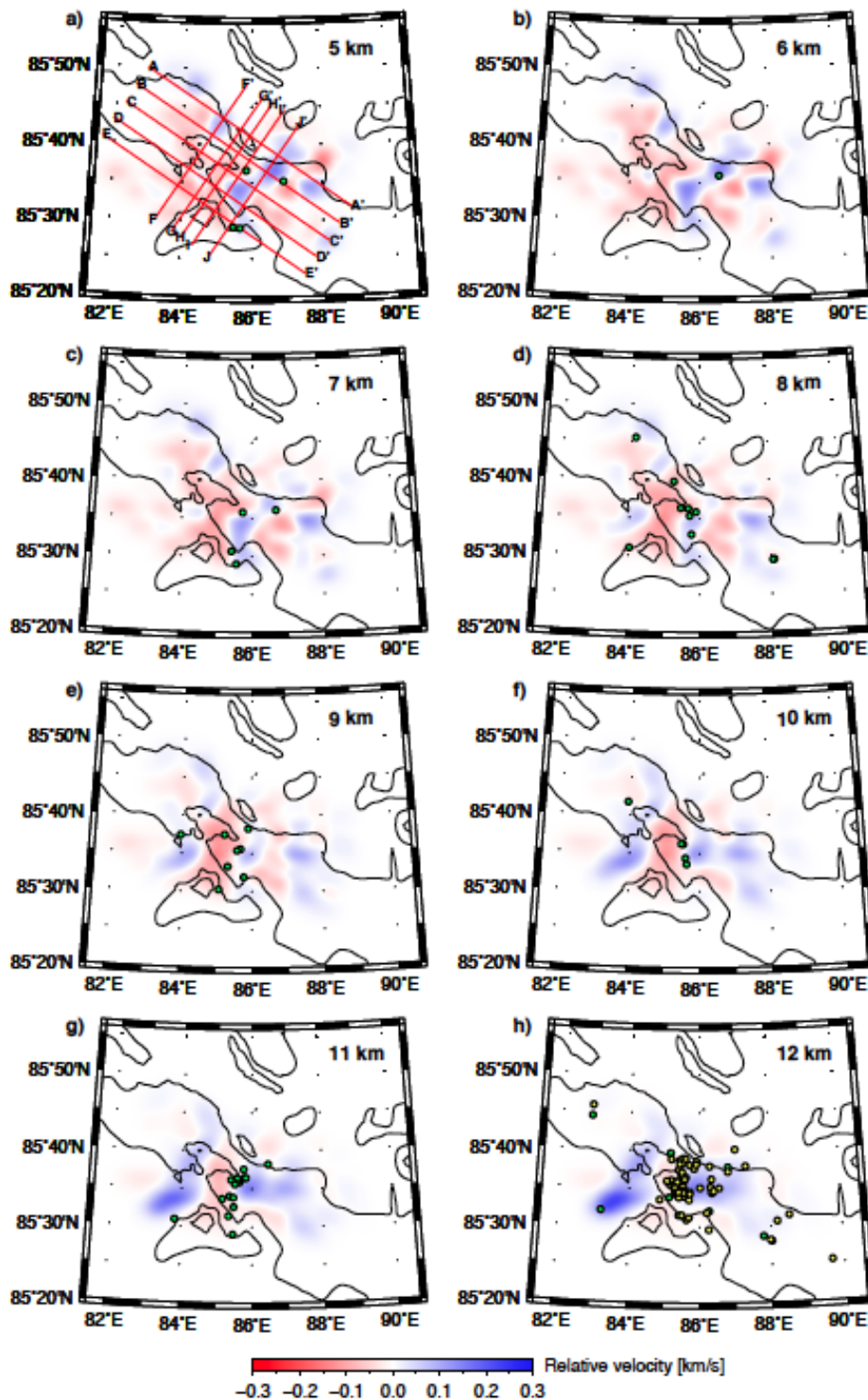


Figure 7.12 – P-wave velocity inversion result in horizontal slices at the given depth (a-h). The red lines in (a) depict vertical profiles along (i-m) and cross axis (n-r) shown in Fig. 7.13. Green circles denote relocated earthquakes within 0.5 vertical km of the respective horizontal slice depth. Yellow circles in (h) show relocated earthquakes deeper than 12.5 km bsl. Bathymetry (a-h) of IBCAO (*Jakobsson et al., 2008*) with 500 m contour spacing. The figure continues in Fig. 7.13 with vertical slices.

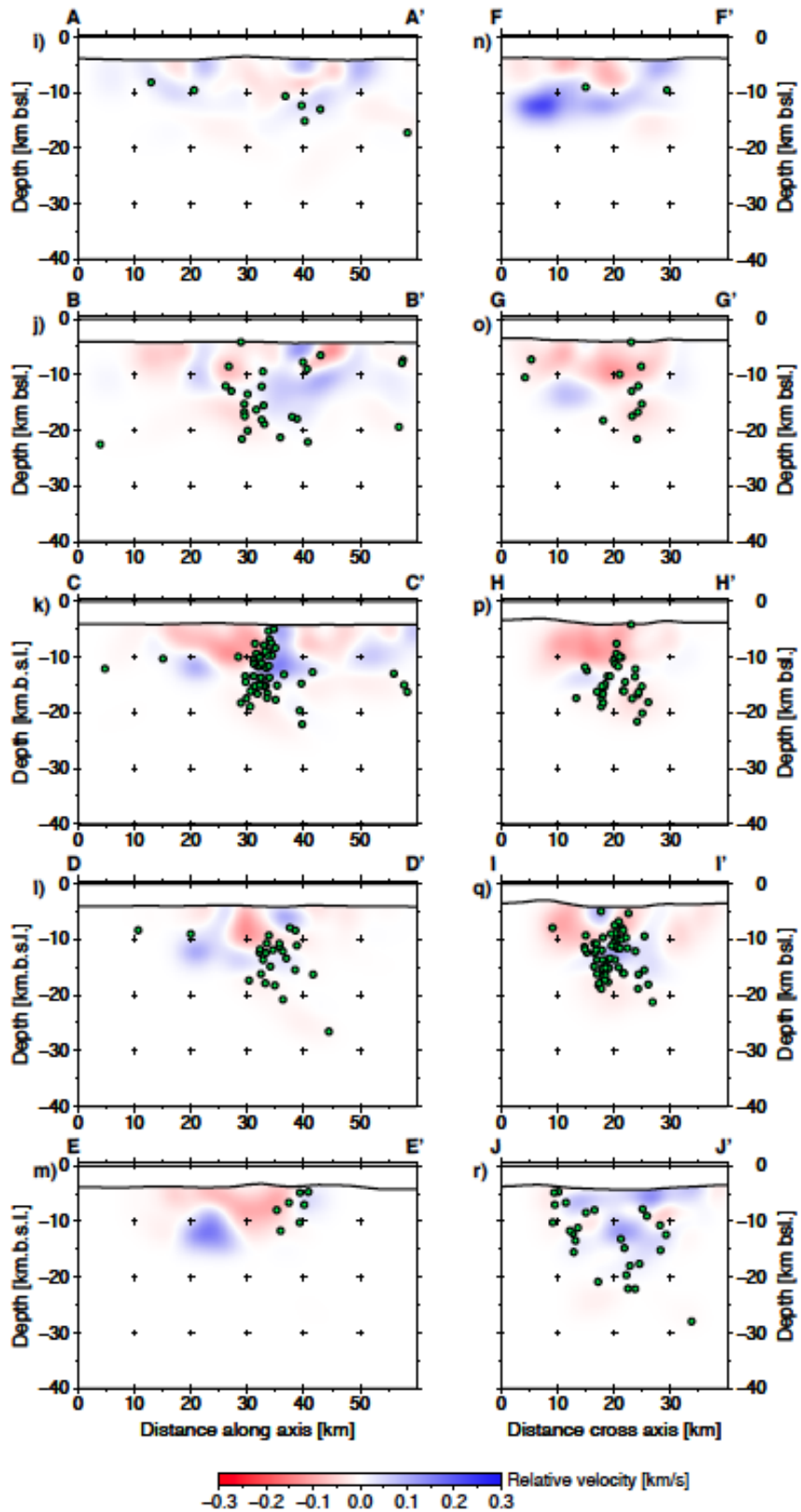


Figure 7.13 – P-wave velocity inversion result in vertical slices at the locations depicted in Fig. 7.12 (a). Green circles denote relocated earthquakes within 2.5 horizontal km of the respective vertical slice. Figure continued from Fig. 7.12.

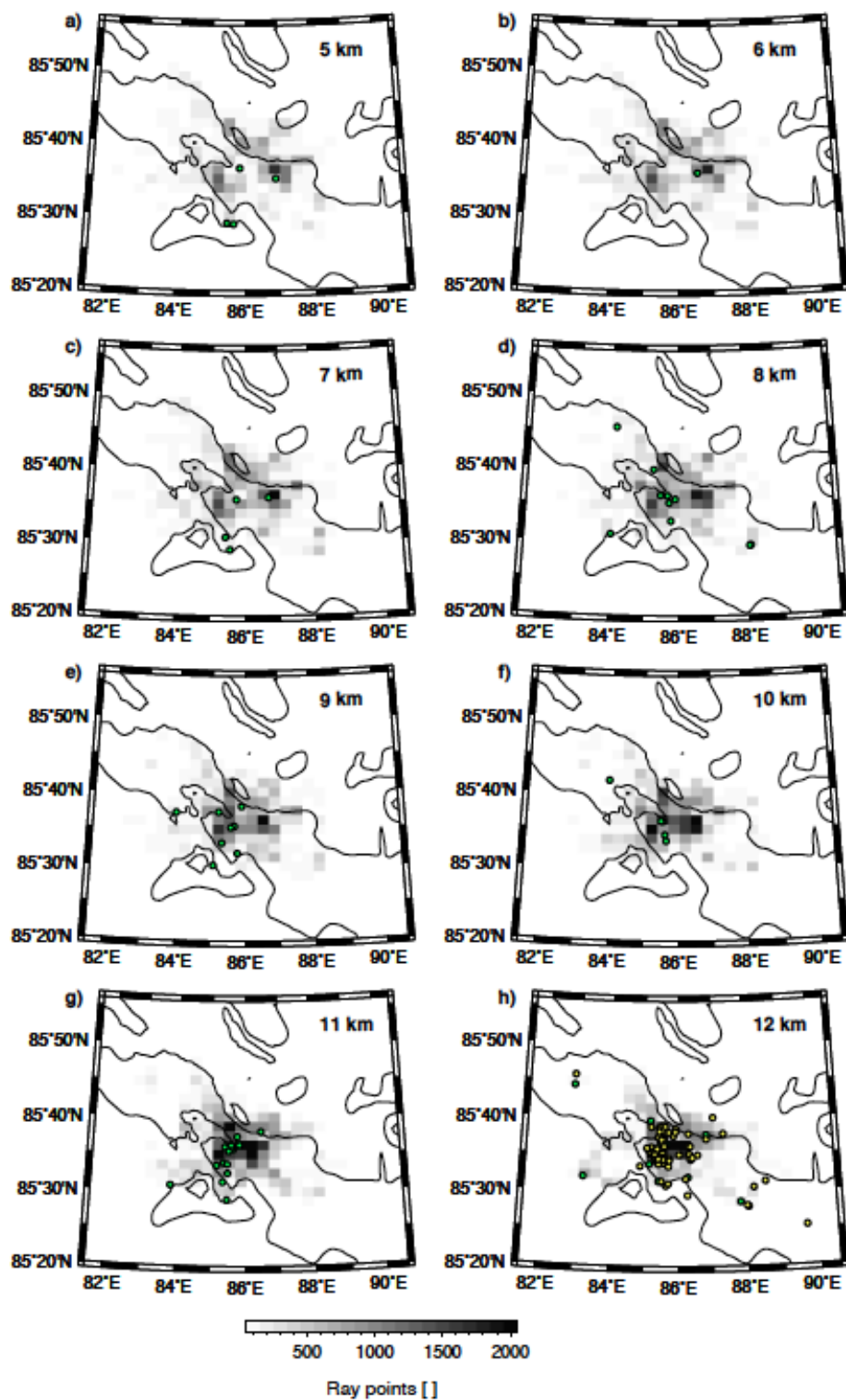


Figure 7.14 – Sum of ray points from FMTOMO in horizontal slices at the given depth (a-h). We summed ray points according to velocity grid node spacing and showed in each slice the respective sum of ray points in each velocity grid cell. Bathymetry (a-h), and green and yellow circles as in Fig. 7.12. The figure continues in Fig. 7.15 with vertical slices.

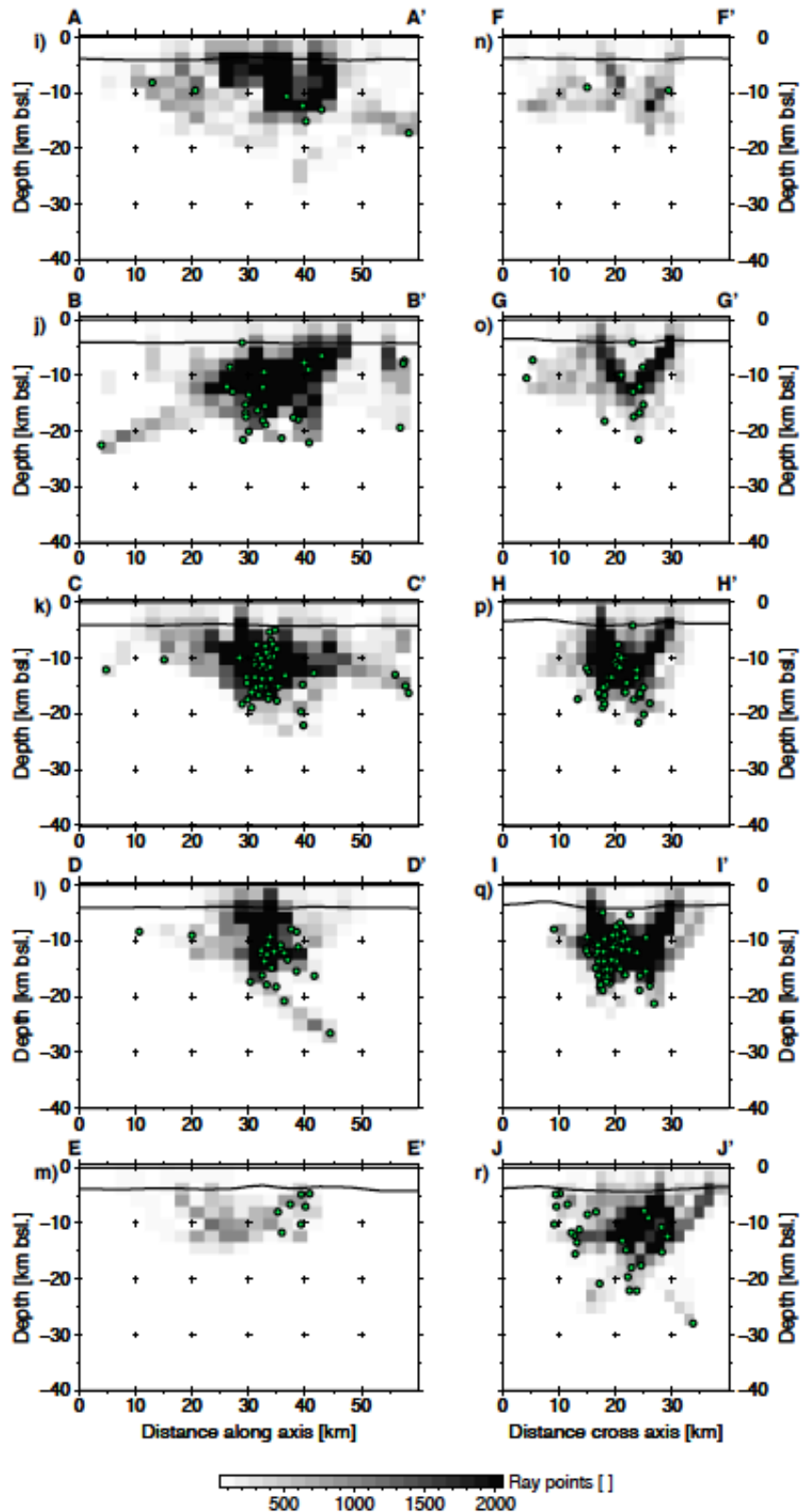


Figure 7.15 – Sum of ray points from FMTOMO in vertical slices at the locations depicted in Fig. 7.14 (a). Green and yellow circles as in Fig. 7.12. Figure continued from Fig. 7.14.

7.9 Literature

- Baker, E. T., H. Edmonds, P. Michael, W. Bach, H. Dick, J. Snow, S. Walker, N. Banerjee, and C. Langmuir (2004), Hydrothermal venting in magma deserts: The ultraslow-spreading Gakkel and Southwest Indian Ridges, *Geochem. Geophys. Geosys.*, 5(Q08002), doi: 10.1029/2004GC000712.
- Barclay, H., and W. Wilcock (2004), Upper crustal seismic velocity structure and microearthquake depths at the Endeavour Segment, Juan de Fuca Ridge, *Geochem. Geophys. Geosys.*, 5(Q01004), doi: 10.1029/2003GC000604.
- Dick, H. J., J. Lin, and H. Schouten (2003), An ultraslow-spreading class of ocean ridge, *Nature*, 426, 405–412, doi: 10.1038/nature02128.
- Edmonds, H., et al. (2003), Discovery of abundant hydrothermal venting on the ultraslow-spreading Gakkel ridge in the Arctic Ocean, *Nature*, 421, 252–256, doi: 10.1038/nature01351.
- Jakobsson, M., R. Macnab, L. Mayer, R. Anderson, M. Edwards, J. Hatzky, H. Schenke, and P. Johnsson (2008), An improved bathymetric portrayal of the Arctic Ocean: Implications for ocean modeling and geological, geophysical and oceanographic analyses, *Geophys. Res. Lett.*, 35(L07602), doi: 10.1029/2008GL033520.
- Jokat, W., and M. Schmidt-Aursch (2007), Geophysical characteristics of the ultraslow spreading Gakkel Ridge, Arctic Ocean, *Geophys. J. Int.*, 168, doi: 10.1111/j.1365-246X.2006.03278.x.
- Jokat, W., O. Ritzmann, M. Schmidt-Aursch, S. Drachev, S. Gauger, and J. Snow (2003), Geophysical evidence for reduced melt production on the Arctic ultraslow Gakkel mid-ocean ridge, *Nature*, 423, 962–965, doi: 10.1038/nature01706.
- Jokat, W., J. Kollofrath, W. Geissler, and A. Jensen (2012), Crustal thickness and earthquake distribution south of the Logachev Seamount, Knipovich Ridge, *Geophys. Res. Lett.*, 39(L08302), doi: 10.1029/2012GL051199.
- Kennett, B., M. Sambridge, and P. Williamson (1988), Subspace methods for large scale inverse problems involving multiple parameter classes, *Geophysical Journal*, 94, 237–247.
- Kissling, E., S. Husen, and F. Haslinger (2001), Model parametrization in seismic tomography: a choice of consequences for the solution quality, *Phys. Earth planet. Inter.*, 123, doi: 10.1016/S0031-9201(00)00203-X.
- Korger, E. I. M., and V. Schlindwein (2012), Performance of localisation algorithms for teleseismic mid-ocean ridge earthquakes: The 1999 Gakkel ridge earthquake swarm and its geological interpretation, *Geophys. J. Int.*, 188(2), doi: 10.1111/j.1365-246X.2011.05282.x.
- Läderach, C., and V. Schlindwein (2011), Seismic arrays on drifting ice floes: experiences from

-
- four deployments in the Arctic Ocean, *Seismological Research Letters*, *82*(4), 488–497, doi: 10.1785/gssrl.82.4.494.
- Läderach, C., V. Schlindwein, H.-W. Schenke, and W. Jokat (2011), Seismicity and active tectonic processes in the ultra-slow spreading Lena Trough, Arctic Ocean, *Geophys. J. Int.*, *184*(3), doi: 10.1111/j.1365-246X.2010.04926.x.
- McKenzie, D., J. Jackson, and K. Priestley (2005), Thermal structure of oceanic and continental lithosphere, *Earth Planet. Sci. Lett.*, *233*(3-4), doi: 10.1016/j.epsl.2005.02.005.
- Michael, P., et al. (2003), Magmatic and amagmatic seafloor generation at the ultraslow-spreading Gakkel ridge, Arctic Ocean, *Nature*, *423*, 956–961, doi: 10.1038/nature01704.
- Montesi, L., and M. Behn (2007), Mantle flow and melting underneath oblique and ultraslow mid-ocean ridges, *Geophys. Res. Lett.*, *34*(L24307), doi: 10.1029/2007GL031067.
- Mueller, C., and W. Jokat (2000), Seismic Evidence for Volcanic Activity Discovered in Central Arctic, *Eos, Trans. Am. geophys. Un.*, *81*(24), 265–269, doi: 10.1029/00EO00186.
- Pontbriand, C., S. Soule, R. Sohn, S. Humphris, C. Kunz, H. Singh, K. Nakamura, M. Jakobsson, and T. Shank (2012), Effusive and explosive volcanism on the ultraslow-spreading Gakkel Ridge, 85°E, *Geochem. Geophys. Geosys.*, *13*(10), doi: 10.1029/2012GC004187.
- Rawlinson, N., and B. Kennett (2008), Teleseismic tomography of the upper mantle beneath the southern Lachlan Orogen, Australia, *Phys. Earth Planet. Int.*, *3167*, doi: 10.1016/j.pepi.2008.02.007.
- Rawlinson, N., and M. Sambridge (2003), Seismic traveltime tomography of the crust and lithosphere, *Advances in Geophysics*, *46*, 81–197.
- Rawlinson, N., M. de Kool, and M. Sambridge (2006), Seismic wavefront tracking in 3D heterogeneous media: applications with multiple data classes, *Exploration Geophysics*, *37*, doi: 10.1071/EG06322.
- Riedel, C., and V. Schlindwein (2010), Did the 1999 earthquake swarm on Gakkel Ridge open a volcanic conduit? A detailed teleseismic data analysis, *Journal of Seismology*, *14*(3), 505–522, doi: 10.1007/s10950-009-9179-6.
- Schlindwein, V., and J. Linder (2007), Characteristic microearthquakes of the active submarine volcanic complex at 85°E, Gakkel Ridge, *Eos Trans. AGU, Fall Meet. Suppl.*, *88*(52), OS42A–02.
- Schlindwein, V., and C. Riedel (2010), Location and source mechanism of sound signals at Gakkel ridge, Arctic Ocean: Submarine Strombolian activity in the 1999-2001 volcanic episode, *Geochem. Geophys. Geosys.*, *11*(Q01002), doi: 10.1029/2009GC002706.

- Schlundwein, V., C. Müller, and W. Jokat (2005), Seismoacoustic evidence for volcanic activity on the ultraslow-spreading Gakkel Ridge, Arctic Ocean, *Geophys. Res. Lett.*, *32*(L18306), doi: 10.1029/2005GL023767.
- Schlundwein, V., C. Müller, and W. Jokat (2007), Microseismicity of the ultraslow-spreading Gakkel ridge, Arctic Ocean: a pilot study, *Geophys. J. Int.*, *169*, doi: 10.1111/j.1365-246X.2006.03308.x.
- Schlundwein, V., A. Demuth, W. Geissler, and W. Jokat (2013), Seismic gap beneath Logachev seamount: indicator for melt focusing at an ultraslow mid-ocean ridge?, *Geophys. Res. Lett.*, doi: 10.1002/grl.50329.
- Schweitzer, J. (2001), HYPOSAT - an enhanced routine to locate seismic events, *Pure applied Geophysics*, *158*, 277–289.
- Sella, G., T. Dixon, and A. Mao (2002), REVEL: A model for recent plate velocities from space geodesy, *J. Geophys. Res.*, *107*(B4), ETG 11–1 – ETG 11–30, doi: 10.1029/2000JB000033.
- Sethian, J. A. (1996), A fast marching level set for monotonically advancing fronts, *Proceedings of the National Academy of Sciences*, *93*, 1591–1595.
- Sethian, J. A., and A. Popovici (1999), 3-D travelttime computation using the fast marching method, *Geophysics*, *64*, 516–523.
- Sohn, R. A., A. H. Barclay, and S. C. Webb (2004), Microearthquake patterns following the 1998 eruption of Axial Volcano, Juan de Fuca Ridge: Mechanical relaxation and thermal strain, *J. geophys. Res.*, *109*(B01101), doi: 10.1029/2003JB002499.
- Sohn, R. A., et al. (2008), Explosive volcanism on the ultraslow-spreading Gakkel ridge, Arctic Ocean, *Nature*, *453*, 1236–1238, doi: 10.1038/nature07075.
- Solomon, S. C., P. Y. Huang, and L. Meinke (1988), The seismic moment budget of slowly spreading ridges, *Nature*, *334*, 58–60, doi: 10.1038/334058a0.
- Standish, J. J., J. Dick, P. Michael, W. Melson, and T. O’Hearn (2008), MORB generation beneath the ultraslow spreading Southwest Indian Ridge (9 – 25°E): Major element chemistry and the importance of process versus source, *Geochem. Geophys. Geosys.*, *9*(5), doi: 10.1029/2008GC001959.
- Stranne, C., R. A. Sohn, B. Liljebladh, and K. ichi Nakamura (2010), Analysis and modeling of hydrothermal plume data acquired from the 85°E segment of the Gakkel Ridge, *J. geophys. Res.*, *115*(C06028), doi: 10.1029/2009JC005776.
- Tolstoy, M., D. Bohnenstiehl, M. Edwards, and G. Kurras (2001), Seismic character of volcanic activity at the ultraslow-spreading Gakkel Ridge, *Geology*, *29*(12), 1139–1142, doi: 10.1130/0091-7613(2001)029.

Tolstoy, M., et al. (2006), A Sea-Floor Spreading Event Captured by Seismometers, *Science*, *314*, 1920–1922, doi: 10.1126/science.1133950.

Toomey, D. R., S. C. Solomon, G. Purdy, and M. H. Murray (1985), Microearthquakes Beneath the Median Valley of the Mid-Atlantic Ridge Near 23°N: Hypocenters and Focal Mechanisms, *J. geophys. Res.*, *90*(B7), 5443–5458.

Toomey, D. R., G. Purdy, S. Solomon, and W. Wilcock (1990), The Three-Dimensional seismic velocity structure of the East Pacific Ridge near latitude 9°30'N, *Nature*, *347*, 639–645.

Zhao, H. (1992), Tomographic imaging of P and S wave velocity structure beneath northeastern Japan, *J. geophys. Res.*, *97*, 19,909–19,928.

8 Conclusion and Outlook

In my PhD thesis I have focused on a class of ridges which has received little attention up till now. Ultraslow spreading ridges are found at remote locations where local investigations have to deal with sea-ice cover or frequent stormy weather. Therefore, local seismic surveys with traditional survey methods could not be conducted and only teleseismic datasets have been available. Due to these challenges, processes which drive seismicity at these kind of ridges are still not completely understood.

The teleseismically registered 1999 earthquake sequence at the 85°E/85°N volcanic complex, Gakkel Ridge, provided an unprecedented opportunity to study a spreading episode at an ultraslow spreading magmatic centre. However, the teleseismical recording of phases leaves it to suffer from a less than ideal azimuthal distribution of recording stations and a lack of recorded phases from nearby stations which could better constrain earthquake locations.

The first publication of my PhD project stresses the importance of the choice of the localization algorithm for locating earthquakes at such a remote location. Comparing well-located events by three conceptually different localization algorithms, the absolute localization algorithm NonLinLoc placed epicentres closest to the epicentres calculated by the relative localization Mlocate. I therefore preferred NonLinLoc for single-event locations and well-defined events, as a relative localization can only be used when clustered seismicity is indicated. In a spatio-temporal analysis, it was possible to confidently relate the seismic sequence of 1999 to a tectonomagmatic spreading episode. I discerned three distinct temporal phases, identifying geological processes which lead to the observed character of seismicity at this ultraslow spreading magmatic centre. In the first, short phase of seismicity, *Korger and Schlindwein (2012)* inferred a breaking of crust either as a result or enabling a magmatic intrusion, followed by the second phase of seismicity where the centre of seismic activity expanded. In the third and final phase of seismicity, *Korger and Schlindwein (2012)* interpreted a change in physical process, either a transition to an effusive stage of volcanism or a post-intrusion adjustment of the stress field.

Placing clustered seismicity observations at ultraslow mid-ocean ridges in a global context, I made use of the modified Omori-Law in an analysis of four seismic sequences as contribution to *Läderach et al. (2012)*, placed on the Orthogonal Supersegment of the Southwest Indian Ridge, which were regionally registered at the VNA2 array at the German Antarctic research station. I also analyzed four earthquake sequences for *Schlindwein (2012)*, also failing to fit the modified Omori-Law to these seismicity clusters. One of these sequences constituted the teleseismic dataset of the 1999 seismicity sequence at 85°E/85°N.

As seismicity sequences at ultraslow spreading mid-ocean ridges are almost exclusively found at centres of focused magmatic activity, the complete failure to fit a calculated function for purely tectonic events to the actual earthquake activity indicates a magmatic influence in driving seismicity.

A microseismicity study of an ultraslow spreading ridge was completed in 2007, when the AGAVE expedition monitored seismicity in the aftermath of the last spreading episode at $85^{\circ}\text{E}/85^{\circ}\text{N}$ with an unusual survey method of mounting seismometer arrays on ice-floes. This dataset links high-magnitude seismic spreading activity in 1999 with microseismicity recorded eight years later. The third publication of my thesis, *Korger and Schlindwein* (2013), distinguishes itself by presenting the very first local earthquake tomography of a magmatic spreading centre at an ultraslow spreading ridge.

In spite of the high noise level, I identified and picked first arrivals of a host of events, confidently locating 248 events with a local velocity model, which I also compiled newly from these data. I constructed a tomographic model, using 124 events that were recorded by at least two seismometer arrays. My results show a Moho at about 7 km beneath seafloor, which is greater than what was up till now observed at an ultraslow spreading ridge, yet agrees with theoretical considerations that a significantly thicker crust would exist at magmatic centres than at the segments in between. Hypocentre depths are deeper than inferred from theoretical modeling of the brittle-ductile boundary, yet they are comparable to other datasets at ultraslow spreading ridges. This points to a cold lithosphere in spite of recent volcanic activity at this site, and may mean that thermal models for this class of ridges have to be refined. The seismic tomography itself displays an area of slower seismic velocities crossing the rift valley at the most probable site of recent volcanic activity, which I speculated to originate from the presence of warm, intruded material. I attributed the observed seismicity around it to relaxation of thermal stresses following the recent intrusion.

In conclusion, this PhD project has given important insights regarding teleseismic and local seismicity of an ultraslow spreading volcanic centre. It linked the observed teleseismic seismicity in 1999 with a tectono-magmatic spreading episode at $85^{\circ}\text{E}/85^{\circ}\text{N}$, and presented for the first time ever the seismic velocity structure of such a spreading centre. This was done with two very different (teleseismic and local) and less than ideal datasets, yet resulted in the first local earthquake tomography ever done at an ultraslow spreading centre, illuminating seismicity and thermal structure in the aftermath of the 1999 spreading episode at the $85^{\circ}\text{E}/85^{\circ}\text{N}$ volcanic centre on Gakkel Ridge.

Looking ahead, I would recommend placing the resultant seismic tomographic model at $85^{\circ}\text{E}/85^{\circ}\text{N}$ in a wider context, comparing it to yet-to-be-collected datasets at other sections on ultraslow spreading ridges. Lately, there has been speculation that the ice cover of the Arctic Ocean would continue to decrease, which would make microseismicity surveys easier to conduct. For example, collecting such a dataset from one of the isolated volcanic cones at an amagmatic segment would result in a comparison of microseismicity

between segments. An additional line of investigation would be to return to 85°E/85°N a few years from now and collect a microseismicity dataset of comparable quality. This could shed light on long-term magmatic processes taking place beneath this volcanic centre, possibly illustrating thermal processes during recharging of an assumed magma chamber.

After analysis of such a newly collected dataset, I would recommend to connect the results of these three seismicity surveys at the well-established magmatic spreading centre at 85°E/85°N to the newly forming oceanic spreading centre in East Africa at the Afar Triple Junction. There, the Nubian, Arabian and Somalian plates diverge, creating a continental rift which eventually will narrow and form new ocean basins. Easily observable continental magmato-tectonic rifting is currently going on in the Afar depression. At the Dabbahu segment, observed seismicity is similar in spatial and temporal characteristics with patterns found at slow-spreading ridges. Between 1978 and 2001, a complete rifting cycle took place at Asal-Ghoubbet, which has been analyzed extensively (e.g. *Dobre et al.*, 2007a,b). Ideally, spreading cycles at these two spreading centres (Afar, Gakkel Ridge) would then be documented each by snapshots of data covering at least 15 years, which would enable a comprehensive study of similarities and differences between both spreading episodes.

Lately, *Schlindwein et al.* (2013) inferred a shallowing of the 600°C isotherm which depicts the brittle-ductile boundary, at Logachev Seamount on the Knipovich Ridge, from an observed seismicity gap directly beneath the seamount. Yet, this dataset is limited, as it only consists of seismicity collected over 10 days in 2009. The results of my seismic tomography at the 85°E/85°N volcanic centre do not show such a seismicity gap, but in contrast they show exceptionally deep hypocentres. I would recommend to do a longer microseismicity survey at Logachev Seamount, including a stretch of the adjacent ridge, to confirm or disprove the deduced 3D variation of the plate base which guides melts toward volcanic centres.

9 Acknowledgements

Doing a PhD is certainly not a 'group' effort, yet a certain support is, if not absolutely necessary, then at least highly appreciated by the harried, nervous, and stressed individual who struggles through. In this case that is, or was, me.

Three years are a long time, but my supervisor Dr. Vera Schlindwein has been there for me throughout all its highs and lows. Apart from being an excellent scientist with a decided gift for teaching, I especially appreciated her ability to spot logical flaws and constructively set about repairing them. She was always willing to discuss and clarify, and taught me the importance of structural deadlines. I owe more to her than I probably know. Thank you, Vera!

I also want to thank Prof. Dr. Katrin Huhn who consented to be the second referee for this dissertation, and Prof. Dr. Heinrich Villinger as additional supervisor.

I also thank the Emmy Noether Programme of the German Research Foundation (DFG), who funds the young researchers group 'Mid-Ocean Volcanoes and Earthquakes' (MOVE). MOVE provided the framework for my research under grant Schl 853/1-1. Wilfried Jokat, head of the Geophysics Department of the Alfred-Wegener-Institut in Bremerhaven made it possible that I could collect experience on marine surveys, deploying and recovering OBS, and coming to grips with hydrosweep. The Alfred-Wegener-Institut also supported me more materially, extending my contract from two to three years. In the department itself, many scientists were there when I needed a short chat to wrest my mind away from the merry go-round with my data. Certainly I would miss some names, so I will just address you all (you know who you are) with a heartfelt thank you! I want to specially thank Wolfram Geissler and Graeme Eagles, who proof-read and corrected my english. I very much appreciated that, guys!

During my thesis I used geophysical software packages, which were new to me and to my supervisor. I truly appreciated the willingness of Anthony Lomax (NonLinLoc) and Nicholas Rawlinson (FMTOMO) to troubleshoot their respective programs and to send me special instruction or advice. I also owe thanks to Doug Wiens for his program Mlocate.

My research group included also Christine Läderach, fellow PhD student for almost the whole time and a real asset when I needed someone to set me straight on all the crazy ideas which I am able to come up with. Many funny and serious discussions originated from our different backgrounds. I would certainly have missed a lot if not for her!

I received a lot of scientific and personal support from more people that I can name here. This includes the encouragement and support of my family, my mother and father for believing in me, and my brother for helping me calculate my first differential equations at the start of university. I received hugs from friends when I needed it or sometimes just because, and the proverbial 'We are going for Sushi in half an hour. Get out of that flat, NOW!'. I want you all to know that I really and truly appreciated you being there!

10 Complete Bibliography

- Akaike, H. (1974), A new look at the statistical model identification, *IEEE Trans. Autom. Control*, *AC-19*, 716–723.
- Baker, E. T., H. Edmonds, P. Michael, W. Bach, H. Dick, J. Snow, S. Walker, N. Banerjee, and C. Langmuir (2004), Hydrothermal venting in magma deserts: The ultraslow-spreading Gakkel and Southwest Indian Ridges, *Geochem. Geophys. Geosys.*, *5*(Q08002), doi: 10.1029/2004GC000712.
- Barclay, H., and W. Wilcock (2004), Upper crustal seismic velocity structure and microearthquake depths at the Endeavour Segment, Juan de Fuca Ridge, *Geochem. Geophys. Geosys.*, *5*(Q01004), doi: 10.1029/2003GC000604.
- Belachew, M., C. Ebinger, D. Coté, D. Keir, J. Rowland, J. Hammond, and A. Ayele (2011), Comparison of dike intrusions in an incipient seafloor-spreading segment in Afar, Ethiopia: Seismicity perspectives, *J. geophys. Res.*, *116*(B06405), 23 PP., doi: 10.1029/2010JB007908.
- Bergman, E. A., and S. C. Solomon (1990), Earthquake Swarms on the Mid-Atlantic Ridge: Products of Magmatism or Extensional Tectonics?, *J. geophys. Res.*, *95*(B4), 4943–4965.
- Björnsson, A. (1985), Dynamics of Crustal Rifting in NE Iceland, *J. geophys. Res.*, *90*(B12), 10,151–10,162.
- Bohnenstiehl, D., and R. Dziak (2008), Mid-ocean ridge seismicity, in *Encyclopedia of Ocean Sciences*, edited by J. Steele, S. Thorpe, and K. Turekian, p. 15, Academic Press, London, First online update.
- Bormann, P. (2002), Seismic Scaling Relations, Sources and Source parameters, in *New manual of seismological observatory practice (NMSOP): Chapter 3 Seismic Sources and Source Parameters*, edited by P. Bormann, pp. 82–93, Deutsches GeoForschungsZentrum GFZ, Potsdam, doi: 10.2312/GFZ.NMSOP_r1_ch3.
- Bown, J. W., and R. S. White (1994), Variations with spreading rate of oceanic crustal thickness and geochemistry, *Earth planet. Sci. Lett.*, *121*, 435–449.
- Buck, W., P. Einarsson, and B. Brandsdóttir (2006), Tectonic stress and magma chamber size as controls on dike propagation: Constraints from the 1975-1984 krafla rifting episode, *J. geophys. Res.*, *111*(B12404), doi: 10.1029/2005JB003879.

- Cannat, M. (1993), Emplacement of Mantle Rocks in the Seafloor at Mid-Ocean Ridges, *J. geophys. Res.*, *98*(B3), 4163–4172.
- Cannat, M., C. Romevaux-Jestin, and H. Fujimoto (2003), Melt supply variations to a magma-poor ultra-slow spreading ridge (Southwest Indian Ridge 61° to 69°E), *Geochem. Geophys. Geosys.*, *4*(9104), doi: 10.1029/2002GC000480.
- Cannat, M., D. Sauter, V. Mendel, E. Ruellan, K. Okino, J. Escartin, V. Combiér, and M. Baala (2006), Modes of seafloor generation at a melt-poor ultraslow-spreading ridge, *Geology*, *34*(7), doi: 10.1130/G22486.1.
- Cannat, M., D. Sauter, A. Bezos, C. Meyzen, E. Humler, and M. L. Rigoleur (2008), Spreading rate, spreading obliquity, and melt supply at the ultraslow spreading Southwest Indian Ridge, *Geochem. Geophys. Geosys.*, *9*(Q04002), doi: 10.1029/2007GC001676.
- Crane, K., L. Johnson, B. Appelgate, C. Nishimura, R. Buck, C. Jones, P. Vogt, and R. Kos'yan (1997), Volcanic and Seismic Swarm Events on the Reykjanes Ridge and Their Similarities to Events on Iceland: Results of a Rapid Response Mission, *Marine Geophysical Researches*, *19*(4), 319–338, doi: 10.1023/A:1004298425881.
- DeMets, C., R. Gordon, D. Argus, and S. Stein (1994), Current plate motions, *Geophys. J. Int.*, *101*, 425–478.
- Dick, H. J., J. Lin, and H. Schouten (2003), An ultraslow-spreading class of ocean ridge, *Nature*, *426*, 405–412, doi: 10.1038/nature02128.
- Dieterich, J. (1994), A constitutive law for rate of earthquake production and its application to earthquake clustering, *J. Geophys. Res.*, *99*, 2601–2618.
- Dobre, C., I. Manighetti, L. Dorbath, C. Dorbath, D. Bertil, and J. Delmond (2007a), Crustal structure and magmato-tectonic processes in an active rift (Asal-Ghoubbet, Afar, East Africa): 2. Insights from the 23-year recording of seismicity since the last rifting event, *J. geophys. Res.*, *112*(B05406), doi: 10.1029/2006JB004333.
- Dobre, C., I. Manighetti, L. Dorbath, C. Dorbath, D. Bertil, and J. Delmond (2007b), Crustal structure and magmato-tectonic processes in an active rift (Asal-Ghoubbet, Afar, East Africa): 1. Insights from a 5-month seismological experiment, *J. geophys. Res.*, *112*(B05405), doi: 10.1029/2005JB003940.
- Dziak, R., D. Bohnenstiehl, J. Cowen, E. Baker, K. Rubin, J. Haxel, and M. Fowler (2007), Rapid dike emplacement leads to eruptions and hydrothermal plume release during seafloor spreading events, *Geology*, *35*(7), doi: 10.1130/G23476A.
- Dziak, R. P., and C. G. Fox (1999), The January 1998 earthquake swarm at Axial Volcano, Juan de Fuca Ridge: hydroacoustic evidence of seafloor volcanic activity, *Geophys. Res. Lett.*, *26*(23), 3429–3432, doi: 10.1029/1999GL002332.

- Dziak, R. P., C. G. Fox, and A. E. Schreiner (1995), The June-July 1993 seismo-acoustic event at CoAxial segment, Juan de Fuca Ridge: Evidence for a lateral dike injection, *Geophys. Res. Lett.*, *22*(2), 135–138, doi: 10.1029/94GL01857.
- Dziak, R. P., D. K. Smith, D. R. Bohnenstiehl, C. G. Fox, D. Desbruyeres, H. Matsumoto, M. Tolstoy, and D. J. Fornari (2004), Evidence of a recent magma dike intrusion at the slow spreading Lucky Strike segment, Mid-Atlantic Ridge, *J. geophys. Res.*, *109*(B12102), doi: 10.1029/2004JB003141.
- Edmonds, H., et al. (2003), Discovery of abundant hydrothermal venting on the ultraslow-spreading Gakkel ridge in the Arctic Ocean, *Nature*, *421*, 252–256, doi: 10.1038/nature01351.
- Edwards, M., G. Kurras, M. Tolstoy, D. Bohnenstiehl, B. Coakley, and J. Cochran (2001), Evidence of recent volcanic activity on the ultraslow-spreading Gakkel Ridge, *Nature*, *409*, 808–812, doi: 10.1038/35057258.
- Einarsson, P. (1991), Earthquakes and present-day tectonism in Iceland, *Tectonophysics*, *189*, 261–279, doi: 10.1016/0040-1951(91)90501-I.
- Einarsson, P., and B. Brandsdottir (1980), Seismological evidence for lateral magma intrusion during the July 1978 deflation of the Krafla volcano in NE-iceland, *Journal of Geophysics*, *47*, 160–165.
- Ekström, G. (1994), Anomalous earthquakes on volcano ring-fault structures, *Earth planet. Sci. Lett.*, *128*, 707–712, doi: 10.1016/0012-821X(94)90184-B.
- Ekström, G., A. Dziewonski, N. Maternovskaya, and M. Nettles (2005), Global seismicity of 2003: Centroid-moment-tensor solutions for 1087 earthquakes, *Earth and Planetary Inter.*, *148*, 327–351, doi: 10.1016/j.pepi.2004.09.006.
- Escartin, J., D. Smith, J. Cann, H. Schouten, C. Langmuir, and S. Escrig (2008), Central role of detachment faults in accretion of slow-spreading oceanic lithosphere, *Nature*, *455*, 790–795, doi: 10.1038/nature07333.
- Evans, J., D. Eberhart-Phillips, and C. Thurber (1994), User Manual for SIMULPS12 for imaging Vp and Vp/Vs: A derivative of the Thurber tomographic inversion SIMUL3 for local earthquakes and explosives, *USGS Open file report*, *455*, 94–431.
- Fitch, T. (1975), Compressional velocity in source regions of deep earthquakes: an application of the master event technique, *Earth planet. Sci. Lett.*, *26*(2), 156–166, doi: 10-1016/0012-821X(75)90083-7.
- Font, Y., H. Kao, S. Lallemand, C.-S. Liu, and L.-Y. Cio (2004), Hypocentral determination offshore Eastern Taiwan using the Maximum Intersection method, *Geophys. J. Int.*, *158*(2), 655–675, doi: 10.1111/j.1365-246X.2004.02317.x.

- Foulger, G., R. Long, P. Einarsson, and A. Bjornsson (1989), Implosive earthquakes at the active accretionary plate boundary in northern Iceland, *Nature*, *337*, 640–642, doi: 10.1038/337640a0.
- Foulger, G. R., and B. R. Julian (1993), Non-Double-Couple Earthquakes at the Hengill-Grensdalur Volcanic Complex, Iceland: Are they Artifacts of Crustal Heterogeneity?, *Bull. seism. Soc. Am.*, *83*(1), 38–52.
- Fox, C., and R. Dziak (1998), Hydroacoustic detection of volcanic activity on the Gorda Ridge, February-March 1996, *Deep-Sea Res.*, *45*(12), 2513–2530, doi: 10.1016/S0967-0645(98)00081-2.
- Ghilani, C. (2010), Error Ellipse, in *Adjustment Computations: Spatial Data Analysis*, edited by C. Ghilani and P. Wolf, Fifth ed., Wiley Online Library, doi: 10.1002/9780470586266.ch19.
- Goslin, J., et al. (2012), Spatiotemporal distribution of the seismicity along the Mid-Atlantic Ridge north of the Azores from hydroacoustic data: Insights into seismogenic processes in a ridge-hot spot context, *Geochem. Geophys. Geosys.*, *13*(2), doi: 10.1029/2011GC003828.
- Grandin, R., et al. (2011), Seismicity during lateral dike propagation: Insights from new data in the recent Manda Hararo-Dabbahu rifting episode (Afar, Ethiopia), *Geochem. Geophys. Geosys.*, *12*(Q0AB08), doi: 10.1029/2010GC003434.
- Grindlay, N., J. Madsen, C. Rommevaux-Jestin, and J. Sclater (1998), A different pattern of ridge segmentation and mantle Bouguer gravity anomalies along the ultra-slow spreading Southwest Indian Ridge (15°30'E to 25°E), *Earth planet. Sci. Lett.*, *161*, 243–253.
- Gutenberg, B., and C. Richter (1944), Frequency of earthquakes in California, *Bull. Seism. Soc. Am.*, *34*, 185–188.
- Gutenberg, B., and C. Richter (1954), Frequency and energy of earthquakes, in *Seismicity of the Earth and Associated Phenomena*, pp. 17–19, Princeton University Press.
- Gutenberg, B., and C. Richter (1956), Magnitude and energy of earthquakes, *Ann. Geophys.*, *53*, 7–12.
- Hainzl, S. (2002), Self-organization of earthquake swarms, *J. Geodynamics*, *35*(1-2), doi: 10.1016/S0264-3707(02)00060-1.
- Hainzl, S., and D. Marsan (2008), Dependence of the Omori-Utsu law parameters on main shock magnitude: Observations and modeling, *J. Geophys. Res.*, *113*(B10309), doi: 10.1029/2007JB005492.
- Helmstetter, A., and B. Shaw (2006), Relation between stress heterogeneity and aftershock rate in the rate-and-state model, *J. Geophys. Res.*, *111*(B07304), doi: 10.1029/2005JB004077.

- Hjaltadóttir, S., K. Vogfjörð, and R. Slunga (2011), A seismological image of the Eyjafjallajökull Plumbing System during 2009-2010, *Geophys. Res. Abstr.*, 13, EGU2011-12,221.
- Hooft, E. E. E., et al. (2010), A seismic swarm and regional hydrothermal and hydrologic perturbations: The northern Endeavour segment, February 2005, *Geochem. Geophys. Geosys.*, 11(12), doi: 10.1029/2010GC003264.
- Humphreys, E., and R. Clayton (1988), Adaption of back projection tomography to seismic travel time problems, *J. geophys. Res.*, pp. 1073–1085.
- Husen, S., and J. Hardebeck (2010), Earthquake location accuracy, *Community Online Resource for Statistical Seismicity Analysis*, doi: 10.5078/corssa-55815573.
- Husen, S., E. Kissling, N. Deichmann, S. Wiemer, D. Giardini, and M. Baer (2003), Probabilistic earthquake location in complex three-dimensional velocity models: Application to Switzerland, *J. geophys. Res.*, doi: 10.1029/2002JB001778.
- ISC (2008), International seismological centre, on-line bulletin, http://www.isc.ac.uk/Bull_thatcham, UK.
- Ishimoto, M., and K. Iida (1939), Observations sur les seisms enregistré par le microseismograph construite dernièrement (I), *Bull. Earthq. Res. Inst.*, 17, 443–478.
- Iyer, H. (1971), Variation of apparent velocity of teleseismic P Waves across the large-aperture seismic array, Montana, *J. geophys. Res.*, 76, 8554–8567.
- Jakobsson, M., R. Macnab, L. Mayer, R. Anderson, M. Edwards, J. Hatzky, H. Schenke, and P. Johnsson (2008), An improved bathymetric portrayal of the Arctic Ocean: Implications for ocean modeling and geological, geophysical and oceanographic analyses, *Geophys. Res. Lett.*, 35(L07602), doi: 10.1029/2008GL033520.
- Jokat, W., and M. Schmidt-Aursch (2007), Geophysical characteristics of the ultraslow spreading Gakkel Ridge, Arctic Ocean, *Geophys. J. Int.*, 168, doi: 10.1111/j.1365-246X.2006.03278.x.
- Jokat, W., O. Ritzmann, M. Schmidt-Aursch, S. Drachev, S. Gauger, and J. Snow (2003), Geophysical evidence for reduced melt production on the Arctic ultraslow Gakkel mid-ocean ridge, *Nature*, 423, 962–965, doi: 10.1038/nature01706.
- Jokat, W., J. Kollofrath, W. Geissler, and A. Jensen (2012), Crustal thickness and earthquake distribution south of the Logachev Seamount, Knipovich Ridge, *Geophys. Res. Lett.*, 39(L08302), doi: 10.1029/2012GL051199.
- Jordan, T., and K. Sverdrup (1981), Teleseismic location techniques and their application to earthquake clusters in the south-central Pacific, *Bull. seism. Soc. Am.*, 71(4), 1105–1130.
- Kagan, Y. Y., and H. Houston (2005), Relation between mainshock rupture process and Omori's

- law for aftershock moment release rate, *Geophys. J. Int.*, *163*, 1039–1048, doi: 10.1111/j.1365-246X.2005.02772.x.
- Kagan, Y. Y., and D. D. Jackson (1998), Spatial aftershock distribution: Effect of normal stress, *J. geophys. Res.*, *103*(B10), 24,453–24,467.
- Kanamori, H. (1977), The energy release of earthquakes, *J. geophys. Res.*, *82*, 2981–2987.
- Keir, D., et al. (2009), Evidence for focused magmatic accretion at segment centers from lateral dike injections captured beneath the Red Sea rift in Afar, *Geology*, *37*, 59–62, doi: 10.1130/G25147A.1.
- Kennett, B. (1992), Locating oceanic earthquakes: the influence of regional models and location criteria, *Geophys. J. Int.*, *188*(2), 848–854.
- Kennett, B., and E. Engdahl (1991), Traveltimes for global earthquake location and phase identification - IASP91 model, *Geophys. J. Int.*, *105*, 429–465.
- Kennett, B., M. Sambridge, and P. Williamson (1988), Subspace methods for large scale inverse problems involving multiple parameter classes, *Geophysical Journal*, *94*, 237–247.
- Kissling, E., W. Ellsworth, D. Eberhart-Phillips, and U. Kradorfler (1994), Initial reference models in local earthquake tomography, *J. geophys. Res.*, *99*(B10), doi: 10.1029/93JB03138.
- Kissling, E., S. Husen, and F. Haslinger (2001), Model parametrization in seismic tomography: a choice of consequences for the solution quality, *Phys. Earth planet. Inter.*, *123*, doi: 10.1016/S0031-9201(00)00203-X.
- Kisslinger, C. (1996), Aftershocks and fault-zone properties, *Adv. geophys.*, *38*, 1–36.
- Klein, F. W., T. Wright, and J. Nakata (2006), Aftershock decay, productivity, and stress rates in Hawaii: Indicators of temperature and stress from magma sources, *J. geophys. Res.*, *111*(B7), doi: 10.1029/2005JB003949.
- Korger, E. (2010), The Volcanic Earthquake Swarm of 1999 at the Eastern Gakkel Ridge, Arctic Ocean: A Case Study for a Comparison between a Probabilistic- and a Conventional Teleseismic Algorithm, Master’s thesis, University of Vienna.
- Korger, E. I. M., and V. Schlindwein (2012), Performance of localisation algorithms for teleseismic mid-ocean ridge earthquakes: The 1999 Gakkel ridge earthquake swarm and its geological interpretation, *Geophys. J. Int.*, *188*(2), doi: 10.1111/j.1365-246X.2011.05282.x.
- Korger, E. I. M., and V. Schlindwein (2013), Seismicity and structure of the 85°E volcanic complex at the ultraslow spreading Gakkel ridge from local earthquake tomography, Submitted to *Geophys. J. Int.* on June 6th, 2013.

- Koulakov, I. (2009), LOTOS code for local earthquake tomographic inversion. Benchmarks for testing tomographic algorithms, *Bull. seism. Soc. Am.*, *99*(1), 194–214, doi: 10.1785/0120080013.
- Läderach, C., and V. Schlindwein (2011), Seismic arrays on drifting ice floes: experiences from four deployments in the Arctic Ocean, *Seismological Research Letters*, *82*(4), 488–497, doi: 10.1785/gssrl.82.4.494.
- Läderach, C., V. Schlindwein, H.-W. Schenke, and W. Jokat (2011), Seismicity and active tectonic processes in the ultra-slow spreading Lena Trough, Arctic Ocean, *Geophys. J. Int.*, *184*(3), doi: 10.1111/j.1365-246X.2010.04926.x.
- Läderach, C., E. Korger, V. Schlindwein, C. Müller, and A. Eckstaller (2012), Characteristics of tectonomagmatic earthquake swarms at the Southwest Indian Ridge between 16°E and 25°E, *Geophys. J. Int.*, *190*, 429–441, doi: 10.1111/j.1365-246X.2012.05480.x.
- Le Pichon, X. (1968), Sea-floor spreading and continental drift, *J. Geophys. Res.*, *73*, 3661–3996.
- Lin, G., and P. Shearer (2005), Tests of relative earthquake location techniques using synthetic data, *J. geophys. Res.*, *110*(B04304), doi: 10.1029/2004JB003380.
- Lomax, A., J. Virieux, P. Volant, and C. Berge (2000), Probabilistic earthquake location in 3D and layered models: Introduction of a Metropolis-Gibbs method and comparison with linear locations, *Advance in Seismic Event Location*, *452*, 101–134.
- Lomax, A., A. Michelini, and A. Curtis (2009), Earthquake Location, Direct, Global-Search Methods, *Encyclopedia of Complexity and System Science*, *5*.
- Macdonald, K. C. (1982), MID-OCEAN RIDGES: Fine Scale Tectonic, Volcanic and Hydrothermal Processes Within the Plate Boundary Zone, *Ann. rev. Earth Planet. Sci.*, *10*, 155–190.
- Magde, L., A. Barclay, D. Toomey, R. Detrick, and J. Collins (2000), Crustal magma plumbing within a segment of the Mid-Atlantic Ridge, 35°N, *Earth Planet. Sci. Lett.*, *175*, doi: 10.1016/S0012-821X(99)00281-2.
- Maus, S. (2009), EMAG2: A 2-arc min resolution earth magnetic anomaly grid compiled from satellite, airborne, and marine magnetic measurements, *Geochem. Geophys. Geosys.*, *10*(8), doi: 10.1029/2009GC002471.
- McKenzie, D., J. Jackson, and K. Priestley (2005), Thermal structure of oceanic and continental lithosphere, *Earth Planet. Sci. Lett.*, *233*(3-4), doi: 10.1016/j.epsl.2005.02.005.
- McNutt, S. (1996), Seismic Monitoring and Eruption Forecasting of Volcanoes: A Review of the State of the Art and Case Histories, in *Monitoring and Mitigation of Volcano Hazards*, edited by R. Scarpa and R. Tilling, pp. 99–146, Springer-Verlag, Berlin.

- Michael, P., et al. (2003), Magmatic and amagmatic seafloor generation at the ultraslow-spreading Gakkel ridge, Arctic Ocean, *Nature*, *423*, 956–961, doi: 10.1038/nature01704.
- Mikumo, T., and T. Miyatake (1979), Earthquake sequences on a frictional fault model with non-uniform strengths and relaxation times, *Geophys. J. R. Astron. Soc.*, *59*, 497–522.
- Mikumo, T., and T. Miyatake (1983), Numerical modeling of space and time variations of seismic activity before major earthquakes, *Geophys. J. R. Astron. Soc.*, *74*, 559–583.
- Mogi, K. (1963), Some Discussion on Aftershocks, Foreshocks and Earthquake Swarms - the Fracture of a Semi-infinite Body Caused by an Inner Stress Origin and Its Relation to the Earthquake Phenomena, *Bulletin of the Earthquake Research Institute*, *41*, 615–658.
- Mogi, K. (1967), Earthquakes and fractures, *Tectonophysics*, *5*, 35–55.
- Montesi, L., and M. Behn (2007), Mantle flow and melting underneath oblique and ultraslow mid-ocean ridges, *Geophys. Res. Lett.*, *34*(L24307), doi: 10.1029/2007GL031067.
- Moser, T., and T. V. Eck (1992), Hypocenter Determination in Strongly Heterogeneous Earth Models Using the Shortest Path Method, *J. geophys. Res.*, *97*(B5), 6563–6572.
- Mueller, C., and W. Jokat (2000), Seismic Evidence for Volcanic Activity Discovered in Central Arctic, *Eos, Trans. Am. geophys. Un.*, *81*(24), 265–269, doi: 10.1029/00EO00186.
- Narteau, C., P. Shebalin, and M. Holschneider (2002), Temporal limits of the power law aftershock decay rate, *J. Geophys. Res.*, *107*(B12), doi: 10.1029/2002JB001868.
- Nyffenegger, P., and C. Frohlich (1998), Recommendations for Determining p Values for Aftershock Sequences and Catalogs, *Bull. seism. Soc. Am.*, *88*(5), 1144–1154.
- Ogata, Y. (1983), Estimation of the parameters in the modified Omori formula for aftershock frequencies by the maximum likelihood procedure, *J. Phys. Earth*, *31*, 115–124.
- Ogata, Y. (2006), Statistical analysis of seismicity - updated version (saseis2006), in *Computer Science Monographs*, vol. 33, p. pp 29, The Institute of Statistical Mathematics, Tokyo, Japan.
- Omori, F. (1894), On the after-shocks of earthquakes, *J. Coll. Sci., Tokyo Imp. Univ.*, pp. 111–200.
- Pan, J., M. Antolik, and A. Dziewonski (2001), Locations of mid-oceanic earthquakes constrained by seafloor bathymetry, *J. geophys. Res.*, *107*(B11), doi: 10.1029/2001JB001588.
- Pontbriand, C., S. Soule, R. Sohn, S. Humphris, C. Kunz, H. Singh, K. Nakamura, M. Jakobsson, and T. Shank (2012), Effusive and explosive volcanism on the ultraslow-spreading Gakkel Ridge, 85°E, *Geochem. Geophys. Geosys.*, *13*(10), doi: 10.1029/2012GC004187.

- Rawlinson, N., and B. Kennett (2008), Teleseismic tomography of the upper mantle beneath the southern Lachlan Orogen, Australia, *Phys. Earth Planet. Int.*, 3167, doi: 10.1016/j.pepi.2008.02.007.
- Rawlinson, N., and M. Sambridge (2003), Seismic traveltime tomography of the crust and lithosphere, *Advances in Geophysics*, 46, 81–197.
- Rawlinson, N., M. de Kool, and M. Sambridge (2006), Seismic wavefront tracking in 3D heterogeneous media: applications with multiple data classes, *Exploration Geophysics*, 37, doi: 10.1071/EG06322.
- Reid, I., and H. Jackson (1981), Oceanic spreading rate and crustal thickness, *Mar. Geophys. Res.*, 5, 165–172.
- Riedel, C., and V. Schlindwein (2010), Did the 1999 earthquake swarm on Gakkel Ridge open a volcanic conduit? A detailed teleseismic data analysis, *Journal of Seismology*, 14 (3), 505–522, doi: 10.1007/s10950-009-9179-6.
- Rubin, A. M., and D. Gillard (1998), Dike-induced earthquakes: theoretical considerations, *J. geophys. Res.*, 103(B5), 10,017–10,030.
- Rundquist, D., and P. Sobolev (2002), Seismicity of mid-ocean ridges and its geodynamic implications: a review, *Earth-Science Reviews*, 58, 143–161, doi: 10.1016/S0012-8252(01)00086-1.
- Rydelek, P. A., and I. S. Sacks (1989), Testing the completeness of earthquake catalogues and the hypothesis of self-similarity, *Nature*, 337, 251–253.
- Sauter, D., and M. Cannat (2010), The Ultraslow Spreading Southwest Indian Ridge, in *Diversity of Hydrothermal Systems on the Slow Spreading Ocean Ridges*, *Geophysical Monograph Series*, vol. 188, American Geophysical Union, Washington, DC.
- Schlindwein, V. (2012), Teleseismic earthquake swarms at ultraslow spreading ridges: indicator for dike intrusions?, *Geophys. J. Int.*, 11, doi: 10.1111/j.1365-246X.2012.05502.x.
- Schlindwein, V., and J. Linder (2007), Characteristic microearthquakes of the active submarine volcanic complex at 85°E, Gakkel Ridge, *Eos Trans. AGU, Fall Meet. Suppl.*, 88(52), OS42A–02.
- Schlindwein, V., and C. Riedel (2010), Location and source mechanism of sound signals at Gakkel ridge, Arctic Ocean: Submarine Strombolian activity in the 1999–2001 volcanic episode, *Geochem. Geophys. Geosys.*, 11(Q01002), doi: 10.1029/2009GC002706.
- Schlindwein, V., C. Müller, and W. Jokat (2005), Seismoacoustic evidence for volcanic activity on the ultraslow-spreading Gakkel Ridge, Arctic Ocean, *Geophys. Res. Lett.*, 32(L18306), doi: 10.1029/2005GL023767.

- Schlundwein, V., C. Müller, and W. Jokat (2007), Microseismicity of the ultraslow-spreading Gakkel ridge, Arctic Ocean: a pilot study, *Geophys. J. Int.*, *169*, doi: 10.1111/j.1365-246X.2006.03308.x.
- Schlundwein, V., A. Demuth, W. Geissler, and W. Jokat (2013), Seismic gap beneath Logachev seamount: indicator for melt focusing at an ultraslow mid-ocean ridge?, *Geophys. Res. Lett.*, doi: 10.1002/grl.50329.
- Scholz, H. (1990), *The Mechanics of Earthquakes and Faulting*, Cambridge University Press, Cambridge, UK.
- Schweitzer, J. (2001), HYPOSAT - an enhanced routine to locate seismic events, *Pure applied Geophysics*, *158*, 277–289.
- Schweitzer, J., and B. Kennett (2007), Comparison of Location Procedures: The Kara Sea Event of 16 August 1997, *Bull. seism. Soc. Am.*, *97*, doi: 10.1785/0120040017.
- Schweitzer, J., J. Fyen, S. Mykkeltveit, and T. Kvaerna (2009), xxx, in *New Manual of Seismological Observatory Practice*, p. 52, GFZ, Potsdam.
- Scordilis, E. (2006), Empirical global relations converting m_s and m_b to moment magnitude, *Journal of Seismology*, *10*, 225–236.
- Sella, G., T. Dixon, and A. Mao (2002), REVEL: A model for recent plate velocities from space geodesy, *J. Geophys. Res.*, *107*(B4), ETG 11–1 – ETG 11–30, doi: 10.1029/2000JB000033.
- Sethian, J. A. (1996), A fast marching level set for monotonically advancing fronts, *Proceedings of the National Academy of Sciences*, *93*, 1591–1595.
- Sethian, J. A., and A. Popovici (1999), 3-D traveltime computation using the fast marching method, *Geophysics*, *64*, 516–523.
- Shcherbakov, R., D. Turcotte, and J. Rundle (2004), A generalized Omori’s law for earthquake aftershock decay, *Geophys. Res. Lett.*, *31*(L11613), doi: 10.1029/2004GL019808.
- Shuler, A., and G. Ekström (2009), Anomalous earthquakes associated with Nyiragongo Volcano: Observations and potential mechanisms, *J. Volc. Geotherm. Res.*, *181*, 219–230, doi: 10.1016/j.volgeo.2009.01.011.
- Simao, N., J. Escartin, J. Haxel, M. Cannat, and R. Dziak (2010), Regional seismicity of the Mid-Atlantic Ridge: observations from autonomous hydrophone arrays, *Geophys. J. Int.*, *183*, 1559–1578, doi: 10.1111/j.1365-246X.2010.04815.x.
- Smith, D., M. Tolstoy, C. Fox, D. Bohnenstiehl, H. Matsumoto, and M. Fowler (2002), Hydroacoustic monitoring of seismicity at the slow-spreading Mid-Atlantic Ridge, *Geophys. Res. Lett.*, *29*, doi: 10.1029/2001GL013912.

-
- Smith, W., and D. Sandwell (1997), Global seafloor topography from satellite altimetry and ship depth soundings, *Science*, *277*, 1956–1962.
- Sohn, R. A., and J. Hildebrand (2001), Hydroacoustic earthquake detection in the Arctic Basin with the Spinnaker Array, *Bull. seism. Soc. Am.*, *91*(3), 572–579.
- Sohn, R. A., A. H. Barclay, and S. C. Webb (2004), Microearthquake patterns following the 1998 eruption of Axial Volcano, Juan de Fuca Ridge: Mechanical relaxation and thermal strain, *J. geophys. Res.*, *109*(B01101), doi: 10.1029/2003JB002499.
- Sohn, R. A., et al. (2008), Explosive volcanism on the ultraslow-spreading Gakkel ridge, Arctic Ocean, *Nature*, *453*, 1236–1238, doi: 10.1038/nature07075.
- Solomon, S. C. (1992), The structure of mid-ocean ridges, *Annu. rev. Earth Planet. Sci.*, *20*, 329–364.
- Solomon, S. C., P. Y. Huang, and L. Meinke (1988), The seismic moment budget of slowly spreading ridges, *Nature*, *334*, 58–60, doi: 10.1038/334058a0.
- Spakman, W., and G. Nolet (1988), Imaging algorithms, accuracy and resolution in delay time tomography, in *Mathematical Geophysics*, pp. 155–187, Springer Netherlands.
- Standish, J. J., and K. W. Sims (2010), Young off-axis volcanism along the ultraslow-spreading Southwest Indian Ridge, *Nature*, doi: 10.1038/NGEO824.
- Standish, J. J., J. Dick, P. Michael, W. Melson, and T. O’Hearn (2008), MORB generation beneath the ultraslow spreading Southwest Indian Ridge (9 – 25°E): Major element chemistry and the importance of process versus source, *Geochem. Geophys. Geosys.*, *9*(5), doi: 10.1029/2008GC001959.
- Stranne, C., R. A. Sohn, B. Liljebladh, and K. ichi Nakamura (2010), Analysis and modeling of hydrothermal plume data acquired from the 85°E segment of the Gakkel Ridge, *J. geophys. Res.*, *115*(C06028), doi: 10.1029/2009JC005776.
- Tarantola, A., and B. Valette (1982), Inverse problems = quest for information, *J. Geophys.*, *50*, 159–170.
- Tarasewicz, J., B. Brandsdóttir, R. White, M. Hensch, and B. Thorbjarnardóttir (2012), Using microearthquakes to track repeated magma intrusions between the Eyjafjallajökull stratovolcano, Iceland, *J. geophys. Res.*, *117*, doi: 10.1029/2011JB008751.
- Tolstoy, M., A. Harding, and J. Orcutt (1993), Crustal thickness on the Mid-Atlantic Ridge: bull’s-eye gravity anomalies and focused accretion, *Science*, *262*, 726–729.
- Tolstoy, M., D. Bohnenstiehl, M. Edwards, and G. Kurras (2001), Seismic character of vol-

- canic activity at the ultraslow-spreading Gakkel Ridge, *Geology*, *29*(12), 1139–1142, doi: 10.1130/0091-7613(2001)029.
- Tolstoy, M., et al. (2006), A Sea-Floor Spreading Event Captured by Seismometers, *Science*, *314*, 1920–1922, doi: 10.1126/science.1133950.
- Tolstoy, M., F. Waldhauser, D. Bohnenstiehl, R. Weekly, and W.-Y. Kim (2008), Seismic identification of along-axis hydrothermal flow on the East Pacific Rise, *Nature*, *451*, 181–185, doi: 10.1038/nature06424.
- Toomey, D. R., S. C. Solomon, G. Purdy, and M. H. Murray (1985), Microearthquakes Beneath the Median Valley of the Mid-Atlantic Ridge Near 23°N: Hypocenters and Focal Mechanisms, *J. geophys. Res.*, *90*(B7), 5443–5458.
- Toomey, D. R., G. Purdy, S. Solomon, and W. Wilcock (1990), The Three-Dimensional seismic velocity structure of the East Pacific Ridge near latitude 9°30'N, *Nature*, *347*, 639–645.
- Tryggvason, A. (2009), User manual *PSTOMO_eq*, uppsala University, Sweden.
- Tsapanos, T. M. (1995), The temporal distribution of aftershock sequences in the subduction zones in the Pacific, *Geophys. J. Int.*, *123*, 633–636.
- Utsu, T. (1961), A statistical study on the occurrence of aftershocks, *Geophys. Mag.*, *30*, 521–605.
- Utsu, T. (2002), Statistical features of seismicity, in *International Handbook of Earthquake and Engineering Seismology, Part A*, edited by W. Lee, H. Kanamori, P. Jennings, and C. Kisslinger, pp. 719–732, Academic Press, New York, doi: 10.1016/S0074-6142(02)80246-7.
- Utsu, T., Y. Ogata, and R. S. Matsu'ura (1995), The Centenary of the Omori Formula for a Decay Law of Aftershock Activity, *J. Phys. Earth*, *43*, 1–33.
- Vine, F., and D. Matthews (1963), Magnetic anomalies over oceanic ridges, *Nature*, *199*, 947–949.
- Wadati, K. (1933), On the travel time of earthquake waves, *Geophys. Mag.*, *7*, 101–111.
- Wessel, P., and W. Smith (1998), New, improved version of generic mapping tools released, *Eos, Trans. Am. geophys. Un.*, *79*, 579.
- Wiens, D., J. McGuire, P. Shore, and M. Bevis (1994), A deep earthquake aftershock sequence and implications for the rupture mechanism of deep earthquakes, *Nature*, *372*, 540–543.
- Wittlinger, G., G. Herquel, and T. Nakache (1993), Earthquake location in strongly heterogeneous media, *Geophys. J. Int.*, *115*, 759–777.

- Woessner, J., and S. Wiemer (2005), Assessing the quality of earthquake catalogues: estimating the magnitude of completeness and its uncertainty, *Bull. seism. Soc. Am.*, *95*, 684–698.
- Wolfe, C. (2002), On the Mathematics of Using Difference Operators to Relocate Earthquakes, *Bull. seism. Soc. Am.*, *92*(8), 2879–2892.
- Zhao, H. (1992), Tomographic imaging of P and S wave velocity structure beneath northeastern Japan, *J. geophys. Res.*, *97*, 19,909–19,928.
- Zhou, H. (1994), Rapid 3D hypocentral determination using a master station method, *J. geophys. Res.*, *99*, 15,439–15,455.

11 List of Figures

1.1	Cross section of MORs with different spreading rates	1
1.2	Hemispheric overview of southern and northern hemisphere	3
1.3	Overview of the Southwest Indian Ridge	4
1.4	Overview of Gakkel Ridge	5
1.5	Detailed overview of Gakkel Ridge	6
1.6	Schematic 3D along-axis cross section illustrating the tectonomagmatic mid-ocean ridge basalt generation model	8
1.7	Bathymetric chart of the area at 85°E/85°N	11
2.1	Drift paths and 128 epicentres localized by Hyposat localized earthquakes .	17
2.2	Ray coverage for 128 events localized by Hyposat	18
3.1	Comparison of epicentres of the well-located dataset by EHB, NonLinLoc and Hyposat	22
3.2	Relocated epicentres of events at Lena Trough between 1963 and 2009 by Hyposat and NonLinLoc, more than or equal to 50 phases used in localization	23
3.3	Relocated epicentres of events at Lena Trough between 1963 and 2009 by Hyposat and NonLinLoc, less than 50 phases used in localization	24
3.4	Three different types of seismic sequences	26
3.5	Fit of the modified Omori-Law to the Fukui earthquake sequence.	31
3.6	Fit of the modified Omori-Law to three seismic sequences at the Mid-Atlantic Ridge	31
3.7	Location of earthquake sequences at the SWIR	33
3.8	Location of earthquake clusters at the Gakkel Ridge	34
3.9	Fit of the modified Omori-Law to the earthquake cluster 'swirdisgal21' . .	36
3.10	Magnitudes of the earthquake cluster 'arevz37'	37
3.11	Fit of the modified Omori-Law to different parts of the 1999 earthquake sequence	38
3.12	Examples of an emergent P-phase and and impulsive P-phase	40
3.13	Comparison of the average quality parameters for all tested velocity models with individually free and fixed depth location averaged	42
3.14	Comparison of the average quality parameters for all velocity models for all selected solutions	43
3.15	Flow chart for use of the travelttime tomography algorithm FMTOMO . . .	44
5.1	Overview of Gakkel ridge	53
5.2	Epicentral and backazimuth distribution of the 1999 swarm	55

5.3	Comparison of epicentres of the 1999 swarm relocalized by HYPOSAT, NonLinLoc and Mlocate	61
5.4	Temporal evolution of the 1999 swarm	64
5.5	NonLinLoc maximum likelihood epicentres for well located events of the 1999 swarm	66
5.6	Visualization of NonLinLoc pdfs of all well-located events and of two exemplary scatterclouds	67
5.7	Spatial evolution of the 1999 swarm: NonLinLoc scatterpoints and Mlocate epicenters for three temporal phases	69
6.1	Overview of the Southwest Indian Ridge	78
6.2	Overview of the Oblique and Orthogonal Supersegments and VNA2 array detections	80
6.3	Teleseismic relocalization	81
6.4	Regional seismicity of the Oblique and Orthogonal Supersegment	87
6.5	Magnitude comparison and waveform examples	89
6.6	Cumulative number and location of swarm events	91
6.7	Waveform coherence of swarm events	92
6.8	Characterization of swarm duration, moment release and event rate	94
6.9	3D-bathymetric view of the swarm location	95
7.1	Overview of Gakkel ridge	106
7.2	Survey region of the 85°E/85°N volcanic complex with driftpaths of the icefloes	108
7.3	Distance of microseismicity epicentres to Oden volcano	109
7.4	95 randomly created velocity models, specially indicated are velocity models used in preliminary location and tomographic inversion	111
7.5	EW slice through the modelled region by FMTOMO	113
7.6	Model perturbation and model roughness for the tested combination of parameters	114
7.7	Result of the P-wave velocity inversion based on the different reference velocity models	117
7.8	P-wave velocity inversion result	118
7.9	Sum of ray points	119
7.10	Synthetic and recovered checkerboard and restoration model	121
7.11	P-wave inversion result and bathymetric structure as horizontal and along axis plot	125
7.12	Supplementary figure showing P-wave velocity inversion result in horizontal slices and hypocentre locations	128
7.13	Supplementary figure showing P-wave velocity inversion result in vertical slices and hypocentre locations	129
7.14	Supplementary figure showing sum or ray points from FMTOMO in horizontal slices and hypocentre locations	130
7.15	Supplementary figure showing sum or ray points from FMTOMO in vertical slices and hypocentre locations	131

12 List of Tables

3.1	Number of events and magnitude of completeness of four seismicity clusters at the SWIR for which a fit with the MOL was attempted.	32
3.2	Number of events and magnitude of completeness of four seismicity clusters at the SWIR and the GR which were attempted to be fitted by the MOL.	34
3.3	Calculated MOL parameters for the four earthquake clusters at the SWIR.	35
3.4	Calculated MOL parameters for two earthquake clusters at the SWIR.	36
3.5	Calculated MOL parameters for the 1999 earthquake sequence.	37
5.1	Local velocity model for the 85°E/85°N region from <i>Riedel and Schlindwein</i> (2010), (<i>Korger and Schlindwein</i> , 2012)	58
5.2	Mean difference in epicentres of the 1999 swarm between three localization algorithms (<i>Korger and Schlindwein</i> , 2012)	60
5.3	Mean 95% error ellipse semi-axes of the 1999 swarm of three localization algorithms (<i>Korger and Schlindwein</i> , 2012)	60
5.4	Mean 95% quality parameters for the well- and badly located dataset of the 1999 swarm for three localization algorithms (<i>Korger and Schlindwein</i> , 2012)	62
6.1	Summary of the four seismicity clusters at the Southwest Indian Ridge (<i>Läderach et al.</i> , 2012)	93
7.1	Overall traveltime residual RMS of each combinations of grid cells of propagation and velocity grid (<i>Korger and Schlindwein</i> , 2013)	113



Edith I.M. Korger

Georg-Seebeck-Str 60
D-27570 Bremerhaven
E-mail: eim:at:ekorger.de
Tel: +49 152 08987328
13.9.1975

Education:

- Alfred Wegener Institute for Polar and Marine Research, Bremerhaven, Germany
c/o University of Bremen, Department of Geoscience, Germany:
PhD. Geophysics, May 2010 - *ongoing*
Seismicity and structure of a magmatic accretionary centre at an ultraslow spreading ridge: The volcanic centre at 85°E/85°N, Gakkel ridge'
- University of Vienna, Vienna, Austria:
Mag. rer. nat, Geophysics, Oct 2005 - Oct 2010
'The Volcanic Earthquake Swarm of 1999 at the Eastern Gakkel Ridge, Arctic Ocean: A Case Study for a Comparison between a Probabilistic- and a Conventional Teleseismic Algorithm'
- General qualification for university entrance: May 1995

Teaching experience, Internships, Voluntary Service:

- 2012: TUTech Innovation, Research Management Training Workshop
- 2011: AWI Bremerhaven, Voluntary representative of doctorate students to directorate of AWI
- 2008: Zentralanstalt für Meteorologie und Geodynamik (ZAMG), Internship Seismological Service
- 2007, 2008, 2009: Leopold Franzens University Innsbruck, Teaching Assistant, Geophysical Data Acquisition
- 2006, 2007, 2008: OMV Exploration and Production GmbH, Internship Seismics Dept.

Field work:

- 2012: AWI Bremerhaven, FS Polarstern, Antarctica, OBS deployment, Bathymetric interpretation
- 2010: AWI Bremerhaven, FS Polarstern, Baffin Bay, OBS deployment and recovery
- 2008: AWI Bremerhaven, FS Polarstern, Lena Trough, Seismological stations on ice floes
- 2006: GFZ Potsdam, Israel, Reflection seismics

Publications, scientific papers:

- E. I. M. Korger and V. Schlindwein (2013), *Seismicity and structure of the 85°E volcanic complex at the ultraslow spreading Gakkel ridge from local earthquake tomography (submitted, in review)*.
- C. Läderach, Korger E., Schlindwein V., Müller C. and Eckstaller A. (2012), Characteristics of tectono-magmatic earthquake swarms at the Southwest Indian Ridge between 16°E and 25°E. *Geophysical Journal International*, 190(1), pp 429-441, doi: 10.1111/j.1365-246X.2012.05480.x
- E. I. M. Korger and V. Schlindwein (2012), Performance of localization algorithms for teleseismic mid-ocean ridge earthquakes: the 1999 Gakkel Ridge earthquake swarm and its geological interpretation. *Geophysical Journal International*, 188(2), pp 613-625, doi: 10.1111/j.1365-246X.2011.05282.x

Publications, selected posters:

- E. I. M. Korger and V. Schlindwein (2013), Insights into an ultraslow volcanic spreading centre by an unusual LET: Seismometers mounted on ice floes. EGU 2013, Vienna.
- E. I. M. Korger and V. Schlindwein (2012), The 2007 seismological aftermath of the spreading episode of 1999 at Gakkel ridge, Arctic Ocean. 72. Jahrestagung der Deutschen Geophysikalischen Gesellschaft, Hamburg.
- E. Korger and Schlindwein, V. (2011), Teleseismic location of earthquakes along the Arctic mid-ocean ridge system. European Seismological Commission 32nd General Assembly, Vienna.

Research interests:

I am especially interested in computational seismology and statistical analysis of local earthquake datasets. Also, I would like to study volcano-induced seismicity during repose time as well as during actual dike migration.

Job experience prior to University entrance (prior to Oct 2005):

- 2004/2005: UPS-SCS Logistics, Assistant of Management
- 2003/2004: Docu AG, Assistant of Management
- 2002/2003: Boehringer Ingelheim Austria, Project Assistant
- 2001/2002: SAE Technology College (Multimedia Designer)
- 1999/2000: Melbrosin International GesmbH, Desk Clerk
- 1997/1999: Psychotechnisches Institut Wien, Back Office
- 1996/1997: Torrex Pharma GesmbH, Desk Clerk

An assessment of my performance can be given by the following persons:

- Dr. Vera Schlindwein: Alfred-Wegener Institute, Helmholtz Centre for Polar and Marine Science; vera.schlindwein@awi.de
- Em.O.Univ.Prof.Dipl.-Ing.Dr.phil. Ewald Brückl: Vienna University of Technology; ebrueckl@mail.tuwien.ac.at
- Prof. Dr. Wilfried Jokat: Alfred-Wegener Institute, Helmholtz Centre for Polar and Marine Science; wilfried.jokat@awi.de

BIS DAHIN HAB' ICH JEDENFALLS WEISSGOTT MEINEN SPASS GEHABT...!! JETZT IST
ABER FEIERABEND!

WALTER MÖRS (VON GANZEM HERZEN)